

CUBESAT SYSTEM DESIGN BASED ON METHODOLOGIES ADOPTED FOR  
DEVELOPING WIRELESS ROBOTIC PLATFORM

By

SHARANABASAWESHWARA ASHOK ASUNDI

A DISSERTATION PRESENTED TO THE GRADUATE SCHOOL  
OF THE UNIVERSITY OF FLORIDA IN PARTIAL FULFILLMENT  
OF THE REQUIREMENTS FOR THE DEGREE OF  
DOCTOR OF PHILOSOPHY

UNIVERSITY OF FLORIDA

2011

© 2011 Sharanabasaweshwara Ashok Asundi

Dedicated to my parents, Smt. Nagarathna A. Asundi and Dr. Ashok Y. Asundi

## ACKNOWLEDGMENTS

Dr. Norman G. Fitz-Coy has not only been an academic advisor but has taught me the way to lead life. For long I've believed "Work is Worship" but through my advisor, I've come to realize its true meaning and ways of practicing it. I'm ever grateful to him for supporting me throughout my graduate studies and assisting me in earning my PhD.

I'd like to express my deepest gratitude towards Dr. Warren Dixon, Dr. John Schueller and Dr. Haniph Latchman for agreeing to serve on my committee and providing valuable inputs in completing my dissertation.

I'd like to take this opportunity to thank all my Space Systems Group colleagues, past and present, for being there with me all along and showing up on short notices. I'd also like to thank my course teachers, specially Dr. Anil Rao, for teaching me what I know today.

Lastly, I'd like to acknowledge and dedicate this dissertation to my parents for their never ending support and love throughout this endeavor.

## TABLE OF CONTENTS

	<u>page</u>
<b>ACKNOWLEDGMENTS . . . . .</b>	<b>4</b>
<b>LIST OF TABLES . . . . .</b>	<b>8</b>
<b>LIST OF FIGURES . . . . .</b>	<b>10</b>
<b>LIST OF ABBREVIATIONS . . . . .</b>	<b>12</b>
<b>ABSTRACT . . . . .</b>	<b>18</b>
 <b>CHAPTER</b>	
<b>1 INTRODUCTION . . . . .</b>	<b>20</b>
1.1 Definition and Classification of CubeSats . . . . .	21
1.2 Poly Picosatellite Orbital Deployer (P-POD) . . . . .	22
1.3 CubeSat Missions as Technology Demonstrators . . . . .	23
1.3.1 On Board Computing and Satellite Bus . . . . .	24
1.3.2 Electrical Power . . . . .	25
1.3.3 Telemetry, Tracking and Command . . . . .	27
1.3.4 Structural and Thermal . . . . .	28
1.3.5 Space Qualification and Testing . . . . .	29
1.3.6 Attitude Determination and Control . . . . .	29
1.4 CubeSats as Utility Spacecraft . . . . .	30
1.4.1 National Aeronautics and Space Administration's 3U CubeSats - Space Science . . . . .	30
1.4.2 Earth and Space Observing . . . . .	31
1.5 New Paradigms . . . . .	32
1.6 Motivation and Scope . . . . .	36
<b>2 LESSONS LEARNED FROM THE DESIGN AND DEVELOPMENT OF A TERRESTRIAL GROUND ROBOT . . . . .</b>	<b>41</b>
2.1 Definition of Unmanned Ground Vehicle (UGV) . . . . .	41
2.2 Classification of UGVs . . . . .	41
2.2.1 Teleoperated UGV . . . . .	42
2.2.2 Autonomous UGV . . . . .	42
2.2.2.1 Actuators . . . . .	43
2.2.2.2 Sensors . . . . .	43
2.2.2.3 Sensory Processing . . . . .	44
2.2.2.4 World Model . . . . .	44
2.2.2.5 Value Judgment . . . . .	44
2.2.2.6 Task Decomposition . . . . .	44
2.3 Design and Development of Terrestrial Ground Robot . . . . .	45
2.3.1 Customized Physical Platform . . . . .	47

2.3.2	System Hardware . . . . .	47
2.3.3	System Software . . . . .	49
2.3.4	Sensor Suite . . . . .	50
2.3.5	Modes of Operation . . . . .	52
2.3.6	Livingstone (L2) Based Health Management System . . . . .	53
2.3.6.1	Model Based Diagnosis and Modeling Approach . . . . .	54
2.3.6.2	L2 Based Health Management of LAWS-V . . . . .	54
<b>3</b>	<b>A SYSTEMS ENGINEERING APPROACH FOR DESIGN AND DEVELOPMENT OF PICO- AND NANO-CLASS CUBESATS . . . . .</b>	<b>59</b>
3.1	SwampSat Mission - Precision Pointing and Rapid Retargeting . . . . .	59
3.2	Design and Development Approach . . . . .	62
3.2.1	Mission Definition . . . . .	65
3.2.2	Mission Objectives . . . . .	65
3.2.2.1	Primary Mission Objectives (PMO) . . . . .	66
3.2.2.2	Secondary Mission Objectives (SMO) . . . . .	66
3.2.3	Mission Requirements - Functional and Performance Requirements . . . . .	66
3.2.3.1	Allocated Mission Requirements (AMR) . . . . .	66
3.2.3.2	Derived Mission Requirements (DMR) . . . . .	67
3.2.4	Mission Mapping . . . . .	69
3.2.5	Components, Interfaces and Tasks . . . . .	69
3.2.6	Concept of Operations (CONOPS) . . . . .	75
<b>4</b>	<b>DESIGN AND DEVELOPMENT OF ELECTRICAL POWER SYSTEM . . . . .</b>	<b>81</b>
4.1	Commercial-off-the-shelf Components of the Electrical Power System . . . . .	81
4.1.1	EPS Board . . . . .	82
4.1.2	Battery Board . . . . .	84
4.1.3	Solar Cells . . . . .	85
4.2	Multifunctional Solar Panel Design . . . . .	85
4.2.1	Solar Panel Design Implementation . . . . .	88
4.2.1.1	Carbon fiber composite solar panel . . . . .	88
4.2.1.2	Printed circuit board solar panel . . . . .	88
4.2.2	Solar Panel Tests, Results and Comparison . . . . .	89
4.3	Power Budget and Balance . . . . .	93
4.4	Software Architecture . . . . .	94
<b>5</b>	<b>DESIGN OF COMMAND, DATA AND TELEMETRY HANDLING . . . . .</b>	<b>98</b>
5.1	Safe-Hold Operating Mode . . . . .	99
5.1.1	Satellite Beacon . . . . .	100
5.1.2	Safe-hold Mode Uplink Command . . . . .	102
5.2	Detumble Operating Mode . . . . .	104
5.2.1	Detumble mode downlink telemetry . . . . .	106
5.2.2	Detumble mode uplink command . . . . .	107
5.3	Comms Operating Mode . . . . .	109

5.3.1	Comms mode uplink command . . . . .	110
5.4	ADS Operating Mode . . . . .	112
5.4.1	ADS mode downlink telemetry . . . . .	114
5.4.2	ADS mode uplink command . . . . .	114
5.5	CMG Ops Operating Mode . . . . .	116
5.5.1	CMG Ops mode downlink telemetry . . . . .	118
5.5.2	CMG Ops mode uplink command . . . . .	119
6	<b>DESIGN OF ATTITUDE DETERMINATION AND ESTIMATION SYSTEM</b> . . . . .	122
6.1	Deterministic Attitude Determination . . . . .	122
6.2	Stochastic Attitude Estimation . . . . .	127
6.3	Spacecraft Attitude Kinematics . . . . .	130
6.4	Distributed Attitude Determination and Estimation System . . . . .	132
6.4.1	Attitude Sensors . . . . .	133
6.4.1.1	Attitude sensor model . . . . .	134
6.4.2	Inertial Measurement Unit (IMU) . . . . .	135
6.4.2.1	Gyro model . . . . .	136
6.4.3	Attitude Estimation . . . . .	137
6.4.3.1	Attitude estimation using Sun sensors and magnetometer	137
6.4.3.2	Attitude estimation using magnetic field vector and its time derivative . . . . .	140
6.4.3.3	Attitude estimation using magnetic field vector . . . . .	143
6.5	Simulation and Results . . . . .	143
6.5.1	Estimation Results Using Sun Sensors and Magnetometer . . . . .	146
6.5.2	Estimation Results Using Magnetic Field Vector . . . . .	147
6.5.3	Estimation Results Using Magnetic Field Vector and its Time Derivative	151
7	<b>CONCLUSION AND FUTURE WORK</b> . . . . .	158
7.1	Conclusion . . . . .	158
7.2	Future Work . . . . .	160
	<b>APPENDIX: TESTS TO QUALIFY ELECTRICAL POWER SYSTEM</b> . . . . .	162
	<b>REFERENCES</b> . . . . .	208
	<b>BIOGRAPHICAL SKETCH</b> . . . . .	218

## LIST OF TABLES

<u>Table</u>	<u>page</u>
1-1 Sampled CubeSat Missions . . . . .	33
2-1 System Level Similarities Between LAWS-V and a CubeSat . . . . .	46
2-2 Simulated L2 scenarios and diagnosed failure causes . . . . .	57
3-1 Mapping Primary Mission Objectives to Building Blocks . . . . .	73
3-2 Mapping Secondary Mission Objectives to Building Blocks . . . . .	74
3-3 Communication Interfaces . . . . .	75
3-4 Peripheral Components, Sensors and Subsystem Boards . . . . .	76
3-5 Satellite Tasks . . . . .	77
4-1 Battery cell characteristics . . . . .	85
4-2 Composite Solar Panel vs PCB Solar Panel . . . . .	93
4-3 Detailed power budget . . . . .	94
4-4 Operating Modes Power Budget . . . . .	95
4-5 Tests to Qualify Electrical Power System . . . . .	96
5-1 Satellite Beacon - Safe-hold Mode Downlink Telemetry . . . . .	104
5-2 Safe-hold Mode Uplink Command . . . . .	105
5-3 Detumble Mode Downlink Telemetry . . . . .	108
5-4 Detumble Mode Uplink Command . . . . .	109
5-5 Comms Mode Uplink Command . . . . .	113
5-6 ADS Mode Downlink Telemetry . . . . .	116
5-7 ADS Mode Uplink Command . . . . .	117
5-8 CMG Ops Mode Downlink Telemetry . . . . .	120
5-9 CMG Ops Mode Uplink Command . . . . .	121
6-1 Computational Effort of Estimation Algorithm in FLOPS . . . . .	127
6-2 LEO Parameters for STK Scenario . . . . .	144
6-3 Attitude Data Generated for Simulation . . . . .	144

6-4	Simulation Parameters for Estimation Using Sun Sensors and Magnetometer . . . . .	148
6-5	Simulation Parameters for Estimation Using Magnetic Field Vector . . . . .	150
6-6	Simulation Parameters for Estimation Using Magnetic Field Vector and its Derivative	154
6-7	EKF Performance Comparison for Three Sensor Configurations . . . . .	156

## LIST OF FIGURES

<u>Figure</u>		<u>page</u>
1-1	Single CubeSats . . . . .	25
1-2	QuakeSat-1 . . . . .	26
1-3	NASA's 3U CubeSats . . . . .	32
2-1	Elements of an Intelligent System and their Relationship to Each Other . . . . .	43
2-2	System Level Composition of LAWS-V and a CubeSat . . . . .	46
2-3	LAWS-V System Design . . . . .	47
2-4	LAWS-V Hardware and Sensors . . . . .	48
2-5	PC104 Boards on LAWS-V . . . . .	50
2-6	LAWS-V Proximity and Range Sensors . . . . .	51
2-7	Object Sensing and Tracking Sensors . . . . .	52
2-8	L2 Model of LAWS-V . . . . .	55
2-9	Probable Causes for Failure of Steering Servo . . . . .	56
3-1	Rapid Retargeting and Precision Pointing . . . . .	61
3-2	Requirements Flowdown . . . . .	63
3-3	Subsystem Level Flowdown . . . . .	64
3-4	Mission Mapping of Primary Mission Objectives . . . . .	70
3-5	Mission Mapping of Secondary Mission Objectives . . . . .	71
3-6	Mapping Mission Objectives to Building Blocks . . . . .	72
3-7	SwampSat N2 Diagram . . . . .	75
3-8	SwampSat Mission CONOPS . . . . .	79
4-1	EPS Board Design Schematic . . . . .	83
4-2	Design for Implementing RBF Switch and Deployment Switch . . . . .	84
4-3	Solar Cell and Corresponding PCB Solar Panel . . . . .	86
4-4	Solar Panel Design . . . . .	87
4-5	A Multifunctional PCB Solar Panel . . . . .	90

4-6	Composite and PCB Solar Panel Implementations . . . . .	91
4-7	Plot of Supply Current vs Power Consumed . . . . .	92
4-8	SwampSat Software Architecture . . . . .	97
5-1	Power-Up Deploy and Safe-Hold Operating Modes . . . . .	101
5-2	Query Beacon Function . . . . .	102
5-3	Power-Up & Deploy and Safe-hold Operating Mode Functions . . . . .	103
5-4	Detumble Operating Mode . . . . .	106
5-5	Detumble Operating Mode Functions . . . . .	107
5-6	Battery Capacity Expressed as Voltage . . . . .	110
5-7	Comms Operating Mode . . . . .	111
5-8	Comms Operating Mode Functions . . . . .	112
5-9	ADS Operating Mode . . . . .	115
5-10	CMG Ops Operating Mode . . . . .	118
6-1	Spacecraft Body and Inertial Reference Frames . . . . .	131
6-2	SwampSat ADS as a Distributed System . . . . .	133
6-3	IMU Calibration Experiment . . . . .	136
6-4	Attitude Estimation Algorithm for SwampSat . . . . .	138
6-5	ADS Error - Eigen Angle of Error Quaternion . . . . .	145
6-6	Estimation Error - Eigen Angle of Error Quaternion . . . . .	147
6-7	Error in Estimated and True Angular Rates . . . . .	148
6-8	Error in Attitude Quaternion . . . . .	149
6-9	Estimation Error - Eigen Angle of Error Quaternion . . . . .	150
6-10	Error in Estimated and True Angular Rates . . . . .	151
6-11	Error in Attitude Quaternion . . . . .	152
6-12	Estimation Error - Eigen Angle of Error Quaternion . . . . .	153
6-13	Error in Estimated and True Angular Rates . . . . .	154
6-14	Error in Attitude Quaternion . . . . .	155

## LIST OF ABBREVIATIONS

A/D	Analog to Digital
AAUSAT	Aalborg University Satellite
ACS	Attitude Control System
ADS	Attitude Determination System
AEKF	Additive Extended Kalman Filter
AGI	Analytical Graphics, Inc.
AMR	Allocated Mission Requirements
ASCII	American Standard Code for Information Interchange
ASTREC	Advanced Space Technologies Research and Engineering Center
AWG	American Wire Gauge
BCR	Battery Charge Regulator
BIOS	Basic Input Output System
BPSK	Binary Phase Shift Keying
Cal Poly	California Polytechnic State University
CanX	Canadian Advanced Nanospace Experiment
CAPE	Cajun Advanced Picosat Experiment
CCD	Charge-Coupled Device
CDH	Command and Data Handling
CdS	Cadmium-Sulfide
CIC	Cell-Interconnect-Cover
CMG	Control Moment Gyroscope
CMOS	Complementary MetalOxideSemiconductor

CONOPS	Concept of Operations
COTS	Commercial-off-the-shelf
CP	Cal Poly
CPU	Central Processing Unit
CSTB	CubeSat Test Bed
CUTE	CUBical Titech Engineering
DC	Direct Current
DCM	Direction Cosine Matrix
DMR	Derived Mission Requirement
DoD	Department of Defense
DoDAF	Department of Defense Architectural Framework
DOF	Degree of Freedom
DSP	Digital Signal Processor
DTUSat	Technical University of Denmark Satellite
ECI	Earth Centered Inertial
EEPROM	Electronically Erasable Programmable Read-Only Memory
EIDE	Enhanced Integrated Drive Electronics
EKF	Extended Kalman Filter
ELaNa	Educational Launch of Nanosatellites
EPS	Electrical Power System
ESA	European Space Agency
FLOPS	Floating Point Operations
GCC	GNU Compiler Collection
GM	Global Memory

GNC	Guidance Navigation and Control
GPIO	General Purpose Input Output
GPS	Global Positioning System
HALT	Highly Accelerated Life Testing
HASS	Highly Accelerated Stress Screen
I/O	Input/Output
I/UCRC	Industry/University Cooperative Research Center
I2C	Inter Integrated Circuit
ICD	Interface Control Document
IMU	Inertial Measurement Unit
IR	Infrared
ISO	International Organization for Standardization
ISR	Intelligence Surveillance Reconnaissance
KSC	Kennedy Space Center
L2	Livingstone
LAWS-V	Linux-based Autonomous Wireless-capable Self-diagnosing Vehicle
LED	Light Emitting Diode
LEO	Low Earth Orbit
Li-Po	Lithium Poly
LSP	Launch Services Program
LSS	Laboratory of Space Systems
LTV	Light to Voltage
LV	Launch Vehicle

MB	Megabyte
MBD	Model Based Diagnosis
MEKF	Multiplicative Extended Kalman Filter
MEMS	Micro-Electro Mechanical System
MIL-SPEC	Military Specification
N2 or N <sup>2</sup>	N-squared
NASA	National Aeronautics and Space Administration
NORAD	North American Aerospace Defense Command
NSF	National Science Foundation
O/OREOS	Organism/Organic Exposure to Orbital Stresses
OAP	On-orbit Average Power
OCT	Office of the Chief Technologist
ORS	Operationally Responsive Space
OS	Operating System
P-POD	Poly Picosatellite Orbital Deployer
PCB	Printed Circuit Board
PCMCIA	Personal Computer Memory Card International Association
PMO	Primary Mission Objective
PSLV	Polar Satellite Launch Vehicle
QUEST	Quaternion Estimator
R2P2	Rapid Retargeting and Precision Pointing
RAX	Radio Aurora Explorer
RBF	Remove Before Flight

REQUEST	Recursive Quaternion Estimator
RTC	Real Time Clock
SFC	SwampSat Flight Computer
SMO	Secondary Mission Objective
SP	Sensory Processing
SPI	Serial Peripheral Interface
SSA	Space Situational Awareness
SSC	Serial Servo Controller
SSDL	Space Systems Development Laboratory
SSH	Secure Shell
STK	Satellite Tool Kit
SWaP	Size Weight and Power
TCP/IP	Transmission Control Protocol / Internet Protocol
TD	Task Decomposition
TI	Texas Instruments
TJ	Triple Junction
TLE	Two Line Element
TML	Total Mass Loss
TRIAD	TRIxial Attitude Determination
TRL	Technology Readiness Level
TT&C	Telemetry Tracking and Command
U.S.	United States
UGV	Unmanned Ground Vehicles

USB Universal Serial Bus

UV Ultraviolet

VHF Very High Frequency

VJ Value Judgement

VNC Virtual Network Computing

WM World Model

XI-IV Sai Four

YAHU Yet Another Housekeeping Unit

Abstract of Dissertation Presented to the Graduate School  
of the University of Florida in Partial Fulfillment of the  
Requirements for the Degree of Doctor of Philosophy

CUBESAT SYSTEM DESIGN BASED ON METHODOLOGIES ADOPTED FOR  
DEVELOPING WIRELESS ROBOTIC PLATFORM

By

Sharanabasaweshwara Ashok Asundi

August 2011

Chair: Norman G. Fitz-Coy

Major: Mechanical and Aerospace Engineering

CubeSats have been recognized globally for their potential utility for revolutionizing the space industry. However, with the exception of the CubeSat specification, the development approach to date has been mostly ad hoc. Based on lessons learned from the design and development of a terrestrial ground robot, a systematic approach utilizing systems engineering techniques has been developed for CubeSats. The approach uses a top-down design methodology to translate mission definitions into basic building blocks that then facilitate a bottom-up development and fabrication process. The limitations imposed by the CubeSats size, weight, and power on the design process are addressed in the developed approach. To describe the traceability from mission requirements to subsystem component selection, design, and integration, SwampSat, a University of Florida CubeSat, is used as an example. Within this context of traceability, several unique design features of CubeSats are identified and described. These include (i) novel multifunctional structural elements, (ii) distributed processing to reduce power consumption yet provide complex computational capability, and (iii) efficient computational algorithm amenable to low power device implementations. To demonstrate features (ii) and (iii), Murrells version of the extended Kalman filter is adapted for SwampSats attitude determination subsystem and demonstrated for three sensor configurations. The considered sensor configurations were based on (a) sun sensor and magnetometer combination, (b) magnetometer and synthesized magnetic

rate combination, and (c) magnetometer only. All three sensor configuration utilized spacecraft angular rate information for attitude propagation. Simulations involving detailed sensor characteristics were performed to evaluate the performance of the three sensor configurations and it was demonstrated that configuration (c) was best in terms of overall error but worst in terms of convergence.

## CHAPTER 1 INTRODUCTION

Traditionally, spacecraft have been associated with budget of millions of dollars and development timelines on the order of a decade. Spacecraft systems have been considered to be complex and their development has sought specialized skills. In an effort to develop reliable assets and address the risk associated with the failure of a component or subsystem, designs that accommodated multiple redundancies have been in each spacecraft system. Effectively, spacecraft systems traditionally have been a commodity of the privileged [1].

CubeSats [2, 3], conceived as educational satellites, are challenging this paradigm and are being recognized for their potential utility [4–7]. The terms satellite and spacecraft are used interchangeably in this document. The CubeSat concept was initiated as a tool to teach students the process of developing, launching and operating satellite and formally proposed by Professor Twiggs at University Space Systems Symposium 1999 [8]. CubeSats are currently designed for low Earth orbits and are suited well for applications involving distributed sensing (e.g., space weather), and systems involving low data rate communications (e.g., automatic identification system). Similar to their traditional counterparts, these class of satellites have sought innovation in design and development but have also made use of commercial off the shelf (COTS) components [9] to explore options not considered for traditional satellites. Such approaches have so far resulted in shorter development cycles and reduced costs, thus making CubeSats attractive to an audience beyond academia.

One of the earliest launch of CubeSats was in June 2003 by Eurockot Launch Services from Plesetsk, Russia aboard the Russian launch system Rockot. The CubeSats, which included CUTE-I [8], XI-IV, [10], AAU CubeSat [11, 12], DTUSat [13], CanX-1 [14] and QuakeSat [15], were put into a Sun synchronous orbit. All the CubeSats aboard Rockot, except QuakeSat which was a triple cube, were single

CubeSats. The next set of CubeSat launches were attempted on a Dnepr launch vehicle in July 2006. The Dnepr carried 13 1U CubeSats and a 2U CubeSat in five P-PODs [16, 17]. Although the CubeSats never made it to orbit due to the launch vehicle failure [17], invaluable experience was gained in designing and developing CubeSats. The design and development experience gained by teams who had their CubeSats on board the launch vehicle was leveraged towards designing replacements for the April 2007 Dnepr launch. The second Dnepr launch occurred in April 2007 with Cal Poly (CP) replacing their CP1, CP2 by CP3, CP4 and The Aerospace Corporation replacing its AeroCube-1 by AeroCube-2. The other secondary payloads aboard the launch vehicle (LV) included Columbia's Libertad 1, Boeing Company's CSTB1, University of Louisiana's CAPE1 and Tethers Unlimited's MAST. This Dnepr carried seven CubeSats in three P-PODs and has since proved to be a very successful launch vehicle for CubeSats. The experiences of the Dnepr 2006 failures and its success in 2007 demonstrated that CubeSats could be designed, built and launched in a short period of time and at a relatively lower cost.

### **1.1 Definition and Classification of CubeSats**

Small satellites, a class of satellites with net mass less than 500 kg, are categorized as picosatellites (1 kg or less), nanosatellites (1–10 kg), microsatellites (10–100 kg) and minisatellites (100–500 kg) [18]. CubeSats are identified as belonging to the picosatellite and nanosatellite categories of small satellites. The CubeSat specification [19], which defines the various configurations of a CubeSat, was introduced as an effort to provide a standard platform for satellite development by California Polytechnic State University, San Luis Obispo (Cal Poly) and Stanford University's Space Systems Development Laboratory (SSDL) in 2001 [2]. The most commonly recognized configurations of the CubeSats are 1U, 2U, and 3U, with each "U" representing a 10 cm cube. Originally, the CubeSat specification defined a 1U CubeSat as a picosatellite with mass up to 1 kg and a nominal dimension of  $10 \times 10 \times 10$  cm [1]. The mass specification for the 1U CubeSat

has been changed recently to be less than 1.33 kg. Accordingly, a 3U CubeSat is identified as a nanosatellite with mass less than 4 kg and occupying the volume of three 1U CubeSats plus the additional 2 cm between each cube ( $10 \times 10 \times 34$ ). The CubeSat form factor has been influenced by commercially available components. For example as stated in Reference 20, “the 3 V to 5 V requirements of the standard electronics were met by 2 solar cells of dimensions  $30 \times 70$  mm $s$  which could be fit on a  $10 \times 10$  cm surface. The size of cylindrical and prismatic cell batteries could be conveniently packaged in the  $10 \times 10 \times 10$  cm volume. The mass limit of 1 kg, adopted originally for the 1U Cubesat, helped define the launch cost.” The 1U and 3U form factor have been the more popular CubeSats considered for research and development by the CubeSat community due to the constraints of the Poly Picosatellite Orbital Deployer (P-POD) [21]. However, there are launch configurations being developed that considers multiple P-PODs assembled together.

## 1.2 Poly Picosatellite Orbital Deployer (P-POD)

The cost associated with launching a spacecraft has been known to be significantly high and particularly so for university programs. One of the significant contributions towards the CubeSat program has been Cal Poly’s P-POD [21]. A single P-POD is capable of deploying any configuration of three single CubeSats. Its ability to combine satellites as one secondary payload has reduced the mission cost and accelerated development time [22]. CubeSat developers have leveraged the P-POD interface to the launch vehicle by conforming primarily to the P-POD specifications and not particularly to those imposed by a LV. The P-POD, by getting certified for a wide range of domestic and foreign launch vehicles [1, 9, 23], has made a case to the launch providers for considering CubeSats as secondary payloads. The P-POD design also ensures the CubeSat are deployed with relatively small angular rates. With the CubeSat specification in effect the integrated P-POD mass can be less than 7 kg and typically the margin available for primary payloads has been much greater.

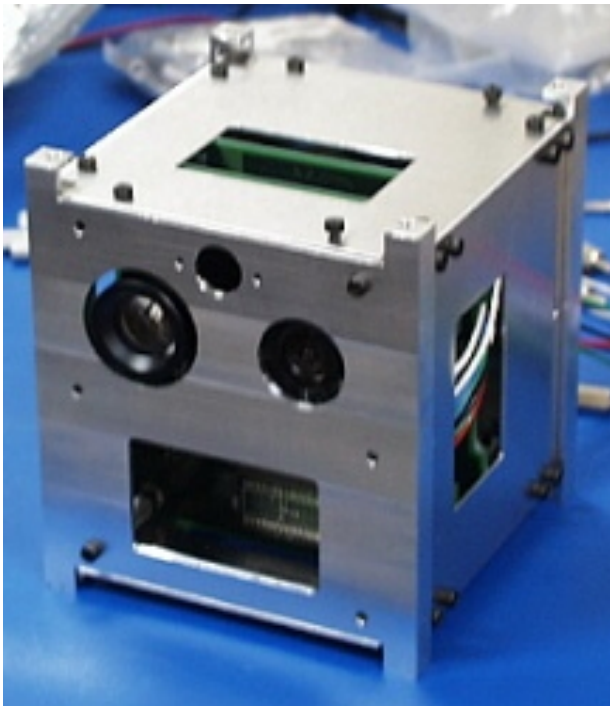
Although the P-POD is functionally designed to deploy CubeSats, protecting the primary payload and the LV from any malfunctioning of the CubeSats is its primary objective and assuring the safety of the CubeSats is a secondary objective. The P-POD has virtually isolated CubeSats from the primary payload on an integrated launch vehicle and in effect significantly reduced the risk associated with the failure of CubeSats to the primary payload and possibly to other CubeSats. To ensure reliability the requirements imposed by a launch provider on its payload developer have been stringent and rigorous. The P-POD has led to a containerization approach to space access. The containerization approach, which was introduced as a system of intermodal freight transport, enabled the use of standard intermodal containers as prescribed by the International Organization for Standardization (ISO) to be loaded and sealed into container ships, railroad cars, cargo planes and semi-trailer trucks [24]. The approach improved handling efficiency and in effect resulted in lower transportation cost. A similar trend is being seen with the P-POD approach to launching satellites.

### **1.3 CubeSat Missions as Technology Demonstrators**

CubeSats launched as part of university programs have mainly served the purpose of technology evaluation, verification, and validation. Some others, like those launched by National Aeronautics and Space Administration (NASA), have contributed to science and Earth sensing. Traditional satellites have typically used radiation hardened components specifically designed for space applications. Contrary to this practice, CubeSat missions have demonstrated the successful use of COTS based technologies, including COTS based microprocessors, micro-controllers used for designing ground based autonomous systems, off the shelf sensor modules, sensor electronics, communication boards and structural components. This section investigates some of the COTS based technologies used on early CubeSat missions and the rationale for adopting these technologies.

### 1.3.1 On Board Computing and Satellite Bus

Due to the availability of military grade variations and the target orbit being mostly a LEO, CubeSats have successfully used COTS based components to design their electronics. CanX-1 [14] (Fig. 1-1A), the first picosatellite of the Canadian Advanced Nanospace eXperiment (CanX) program of the Space Flight Laboratory at the University of Toronto Institute for Aerospace Studies, hosted a custom designed housekeeping computer based on an off the shelf ARM7 processor. The rationale for adopting an ARM based processor was its heritage on YAHU [25]. CP1, shown in Fig. 1-1B, was the first CubeSat developed by the Polysat team at Cal Poly with the objective of flight validating a bus system to accommodate small sensors and attitude control devices [3]. The rationale for validating the bus system was to prove that efficient bus systems allowed the payload to accommodate 30% of the total mass, volume and power. The command, data acquisition and data handling system for CP1 was built around the Netmedia BasicX-24, a computer module was not particularly designed for space use. At the core of the computer module was an Atmel 8535 microcontroller running at 8 MHz. The computing and power systems of CP1 were designed on a single PCB. Unlike CP1, CanX-1 design accommodated four electronic boards held together by spacers, an approach commonly used for design and development of PC104 based unmanned ground, air and underwater vehicles [26, 27]. This feature has since been established as a standard integration approach with subsystems designed on PC104 form factor PCBs. QuakeSat-I [15, 28], shown in Fig. 1-2A, was one of the CubeSats on board Eurokot, launched in June 2003. North American Aerospace Defense Command (NORAD) object tracking data confirmed the launch of four CubeSats on board this LV. One of the interesting features of this CubeSat was the use of a PC104 based computing unit, shown in Fig. 1-2B, and a Linux based operating system. QuakeSat-I provided data for early detection of earthquakes and demonstrated the utility of 3U CubeSats.



A CanX-1

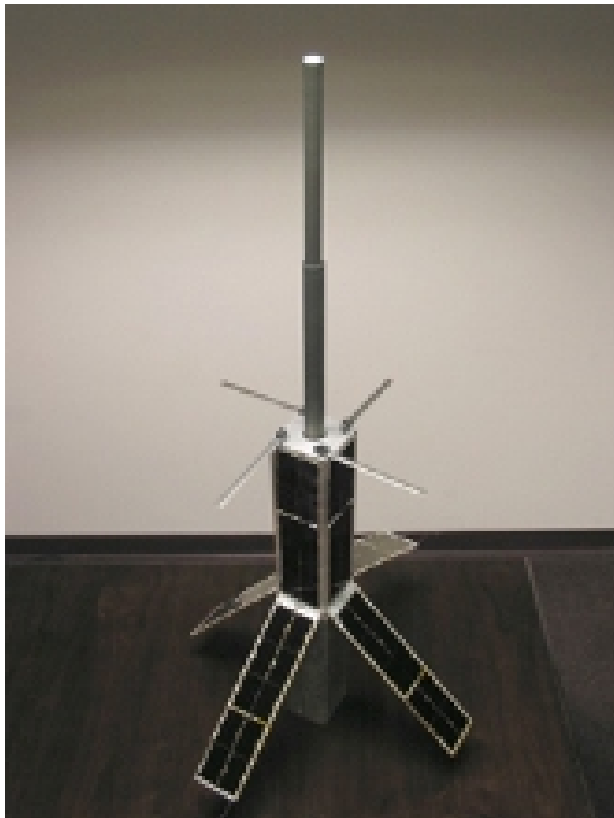


B CP1

Figure 1-1. Single CubeSats

### 1.3.2 Electrical Power

The CubeSat form factor limits the space available for surface mount solar cells, thus research approaches to improve power generation is ongoing; these include the development of more efficient solar cells. Other approaches include deployable solar arrays and thin film solar cells [29]. Body mounted solar arrays for triple CubeSats like AAUSAT-2, GeneSat and PharmaSat have proved to generate up to 6W of on-orbit average power (OAP). Deployable solar arrays, like those on Delfi-C3 [29] and QuakeSat have proved larger power generation capability with an increased design complexity. CubeSat designs in progress are capable of generating between 20-60 watts of power in full sunlight [30]. Tokyo Institute of Technology's CUTE-I was one of the first CubeSat missions to successfully demonstrate a solar array deployment mechanism [8]. Unlike most CubeSat designs which followed, the CP-1 accommodated its power management system and on board computing on a single PCB. CanX-1, designed for a 650 Km



A 3U Unit



B PC104 Based On-board Computer

Figure 1-2. QuakeSat-1

Sun synchronous baseline orbit, gave careful considerations to power generation and thermal variations. The power system was designed to switch on and switch off all payloads and the custom designed magnetic coils [14]. The mass of power system was 35% of the total mass and the operating temperature range was  $-20^{\circ}\text{ C}$  to  $+85^{\circ}\text{ C}$ . Polymer lithium ion (Li-Po) cells, with a capacity of 3600 mAh, connected in parallel, were used on CanX-1. Similar battery technologies have been used on almost every CubeSat launched and have proved to be critical for demonstrating power intensive operations. The PilsenCUBE, a pico-class CubeSat developed at the University of West Bohemia with the primary objective of monitoring space weather based on a single particle pixel detector, uses super capacitors as battery replacements [31]. In addition to the primary objective, the project proposes to study the use of super capacitors as complementary technology to accumulators in a vacuum environment

[32]. Power systems for CubeSats are being researched and redesigned for maximum power extraction from solar cells [33]. Higher density batteries, specifically for CubeSat systems, are being designed to store more power. CubeSat programs are also seeking power efficient alternatives of subsystem components, on board computers and sensors to make efficient use of the available power resources.

### 1.3.3 Telemetry, Tracking and Command

Similar to on board computers, communication electronics and antenna systems for CubeSat missions have been designed around COTS based components. Amateur radio band has been the most commonly used frequency spectrum for beacon purposes and for data uplink/downlink [1]. The power consumption of the communication board, particularly the transmitter, has been a significant component on early CubeSat missions. For instance, the transmitter on board CanX-1 was based on a 900MHz BPSK design and the receiver was based on a 900 MHz frequency modulated design. The transmitter and receiver consumed 330 mW and 33 mW of power respectively and both were attached to a push-to-talk circuit [14]. As part of the telemetry data, solar cell voltage, temperature and current were monitored on a regular basis. The Laboratory for Space Systems (LSS) at Tokyo Institute of Technology, under the supervision of Professor Saburo Matunga, launched their CUBical Titech Engineering (CUTE-I) CubeSat in June 2003. CUTE-I accomplished its mission objective of establishing a successful communication link between the satellite and a ground station. CUTE-I, one of the longest operating satellites to be launched and operated by a university program [34], has been operational on orbit for over five years now. Based on the lessons learned from the development, launch and operation of CUTE-I, the team at Tokyo Tech launched the successor Cute-1.7+APD, a 2U CubeSat, on 22nd February 2006 [35]. The communication system for CP1 was designed around the amateur band frequencies and modes. The rationale behind adopting it was to enable the amateur radio community to communicate CP1's findings to Cal Poly. The communication system

accommodated two redundant transceivers operating at 330 mW. Primary telemetry data was transmitted every minute for CanX-1 and every 3 minutes for CP1. Mission specific data was designed to be downloaded during the CubeSat's pass over Cal Poly at 15 characters per second (60 baud). While the 1U CubeSats have primarily adopted the amateur band, 2U and 3U CubeSats like CanX-2, SEEDS and OUFTI-1 have used communication systems with higher data rates and bandwidth. CanX-2 hosted 3 communication transmitters: a VHF beacon, a high data rate S-band transmitter, and a full duplex amateur radio transmitter [36]. CAPE2, a University of Louisiana at New Orleans CubeSat, hosted a software defined radio for reducing power consumption [37]. To enable missions such as blue force tracking and flood monitoring communication capabilities for CubeSats are being researched. Researchers are considering laser based communication and directional antenna systems for enabling these missions.

#### 1.3.4 Structural and Thermal

Early CubeSats structures were designed around aluminum chassis and aluminum walls. The structure thus significantly influenced the satellite mass budget. For instance, CanX-1 structure contributed to 30% of the total mass of the CubeSat, excluding the mass of PCB panels. PCB panels for hosting solar cells were mounted on the 2 mm thick aluminum walls held together by stainless steel screws. CubeSat designs, since, have researched the possibility of using composite and PCB panels with embedded magnetic coils for replacing aluminum walls [3, 38], reducing the structural mass by up to 15% of total mass [20]. As part of thermal management, MIL-SPEC grade components have been used to operate in a space environment. Battery operation has been identified to be a major challenge for CubeSat missions. The issue has been addressed by charging and discharging batteries above 0° C. CubeSat missions have also considered the issue of internal thermal management. Internal electronics have been designed to be isolated from the structure to maintain PCBs at a favorable temperature range [14]. Alternatively, PCB panels have been designed with copper pads

on the surface to facilitate a good conduction path between the structure and the panels [3].

### 1.3.5 Space Qualification and Testing

As with the design and development methodologies, CubeSat teams have adopted lateral techniques to test and qualify their satellites for space operation. Cal Poly in particular, due to its contribution in designing and developing the P-POD, has contributed significantly to establish testing methodologies. Cal Poly identified and addressed the need for testing as part of a CubeSat's development. Highly accelerated life testing (HALT) and highly accelerated stress screen (HASS) methodologies have been adopted for testing the effects of launch loads. The approach tests a complete CubeSat model by subjecting it to 150% launch load profiles of known launch vehicles like Delta II, Pegasus, Shuttle, Dnepr, until destruction and the limits are documented.

### 1.3.6 Attitude Determination and Control

A significant deficiency has been identified in the active and high performance attitude determination and control capability of CubeSats [39–41]. Similar to traditional satellites, attitude determination and control is recognized as a utility to harness more power, increase communication bandwidth and regulate thermal variations during sun and eclipse period. Canadian Advanced Nanospace eXperiment (CanX) Program's CanX-1 [14], shown in Fig. 1-1A, primarily tested a complementary metal oxide semiconductor (CMOS) imager and a Honeywell magnetometer as attitude sensors and a COTS base Global Positioning System (GPS) receiver. CanX-I also tested an attitude control system based on active magnetic coils wound for achieving larger magnetic dipole moments. The primary purpose of the ACS was to stabilize CanX-I against disturbance torques using a B-dot controller.

Due to the limited computational resources on board CP1, attitude determination was performed on ground. Data required to compute the CubeSats attitude was downloaded during the CubeSats pass over Cal Poly. An electromagnet with capability

to be switched on and off was used as the on board attitude actuator. The actuator was commanded from ground based on the attitude of the CubeSat. CP1 was equipped with a sun sensor developed by Optical Energy Technologies and magnet torquers developed in house [3].

The payloads on board AAUSAT were a camera and an attitude control system based on magnet torquers. Although AAUSAT was operational for only about a month due to the failure of its onboard batteries, the students from Aalborg University of Denmark gained experience in building these class of satellites and launched AAUSAT-II on 28th April 2008 aboard India's Polar Satellite Launch Vehicle (PSLV). It is worth noting that the series of experiments proved, among other things, that these class of satellites could be replaced in a cost effective and timely manner.

Several other CubeSats (XI-IV, Mea Huaka, GeneSat-1, CAPE-1, Delfi-C3, PharmaSat, UWE-1) [42] have used passive systems to naturally orient the satellite; the most common approaches using a combination of permanent magnets and magnetic hysteresis rods to damp nutation in satellite motion by interacting with the geomagnetic field. QuakeSat-I utilized the gravity gradient stabilization approach for its attitude control.

#### **1.4 CubeSats as Utility Spacecraft**

While single CubeSats have mostly served the purpose of verification and validation of COTS based technologies, triple CubeSats have proven some mission utility. As with the single CubeSats, the P-POD has played a significant role in enabling the launch of these triple CubeSats as secondary payloads at reduced cost. Presented below are examples of 3U CubeSats designed for space science and Earth observing.

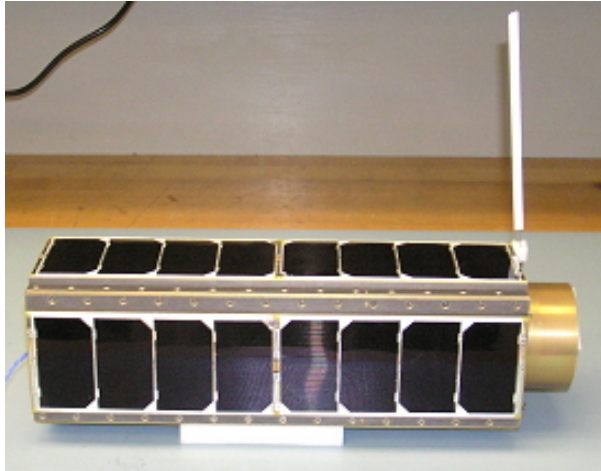
##### **1.4.1 National Aeronautics and Space Administration's 3U CubeSats - Space Science**

The first United States (U.S.) launch of a CubeSat was in December 2006 aboard Minotaur I launch vehicle. GeneSat-1 (Fig. 1-3A), a triple CubeSat developed by

NASA Ames was one of the satellites on this launch vehicle. GeneSat-1 mission [7, 43] tested the growth of e coli in space and more importantly proved the utility of CubeSats for science. PharmaSat [44], shown in Fig. 1-3B, another triple CubeSat developed by NASA Ames was launched in May 2009 also on a Minotaur I launch vehicle. The mission objective for PharmaSat was to detect the growth, density and health of yeast cells and transmit the data to ground. A detailed thermal analysis of PharmaSat [45] was one of the significant technical contributions to the CubeSat community. Two triple CubeSats, PRESat developed by NASA Ames and NanoSail-D developed jointly by NASA Ames and NASA Marshall, were scheduled to launch aboard the SpaceX Falcon 1 launch vehicle. The LV never made it to the orbit but the teams gained valuable experience in designing and building CubeSats. NASAs Organism/Organic Exposure to Orbital Stresses (O/OREOS) CubeSat, launched on November 19th 2010, included two science payload instruments to study space environmental effects on organic compounds and the time-dependent viability of living organisms in space [46]. The CubeSat carried a commercially developed 1/2 cube UV visible spectrometer to demonstrate the capability of simulating a variety of space environments using small satellites.

#### 1.4.2 Earth and Space Observing

QuakeSat-I [15, 28], a triple CubeSat developed by Quakefinder and Stanford, was one of the earliest CubeSats to demonstrate utility by providing data for early detection of earthquakes. FireFly [1, 47], a collaboration between Boston University, Montana State University, and the Aerospace Corporation and funded by National Science Foundation (NSF) proposes to study terrestrial gamma-ray flashes induced by lightning. RAX [1, 48], a 3U CubeSat funded by NSF proposes to examine interactions of plasma electrons in the lower polar thermosphere which will help provide strategies to mitigate communications disruptions. QB50 a joint initiative between the Von Karman Institute, ESA and NASA, proposes to use an international network of 50 double CubeSats (2U)



A GeneSat-1



B PharmaSat

Figure 1-3. NASA's 3U CubeSats

to study in situ the temporal and spatial variations of a number of key constituents and parameters in the lower thermosphere (90 – 320 km) [49]. Table 1-1 [1] summarizes sampled CubeSat missions of the past, present and in progress.

### 1.5 New Paradigms

The utility of CubeSats as secondary payloads is being recognized by space and research agencies around the world; these include NASA [43, 44, 46], U.S. Department of Defense (DoD) [50], the European Space Agency (ESA) [51], Italian Space Agency, British National Space Centre, National Science Foundation (NSF) [47, 48], U.S. National Reconnaissance Office (NRO) [50], the United Nations (UN) [52], the Indian Space Research Organization (ISRO) [53], Japan Aerospace Exploration Agency (JAXA) [54], China National Space Administration [55], National Space Agency of Ukraine, Radio Amateur Satellite Corporation and the Russian Space Agency, to list a few. Within the U.S., NASA's Kennedy Space Center and Launch Services Program

Table 1-1. Sampled CubeSat Missions

Category	Mission	Organization
Astrobiology	O/OREOS: UV/visible spectral monitoring: organic materials; space radiation effects on survival/growth of 2 microbes	NASA/ARC
Astronomy	BRITE/CanX-3/TUGSAT-1: Constellation of nanosatellites for asteroseismology	CSA/U. Vienna/Austrian Research Promotion Agency (FFG)
	SwissCube: telescopic investigation of atmospheric airglow phenomena	Ecole Polytechnique Federale de Lausanne
Atmospheric Science	AtmoCube: Interaction between space radiation and upper atmosphere	Univ. Trieste and commercial sponsors
	FIREFLY: Terrestrial gamma-ray flashes induced by lightning	NSF
	RAX: Plasma interactions of the thermosphere	NSF
Biology	GeneSat-1: E. coli gene expression via fluorescent reporters in microgravity	NASA/ARC, Stanford University, Santa Clara University
Earth observation	QuakeSat: Measure extra-low freq. magnetic waves from earthquakes in space	University of Tokyo
	PRISM: Validation of medium-resolution Earth observation	Norwegian U. of Science and Technology
Ecology	NCube2: Large ship AIS; reindeer tracking (NCube1 was destroyed at launch)	CNES/ESA/Montpellier University
	Robusta: Validate test standards for space radiation impact on electronics	Hawk Institute for Space Sciences
Electronics	HawkSat 1: Commercial materials processing research	NASA/ARC, University of Texas Medical Branch, Santa Clara University
Materials Processing	PharmaSat: Antifungal agent dose response of yeast in microgravity	UTIAS/SFL, CSA
Pharmaceutical Efficacy		Universidad Sergio Arboleda
Technology Demonstration	CANX-2: Tech. evaluation: propulsion system, radios, attitude sensors/actuators, GPS receiver, IR spectrometer for pollution	Tethers Unlimited
	Libertad-1: Colombias 1st satellite; test of basic systems	NASA/Marshall Spaceflight Center
	MAST: Electromagnetic tether technology demonstration	UC Berkeley Space Sciences Lab/Imperial College/NSF
Space Weather	NEMESIS survey spectrum 11300 MHz: document radio-frequency storms	U.S Naval Academy
Telecommunications	CINEMA detection of sub-atomic particles from space magnetic interference	

(LSP) have initiated the Educational Launch of Nanosatellites (ELaNa) program to increase access to space for educational CubeSats [56].

The Operationally Responsive (ORS) program was established in 2007 to affect changes to the traditionally engineered space assets, which are costly to build and require extensive lead times to procure. The ORS has recognized the benefits of reduced cost and development time and the need for a new approaches for satellite development. The new approach proposes a bottom up design, development and validating on-orbit of relevant technologies through the use of small, fast and multiple satellite systems. The new model, apart from developing space talent will also serve as technology test bed for larger satellites. A study sponsored by the ORS office identified the need and benefit of using an architecture framework for shortening development schedules and reducing systems engineering effort associated with fielding space systems. The study has particularly evaluated DoD's Architectural Framework (DoDAF) for integrating satellite system engineering process to increase responsiveness and reduce cost [57].

The ORS program identifies three tiers of the responsive space initiative as described and summarized in References 58, 59, and 60. Tier-3 of the ORS model involves replenishment, reconstitution, and augmentation of space assets with newly developed technologies. Small satellites are particularly appealing to universities for their reduced budgets, educational and research benefits [20] and may be capable of supporting the Tier-3 efforts of the responsive space initiative through basic applied research and technology readiness level (TRL) advancement. The Advanced Space Technologies Research Engineering Center (ASTREC), an NSF's Industry/University Cooperative Research Center (I/UCRC), established in 2008 by the University of Florida and North Carolina State University along with ten industrial/government agency partners is one such program [60]. The ASTREC program proposes to engage teams of interdisciplinary and multidisciplinary university researchers and students to develop

technologies for industry and government agencies leading to satellite systems that have low deployment cost, can operate as constellations, and potentially have more functionality than present day systems [60]. Cal Poly [19, 20, 61], the U.S Air Force Academy [62, 63] and other institutions [64–67] have also initiated educational programs which are relevant to the responsive space discussion.

Similar to the ORS office, the Office of Chief Technologist (OCT) at NASA has initiated the Franklin and Edison programs to advance small satellite technologies. The Franklin program is intended for maturing technologies relevant for small satellites and the Edison program proposes to operate a series of missions to prove these technologies. The overall goal of the two programs is to provide game-changing and crosscutting potential for government and commercial sectors. Maturing the TRL of small satellite technologies from TRL 3-4 to TRL 6-7 is a core objective of these programs. As part of subsystem technology maturation, the Franklin program has identified candidates in the areas of advanced bus architecture, data handling, communications, entry, descent and landing systems, guidance, navigation and control, multifunctional systems, multisatellite operations, payload, power, propulsion, structure and thermal management. Within the guidance, navigation and control scheme the program identifies small-scale CMGs as a candidate [68]. Similar to the Franklin program, the Edison program has identified two types of missions to prove technology and demonstrate utility: (i) Subsystem Validation Missions (ii) Mission Capability Demonstrations. The former type proposes to leverage accessibility and affordability of small spacecraft to rapidly flight validate new subsystem technologies [68]. The later proposes to advance the state-of-the-art in small spacecraft to demonstrate their ability to perform the tasks of larger spacecraft [68]. The following candidates are identified for mission demonstrations [68]:

- Deformable aperture for remote observation
- Distributed aperture for communications or remote observation

- Extended space-based research mission (such as beyond Van Allen Belts)
- Femtosatellite
- Fractional [*Fractionated*] space-based research satellite (such as payload switchout on-orbit)
- Fractional [*Fractionated*] space-based telescope (such as separated occulter)
- Inspection and servicing satellite
- Large deployable aperture for communications, power collection, or remote observation
- Modular satellite
- Orbital debris mitigation
- Payload return
- Precision pointing for remote observation
- Secondary or hosted planetary research mission
- Sensor swarm
- Proposer-generated

While space organizations in general have recognized the potential utility of small satellite, the DoD's ORS office and NASA's Franklin and Edison programs have initiated focused efforts to utilize these class of satellites for specific applications

## 1.6 Motivation and Scope

The CubeSat project was conceived as an education tool by Prof. Jordi Puig-Suari of Cal Poly and Prof. Bob Twiggs of SSDL, Stanford University. Universities around the world have adopted it as a program and have enabled students to complete a space mission in two years [22]. University CubeSat programs have facilitated undergraduate and graduate students to learn:

1. Space mission planning and requirements development
2. Design, analysis and testing of satellite systems
3. Fabrication, assembly and quality control of CubeSat systems

4. System level testing of CubeSat systems
5. Integration and launch operations
6. Ground based satellite operations

Keywords such as operationally responsive space, technology demonstrators, technology testbed for traditional satellites and technology maturation among others have virtually been associated with discussions about small satellites, particularly the pico- and nano-class CubeSats. Although pico- and nano-class CubeSats have successfully demonstrated the use of COTS based technologies their developers have failed to document and demonstrated a systems engineering approach for design and development. This dissertation provides a systems engineering basis for the design and development of pico- and nano-class CubeSats. SwampSat, a pico-class CubeSat under development at the University of Florida, is used as a candidate mission to describe and verify the approach.

The remainder of this dissertation is organized as follows. Chapter 2 discusses the experience gained and lessons learned from the design and development of a terrestrial ground based robot in the context of pico- and nano-class CubeSats. The integration of the PC104 hardware platform draws parallel with the integration of a CubeSat hardware platform. The sensors evaluated, particularly the IMU, digital compass, photoresistors and health monitoring sensors, on LAWS-V can be adopted for a Cubesat. The L2 based health management system evaluated for LAWS-V has applicability for performing ground based diagnosis of pico- and nano-class CubeSats. The modified radio controlled platform and the sensor suite enable LAWS-V to traverse in guided, semi-guided and autonomous modes. The operational understanding has facilitated operations design for CubeSats. The robot is capable of communicating wirelessly and exchange critical information with workstations. The implementation has facilitated understanding of a CubeSat's capability to communicate with a ground station. The lessons learned most importantly lead to the conclusion that a systems engineering approach is required for the design and development of pico- and nano-class CubeSats.

Chapter 3 describes in detail a systems engineering approach, adapted from NASA's Systems Engineering Handbook [69], for the design and development of pico- and nano-class CubeSats. The approach discusses the flowdown from mission definition to system level components, interfaces and tasks through the mission concept of operations. To enable better understanding of the approach, SwampSat's mission objective of demonstrating rapid retargeting and precision pointing is briefly described. Mission definition, mission objectives, mission requirements and the mapping process are discussed as part of the approach. To elaborate on the systems approach, the detail design of components, interfaces and tasks, is addressed in Chapters 4, 5 and 6 as design of subsystems.

Chapter 4 describes how COTS based components can be accommodated in the systems engineering based design and development of CubeSats. An electrical power supply board, battery board and solar cells are selected as COTS components to address some of the requirements of the electrical power system of SwampSat. The process of integrating these COTS based components into the system design is discussed in Chapter 3. Although, COTS components are largely available for the development of pico- and nano-class CubeSats, mission requirements coupled with form factor constraints could limit their use for designing a subsystem. Such a limitation is addressed by the custom design and development of one or more components which can facilitate integration. The design and development of multifunctional solar panels is discussed in this context.

Chapter 5 describes the design of command and data handling software and telemetry formulation from the building blocks obtained through the mission mapping process. The chapter describes the significance of a well designed mission concept of operations and its utility for designing satellite operations. The pico- and nano-class CubeSats are often limited in their power generation capability and such a limitation can be addressed through a distributed architecture for onboard computing. However, the

operational design of such an architecture can be challenging. Additionally, if the power requirements of the mission operations is significantly larger than its power generation capability further challenges can be introduced in the operations design. The chapter addresses such challenges in the context of SwampSat mission and provides solutions through a well defined mission CONOPS. The flight software designed as operating modes with downlink telemetry and uplink command is described in detail. Finally, the chapter briefly describes how cost associated (in terms of power, telemetry and computation) with basic building blocks of Chapter 3 can be used to estimate the cost of an operating mode or the flight software.

Chapter 6 surveys the deterministic and stochastic methods of attitude determination and estimation, particularly relevant for the pico- and nano-class CubeSats. When distributed computing architectures are adopted to address the issue of power limitation, elements of one or more subsystems could get distributed as well. To address such a scenario, the chapter describes the distributed design of the attitude determination and estimation system encountered for SwampSat mission. The chapter describes the distributed architecture of the attitude determination and estimation system. The pico- and nano-class CubeSat have relied on COTS based attitude and inertial sensors. Among them, Sun sensors, magnetometers and inertial measurement units have been most common. The chapters describes how an estimation algorithm can accommodate multiple configurations of the such sensors. Murrell's version of the extended Kalman filter is adapted for addressing attitude estimation for such a scenario. The algorithm's implementation to suit the distributed architecture is presented. The need for an attitude estimation algorithm for a satellite hosting the type of sensors as SwampSat is investigated and justified. Simulations performed to evaluate and compare attitude estimation performance for the three sensor configurations are presented.

Chapter 7 concludes this dissertation by identifying the contributions made towards the design and development of pico- and nano-class CubeSats in the context of

SwampSat mission. The chapter identifies areas of future work to optimize the design and validate SwampSat on orbit.

## CHAPTER 2

### LESSONS LEARNED FROM THE DESIGN AND DEVELOPMENT OF A TERRESTRIAL GROUND ROBOT

Motivated by the requirements of an on-orbit servicing project, the Linux-based Autonomous Wireless-capable Self-diagnosing Vehicle (LAWS-V) was conceived as a wireless robotic platform. The wireless ground robot evaluated PC104 based subsystems, sensor technologies and integration, vehicle health management and control methodologies for autonomous and guided operation. This chapter discusses the design, development of the wireless robotic platform and the lessons learned in the context of pico- and nano-class CubeSat design approach. As a background to the design and development of LAWS-V, the chapter discusses the definition of an unmanned ground vehicle (UGV) or a wheeled robotic platform, the two classes of UGVs - (i) teleoperated (ii) autonomous and the basic elements of an autonomous UGV.

#### **2.1 Definition of Unmanned Ground Vehicle (UGV)**

Unmanned ground vehicles can be defined as robotic platforms used as extensions of human capability which can operate outdoors over a wide variety of terrain. UGVs have been researched for both civilian and military use to perform dull, dirty, and dangerous activities. According to Douglas W Gage, in the broadest sense, an UGV is any piece of mechanized equipment that moves across the surface of the ground and serves as a means of carrying or transporting something but explicitly does not carry a human being [70].

#### **2.2 Classification of UGVs**

The classification of mobile robotic platforms can be based upon multiple factors. Mobile robots can be classified according to their capabilities and these capabilities can be mission specific. Size can be taken into consideration while defining a class of unmanned ground vehicles. Mode of locomotion, navigation techniques and the UGVs intended area of operation are some of the other parameters which can be used for classification. Robots incorporating both mobility and manipulation can be referred to

as mobile robots and are not necessarily UGVs. They can be unmanned air vehicles or unmanned underwater vehicles. The scope of classification has been limited to the area of navigation and control and in that context teleoperated and autonomous UGVs are discussed.

### **2.2.1 Teleoperated UGV**

A teleoperated UGV is a vehicle controlled by a human operator at a remote location via a communication link. All cognitive processes are provided by the operator based on sensory feedback from either line-of-sight visual observation or remote sensory input such as video cameras. A teleoperated vehicle system is one in which navigational guidance is transmitted to the vehicle from an externally situated human operator [70]. Predominantly these vehicles are used to replace humans in hazardous situations such as disposing explosives and bombs.

### **2.2.2 Autonomous UGV**

An autonomous UGV is essentially a mobile robot capable of performing an assigned task by itself. It is self guided and can determine its own course using onboard sensory suite and processing resources [70]. It can incorporate one or more of the following functionalities:

1. Gain information about the environment
2. Work for months or years without human intervention
3. Navigate/traverse from point A to point B, without human assistance
4. Avoid situations that are harmful to people, property or itself
5. Perform a self diagnosis and assess its health on a regular basis

Unmanned ground vehicles, particularly the autonomous UGVs, could be built to be intelligent. In his paper, James Albus proposed a theoretical model of an intelligent system [71]. The model composed of seven basic elements which made an unmanned system intelligent: (i) actuators, (ii) sensors, (iii) sensory processing, (iv) world modeling, (v) task decomposition, (vi) value judgment, and (vii) global memory/communications.

The elements of an intelligent system and their relationship to each other are illustrated in Fig. 2-1 [71].

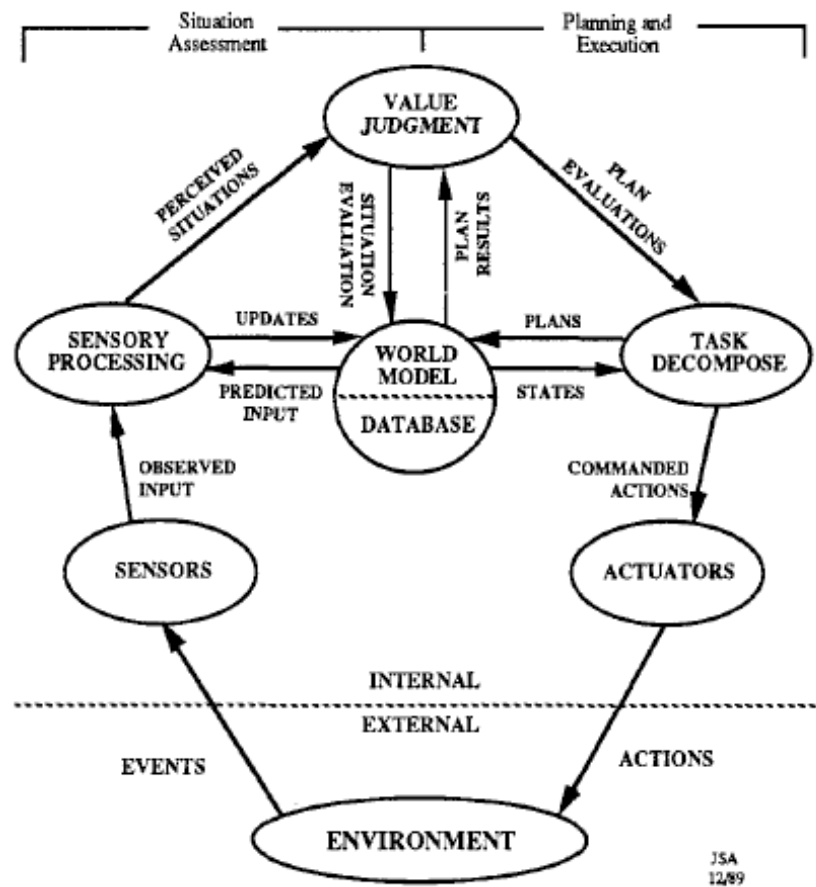


Figure 2-1. Elements of an Intelligent System and their Relationship to Each Other

### 2.2.2.1 Actuators

An intelligent system will be made up of multiple actuators and all these actuators need to be coordinated in order to perform tasks and accomplish goals. Machine actuators may consist of motors, pistons, valves, solenoids and transducers.

### 2.2.2.2 Sensors

Intelligent systems are guided by sensors which may include visual brightness and color sensors; tactile, force, torque, position detectors; velocity, vibration, acoustic, range, smell, taste, pressure, and temperature measuring devices. Sensors serve a dual

purpose i) they monitor the external environment and ii) they monitor the internal state of the intelligent system itself

#### **2.2.2.3 Sensory Processing**

The sensory data is used to perceive the external and the internal environment through comparison with expectations from the internal world model. Sensory processing algorithms compute distance, shape, orientation, surface characteristics, physical and dynamical attributes of objects and regions of space [71].

#### **2.2.2.4 World Model**

Internal to an intelligent system is a world model, which is generally the systems best estimate of the state of the world. The world model provides answers to requests for information to the task decomposition element, so as to enable it to make intelligent plans and behavioral choices. The world model as mentioned previously is also a information source for the sensory processing algorithms to correlate the sensed information with its closest estimate in the world model database.

#### **2.2.2.5 Value Judgment**

Value judgment computes the costs, risks, benefits both of observed situations and of planned activities, the probability of correctness and assigns believability and uncertainty parameters to state variables. The value judgment element thus provides the basis of choosing one action as opposed to another, or for pursuing one object and fleeing from another [71].

#### **2.2.2.6 Task Decomposition**

Behavior generation takes place in a task decomposition element where the planning and execution of tasks is carried out by decomposing them into subtasks and finally into goals. Plans, hypothesized by task decomposition element, are analyzed for results by world model, and evaluated by the value judgment element. The best plans are then selected for execution by the task decomposition element. A system architecture [71] was proposed where the elements of intelligence shown in Fig. 2-1

were organized into a layered hierarchy of processing nodes. Each node was made up of four types of computing modules: task decomposition (TD), world modeling (WM), sensory processing (SP), and value judgment (VJ) modules. An interprocess communication was setup between these modules through a fifth module called the global memory (GM). Outputs from the TD module at the lowest level drove the actuators and inputs to SP was facilitated by the sensors.

The wireless robot, discussed in this chapter, is developed around the seven basic elements of an intelligent system. Similar to LAWS-V, a CubeSat can be argued to be designed around the same seven basic elements of an intelligent system. The elements which form the composition of LAWS-V, particularly the PC104 hardware integration, the inertial and navigation sensor suite, the actuator system, health monitoring sensors, operating mode design, are practically the same elements which form the composition of a CubeSat in general [14, 15]. Some of the similarities between the two systems are listed in Table 2-1 and Fig. 2-2 captures the system level parallels of LAWS-V and a CubeSat. The approach for COTS based design, development of LAWS-V and the lessons learned in the context of design and development approach of CubeSats are presented in the following section. The utility of Livingstone (L2) [72] based vehicle health management as a tool for diagnosing failures and its applicability for pico- and nano-class CubeSats is also discussed in this section.

### 2.3 Design and Development of Terrestrial Ground Robot

Motivated by the need to evaluate subsystems, sensor technologies and health monitoring tools, LAWS-V was conceived as a heterogeneous terrestrial autonomous ground robot. LAWS-V is built on a customized radio controlled platform and the electronics are designed around the PC104 standard. Similar to CubeSat designs, the subsystem electronic boards interface through the PC104 bus. The robotic platform is wireless capable and communicates with other systems in a TCP/IP network. A serial

Table 2-1. System Level Similarities Between LAWS-V and a CubeSat

	LAWS-V	CubeSat
Hardware Platform	CPU	Flight computer
	Power supply	Electrical Power Supply
	Wireless transceiver	CubeSat transceiver
Hardware interface	PC104 (104 pin) bus interface	CubeSat (104 pin) bus interface
Sensor suite	Photoresistors	Light-to-voltage converters
	Digital Compass	Magnetometer
	IMU	IMU
	Health monitoring sensors	Battery monitoring and protection circuits
Actuation	Motors	CMG motors
Motor controller	Mini SSC II	Motor control boards
Actuation Interface	Non PC104 bus interface	Non CubeSat bus interface
Operating modes	Menu driven with provision for human interrupts	Menu driven with provision for human interrupts
Communication	Workstation to LAWS-V	Ground station to CubeSat

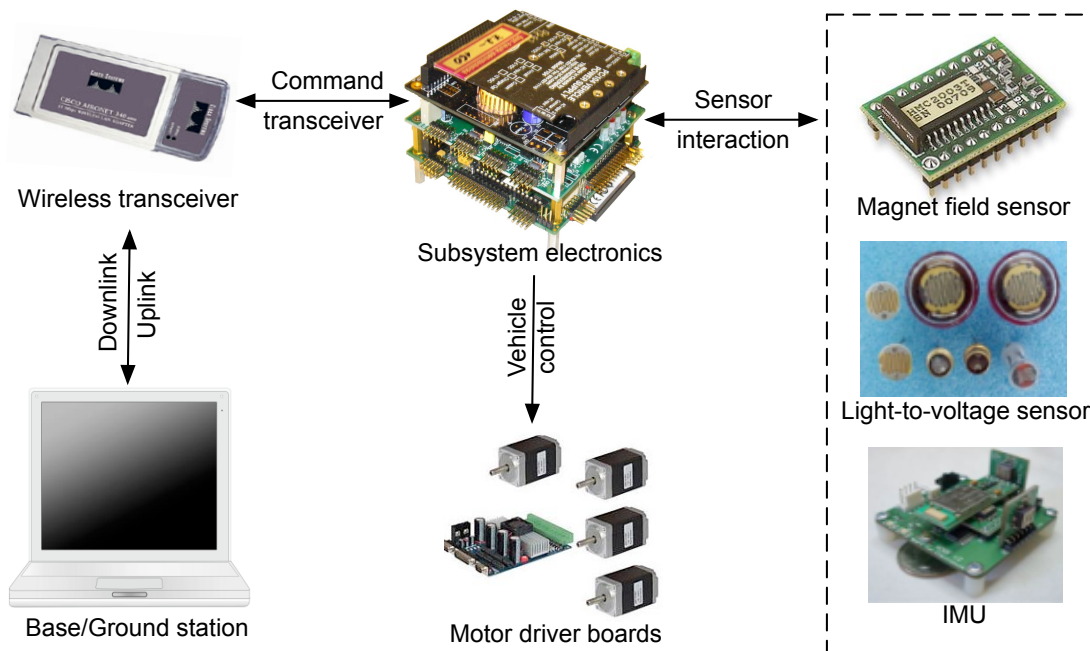


Figure 2-2. System Level Composition of LAWS-V and a CubeSat

servo controller drives the motors attached to the wheels and the steering of the robot.

The system layout of LAWS-V is shown in Fig. 2-3.

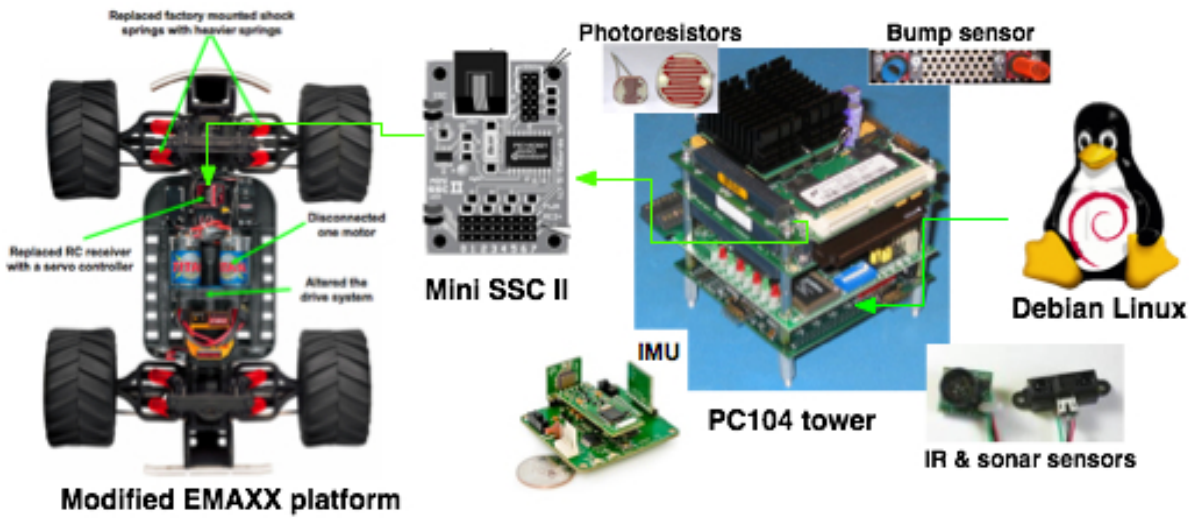


Figure 2-3. LAWS-V System Design

### 2.3.1 Customized Physical Platform

LAWS-V, shown in Fig. 2-4, is built on a customized radio controlled mobile platform. The rationale behind adopting the physical platform is to enable the robot to traverse on different terrains. Originally, the mobile platform was equipped with two motors powered by two batteries in series. The operational speed of the platform is lowered by disconnecting one of the motors and powering the other motor by a single battery. The modification reduced the speed of the mobile platform by approximately  $\frac{1}{6}^{th}$  of its original minimum speed with concurrent increase in control sensitivity. The actuation is made up of a steering servo, a transmission servo and an electronic speed control. The factory mounted shock springs are replaced by heavier springs to support the additional weight of the computer, sensors, and batteries used to power the onboard hardware.

### 2.3.2 System Hardware

The subsystem architecture of LAWS-V is built on a scalable PC104 platform and is comparable to the subsystem architecture of QuakeSat-1. An integrated central processing unit (CPU) board having an Intel Pentium 266 MHz processor and 64 MB of

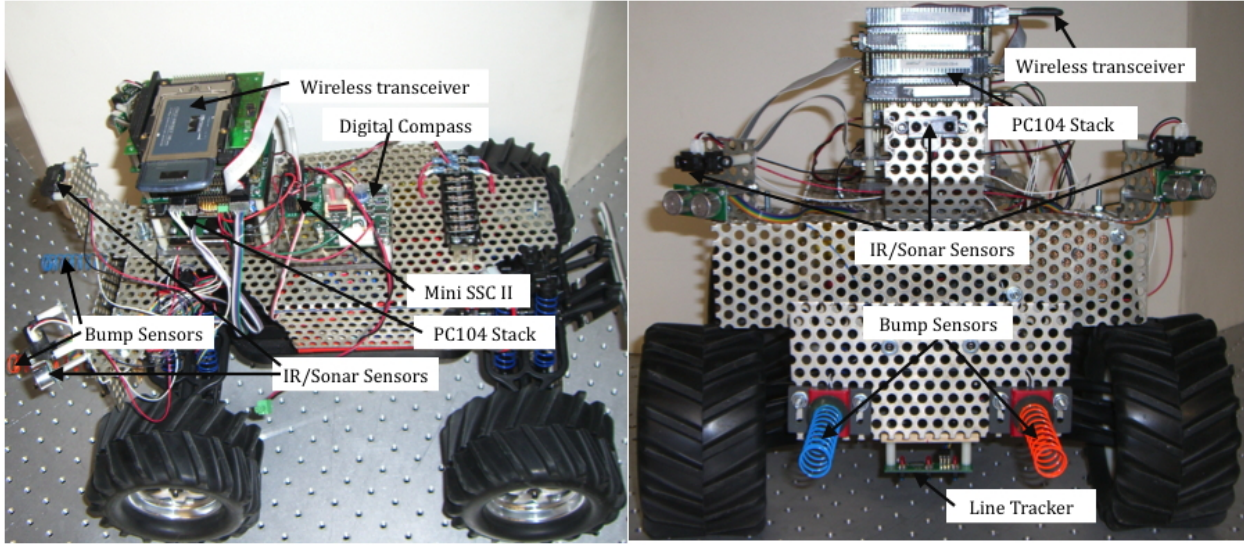


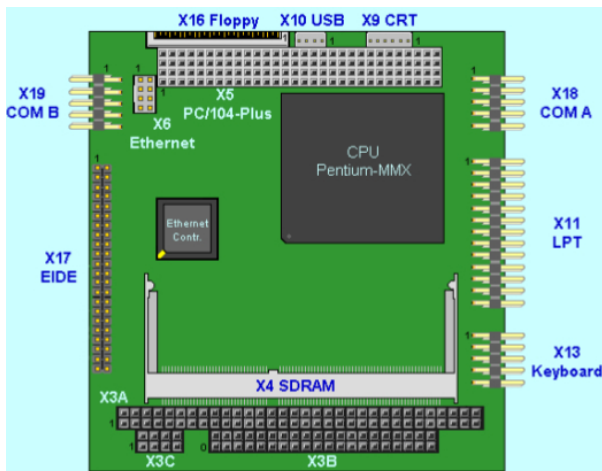
Figure 2-4. LAWS-V Hardware and Sensors

memory constitutes the core of the computing unit. The CPU board, shown in Fig. 2-5A, can connect to peripherals such as keyboard, mouse and serial devices. It is equipped with a watchdog timer and a real-time clock. Specifically the board has i) CPU ii) system BIOS iii) keyboard controller iv) real-time clock v) two RS-232 ports vi) USB interface vii) EIDE hard-disk interface viii) watchdog timer ix) ethernet controller. The V104 vehicle power supply module, shown in Fig. 2-5B with a 25 W output and 6 V to 40 V DC input is used for power management. The power supply module has standard 5 V and 12 V and optional -5 V and -12 V buses. The sensor suite on the robot is made up of digital and analog type sensors. The Diamond-MM-16AT input/output (I/O) board, shown in Fig. 2-5C, is used to interface these sensors to the CPU module. The key features of the I/O board include i) 16 single-ended (8 differential) auto-calibrated analog inputs with 16-bit analog-to-digital (A/D) resolution ii) 100 KHz A/D sampling rate iii) programmable input ranges of up to  $\pm 10$  V iv) four optional auto-calibrated analog outputs v) eight dedicated digital outputs vi) eight dedicated digital inputs vii) 32-bit counter/timer for A/D sampling rate control and viii) 16-bit counter/timer for timing functions. The I/O board is operated of a 5 V supply and has a temperature range

of  $-40^{\circ}$  to  $85^{\circ}C$ . A Kontron dual slot personal computer memory card international association (PCMCIA) adapter, shown in Fig. 2-5D, mounted atop the PC104 tower hosts a wireless transceiver. For programming and debugging purposes the PC104 unit is operated of external power supply through a 12 V DC adapter. A standard 14.4 V Li-Poly battery is used to power the system for autonomous and guided operations. An arrangement where the power supply module is placed at the bottom of the stack and the wireless transceiver on top works best for the system. The CPU connects to a display unit through a PC104 display adapter. A 40 GB, 2.5" laptop hard drive, which connects to the CPU module, is used to store programs, data and control algorithms. The motor actuators on the monster truck are interfaced to the CPU through the mini serial servo controller II. The CPU drives and controls the motor through a serial port at a baud rate of 2400/9600 bps. The motor driver is equipped with a phone-style jack at one end and a standard RS232 male connector on the other. The controller consumes 10 mA at 7 V and drives the servos at 4.8 V to 6.0 V DC.

### 2.3.3 System Software

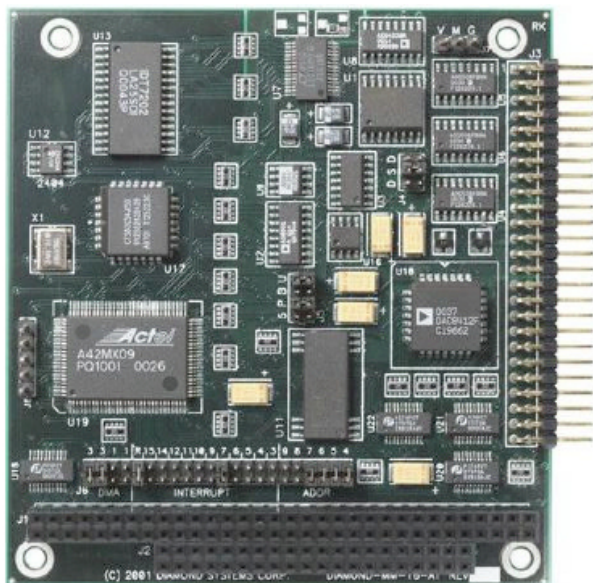
A Debian 3.0 Linux based operating system (OS) having a command line interface is installed on the PC014 computing hardware. The OS hosts a GCC compiler, a text based web browser with SSL support, a secure shell (SSH) and a virtual network computing (VNC) server for remote communication and supporting software for L2. The PCMCIA adapter and the wireless card are made operational by installing relevant drivers on the OS. The I/O board operation requires a recompilation of the operating systems kernel source after including the driver files for the board. SSH is used primarily to communicate with the mobile robot during programming and debugging mode and VNC is used to remotely operate the robot during autonomous and guided operations. The remote operation between the robot and a workstation through SSH or VNC closely emulates the communication between a CubeSat and a ground station.



A MOPSlcd6 integrated CPU board



B V104 vehicle power supply



C Sensor interface board



D V104 vehicle power supply

Figure 2-5. PC104 Boards on LAWS-V

### 2.3.4 Sensor Suite

LAWS-V integrates a suite of sensors including infrared (IR), sonar sensors and bump switches for proximity and range sensing, photoresistors and line tracker for object

tracking, current sensors and fuel gauges for health monitoring, a precision compass and an inertial measurement unit (IMU) for navigation.

**Proximity and range sensing.** The proximity and range sensing package is made up of three Sharp GP2D12 infrared distance detectors, two Devantech SRF05 ultrasonic rangers and two Vex Robotics bump switches. The layout of this package is shown in Fig. 2-6A. The proximity and range sensors are shown in Fig. 2-6B. The infrared sensors use the triangulation principle to detect the distance and have a range of 10 cm to 80 cm. The ultrasonic rangers can detect obstacles in a range of 3 cm to about 4 m. To prevent physical damage to the robot platform due to contact, the reach of bump switches is extended by mounting the replaced factory mounted shock springs on the front.

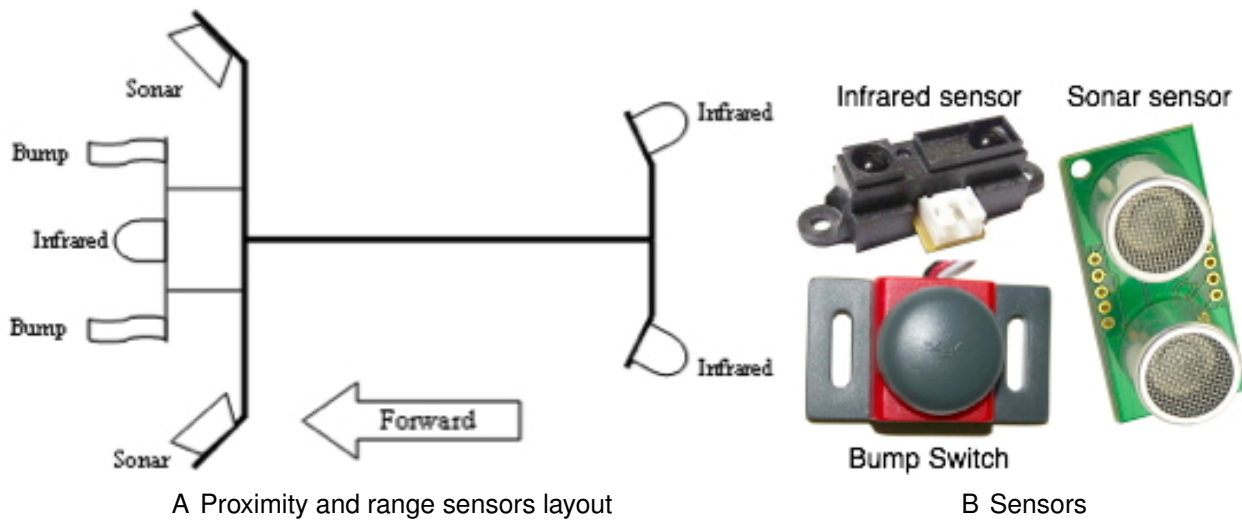


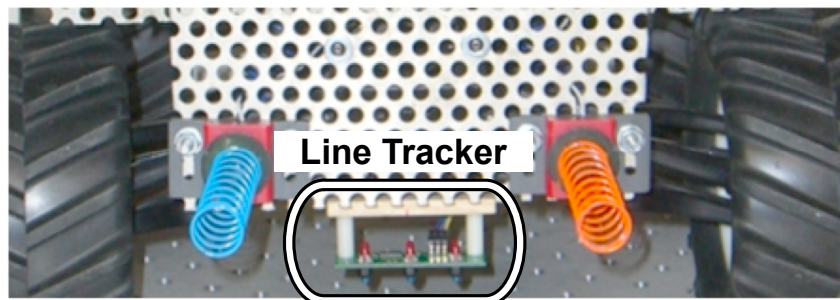
Figure 2-6. LAWS-V Proximity and Range Sensors

**Object sensing and tracking.** Two sets of photoresistors, shown in Fig. 2-7A, and a Lynxmotion line tracker, shown in Fig. 2-7B, are mounted and deployed on the mobile robot for object tracking. Similar photoresistors are evaluated as Sun sensors for CubeSats [73]. The photoresistors for LAWS-V are encased in shrink tubes and mounted on the front side of the robot. The line tracker is mounted on the axle carrying the front wheels. Encasing of the photoresistors in shrink tubes enables them to be

activated by a light source directly in front of them and minimizes the effect of ambient light.



A Photoresistors Sheathed in Shrink Tubes



B Line Tracker

Figure 2-7. Object Sensing and Tracking Sensors

**Miscellaneous Sensors.** For navigation purposes a digital compass, the TCM2 from Precision Navigation Inc., and an inertial measurement unit, the Sparkfun 6DOF IMU are evaluated and interfaced with LAWS-V. Both these sensor types have proved to be critical for CubeSat missions with a need for attitude determination. The mobile robot platform is also equipped with health monitoring sensors. The measurement of signal strength by the drivers installed for the wireless card enables it to be used as a signal strength monitoring sensor. Current sensors and fuel gauges are evaluated for various components and subsystems of the mobile robot platform for monitoring their functioning. The experience and knowledge gained in evaluating these navigation sensors were applied for surveying and identifying similar sensors for SwampSat.

### 2.3.5 Modes of Operation

LAWS-V is capable of traversing in guided, semi-guided and autonomous modes. The line tracker and the photoresistors make it capable of guided operations. The range and proximity sensor package enables the robot to traverse autonomously

avoiding obstacles. The range and proximity sensors and the photoresistors are used in conjunction for object tracking. Considering the range of the sonar sensors the left and right units are configured to sense obstacles on the right and left respectively. This configuration along with an IR sensor mounted in between the two sonar sensors has practically eliminated the region of blind spot. Additionally, two IR sensors mounted on the back enable it to sense obstacles while in reverse mode. The bump switches complement the sonar and IR sensors by detecting obstacles too close to be sensed by either sonar or IR. The IR sensors are calibrated for ambient light before the start of any operation. The sensor package enables the mobile robot to avoid obstacles, detect a dead end, and make an autonomous u-turn. The vehicle is also capable of ignoring an occasional misreported value by the range and proximity sensor suite. The LAWS-V robot is capable of tracking an object mounted with an LED light source using the two sets of photoresistors in front. The photoresistors are mounted with rubber shrink tubes around them and are activated by a light source directly in front of them. To distinguish ambient light from the light source to be tracked the robot is calibrated at the beginning of an operation. During the calibration phase the robot traverses in four directions and then captures the light intensity as a voltage value. Subsequently the robot compares the intensity of the tracking source with the calibrated values and makes its decision. The tracking sensors and the obstacle avoidance sensors together make the robot capable of autonomous and guided operations.

### 2.3.6 Livingstone (L2) Based Health Management System

Livingstone is a discrete, propositional logic based inference engine used for diagnosis of physical systems [72, 74]. This section discusses model-based diagnosis and modeling approach in brief. Livingstone based diagnosis has been specifically designed and implemented for space systems [72, 74]. As stated earlier the system level composition of LAWS-V and a CubeSat are similar. The L2 model of LAWS-V and

the results of diagnosis of simulated failures are described to demonstrate its utility for CubeSat systems.

### **2.3.6.1 Model Based Diagnosis and Modeling Approach**

Model Based Diagnosis (MBD) is the task of identifying faults in a physical system given a model of and observations from that system. For L2, a model is a data structure that represents the real-world device, the faults of which Livingstone diagnoses [74]. An L2 model is made up of components and connections. Components represent parts of a system and are characterized by one or more I/O terminals and modes (nominal and fault). Connections represent the influence of one component over the other. Observations from the system are compared with values predicted by the model to establish a state of representation of the system in the model. This model is used for simulation, diagnosis and recovery. When faults occur in a system there is a change in its behavior. In MBD, the change in the local behavior of a part of a system and the influences between parts due to a failure is modeled [75]. Diagnosis involves making inferences from observations and a range of these observations exist. Knowledge of this range is critical for designing an optimal level of abstraction in the system model. Diagnosing a system is the ability to distinguish a particular diagnosis from another when the observations are known. If a model satisfies this requirement for a particular, predetermined, set of fault scenarios it is an adequate model for that set of faults [75].

### **2.3.6.2 L2 Based Health Management of LAWS-V**

The health management system of LAWS-V consists of a state acquisition phase and a decision making phase. In the state acquisition phase the sensors such as voltage and current sensors provide information on the state of the battery, the servos and the guidance sensors (IR sensors) to the decision making algorithm. In the decision making phase, the inference engine of L2 requests the model of the robot to perform a health diagnosis. An L2 model of the LAWS-V is shown in Fig 2-8. The LAWS-V model is made up of the following components (i) PC104 unit (ii) Mini SSC II (iii) Analog I/O

board (iv) Interface board (v) Wireless card (vi) Power supply unit (vii) Display unit and (viii) Servo motors and (ix) IR sensors. The components being monitored for faulty behavior are (i) servo motors (ii) IR sensors and (iii) Display unit. The failure states of these components are simulated and a diagnosis is requested from the L2 engine.

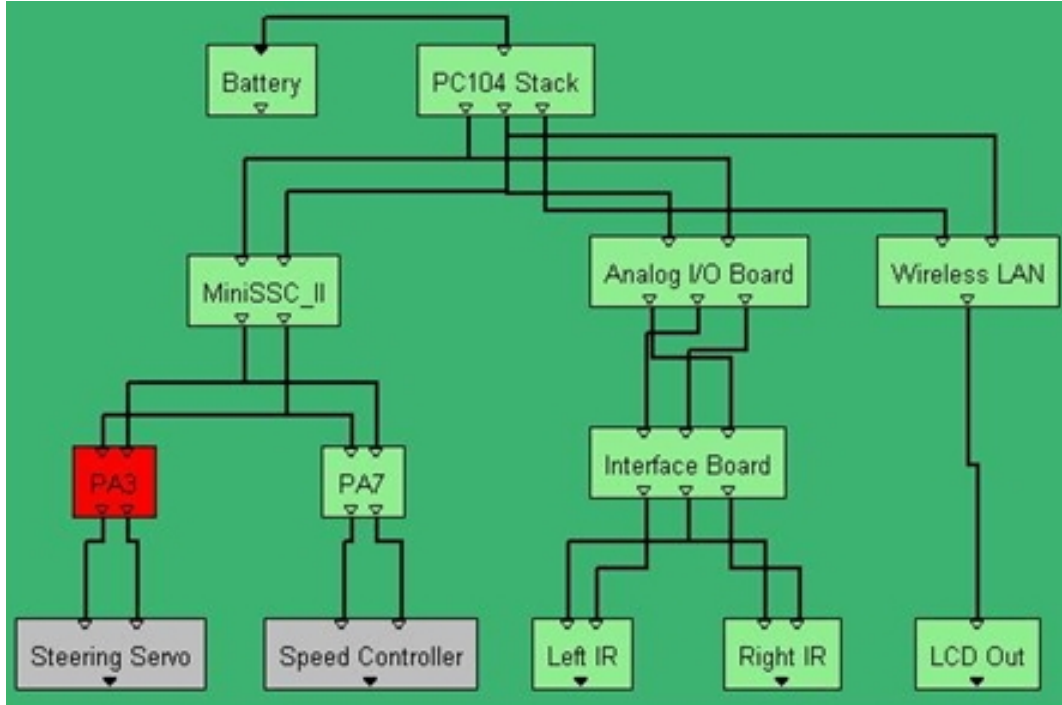


Figure 2-8. L2 Model of LAWS-V

Four scenarios, where one or more components could fail, are considered for evaluating L2 based diagnosis of LAWS-V. These scenarios reflect real-world situations of the robot and L2 based fault diagnosis is used to identify the failure. One of the scenarios and the output of L2 is explained in detail. The simulated failures in the L2 model of LAWS-V can be argued to occur frequently. In the event of such a failure it is shown that L2 performs a diagnosis and identifies the causes of failure and associates a probability to each cause. From observations it can be argued that L2 diagnosis of the failures is effective. Table 2-2 summarizes all four scenarios.

**Scenario Steering servo fails.** LAWS-V is performing a task when the steering servo fails and the robot is not able to turn in either direction. The sensor monitoring the

steering servo sends data to the L2 engine and a diagnosis is requested. L2 performs a diagnosis and presents the probable causes of failure as candidates in a Candidate Manager window as shown in Fig. 2-9. As seen by L2 the most probable causes, indicated by a rank, of failure are (i) a faulty jumper (PA3) on the Mini SSC II or (ii) a faulty steering servo. Both these failure candidates are assigned equal ranks. Apart from the above two causes L2 also associates the failure to a combination of (iii) a faulty Mini SSC and a faulty speed controller (iv) a faulty Mini SSC and a faulty jumper (v) a faulty PC104, a faulty speed controller and a faulty interface board. Although the causes (iii), (iv) and (v) are less likely to occur and hence ranked lower, L2 sees this as another possibility.

The screenshot shows a Windows-style application window titled "Candidate Manager". The main area contains a table with three tabs at the top: "Classes", "Candidates", and "Assignments". The "Candidates" tab is selected, showing the following data:

Num	Ra	nk	Time	Failures
0	10	10	-	pa3=unknownFault
1	10	10	-	strServo=unknownFault
2	20		10	miniSSC=unknownFault
			10	spdCtr=unknownFault
3	20		10	miniSSC=unknownFault
			10	pa7=unknownFault
4	30		10	pc104=unknownFault
			10	spdCtr=unknownFault
			10	intBrd=unknownFault

At the bottom of the window, a status bar displays the message: "CBFS: search found 5 candidate(s), more possible (searched 82)".

Figure 2-9. Probable Causes for Failure of Steering Servo

The design and development of LAWS-V is an effort to build a wireless ground robot for implementing cutting edge sensor technologies and evaluate L2 based health management of autonomous systems. The integration of the PC104 hardware platform draws parallel with the integration of a CubeSat hardware platform. The sensors evaluated, particularly the IMU, digital compass, photoresistors and health

Table 2-2. Simulated L2 scenarios and diagnosed failure causes

No.	Description	Rank	Failure Causes
1	Steering servo fails	10	(i) Faulty PA3 jumper
		10	(i) Faulty steering servo
		20	(i) Faulty Mini SSC II (ii) Faulty speed controller
		20	(i) Faulty Mini SSC II (ii) Faulty PA7 jumper
		30	(i) Faulty PC104 unit (ii) Faulty speed controller (ii) Faulty interface board
		10	(i) Faulty Mini SSC II
2	Both servos fail	20	(i) Faulty analog I/O (ii) Faulty PC104 unit
		20	(i) Faulty PA7 jumper (ii) Faulty PA3 jumper
		20	(i) Faulty speed controller (ii) Faulty PA3 jumper
		20	(i) Faulty steering servo (ii) Faulty speed controller
		1	(i) Interface board is turned off
		10	(i) Faulty interface board
3	Failure of both IR sensors	10	(i) Faulty analog I/O board
		20	(i) Faulty PC104 unit (ii) Faulty Mini SSC II
		20	(i) Faulty left IR (ii) Faulty right IR
		20	(i) Faulty speed controller (ii) Faulty interface board
		20	(i) Faulty speed controller (ii) Faulty analog I/O board
		20	(i) Faulty speed controller (ii) Faulty left IR
4	Failure of an IR sensor and the speed controller	20	(i) Faulty PA7 jumper (ii) Faulty interface board
		20	(i) Faulty analog I/O board (ii) Faulty PA7 jumper
		20	(i) Faulty analog I/O (ii) Faulty PC104 unit

monitoring sensors, on LAWS-V could be used on a CubeSat. Lessons learned from sensor evaluations are applied towards identifying and calibrating sensors relevant for CubeSats. The L2 based health management system evaluated for LAWS-V has

applicability for performing ground based diagnosis of pico- and nano-class CubeSats. The modified radio controlled platform and the sensor suite enable LAWS-V to traverse in guided, semi-guided and autonomous modes. The operational understanding has been leveraged in designing autonomous and ground based tasks and operations for CubeSats. The robot is capable of communicating wirelessly and exchange critical information with workstations. The implementation has facilitated understanding of a CubeSat's capability to communicate with a ground station and is leveraged towards designing on orbit operations for command data and telemetry handling.

Although, the design and development of LAWS-V has facilitated understanding of CubeSat systems, the approach has lacked a systems engineering basis. It can be argued that such an approach may be acceptable for terrestrial autonomous systems but cannot be adopted for designing a CubeSat system. In the event of a failure of a component or a subsystem, the terrestrial robot can be physically diagnosed and the cause of failure can be addressed. For spacecraft on orbit, particularly for pico- and nano-class CubeSats, such a "convenience" mostly does not exist. The most significant lesson learned from the design and development of LAWS-V is that a systems engineering based approach is needed for designing pico- and nano-class CubeSats. The following chapter discusses such an approach adapted from NASA's Systems Engineering Handbook for the design and development of these class of CubeSats.

## CHAPTER 3

### A SYSTEMS ENGINEERING APPROACH FOR DESIGN AND DEVELOPMENT OF PICO- AND NANO-CLASS CUBESATS

CubeSats have been targeted for LEO missions and due to low radiation levels at those altitudes the use of high grade COTS components for design and development has been viable. With the use of high grade COTS based technologies, reduced development cost and time, CubeSats have made space more accessible and space missions highly desirable. However, the design and development approach of these CubeSats has lacked a systems engineering basis and questioned their reliability. To address this issue, a systems engineering approach is presented for the design and development of pico- and nano-class CubeSats. The approach, partially based on the guidelines of NASA's Systems Engineering Handbook, is described and verified using SwampSat as a candidate mission to limit the abstract discussion. The following section briefly describes SwampSat mission to enable better understanding of the systems engineering approach.

#### **3.1 SwampSat Mission - Precision Pointing and Rapid Retargeting**

Although small satellite missions in the past have demonstrated success without active attitude control on board [7, 14, 43, 44], missions with instruments and directional antennas have relied on active attitude control capabilities [76, 77]. Active attitude control is critical for space situational awareness (SSA) and intelligence surveillance reconnaissance (ISR) type of missions and for applications such as blue force tracking, on orbit assembly and communication. Small satellites may be well suited for these type of missions and applications. To date most pico- and nanosatellites have utilized magnetic actuators and gravity gradient techniques for attitude stabilization. However, in addition to their inability to provide full 3-axis attitude control, these methods have yielded lower torques compared to momentum exchange devices like reaction wheels, momentum wheels and control moment gyroscopes. For equivalent SWaP characteristics, CMGs are capable of providing greater torques compared to their

reaction wheel counterparts. Additionally, reaction wheels are required to be treated as individual actuators as opposed to CMG based ACS can be treated as a single system. This feature of CMG based ACS can reduce the complexity of addressing vibration isolation [78] particular for small satellites. Due to the nature of small satellites in low Earth orbits it is often desirable for them to have the capability to rapidly slew, settle and then track feature points. The torque amplification factor, high torque generation capability and the reduced complexity of addressing vibration isolation have made CMGs desirable for enabling rapid retargeting and precision pointing (R2P2) capability on small satellites.

SwampSat is a 1U CubeSat technology demonstrator under development at the University of Florida with the mission objective of demonstrating R2P2 [39] capability for pico- and nanosatellites. The mission objective specifically serves as an example of how 1U CubeSats can support Tier-3 objectives of ORS [60]. A successful mission will provide flight heritage to the mission payload, advance its TRL and in the process address the challenges of DoD's ORS program, and NASA's Franklin and Edison programs. The attitude control system is designed around small scale CMGs and the mission objective directly encompasses precision pointing for remote observation [68]. The mission objective of SwampSat is to demonstrate precision three-axis attitude control with an experimental attitude control system consisting of four single gimbal control moment gyroscopes [39]. The graphics shown in Fig. 3-1 demonstrate two scenarios requiring R2P2 capabilities. The swath shown in blue or the circular region shown in yellow can be of interest to a small satellite in a LEO. The swath can represent an international border or an area affected by a flood that needs satellite monitoring. Similarly, the circular yellow region could represent a city, an area affected by earthquake or quite simply an activity of interest. CubeSats with precision attitude control capability are well suited for such R2P2 tasks and the cost associated could be significantly lower compared to a traditional satellite.

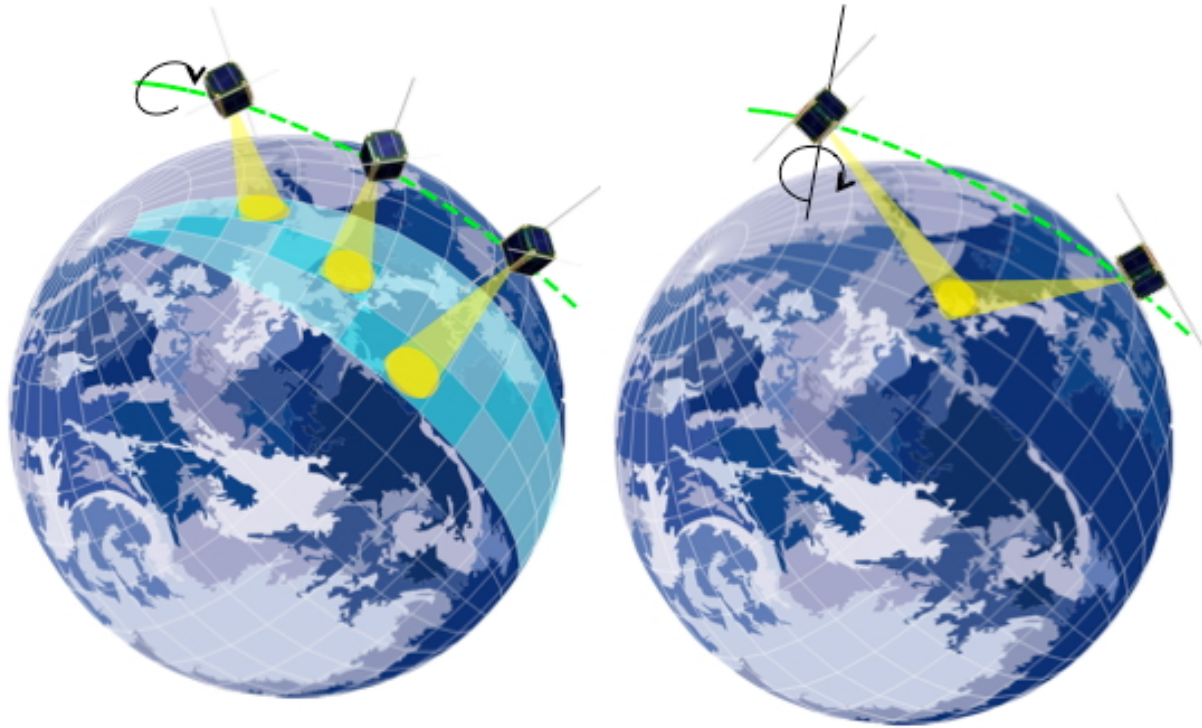


Figure 3-1. Rapid Retargeting and Precision Pointing

An integrated miniature pyramidal arrangement of CMGs for high torque attitude control actuator and the electronics supporting the control laws and steering logic form the SwampSat mission payload. Integrated systems have been argued to perform more efficiently than a comparable distributed system in terms of mass, power, cost, volume, ease of integration, predictability of integrated performance, and fault response [78] and hence are better suited to address the challenges of ORS. The mission proposes to advance the TRL of CMGs appropriate for small satellites and concurrently the utility of small satellites for an operationally responsive space. A Sun pointing maneuver is defined to demonstrate the satellite's precision pointing capability. During this maneuver SwampSat will determine its attitude, compute the desired attitude and execute the maneuver to point one of its faces to the Sun for a predetermined period of time. To demonstrate its rapid retargeting capability, SwampSat will point one of its faces to the Sun, then perform a rapid slew of  $180^{\circ}$  to point the opposite face to the Sun followed by

a settling, tracking and finally slewing to point the original face to the Sun, settling and tracking. SwampSat attitude maneuvers will be validated by characterizing attitude and inertial sensor data designed to be stored on board and downlinked by ground control.

### **3.2 Design and Development Approach**

Although the DoDAF has been argued to be an effective systems engineering approach for addressing the design of operationally responsive spacecraft [57], the framework development, initiated in the 1990s, has not been targeted towards space systems design alone. The DoDAF has primarily addressed the military domain and used by the DoD as a systems based approach for designing terrestrial, air and space systems. Majority of the pico- and nano-class CubeSats in the past have been designed and developed mostly using an ad hoc approach. Contrary to this practice an attempt is made to adopt a systems engineering basis for the design and development of SwampSat. A top-down design approach, partially based on the guidelines of NASA's System Engineering Handbook [69], has been developed as a repeatable process for translating the mission objectives and mission requirements into hardware components, interfaces and operating tasks implementable as software routines. The top-down design approach facilitates a bottom-up development and fabrication process and attempts to address the reliability of these class of CubeSat through a traceability map. In addition the cost elements in terms of power, telemetry and computation associated with each component, interface and task facilitate the estimation of the overall mission overhead. The approach is focused towards addressing the design, development and cost in terms of power, telemetry and computation for pico- and nano-class CubeSats. It is important to note that the cost model being developed does not address any financial overhead associated with these class of CubeSats. SwampSat is used as candidate mission for describing and verifying the approach. The flow diagrams shown in Fig. 3-2 and Fig. 3-3 provide an overview of the approach and the subsystem level flowdown.

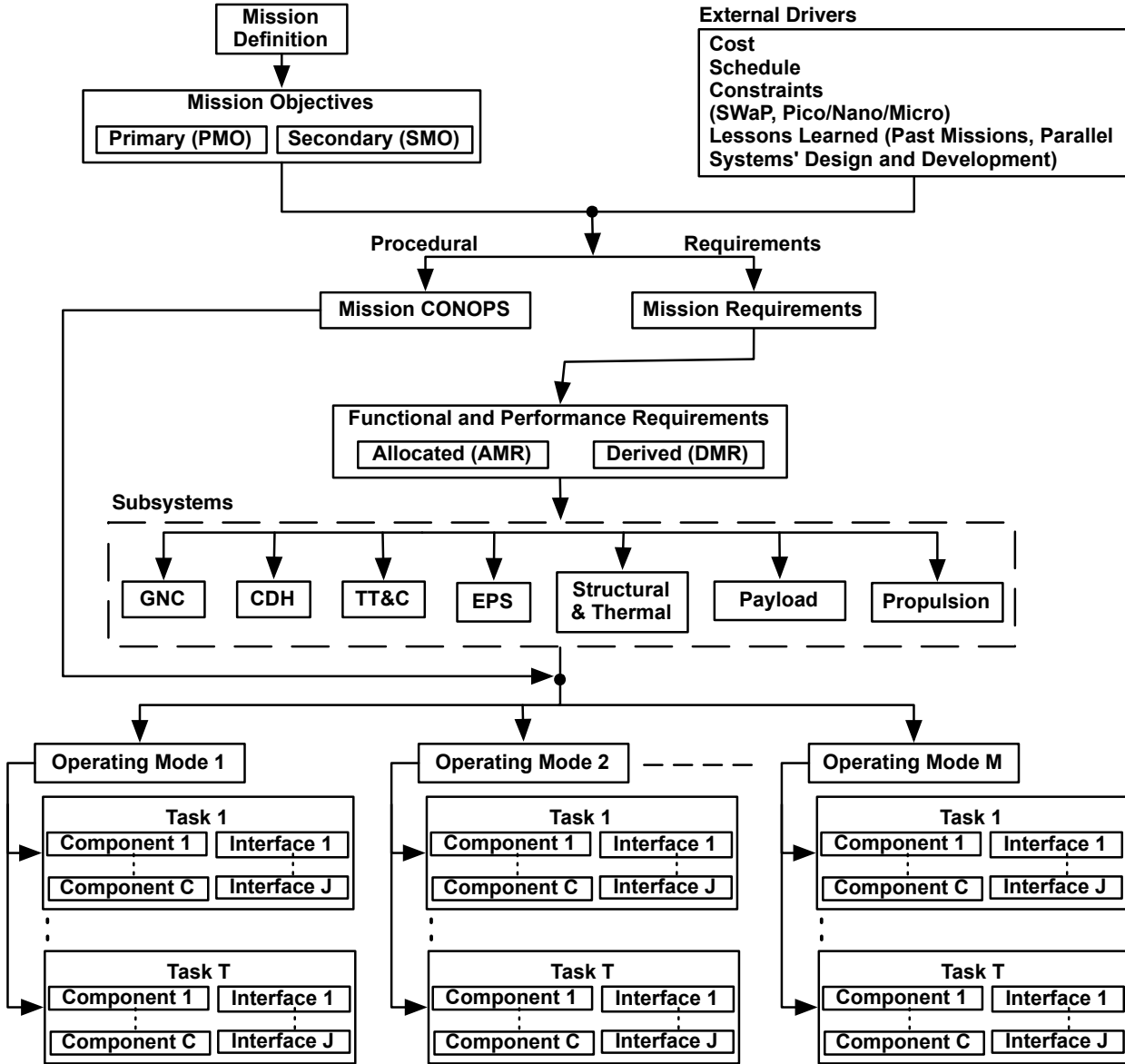


Figure 3-2. Requirements Flowdown

As shown in the Fig. 3-2, mission definition is the starting point of the design process. The mission definition leads to mission objectives, which are categorized as primary and secondary objectives. Mission definition and mission objectives are described using non-technical terminology. Although mission objectives are the primary influence for defining requirements and designing concept of operations (CONOPS), the external drivers, which include cost, schedule, constraints and lessons learned from previous missions or parallel systems design and development, could have a

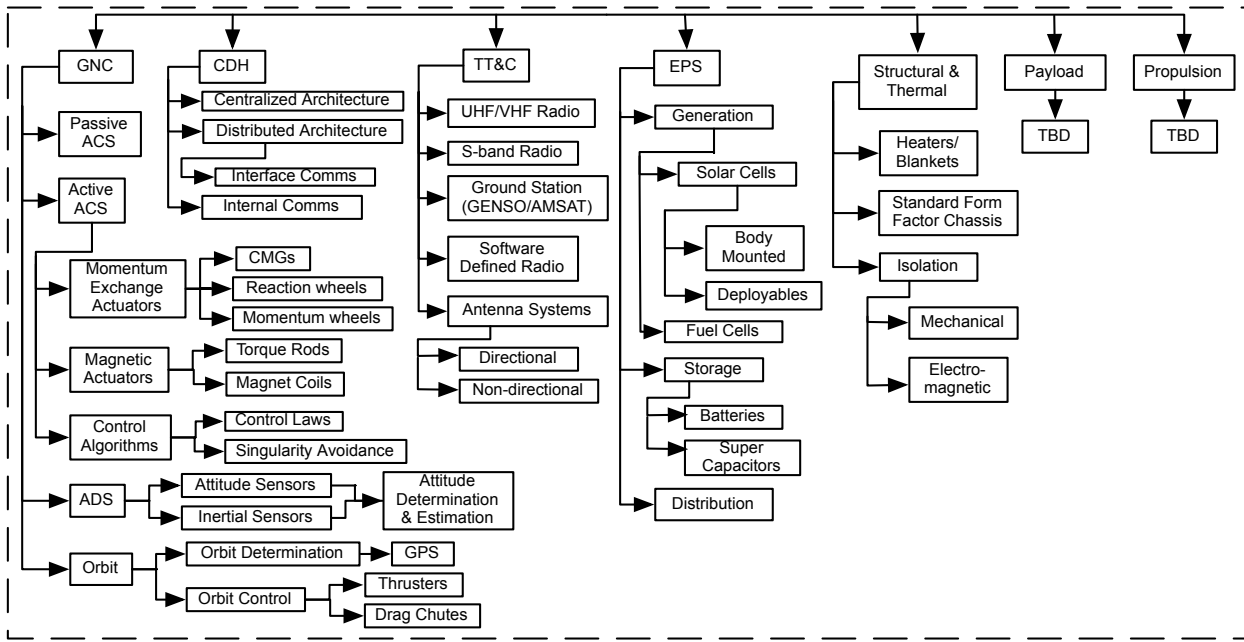


Figure 3-3. Subsystem Level Flowdown

significant influence. Specific mission requirements, both functional and performance, which are described in technical terminology, are identified and associated with the mission objectives. High level requirements are “*allocated*” to accomplish objectives and to facilitate detail design, requirements are “*derived*” where needed. The mission CONOPS is designed to describe the procedure for validating mission objectives on orbit. The requirements are flowed through the subsystem level flowdown, shown in Fig. 3-3, to identify the basic building blocks, which include components, interfaces and tasks. The subsystems block shown in Fig. 3-2, is expanded in Fig. 3-3 to show the various subcategories of each of the following subsystems:

- Guidance, Navigation and Control (GNC)
- Command and Data Handling (CDH)
- Telemetry, Tracking and Command (TTC)
- Electrical Power System (EPS)
- Structural and thermal

- Payload
- Propulsion

The subsystem level flowdown block shown in Fig. 3-3 can be thought of as a coin sorter machine. The system requirements when flowed through this flowdown block get broken down into components, interfaces and tasks as building blocks. Each component is associated with one or more interfaces and the tasks involving components and interfaces are grouped together to form operating modes as per the mission CONOPS. To establish a basis for calculating the mission cost, each component has an associated telemetry and power overhead. Additionally each task is associated with a computational overhead, which could be defined using an absolute scale (e.g., FLOPS) or a scale specific to the satellite computing platform (e.g., MSP430, C8051F120, TI DSP, ARM, PIC24). It is important to note that an operating mode will perform one of more tasks. Each task will involve one of more components and interfaces. One or more tasks may be common across operating modes and one or more components (and interfaces) may be common across tasks. The various levels of the requirements flowdown in Fig. 3-2 are described in the following subsections.

### **3.2.1 Mission Definition**

As defined in the SwampSat mission requirements document [79], the mission “*is to validate on-orbit a compact, three-axis attitude actuator, capable of rapid retargeting and precision pointing (R2P2) on board a pico-satellite built according to the CubeSat standard*”. The actuator is a pyramidal arrangement of CMGs and the intent of the mission is to provide flight heritage of the CMGs. The mission definition, which is the starting point of the mission mapping process, is captured as rapid retargeting and precision pointing (R2P2) terminology.

### **3.2.2 Mission Objectives**

SwampSat primary and secondary mission objectives as described in the mission requirements document [79] are listed as follows:

### **3.2.2.1 Primary Mission Objectives (PMO)**

- A1. The spacecraft shall respond by transmitting “maneuver data” to attitude commands sent from the ground station:
- A2. SwampSat shall perform attitude maneuvers as per the following steps (Steps (a) to (g) during one orbital period and step (h) independently):
- A3. SwampSat shall successfully transmit “maneuver data” defined above to a ground station on the Earth.
- A4. SwampSat shall adhere to the CubeSat Design Specification (CDS) Rev. 12 and the ELaNa CubeSat Interface Control Document (ICD).

### **3.2.2.2 Secondary Mission Objectives (SMO)**

- B1. SwampSat shall gather and transmit data to obtain a solar cell output profile.
- B2. SwampSat shall gather and transmit data to characterize the thermal environment inside SwampSat.
- B3. SwampSat shall validate different ACS algorithms and steering logics after achieving primary objectives (these algorithms are pre-loaded on the flight computer depending on the flight readiness of these algorithms).

## **3.2.3 Mission Requirements - Functional and Performance Requirements**

The mission requirements document [79] identifies specific requirements to achieve the mission objectives. As shown in Fig. 3-2 these requirements are categorized as “*allocated*” and “*derived*” requirements and are listed in the following sub sections. The allocated requirements directly flowdown from the mission objectives and may be too general to be directly implemented in the system design. The allocated requirements are detailed out to form the derived requirements which could include new requirements for realizing the allocated requirements.

### **3.2.3.1 Allocated Mission Requirements (AMR)**

- A1. An attitude control system (ACS) to perform the attitude maneuvers consisting of four CMG actuators in pyramidal configuration and a controller with the attitude control algorithm that shall achieve a pointing accuracy of  $0.1^{\circ}$  over the attitude determination system (ADS) accuracy.

- A2. An ADS and inertial measurement unit (IMU) to determine and propagate the angular states of the satellite interfaced with the ACS for feedback; the ADS information is used to update the angular position which is propagated using the IMU. The accuracy of the IMU and the ADS shall be better than  $5^{\circ}$  within the time window of the maneuver.
- A3. A momentum management system to dump angular momentum of the satellite before ACS operations.
- A4. An onboard transceiver and an antenna system to transmit the maneuver data and real time satellite health data, and receive commands from the ground station.
- A5. Telemetry data format(s) for transmission of maneuver data.
- A6. A flight computer and peripherals required to coordinate ground communication and certain onboard operations.
- A7. Flight software for the flight computer to coordinate ground communication and certain onboard operations.
- A8. A power system to provide electrical power to enable the different operations.
- A9. A satellite bus that shall accommodate the ACS, IMU, ADS, transceiver, antenna system and other support (derived) systems within the CubeSat volume and render the total mass of the satellite to be under 1.33 kg. The bus shall adhere to CubeSat specifications.
- A10. The satellite shall have a flight switch (also called separation switch or deployment switch) for sensing ejection from the P-POD on the Z side of rail 1 per CubeSat ICD.
- A11. The satellite shall have a remove before flight (RBF) switch on the +X face connected in series with the flight switch such that it can be activated (close the circuit) by means of pulling a pin when the satellite is inside the P-POD through the access ports.
- A12. The satellite shall have two separation springs on the Z end of two diagonally opposite rails.
- A13. Ground software for decoding received data and transmitting uplink commands.

### **3.2.3.2 Derived Mission Requirements (DMR)**

- B1. A control moment gyroscope that meets the requirements (physical interface, torque, jitter, thermal, vacuum and vibration) as mentioned in the CMG specification document.

- B2. An ACS control unit consisting of two boards one master with a Texas Instruments (TI) digital signal processor (DSP) and one slave, each controlling two CMGs. The master has an attitude control algorithm, CMG steering logics, attitude determination and estimation algorithm interfaces with ADS devices and flight computer via an ACS-Comm cable and meets requirements as mentioned in the ACS controller interface document.
- B3. A format to store the maneuver data acquired from sensors, called ACS mode telemetry as per the TTC specification document.
- B4. Six Sun sensors with characteristics per ADS specification document and Honeywell magnetometer HMC2003 with specifications per the datasheet.
- B5. Analog Devices IMU ADIS16405 capable of outputting digitized angular rates and pass it on to the ACS controller via SPI protocol for propagation with specifications per datasheet.
- B6. ADS algorithm (software) with filtering to determine (using Sun vector and magnetic field vector) and/or propagate (using angular velocity vector) the satellite attitude with an accuracy better than  $5^{\circ}$ .
- B7. A/D converter(s) for sampling the Sun sensor and magnetometer data.
- B8. A format to store the ADS data acquired from Sun sensor, IMU and magnetometer, called ADS mode telemetry for transmission as per the TTC specification document.
- B9. Three magnet coils with on/off control for detumbling.
- B10. A format to store the detumbling data acquired from the IMU and other sensors, called detumbling mode telemetry for transmission as per the TTC specification document.
- B11. Transceiver (COTS) radio transceiver controlled by the flight computer to:
- B12. Dipole antenna sets (stowed during launch) for transmitting from Transceiver and receiving data from ground station per TTC specifications document.
- B13. Deployment and stowage mechanisms for antennae.
- B14. Flight computer hardware and software per the TTC specifications document to perform the following tasks:
- B15. Mission profile and sequence of operations.

- B16. ClydeSpace (COTS) EPS board with batteries power regulation and interfaces with solar cells and temperature sensors per the EPS datasheet and specifications document.
- B17. 10 Solar cells with two cells per interfacing panel per EPS specifications document.
- B18. Satellite bus design per the satellite bus specifications document to support and accommodate:
- B19. Satellite integrated operations supporting primary objectives.

### **3.2.4 Mission Mapping**

As shown in the requirements flowdown in Fig. 3-2, the mission definition is mapped to mission objectives, which are then mapped to mission requirements followed by other mappings which ultimately translate to components, interfaces, and tasks. The mapping process is described and demonstrated in two levels to accommodate details. The first level mapping shown in Fig. 3-4 and Fig. 3-5 translates mission definition to derived mission requirements. The primary mission objectives are mapped to their corresponding derived mission requirements in Fig. 3-4 and the secondary mission objectives are mapped to their corresponding derived mission requirements in Fig. 3-5.

The next level mapping translates each mission objective into building blocks, which include, sensors, peripheral components, communication interfaces and implementable tasks. This level of mapping ensures every building block, which can contribute to the mission cost in terms of power, telemetry and computation, is derived from the mission definition and contributes towards achieving the mission objective. To demonstrate this second level mapping, primary mission objective A2 is mapped to its basic building blocks as show in Fig. 3-6. The objectives of SwampSat mission defined earlier and the corresponding mapping is summarized in Table 3-1 and Table 3-2.

### **3.2.5 Components, Interfaces and Tasks**

An N-squared (N<sup>2</sup> or N<sup>2</sup>) diagram, also adopted from NASA's Systems Engineering Handbook [69], is used to capture the interfaces, mechanical and electrical, for all the components of the satellite obtained through the mapping process. The electrical

**PMO - Primary Mission Objective**  
**SMO - Secondary Mission Objective**  
**AMR- Allocated Mission Requirement**  
**DMR- Primary Mission Requirement**

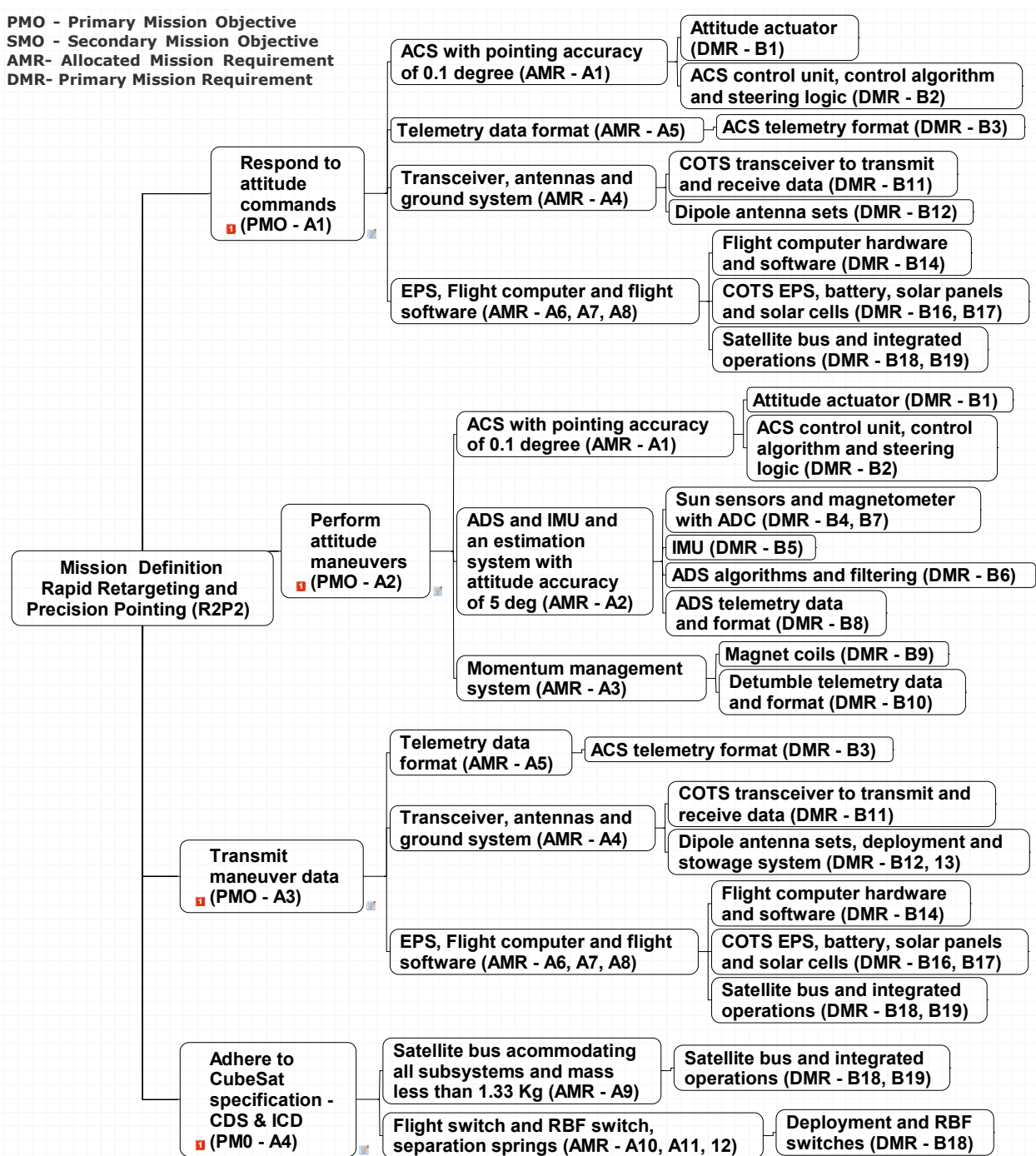


Figure 3-4. Mission Mapping of Primary Mission Objectives

interfaces here include power and communication interfaces. The N2 diagram primarily identifies areas where conflicts could arise in interfaces, and highlights input and output dependency assumptions and requirements [69]. A high level N2 diagram for

**PMO** - Primary Mission Objective  
**SMO** - Secondary Mission Objective  
**AMR**- Allocated Mission Requirement  
**DMR**- Primary Mission Requirement

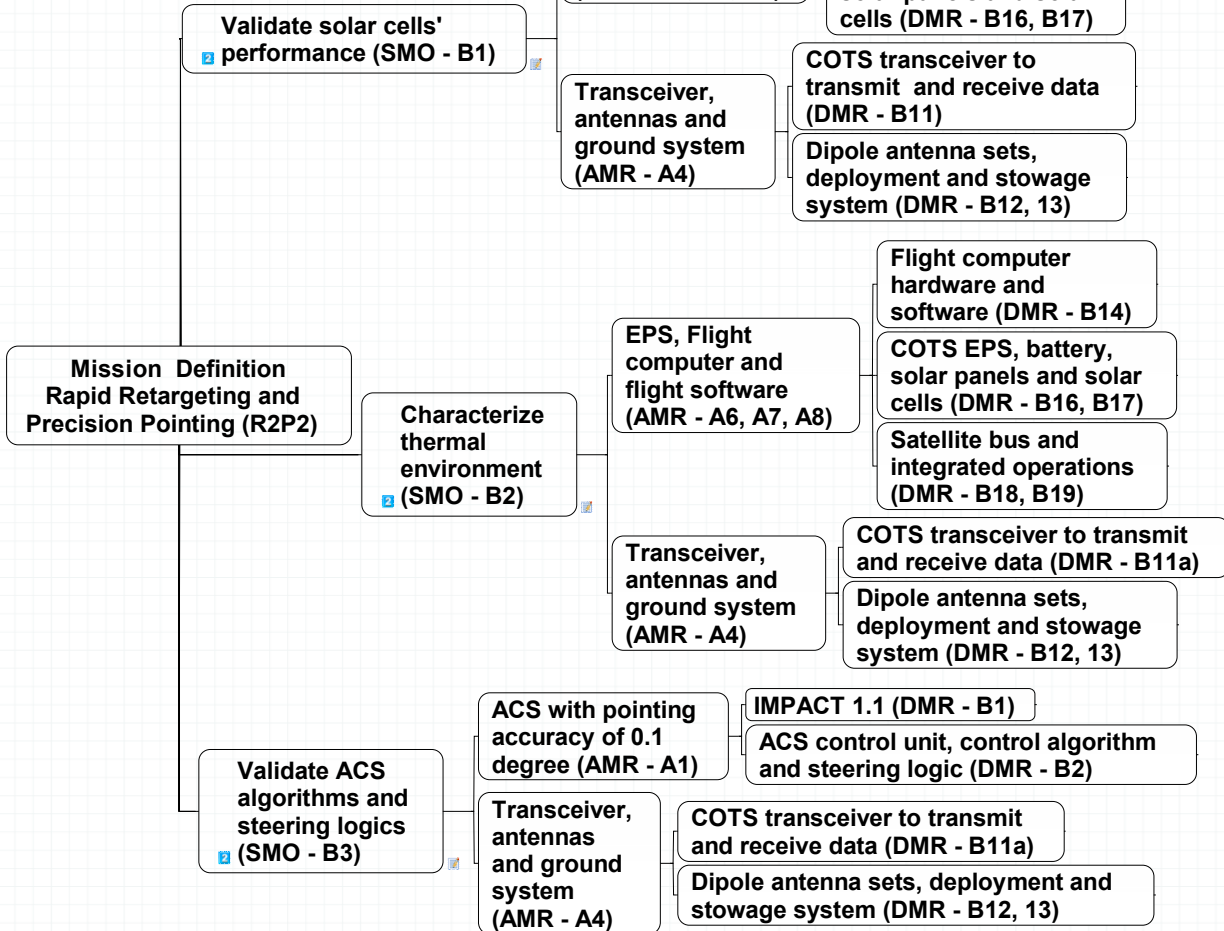


Figure 3-5. Mission Mapping of Secondary Mission Objectives

SwampSat mission capturing the mechanical and electrical interfaces is shown in Fig. 3-7. To illustrate the functionality of the N2 diagram better consider the interface connections between the SwampSat flight computer SFC430, magnetometer and Sun sensors. The triaxial magnetometer and six Sun sensors together require nine analog channels to interface with SFC430. Since the SFC430 is designed around TI's MSP430 microprocessor, it can only accommodate six analog channels. The N2 diagram in this instance will identify this limitation early in the design process and alert the system designer to seek solutions. It is important to note that interfaces can support

**PMO - Primary Mission Objective**  
**AMR- Allocated Mission Requirement**  
**DMR- Primary Mission Requirement**

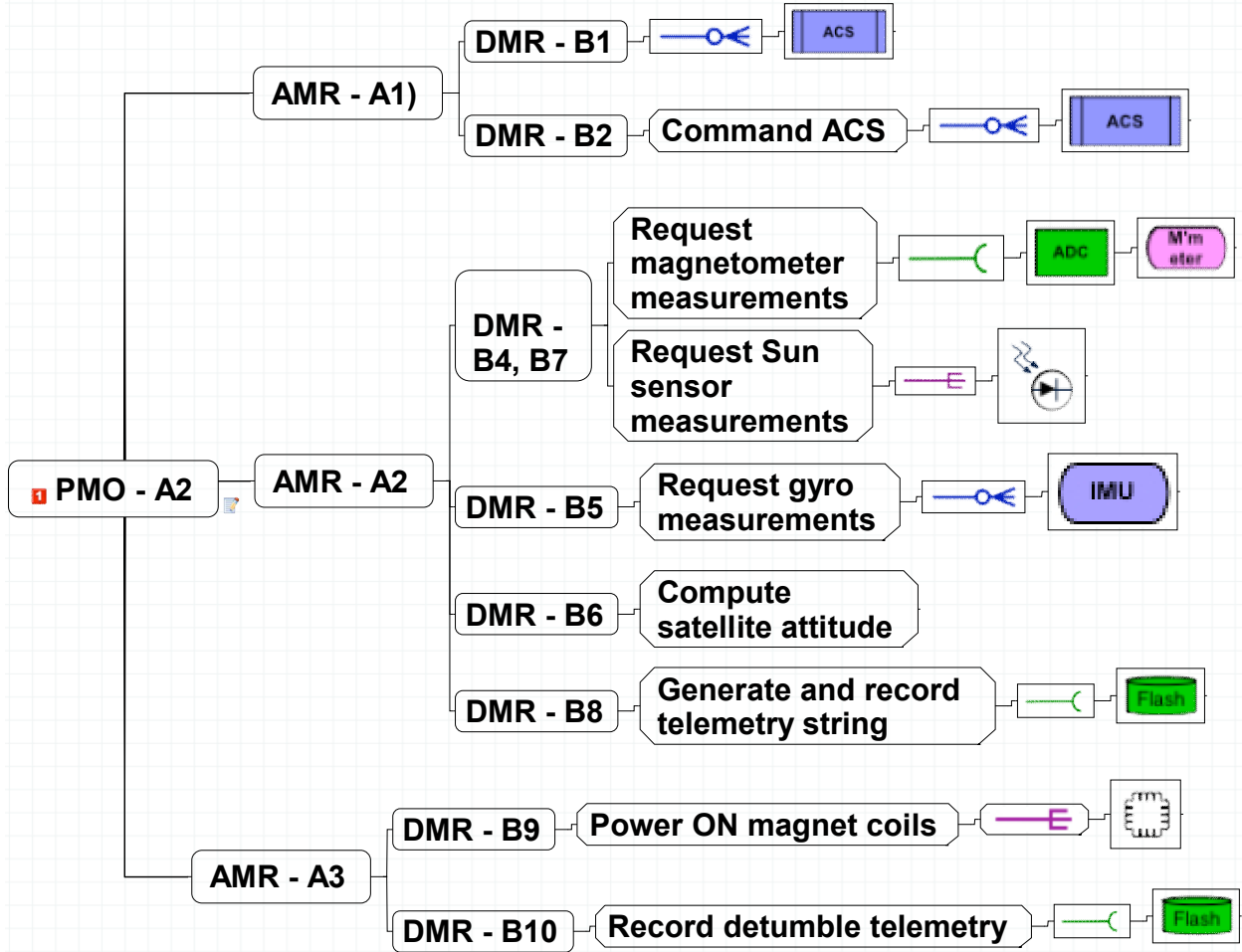


Figure 3-6. Mapping Mission Objectives to Building Blocks

one-to-one, one-to-many or many-to-many type connections. To ensure all components are accommodated, mechanically and electrically, on a satellite bus a more detailed level N2 diagram could be used. The process of identifying specific communication interfaces through detailed N2 diagrams can also facilitate protocol implementation.

The process of identifying non-conflicting components and their corresponding interfaces through the N2 diagram leads into defining a cost model in terms of power, telemetry and computation for a CubeSat mission. To facilitate detail design, components and interfaces can be associated with symbols, connector and color coded.

Table 3-1. Mapping Primary Mission Objectives to Building Blocks

Mission Objective	AMR(s)	DMR(s)	Task(s)	Interface(s)	Component(s)
PMO-A1	AMR-A1	DMR-B1	N/A	SPI	ACS
		DMR-B2	ACS control algorithms	SPI	ACS
		AMR-A5	DMR-B3	I2C	Flash
		AMR-A4	DMR-B11	SPI	ACS
		DMR-B11	Access ACS telemetry	I2C	Radio
	AMR-A6, A7, A8	DMR-B11	Transmit ACS telemetry	ADC	Antenna system
		DMR-B12, B13	N/A	Multiple	Flight computer
		DMR-B14	Flight software	I2C	EPS
		DMR-B16, B17	N/A	Multiple	Multiple
		DMR-B18, B19	Integrated operations		
PMO-A2	AMR-A1	DMR-B1	N/A	SPI	ACS
		DMR-B2	ACS control algorithms	SPI	ACS
	AMR-A2	DMR-B4, B7	N/A	ADC	Sun sensor, magnetometer
		DMR-B5	N/A	SPI	IMU
		DMR-B6	Attitude determination	ADC	Sun sensor, magnetometer
	AMR-A3	DMR-B6	Attitude estimation	N/A	N/A
		DMR-B8	Record ADS telemetry	I2C	Flash
		DMR-B9	Command magnet coils	ADC	Magnet coils
		DMR-B10	Record detumble telemetry	I2C	Flash
PMO-A3	AMR-A5	DMR-B3	Record ACS telemetry	I2C	Flash
		DMR-B11	Access ACS telemetry	SPI	ACS
		DMR-B11	Transmit ACS telemetry	I2C	Radio
		DMR-B12, B13	N/A	ADC	Antenna system
	AMR-A6, A7, A8	DMR-B14	Flight software	Multiple	Flight computer
		DMR-B16, B17	N/A	I2C	EPS
		DMR-B18, B19	Integrated operations	Multiple	Multiple
PMO-A4	AMR-A9	DMR-B18, B19	Integrated operations	Multiple	Multiple
	AMR-A10, A11, A12	DMR-B18	N/A	Multiple	Flight computer

The communication interfaces obtained from the mapping process in the context of SwampSat are listed in Table 3-3. As a special case, the communication interface between the satellite and ground station is also included in the list. The communication

Table 3-2. Mapping Secondary Mission Objectives to Building Blocks

Mission Objective	AMR(s)	DMR(s)	Task(s)	Interface(s)	Component(s)
SMO-B1	AMR-A6, A7, A8	DMR-B14	Flight software	Multiple	Flight computer
		DMR-B16, B17	N/A	I2C	EPS
	AMR-A4	DMR-B11	Access detumble telemetry	SPI	ACS
		DMR-B11	Transmit detumble telemetry	I2C	Radio
		DMR-B12, B13	N/A	ADC	Antenna system
SMO-B2	AMR-A6, A7, A8	DMR-B14	Flight software	Multiple	Flight computer
		DMR-B16, B17	N/A	I2C	EPS
	AMR-A4	DMR-B18, B19	Integrated operations	Multiple	Multiple
		DMR-B11	Access detumble telemetry	SPI	ACS
		DMR-B11	Transmit detumble telemetry	I2C	Radio
		DMR-B12, B13	N/A	ADC	Antenna system
SMO-B3	AMR-A1	DMR-B1	N/A	SPI	ACS
		DMR-B2	ACS control algorithms	SPI	ACS
	AMR-A4	DMR-B11	Access ACS telemetry	SPI	ACS
		DMR-B11	Transmit ACS telemetry	I2C	Radio
		DMR-B12, B13	N/A	ADC	Antenna system

interfaces are identified with a color code and connector type. Similarly the components, which include subsystem boards, sensors and peripheral devices are listed in Table 3-4 and each item is associated with a symbol, an interface and a telemetry overhead where applicable. The components are color coded to identify their primary communication interface. Finally, the tasks identified through the mapping process are linked with zero or more components and their corresponding interfaces. A computation overhead can be associated with each task to facilitate estimation of mission cost discussed earlier. The tasks in Table 3-5 are identified in the context of SwampSat. The process of assimilating components, interfaces, tasks and their associated overhead leads into their

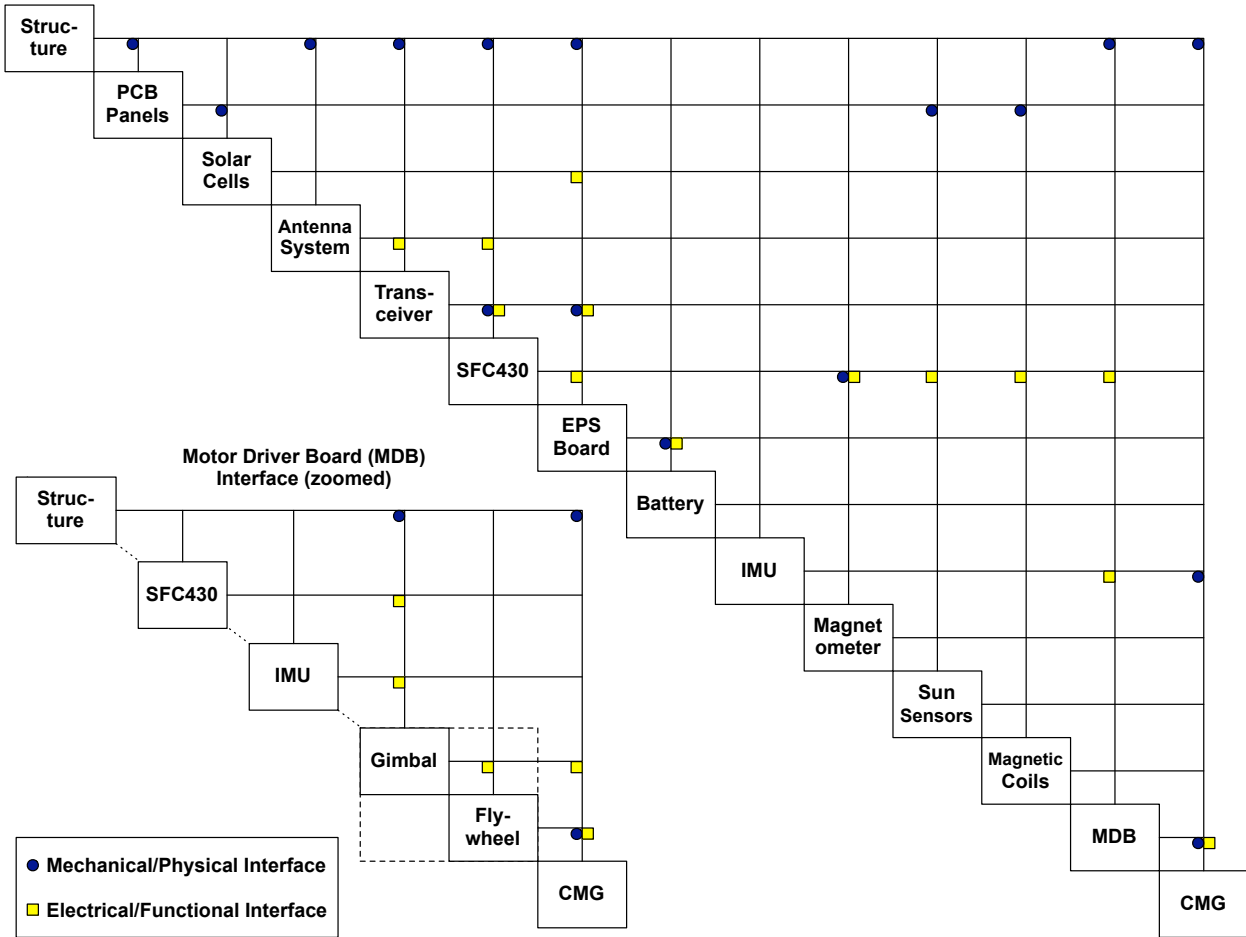


Figure 3-7. SwampSat N2 Diagram

detail design in the form of subsystem designs. However a critical element required for addressing the detail design is the mission concept of operations.

Table 3-3. Communication Interfaces

#	Name and description	Symbol
1	I2C - Inter Integrated Circuit	
2	SPI - Serial Peripheral Interface	
3	Digital (GPIO)	
4	ADC (Analog)	
5	Radio	

### 3.2.6 Concept of Operations (CONOPS)

Mission CONOPS facilitates a systematic approach of realizing the mission objective and is critical for organizing mission operations. The pico- and nano-class

Table 3-4. Peripheral Components, Sensors and Subsystem Boards

#	Name and description	Symbol	Interface	Telemetry (Bits)
1	IMU - Gyros			Gyro X, Y, Z (14×3) IMU temperature (12)
2	Flash Storage (EEPROM)			N/A
3	RTC			Year (12) Month (4) Date (8) Hour (8) Minute (8) Seconds (8)
4	External ADC			N/A
5	Load switch			N/A
6	Temperature sensor			Temperature (10)
7	Sun sensor			Voltage (12)
8	Magnetometer			Magnetometer X, Y, Z (12×3)
9	Magnet coils			Voltage (12)
10	Solar cells			Array voltages (10×5) Array currents (10×5)
11	Battery			Voltage (10) Current (10) Current direction (10) Temperature (10)
12	Antenna system			N/A
13	ACS controller			N/A
14	Electrical Power Supply			N/A
15	Transceiver			N/A

Table 3-5. Satellite Tasks

Id	Name and description	Components	Interface(s)	Power
1	Read RTC	RTC	—	$\sim 10 \text{ mW}$
2	Read flash	Flash	—	$\sim 10 \text{ mW}$
3	Write flash	Flash	—	$\sim 10 \text{ mW}$
4	Deploy antenna and verify	Out Ground Sense Set ON	—	$\sim 250 \text{ mW}$
	ACS	—	—	
	Flash	—	—	
5	Check receiver	RADIO	—	$\sim 50 \text{ mW}$
			—	
6	Transmit beacon/telemetry	RADIO	—	$\sim 1000 \text{ mW}$
			—	
7	Query Beacon	ACS	—	$\sim 250 \text{ mW}$
			—	
			—	
			—	
			—	
8	Power ON magnetic actuators	ACS	—	$\sim 600 \text{ mW}$
9	Record detumble telemetry		—	$\sim 10 \text{ mW}$
			—	
			—	
10	Record ADS and ACS telemetry	Flash	—	$\sim 50 \text{ mW}$
11	Access SFC430 telemetry	Flash	—	$\sim 10 \text{ mW}$
12	Access ACS and ADS telemetry	ACS	—	$\sim 50 \text{ mW}$

CubeSats particularly cannot be teleoperated on a continuous basis and hence its critical to design a diagnosing capability through the mission CONOPS. The mission CONOPS, specialized for SwampSat mission is shown in Fig. 3-8. Upon successful

launch and deployment from the P-POD, SwampSat enters the power-up and deploy mode, designed as a one time operation for antenna deployment and verification. The spacecraft enters the safe-hold mode, the primary operating mode, upon completing its power-up and deploy mode. During the safe-hold mode SwampSat communicates real time telemetry, which includes solar cell voltages, currents, temperatures, battery capacity and satellite angular rates to a ground station. The real time telemetry, SwampSat beacon, is designed to relay satellite health and assist ground control in decision making. From the safe-hold mode, SwampSat can transfer to any of the four operating modes: (i) detumble mode (ii) ADS mode (iii) CMG Ops mode and (iv) Comms mode. During the detumble mode, SwampSat stabilizes itself by using the magnetic actuators. The detumble mode, apart from stabilizing the satellite, is also designed to evaluate the performance of the solar cells by recording their voltage, current and temperature. The ADS modes is designed to validate the attitude determination system and assist in diagnosing the attitude and inertial sensors on board the satellite. During the ADS mode, measurements from Sun sensors, magnetometer and IMU, are fused together for estimating the CubeSat attitude. The estimated attitude along with satellite angular rates is stored on board the satellite. During the CMG Ops (Mission Ops) mode the primary mission goal of rapid retargeting and precision pointing is demonstrated. Similar to the detumble and ADS mode, CMG mode data is stored in on board the satellite. During the Comms mode, the mission validating data from the detumble, ADS and CMG Ops mode is downlinked to a ground station. To facilitate multiple attempts for realizing the mission goal, the operating modes can be executed multiple times. The mission CONOPS is summarized as a bulleted list below.

- Establish communications link in both directions
- Validate supporting subsystems
  - ADS: Sun sensors, magnetometer, and IMU
  - CDH: Software and A/D converters

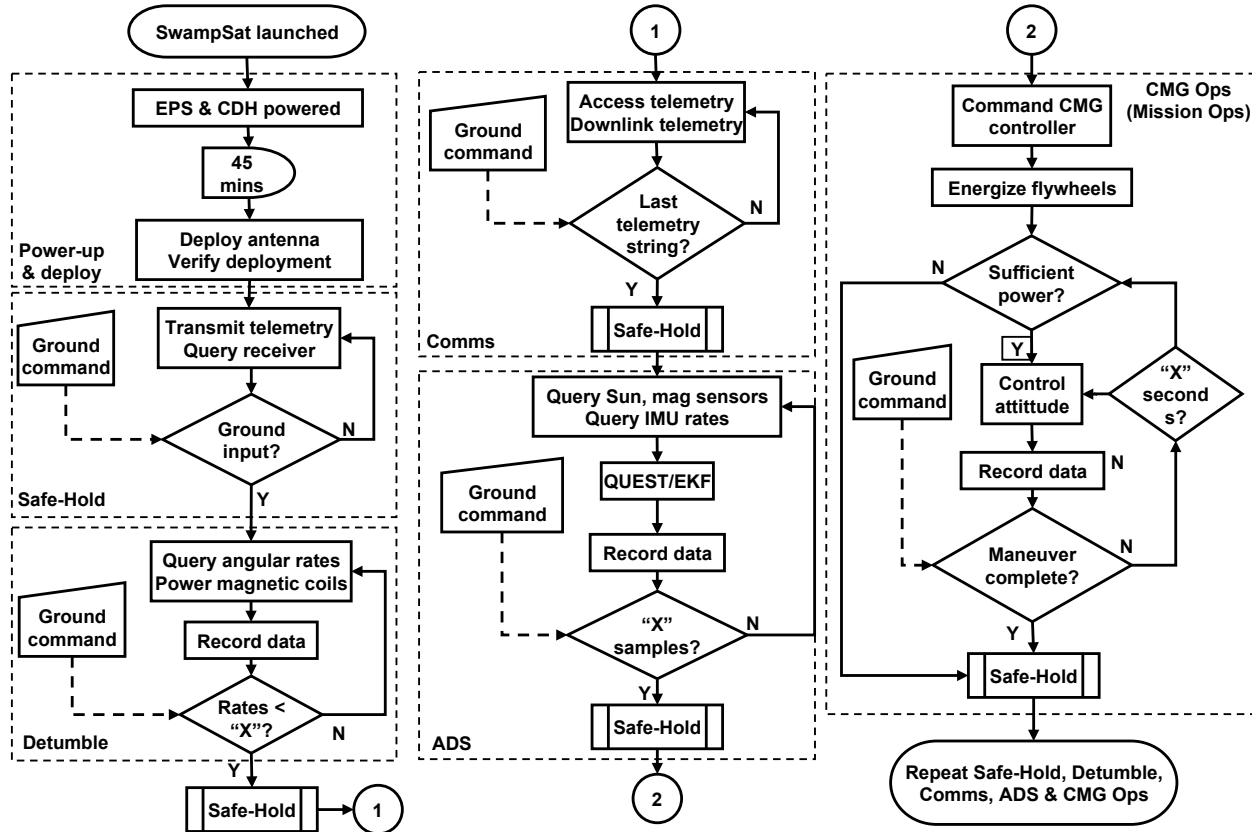


Figure 3-8. SwampSat Mission CONOPS

- EPS: Batteries, solar cells, and power supply board
- Downlink pre-maneuver attitude data
- Perform attitude maneuvers
  - Sun pointing
  - Retargeting
- Downlink post-maneuver attitude data
  - Analysis of pre- and post-maneuver data to validate maneuvers

The mission mapping process without the mission CONOPS, which is critical for operational design, translates mission definition to components, interfaces and tasks. Through the mission CONOPS, the systems engineering approach leads into the detail design and organization of the building blocks as operations. The detail design is

addressed as subsystems design in the remainder of this dissertation. The design and development of electrical power subsystem, command and data handling subsystem, telemetry, tracking and command subsystem and attitude determination and estimation subsystem is described in Chapters 4, 5 and 6.

## CHAPTER 4

### DESIGN AND DEVELOPMENT OF ELECTRICAL POWER SYSTEM

The mission mapping process of Chapter 3, discussed in the context of SwampSat, identifies the requirement for an electrical power system. Although there have been instances where CubeSats have been launched without solar cells [1], most satellites have at least accommodated a power supply board, on board battery, solar arrays and panels as part of their electrical power system. Similarly, the EPS derived from mission mapping process is also composed of: (i) power supply board (ii) battery board (iii) solar cells and (iv) solar panels. Most pico- and nano-class CubeSats have accommodated one or more COTS based components but not all have been successful on orbit [11, 12]. Although failures have been diagnosed for such COTS based development, for most such CubeSats the traceability has been missing due to the lack of a systems engineering basis. A systems engineering approach can be argued to better accommodate COTS based design and development and facilitate better traceability. To address the requirements of the EPS COTS based components are identified for the power supply board, battery and solar cells. Within the context of SwampSat, solar panels have contributed significantly towards integration of the various subsystems, components and this statement can be generalized for many pico- or nano-class CubeSat. The N2 diagram of Chapter 3 captures the multiple mechanical interfaces between the panel and other satellite components. The panel also facilitates multiple power and communication interfaces through embedded circuitry. A brief description of the COTS based components is provided in the following section before delving into the approach for COTS based development and detail design of the solar panels.

#### 4.1 Commercial-off-the-shelf Components of the Electrical Power System

Primarily, the EPS is responsible for harnessing, storing and distributing power to a CubeSat system. For most pico- and nano-class CubeSat, the EPS design is driven by

the requirements of operating subsystems and components at varying power levels and meet the following requirements:

- Maximize power generation in the solar cells
- Interface and harness power from the solar cells
- Regulate +5 V and +3.3 V to the CubeSat bus
- Monitor the EPS components for proper functioning
- Provide a communication interface to the flight computer for accessing EPS telemetry
- Compatibility with the CubeSat specification
- Protect battery by charging and discharging at a temperature  $> 0^{\circ} \text{ C}$

As stated earlier, the EPS subsystem is primarily made up of the EPS board, the battery board, solar arrays, and panels. The EPS board is responsible for power regulation and distribution, battery board hosts a Li-Po battery for storing power and circuitry for monitoring the battery health and the panels host solar arrays for power harnessing. A high level composition of the EPS and its integration with other subsystems is shown in Fig. 4-1. As shown in the figure, the solar arrays interface to the EPS board through the battery charge regulators (BCR), the Li-Po battery interfaces through the battery and communication bus, and the subsystems interface through the 5 V and 3.3 V buses.

#### 4.1.1 EPS Board

The availability of a COTS based power supply board, which specifically meets the above requirements and is particularly designed for a pico- or nano-class CubeSat may be motivating enough to accommodate it in the design process. To control and distribute power within the satellite the 1U CubeSat EPS from Clyde Space [80] is selected as the EPS board. The power module addresses the requirements identified above and is designed specifically for pico-class CubeSats. The EPS board interfaces with up to six solar arrays. The geometry of the CubeSat limits only one of the two opposite faces to

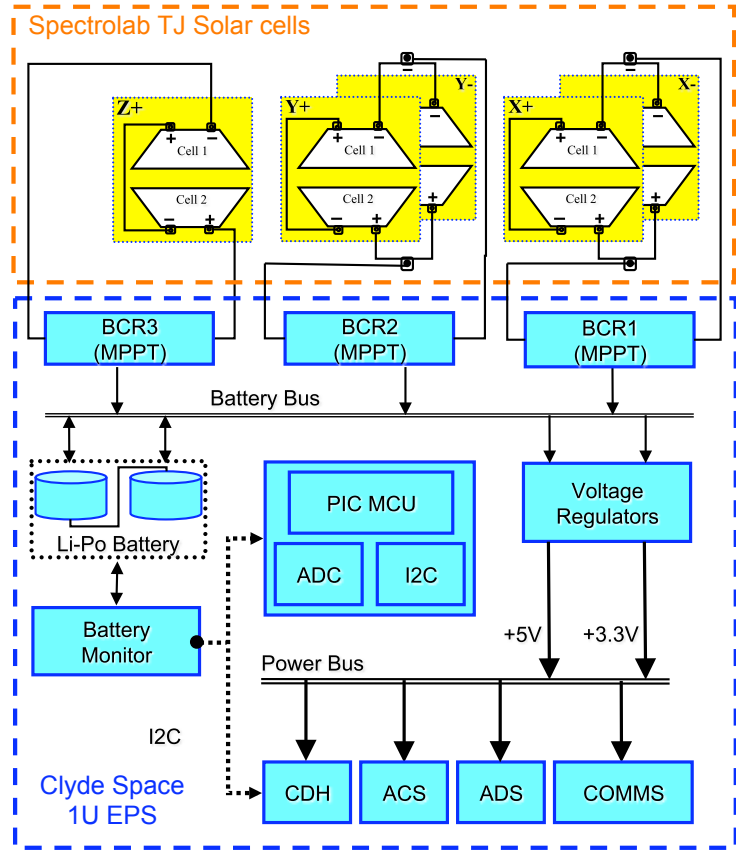


Figure 4-1. EPS Board Design Schematic

generated power at any given point of time. The EPS is designed to exploit this feature by connecting each BCR to solar arrays on opposite faces of the CubeSat. Power harnessed from the solar arrays through these BCRs is stored in lithium poly (Li-Po) battery pack and distributed through the DC-DC regulators on EPS. The EPS board can interface with Li-Po battery packs for charging them and using them as a power source during eclipse time. One of the primary requirement for most pico- and nano-class CubeSats is adhering to the CubeSat design specification. As per this requirement a CubeSat is required to have a deployment switch and a remove before flight (RBF) switch [19]. The RBF switch and the deployment are implemented through the EPS. The design for implementing these switches on the flight computer (SFC430) is shown in Fig. 4-2. A PIC based microprocessor provides telemetry and telecommand functionality

for the EPS through its I2C interface. The telemetry channels of the EPS include solar array voltage, current and temperature, battery voltage, current, temperature and current direction, cell voltage and bus currents.

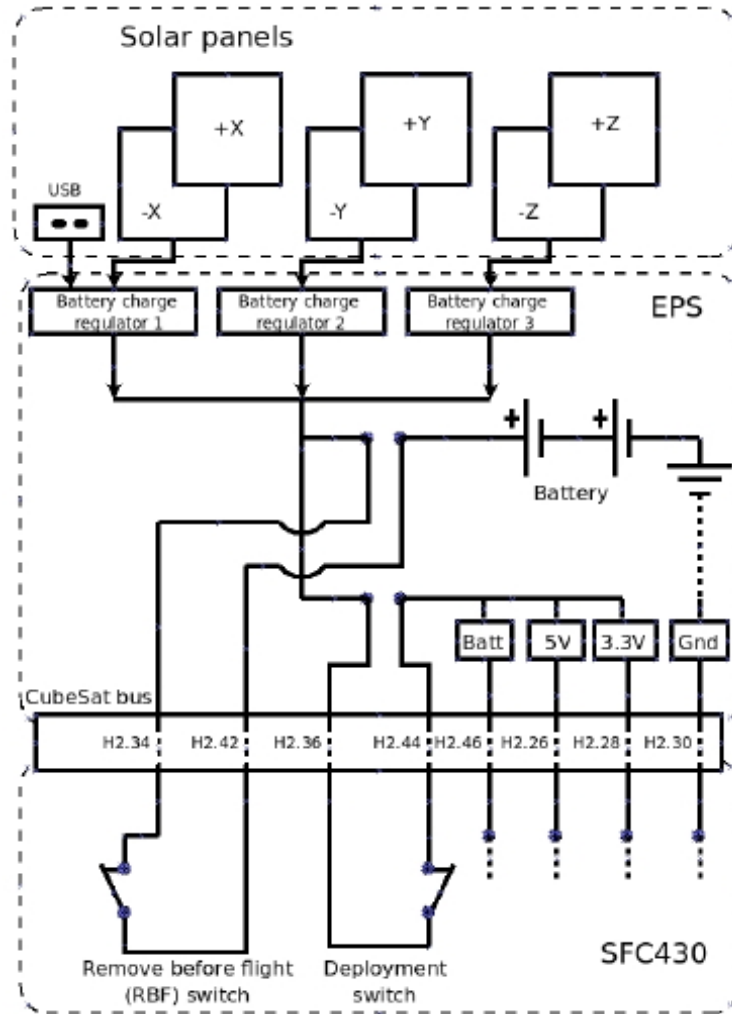


Figure 4-2. Design for Implementing RBF Switch and Deployment Switch

#### 4.1.2 Battery Board

Similar to the EPS board, a 1U battery board, also from Clyde Space, is selected as for storing chemical energy. The battery board connects to the EPS board through a single connector and can be replaced during ground testing. The main characteristics [80] of the cells used to form the battery board are listed in Table 4-1. The battery board incorporates an integrated, thermostatically controlled battery heater, battery current,

voltage and current direction telemetry, cell voltage telemetry and cell protection circuit for under and over voltage and over current. The maximum charge per battery board is 8.2 V and minimum discharge voltage is 6.4 V. The battery capacity is 1250 mAh.

Table 4-1. Battery cell characteristics

Size	58.5 mm x 37 mm x 5 mm
Mass	22.5 g
Capacity	1250 mAh
End of Charge limit	4.1 V
End of Discharge limit	3.2 V

#### 4.1.3 Solar Cells

Triple junction photovoltaic cells from Spectrolab are selected for harnessing solar power on orbit. These solar cells have an efficiency of 25.1%. The solar cells are capable of supply voltages of up to 2.2 V per cell and two such cells connected in series are mounted on each solar panel. The dimensions of a single solar cell and a panel accommodating two such cells are shown in Fig. 4-3. The solar array on each panel is capable of producing a maximum of 2 W of power and 1.5 W average (Average Orbit Power OAP). The solar arrays are monitored for their voltage, temperature and current capacity by the EPS board.

### 4.2 Multifunctional Solar Panel Design

The solar panel design is driven by the requirements to accommodate a surface suitable for mounting solar cells, embed magnetic coils for angular momentum management, provision for mounting Sun sensors, temperature sensors, bypass diodes and their respective electrical circuitry, and provide structural rigidity to the spacecraft. Solar cells used for CubeSat applications are designed to be light in mass and the cell-interconnect-cover (CIC) is susceptible to breakage. Failure of student designed CubeSats are attributed towards failure of solar panel components, specially solar cells [3]. A flat, even mounting surface is desired for favorable bonding between solar cells and panel surface. Coarse, uneven surface can lead to poor bonding which

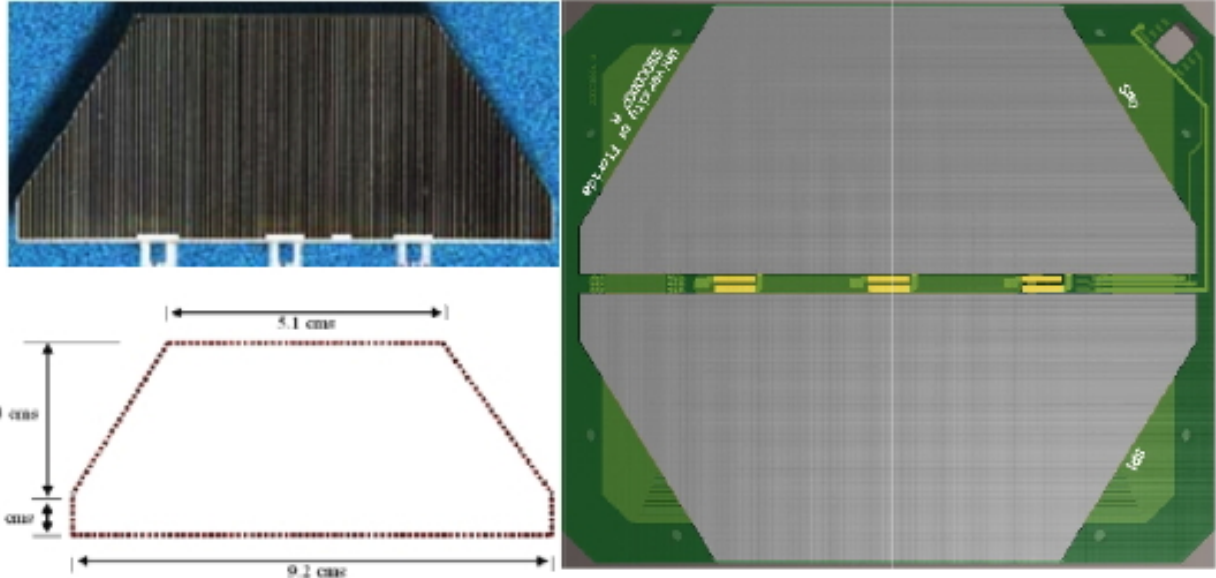


Figure 4-3. Solar Cell and Corresponding PCB Solar Panel

could eventually damage the solar cells. The quantity of the bonding material could increase for coarse surfaces and adversely affect satellite mass budget and thermal heat regulation between the solar cells and panel. To accommodate the angular momentum management requirements [39, 81], the solar panels are designed to host embedded magnetic coils. The allowable panel thickness is dictated by the form factor constraint and the mission requirements. Each panel with magnetic coils is designed to host approximately 70-80 turns with the ability to be driven at 150 mA. The embedded magnetic coils are designed to be accommodated in the area shown between the two dotted lines in Fig. 4-4.

Delrin plates hosting the receive and transmit antenna systems are accommodated between the solar panels and the CubeSat chassis. These requirements limit the options for placement of Sun sensors, temperature sensors and the corresponding circuitry. A side solar panel drawing is shown in Fig. 4-4 detailing the dimensions and the location of the peripheral components. The provision for mounting solar cells, shown as a hatched planes, is designed to be in that orientation for accommodating a Sun sensor and a temperature sensor. Embedded electrical circuitry connects the two cells

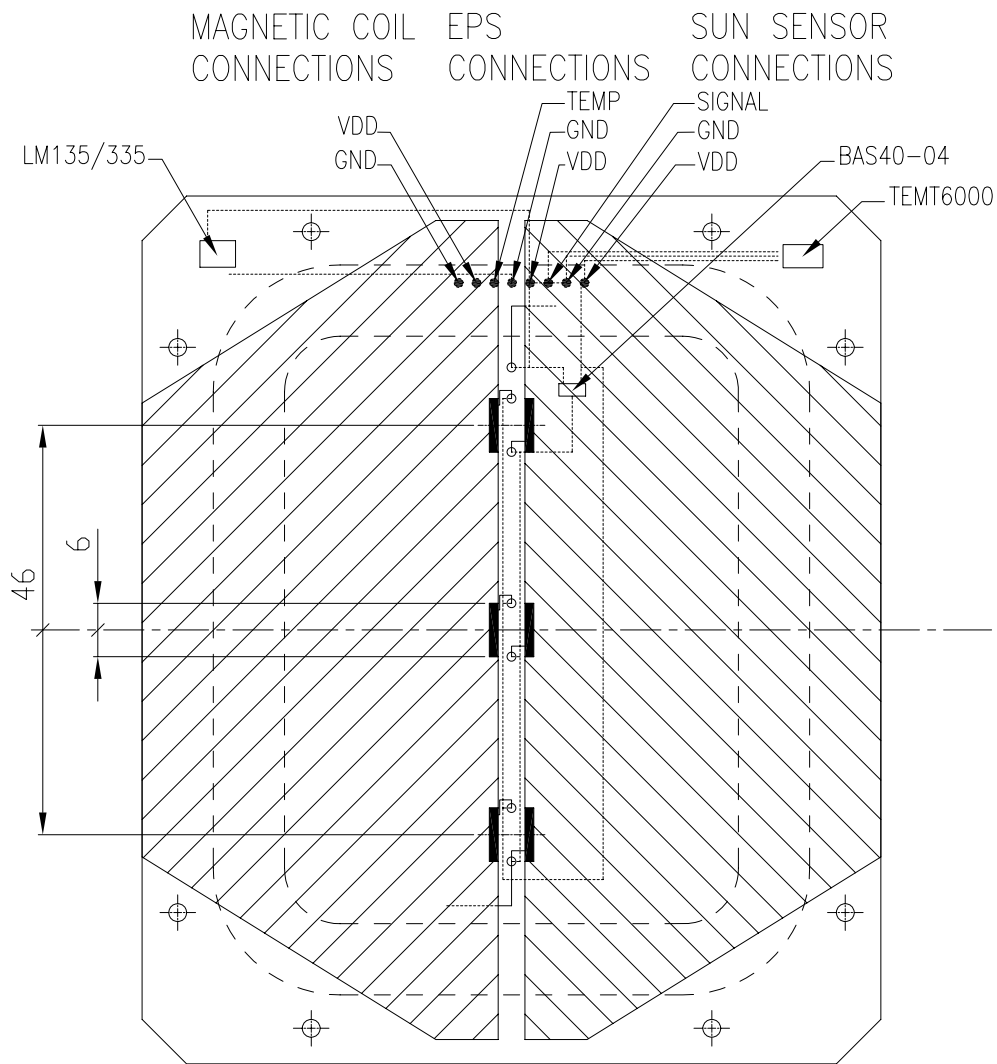


Figure 4-4. Solar Panel Design

in series. This circuitry includes a dual bypass diode to ensure the failure of one cell does not affect the power harnessing capability of the other. A provision is made to accommodate interface connectors between the solar panels and the subsystem boards through the delrin plates on two sides of the CubeSat. Connectors are designed to be hosted on the panels to interface solar cells and temperature sensors to the EPS board; the Sun sensors and the magnetic coils to the flight computer.

## **4.2.1 Solar Panel Design Implementation**

The solar panel design shown in Fig. 4-4 is implemented as: (i) carbon fiber composite solar panel and (ii) printed circuit board (PCB) solar panel.

### **4.2.1.1 Carbon fiber composite solar panel**

Composite solar panel implementation process involves preparation of magnetic coils, laying out fiber composite and machining the product to achieve precise dimensions. Magnetic coils are prepared from enamel coated 30 AWG copper core wire and epoxy. Wet lay up technique using a carbon fiber fabric is chosen for implementing the solar panel design as a composite. As a rule of thumb equal weights of the carbon fabric and epoxy resin are used to prepare the composite panel. A clean glass plate and an aluminum mold are used during the preparation to achieve a smooth mounting surface for the solar cells and ensure the magnetic coils reside in a groove. The precisely dimensioned composite pane is functionally transformed into a multifunctional composite panel by mounting solar cells and laying out electrical traces, bypass diodes and temperature sensors. A combination of conductive epoxy from, conductive pen and metal foil tape with high temperature resistant adhesive is used for laying out electrical traces. To account for the loss of a single solar cell on any panel, bypass diodes are soldered appropriately along the path of the electrical traces. Space grade epoxy and custom designed disposable stencils are used for mounting solar cells on the surface obtained from the glass plate. A temperature sensor is mechanically glued at the corner of the panel and electrically interfaced to the traces on the other side of the pane via the through holes. The composite panel is designed to accommodate a Sun sensor on another corner.

### **4.2.1.2 Printed circuit board solar panel**

A 6-layer, 1 mm thick, printed circuit board with FR-4 cores, 2 oz per square foot copper, dual side solder mask with fully insulated vias, and an immersion gold over electroplated nickel finish is implemented. The implementation has embedded magnetic

coils, pads for mounting solar cells and electrical traces for interfacing them to the EPS. The PCB panel implementation makes provision for mounting a Sun sensor, temperature sensor and surface mount dual bypass diode. Pads are laid on the top layer for mounting solar cells as shown in Fig. 4-5A. Magnetic coils, summing to 71 turns, are laid out on 4 inner layers and the bottom layer of the PCB as shown in Fig. 4-5B and Fig. 4-5C and interconnected by vias. A temperature sensor, bypass diode and connectors are mounted on pads on the bottom layer and electrically interfaced through PCB traces. Temperature sensor and Sun sensor leads are routed from outside of the coils to the inner region via vertical traces on the top layer between the solar cell pads. Solar cell leads on the top layer are connected to the traces on the bottom layer through vias and electrically interfaced to the EPS board through a connector. High current traces for the solar cells and magnetic coils utilize multiple parallel vias. Mounting holes for the PCB panels are machine drilled, and through holes for the sensors, allowing flushing with the top surface, are machine milled. The Sun sensor utilizes a carrier PCB to provide front-looking mounting pads flush with the back surface. The PCB design for three different types of layers and a complete panel are shown in Fig. 4-5.

#### 4.2.2 Solar Panel Tests, Results and Comparison

Prototype panels implemented using the above techniques are shown in Fig. 4-6. The prototype PCB panels were subjected to several tests to evaluate their performance and further improve the design of the flight panels. Outgassing test was performed on the PCB panels in a vacuum chamber and difference in mass was observed before and after the outgassing cycle. The vacuum chamber was pumped down to  $\sim 7.8 \times 10^{-7}$  torr and maintained at this level for 19 hours. A maximum of 0.0236% decrease in mass was observed in the PCB panels. The total mass loss (TML) outgassing levels were observed to be well within the acceptable levels [82].

The PCB panels mounted with solar cells, temperature sensor and embedded magnetic coils were subjected to random vibration loads conforming to the PSD table

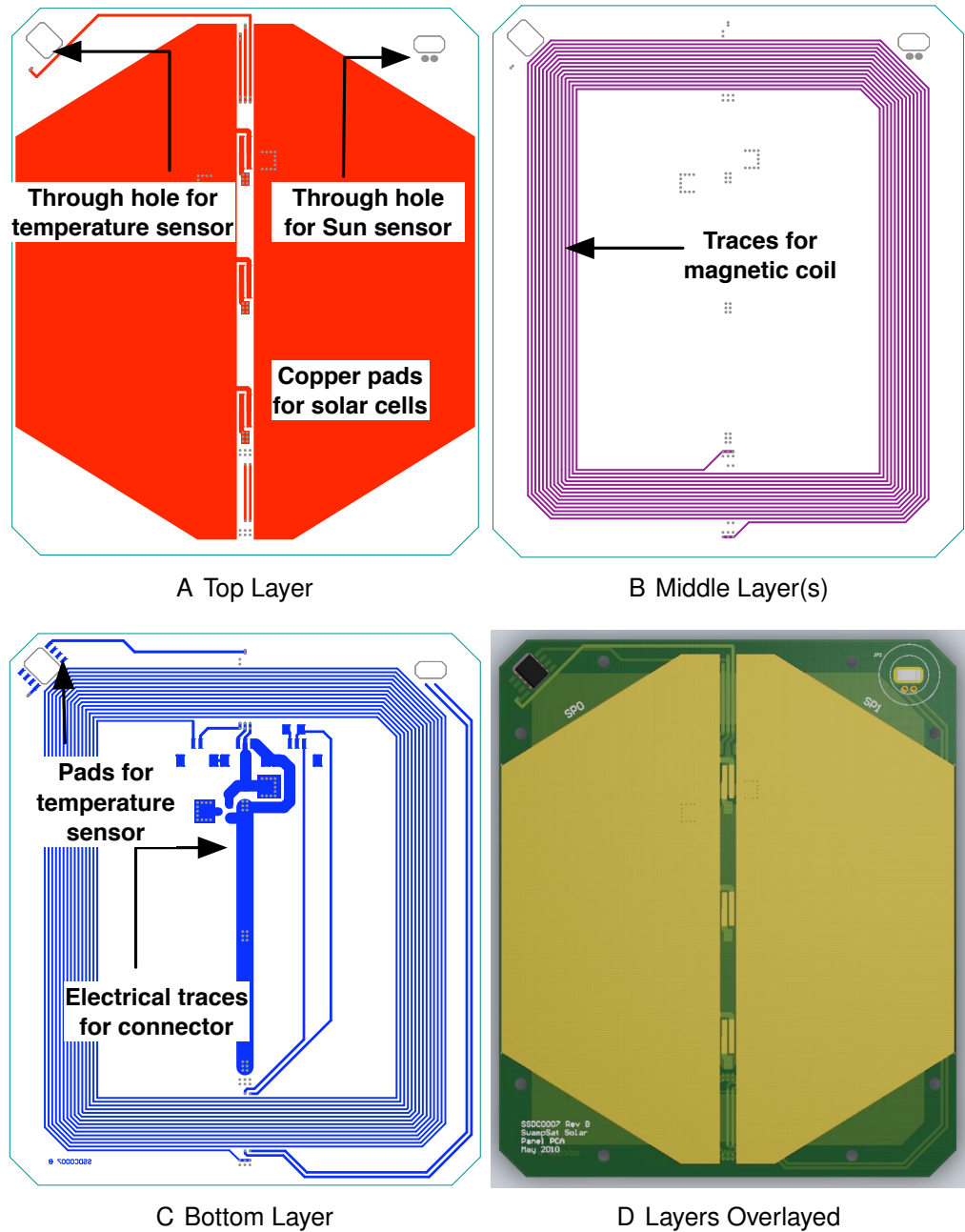
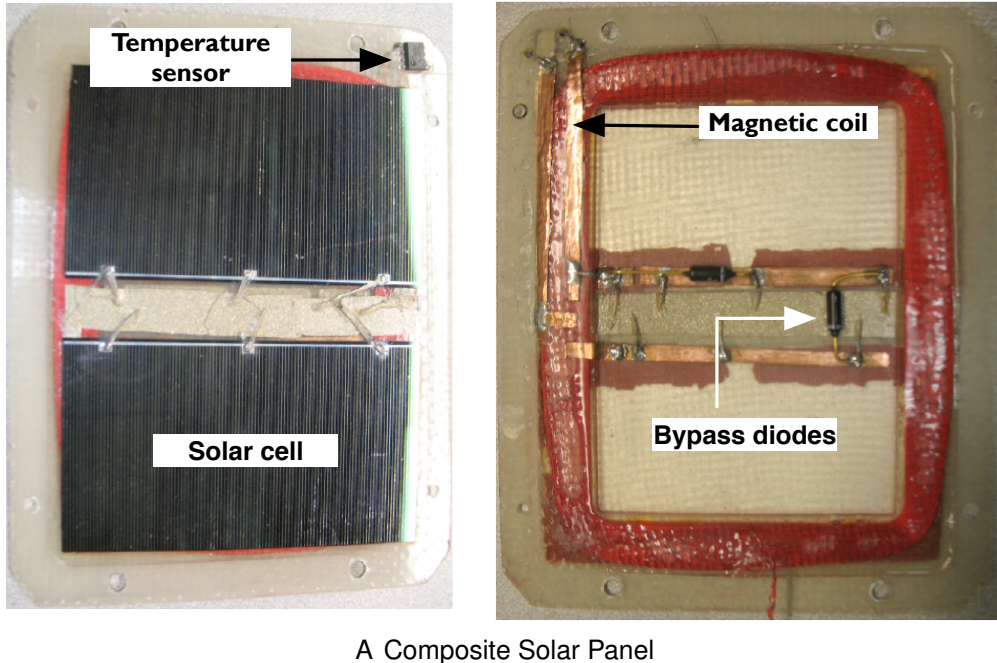
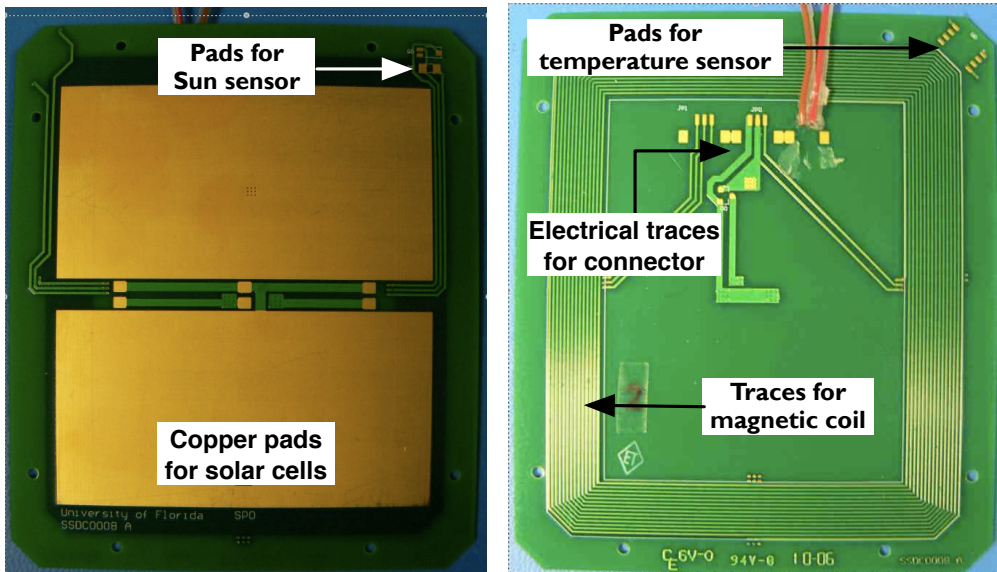


Figure 4-5. A Multifunctional PCB Solar Panel

in the CubeSat to P-POD interface control document [83]. The panel was subjected to vibration loads along each axis and the solar cell functionality was verified before and after the vibration test by measuring the voltage output under a sun simulator. The structural integrity of the panels was inspected and the continuity of the traces for temperature sensor and magnetic coils was verified before and after the vibration test.



A Composite Solar Panel



B PCB Solar Panel

Figure 4-6. Composite and PCB Solar Panel Implementations

The PCB panel assembly was found to be functional and no visual signs of damage were observed from the vibration tests.

The performance of the embedded magnetic coils in both the panel types was evaluated. Each solar panel was designed to accommodate, approximately 70-80

turns in its embedded magnetic coil and sustain a current load of up to 150 mA. Power consumed as a function of supply current was used as a criteria for evaluating the performance. Starting with an initial supply current of 100 mA the voltage to the magnetic coils was varied to increment the current in steps of 10 mA. Precise voltage and current measurements captured during the experiment were used to compute the power consumption. From the evaluation exercise it was determined that the power consumption of the magnetic coils embedded in the PCB panels although higher than that consumed by composite panels, it could be accommodated within the power budget. A plot of power consumption as a function of supply current, shown in Fig. 4-7, evaluated the performance of the coils.

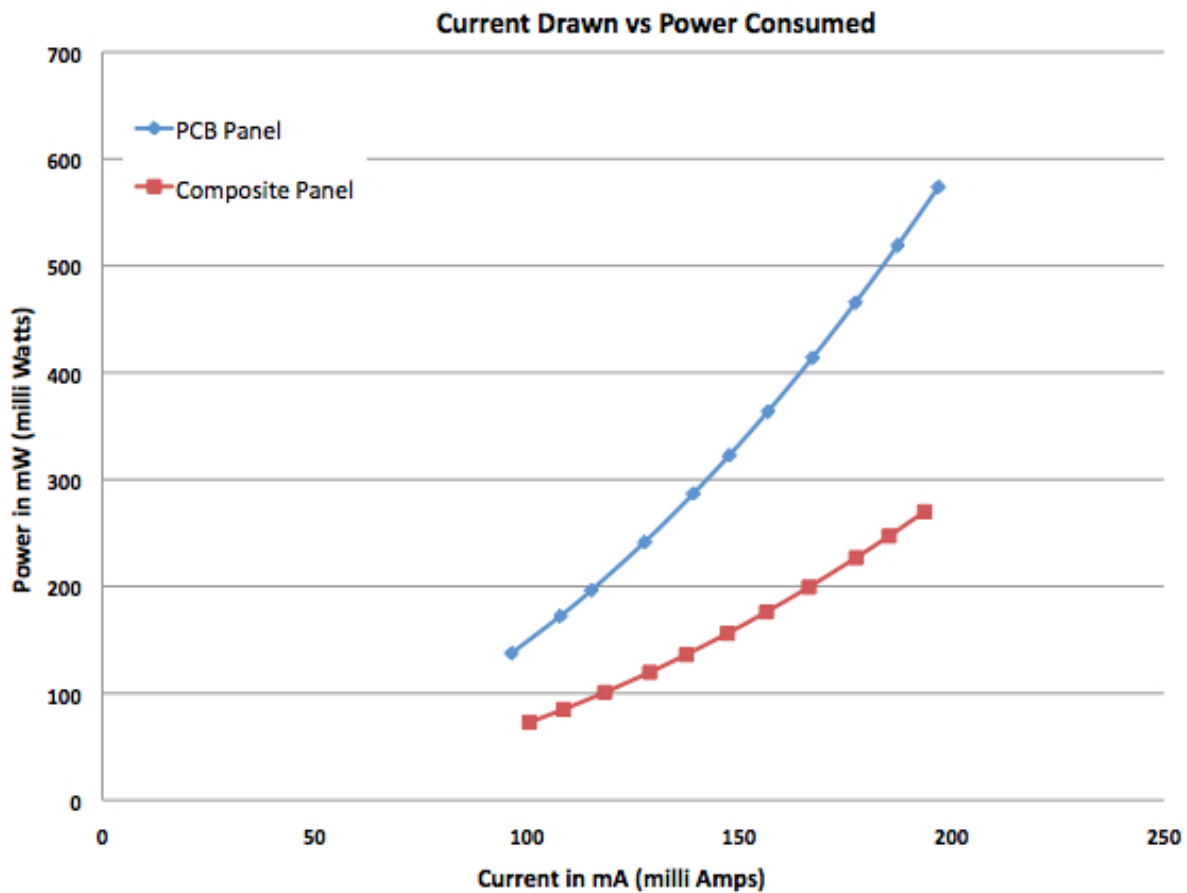


Figure 4-7. Plot of Supply Current vs Power Consumed

The manufacturing technique for PCB panels resulted in lesser volume consumption and made the product better suited for space environment. The fabrication process for composite solar panels introduced air pockets and possible failure due to outgassing. The PCB manufacturing technique made provisions for hosting surface mount components and connectors. PCB panels were observed to be well suited to accommodate delrin plates for hosting the receive and transmit antenna modules. The machine fabricated traces for PCB panels were observed to be reliable and robust to vibration load testing. After analyzing the advantages and limitations of each panel type it was determined that the process of implementing PCB solar panels was better suited to address the requirement of a CubeSat mission. The salient features comparing the two types of panels evaluated is presented in Table 4-2.

Table 4-2. Composite Solar Panel vs PCB Solar Panel

<b>Composite Solar Panel</b>	<b>PCB Solar Panel</b>
Solar panel epoxy can introduce air pockets and lead to outgassing issues	Design accommodates copper pads with solder paste and solder flux
Heat dissipation is not an issue	Heat dissipation might be an issue
Electrical traces and pads are manually laid	Electrical traces and pads are machined into the panel
Mounting holes are manually drilled	Mounting holes are laser cut
Wet layup technique used for fabricating can introduce air pockets	PCB boards are machine fabricated and the technique is better suited to minimize air pockets
Panel thickness (with coils) ~ 2.5mm	Panel thickness (with coils) ~ 1mm
Carbon fiber is electrically conductive	Glass fiber is electrically non-conductive

### 4.3 Power Budget and Balance

The mapping process discussed in the previous chapter translated mission definition to system level components and associated a power overhead with these components. A power budget, shown in Table 4-3, is formulated taking into consideration the power consumption of these components. The OAP, computed for a 90 minute orbit

with about 30 minutes of eclipse time, is approximately 1.5 W which is exceeded by simultaneous operations of the components. Therefore, it is necessary to develop operational modes to duty cycle the higher power consuming components. However, CMG operations are primary to the mission and the operating mode power budget shown in Table 4-4 and the mission CONOPS shown in Fig. 3-8 suggest a means of accomplishing this operation. The satellite is operated in a safehold mode without consuming all the power generated from the solar cells and the excess power is stored in Li-Po battery. Assuming a retention capacity of 80% during the initial phase of the mission the battery can store up to 8 Whrs of power. The CMG operations with their consumption rate can utilize this power for up to 2 hours to demonstrate mission ops.

Table 4-3. Detailed power budget

<b>Module</b>	<b>Sub Component</b>	<b>Max Current (mA)</b>	<b>Voltage (V)</b>	<b>Max Power (mW)</b>	<b>Power (mW)</b>
ACS	Flywheel motors	400	5	2000	3260
	Gimbal motors	200	5	1000	
	Magnetic Coils	50	5	250	
	TI-DSP uP	2	5	10	
ADS	Magnetometer	20	6	120	370
	IMU	33	5	165	
	Sun Sensor	30	2.5	75	
	SFC430	2	5	10	
CDH	Flash	10	4	40	48
	12-bit ADC	2	4	8	
Comms	Transmitter	200	5	1000	1040
	Receiver	8	5	40	
EPS	PIC16F690	2	4	8	12
	Temp Sensors	1	4	4	
<b>Total power (mW)</b>					<b>4730</b>

#### 4.4 Software Architecture

The software architecture, discussed with more details in the next chapter, is an attempt further to utilize the available resources efficiently. To execute the mission profile shown in Fig. 3-8 the software is designed as operating modes and implemented as software tasks as shown in Fig. 4-8. When the safe-hold mode is in operation the

Table 4-4. Operating Modes Power Budget

Module	Sub Component	Max Power (mW)	Max. Power - Operating Modes (mW)				
			Safe-hold	Comms	Detumble Att Det	CMG Ops	
ACS	Flywheel Motors	2000	0	0	0	0	2000
	Gimbal Motors	1000	0	0	0	0	1000
	Magnetic Coils	250	0	0	250	0	0
	Atmel uP	10	10	10	10	10	10
	Magnetometer	120	0	0	0	120	120
	IMU	165	0	0	165	165	165
ADS	Sun Sensor	75	0	0	0	75	75
	SFC430	10	10	10	10	10	10
CDH	Flash	40	40	40	0	40	40
	12-bit ADC	8	8	8	8	8	8
	Transmitter	1000	0	1000	0	0	0
Comms	Receiver	40	40	40	40	40	40
	PIC16F690	8	8	7	7	7	7
EPS	Temp Sensors	4	4	4	4	4	4
	<b>Power consumption (mW)</b>	<b>4730</b>	<b>120</b>	<b>1119</b>	<b>494</b>	<b>479</b>	<b>3479</b>

CubeSat is designed to consume about 15% of the power generated from the solar cells.

The excess power is stored in the Li-Po batteries for use in mission operations.

To address COTS based design and development it is critical to accommodate unit level testing within the systems based design approach. A unit level test plan and test report can be used to address such testing needs. The EPS board, battery boards and the solar panels are subjected to the tests listed in Table 4-5. The corresponding test reports are included as part of Appendix.

The discussions of this chapter primarily address how COTS based components can be accommodated in the systems engineering approach for design and development of CubeSats. When multiple COTS components are selected to address the requirements

Table 4-5. Tests to Qualify Electrical Power System

Item	Description	Observations
1	Power distribution	5 V, 3.3 V and Batt buses operational
2	RBF and Flight Switch operation	Emulated and verified to be functional
3	I2C communication	Battery characteristics - Verified
4	Transceiver powering capability	Power consumed at 1200 baud is 3 times the power consumed at 9600 baud
5	EPS and PCB panel outgassing analysis	EPS and PCB panel board passed the test Battery operation was uncharacteristic
6	PCB panel vibration analysis	Panel passed the test (with solar cells mounted)
7	Battery charging and discharging	Under voltage protection is an issue; possible power dissipation through I2C lines
8	PCB panel functional test	Magnetic coils tested for functionality; being characterized for magnetic field Solar cells tested for functionality and temperature sensor tested for connectivity

of a CubeSat mission it is critical to design one or more custom components to integrate these into a single system. The design, development, and analysis of multifunctional solar panels is discussed in this context. As stated in the beginning of this chapter, the solar panels host multiple components and their electrical circuitry, facilitate power and communication interfaces and play a pivotal role when seen in sight of the N2 diagram. Power budget formulation and evaluating it in the context of operating modes is vital for a CubeSat's success. Testing and evaluating COTS based components is a critical requirement which is addressed as part of the systems engineering based design approach.

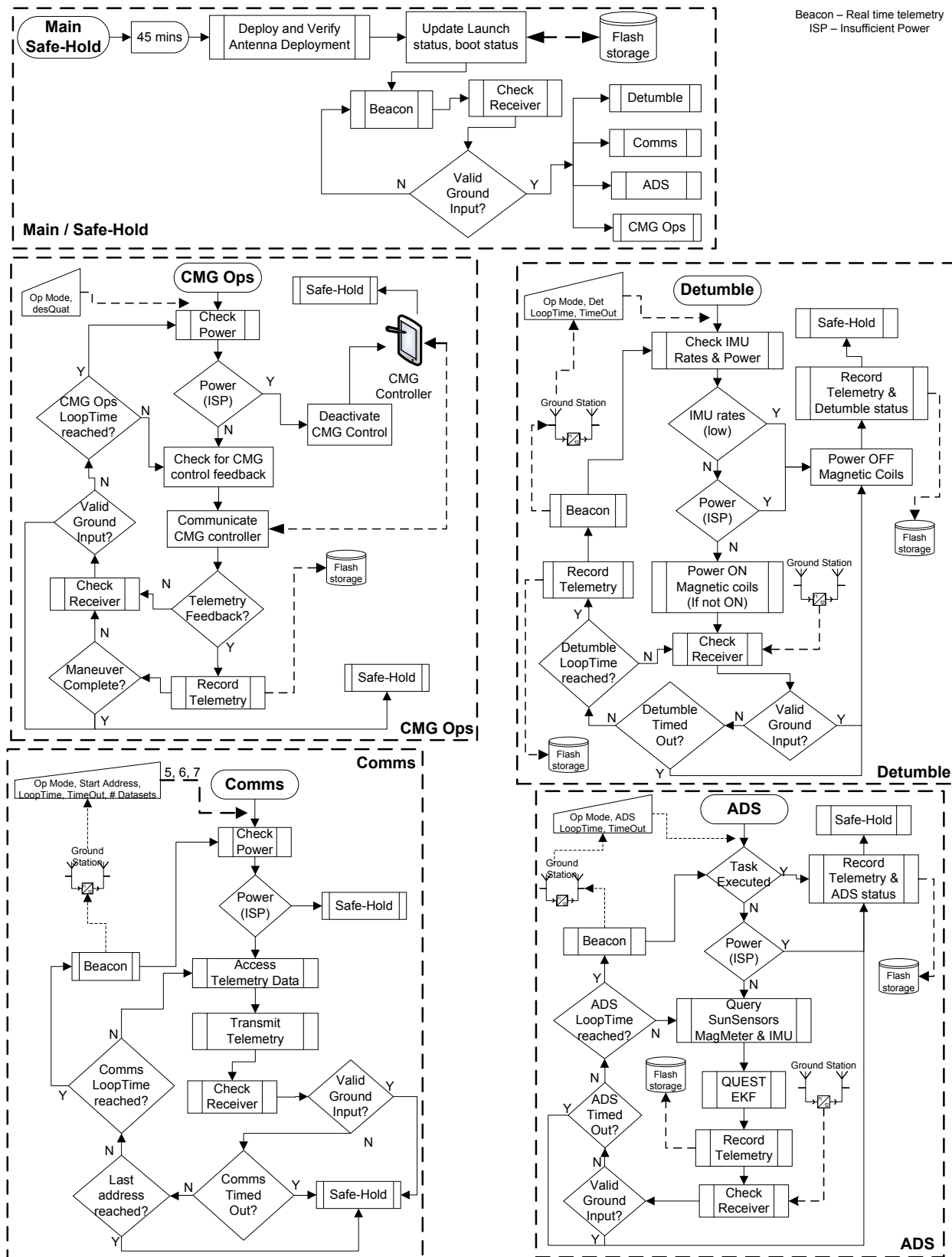


Figure 4-8. SwampSat Software Architecture

## CHAPTER 5

### DESIGN OF COMMAND, DATA AND TELEMETRY HANDLING

The CubeSat form factor, as described in Chapter 3, contributes as an external constraint in the design and development approach. The form factor limits the surface area available for mounting solar cells and as a consequence the power generation capability of a CubeSat. To address the limitation of power generation associated with particularly the pico-class CubeSat form factor, the on board computing may be designed as a distributed system. The mission CONOPS is a critical factor for addressing distributed operation design and the limited power generation capability. The distributed operation design is described in the context of SwampSat's ADS operating mode and CMG Ops mode. Additionally, SwampSat's form factor limits the power generation capability to a maximum of 2 W and an average orbit power of 1.5 W but the on board Li-Po rechargeable battery is capable of storing up to 10 Whrs of electrical power. To accommodate the power requirement of more than 3.5 W for the mission ops, the command and data handling software is designed to operate the spacecraft in a low power mode until the energy stored in the battery is sufficient for demonstrating mission ops.

As described in Chapter 3, a top-down design approach is adopted to facilitate a bottom-up coding scheme for the flight software. Driven by the mission CONOPS, the tasks derived from the mission mapping process are grouped together as operating modes and implemented as software routines for realization. The approach for the overall flight software design is described in the context of SwampSat mission. To date, most pico- and nano-class CubeSats have been flown as a secondary payloads and hence are required to demonstrate the capability of not interfering with the primary payload communications during the initial minutes of launch [22]. The power-up and deploy operation shown in Fig. 5-1 primarily addresses this capability. After a successful execution of the power-up and deploy mode, the CubeSat enters a safe-hold mode. To

make provision for ground based decisions the CDH software operates the CubeSat in a safe-hold mode for a major part of its life on orbit. On successful antenna deployment, the satellite enters the safe-hold mode and proceeds to transmit realtime telemetry, which includes solar cell voltages, currents, temperatures, battery capacity, satellite angular rates among others. The realtime telemetry relays satellite's health and assists ground control to initiate satellite operation as per the mission CONOPS. SwampSat, as described in the mission CONOPS, is operated in 4 other modes from within the safe-hold mode to stabilize the satellite (detumble mode), diagnose its sensors (ADS mode), validate the mission (CMG Ops mode) and downlink validation data (Comms mode). The detail design for these operating modes, including downlink telemetry and uplink command is described in the following sections.

## 5.1 Safe-Hold Operating Mode

A flowchart identifying the power-up & deploy and safe-hold operations is shown in Fig. 5-1. As stated earlier, the power-up & deploy mode is designed to be execute once. The P-POD design and the CubeSat requirement of a separation switch [19] enable the satellite to be powered on as soon as it launched from the P-POD. The CDH software is loaded in to the on board computer memory and the satellite enters the power-up and deploy operation at the “Power ON” block shown in Fig. 5-1. The program communicates with the real time clock (RTC) and records the time as the current boot time on the flash storage. Along with the boot time the boot counter is also updated on the flash storage. The boot counter is designed to track the number of times the satellite reboots due to insufficient power, ground command or due to a watchdog reset. Following the write process the satellite checks the launch flag and based on the status of the flag, it proceeds to either deploy the antennas or turn on the receiver. The antenna deployment, designed to be repeated if necessary, is verified by sensing the change in acceleration and/or satellite angular rates before and after the deployment. To protect the primary payload from any potential electromagnetic interference the satellite

is designed to be idle for 45 minutes after P-POD launch. The launch flag is updated to indicate a successful deployment. After successfully executing the antenna deployment and the wait period the satellite enters safe-hold mode.

During safe-hold mode the onboard transceiver is powered on and the satellite can be located by a ground station or a hand held operator. The safe-hold operating mode is a low power mode designed to validate secondary objectives and facilitate a net positive power generation from the solar cells. Real-time satellite health data is transmitted during this operating mode for ground based decisions to switch to a particular operating mode. As indicated in the flowchart, safe-hold mode is designed as an infinite loop unless interrupted by a ground command or a power reset. The satellite receiver is in an interrupt mode and can be commanded by a ground station. While the satellite is listening for any ground communication via the receiver, the flight software collects real-time health data from the on board sensors and actively transmit it at specific intervals. As shown in Fig. 5-1, the satellite can be commanded into another operating mode through a ground input. The flowcharts shown in Fig. 5-2, Fig. 5-3A, Fig. 5-3B and Fig. 5-3C describe the check receiver, query beacon, transmit beacon, and deploy antenna tasks derived from the mission mapping process in Chapter 3. The standard protocol implementations, like I2C and SPI, are not described as part of the design.

### 5.1.1 Satellite Beacon

Each operating mode is associated with a downlink telemetry and an uplink command. The safe-hold mode downlink telemetry referred to as the satellite beacon is shown in Table 5-1. The power consumption of the transceiver is directly proportional to the length of the beacon and the transmission baud rate [84] (Test report characterizing power consumption of the transmitter for its two baud rates is in Appendix A). The transceiver is limited to transmit only text, punctuation and numerical ASCII characters. Additionally the transceiver is capable of transmitted not more than 200 characters during a single transmission. Within these limitations of the transceiver [84], Satellite

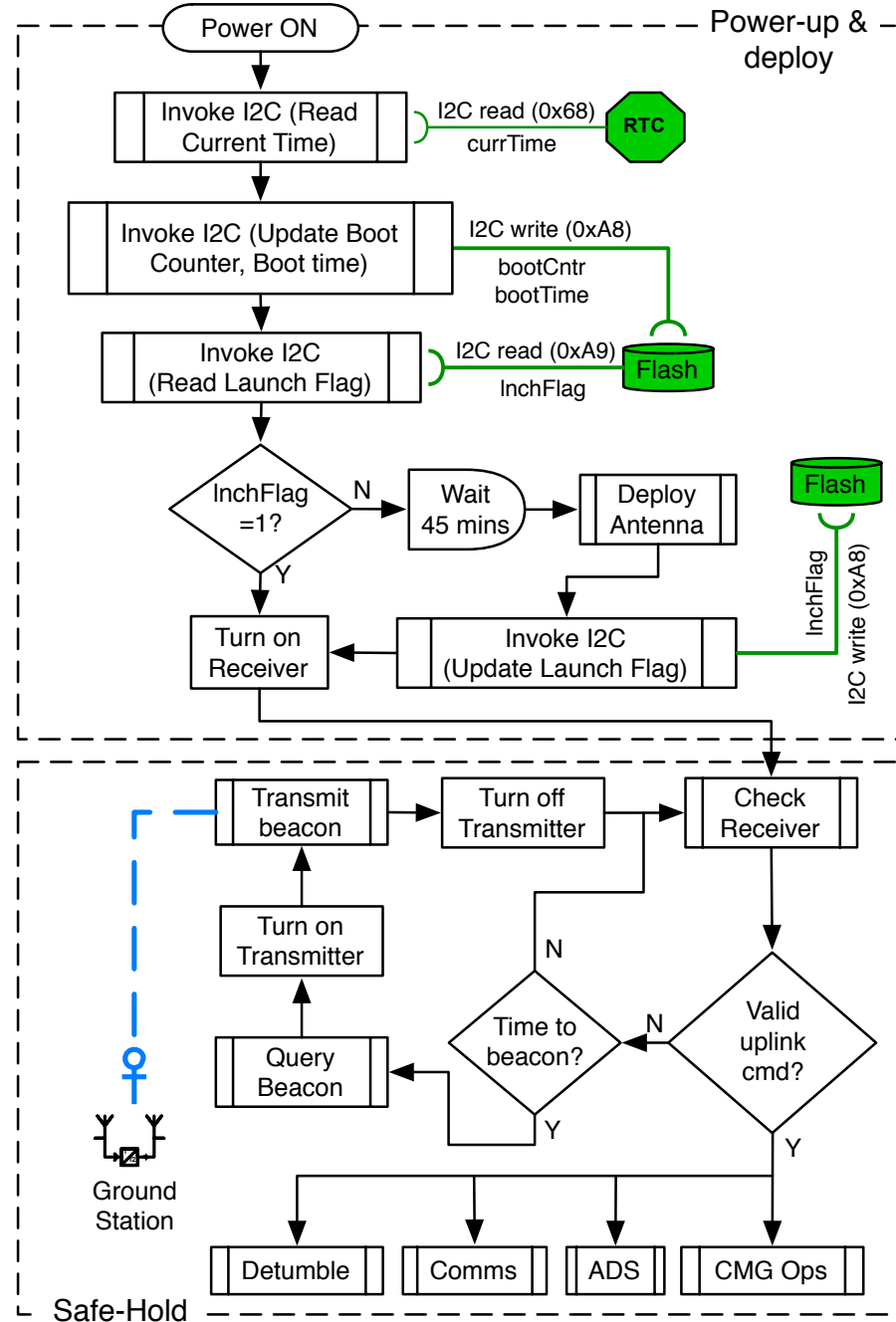


Figure 5-1. Power-Up Deploy and Safe-Hold Operating Modes

beacon effectively relays its health to assist in ground based decisions. The data transmitted as part of satellite beacon is shown in Table 5-1. It is important to note that data is transmitted as hexadecimal characters instead of ASCII characters due to the limitation of the AX.25 protocol on the transceiver [84] and in doing so the effective data

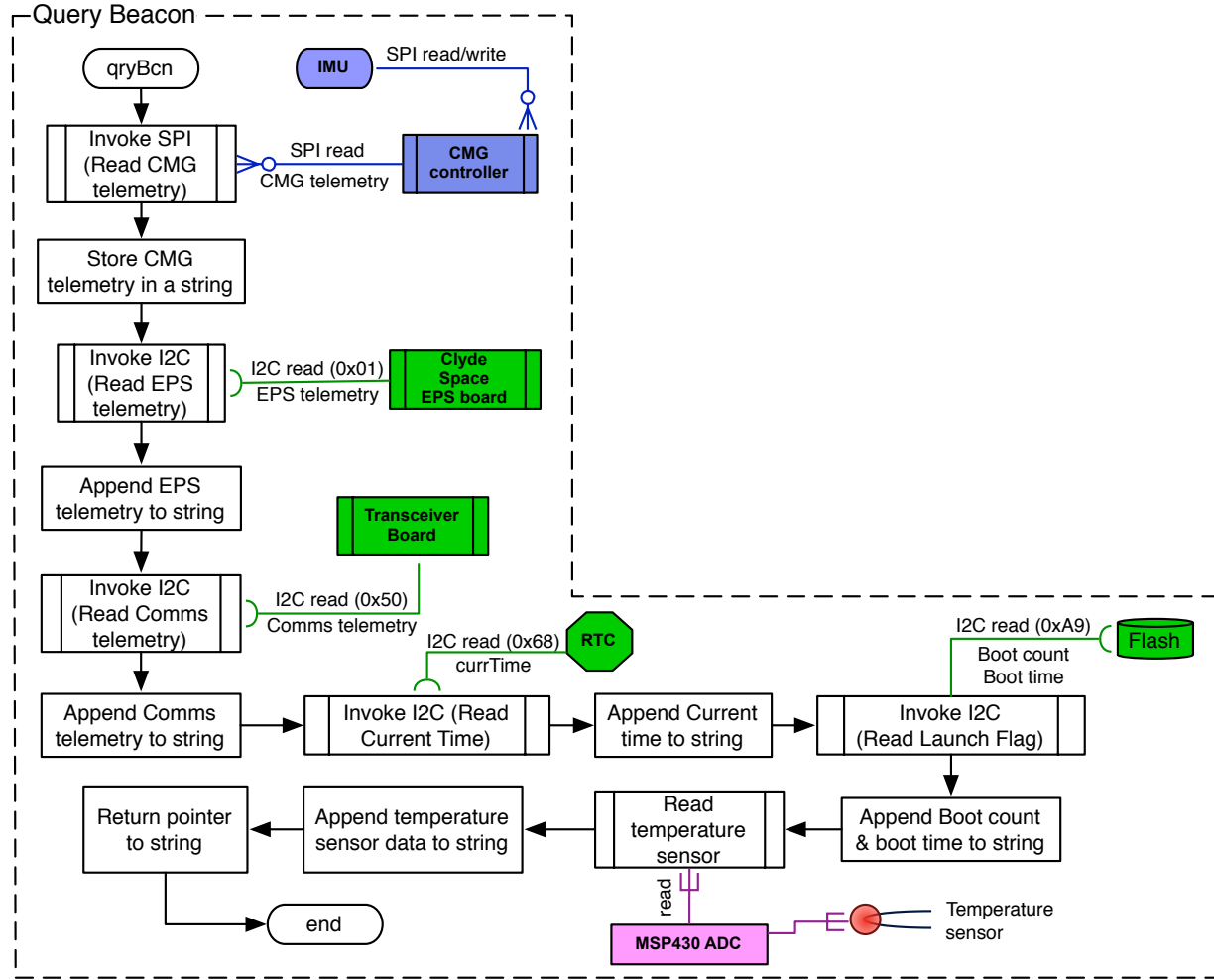


Figure 5-2. Query Beacon Function

rate is reduced by half. However, to maximize the amount of data per transmission the CDH design bit packages and then downlinks the data to ground stations. Considering the computational power available on ground with that available on a CubeSat the CDH design makes data management a more rigorous effort on ground and relatively simple on board the satellite.

### 5.1.2 Safe-hold Mode Uplink Command

Although the safe-hold mode is a part of the main program, parameters within the safe-hold mode are designed as variables which can be altered through an uplink command. Through the safe-hold mode uplink command, the CDH software design

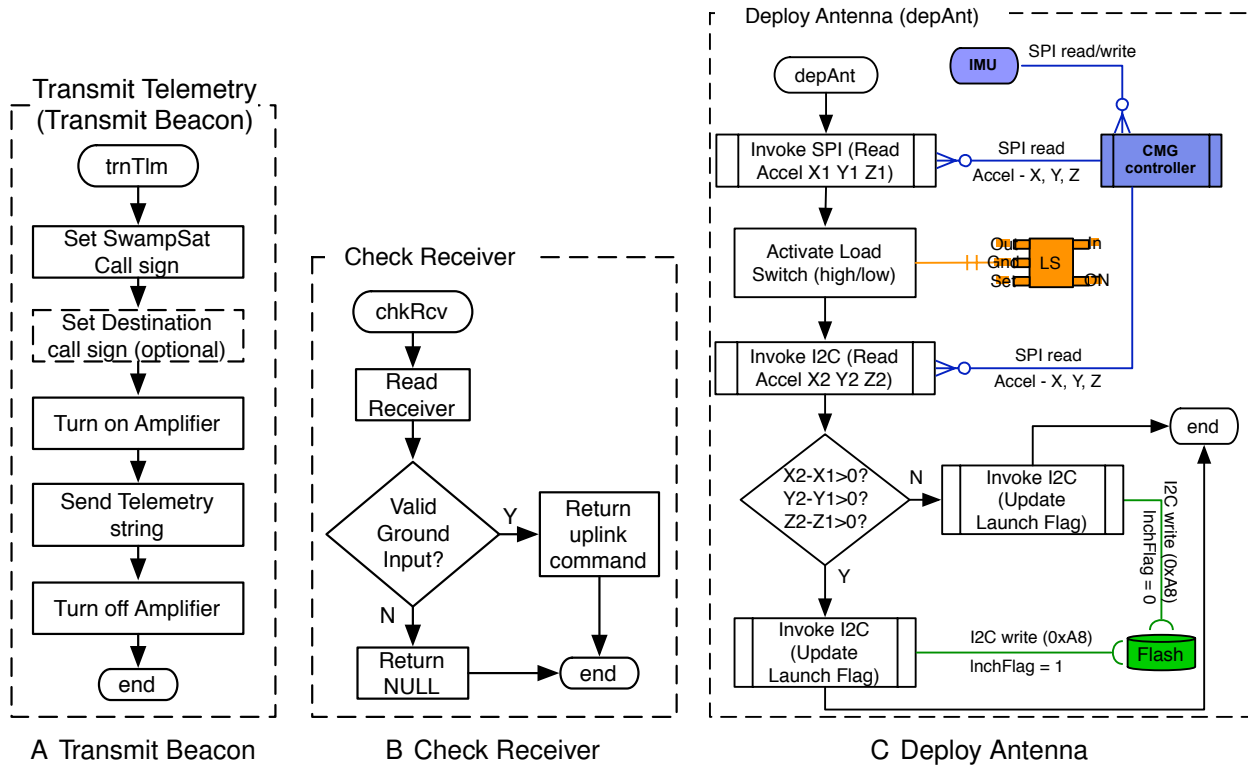


Figure 5-3. Power-Up & Deploy and Safe-hold Operating Mode Functions

makes provision for resetting satellite power. The uplink command for the safe-hold mode and the specific parameters which can be altered are shown in Table 5-2. The beacon interval is inversely proportional to the net power consumed by the onboard transceiver and this relationship is utilized for satellite power management. The minimum beacon interval is set to be 30 seconds and based on the number of data bits allocated for the beacon interval it can be varied up to 42 minutes. By making a provision for varying the beacon interval the satellite can be operated in a “super” safe-hold mode when the power being generated on board the satellite is at its minimum. Through the safe-hold mode uplink command , the CDH software design makes provision to attempt re-deployment through the launch flag variable. In the event of a successful deployment as determined from ground but not sensed by the satellite the launch flag can be used to update the launch status on board the satellite.

Table 5-1. Satellite Beacon - Safe-hold Mode Downlink Telemetry

<b>Quantity</b>	<b>Hardware</b>	<b>Interface</b>	<b>Bits</b>	<b>Hex Characters</b>
time stamp				
year	RTC	I <sup>2</sup> C	12	3
month	RTC	I <sup>2</sup> C	4	1
date	RTC	I <sup>2</sup> C	8	2
hour	RTC	I <sup>2</sup> C	8	2
minute	RTC	I <sup>2</sup> C	8	2
seconds	RTC	I <sup>2</sup> C	8	2
MMDB temperature 1	TI-DSP	SPI	12	3
MMDB temperature 2	TI-DSP	SPI	12	3
SMDB temperature 1	TI-DSP	SPI	12	3
SMDB temperature 2	TI-DSP	SPI	12	3
IMU X	IMU	SPI	14	4
IMU Y	IMU	SPI	14	4
IMU Z	IMU	SPI	14	4
IMU temperature	IMU	SPI	12	3
battery voltage	EPS	I <sup>2</sup> C	10	3
battery current	EPS	I <sup>2</sup> C	10	3
battery bus current	EPS	I <sup>2</sup> C	10	3
battery current direction	EPS	I <sup>2</sup> C	10	3
battery temperature	EPS	I <sup>2</sup> C	10	3
5v bus current	EPS	I <sup>2</sup> C	10	3
3.3v bus current	EPS	I <sup>2</sup> C	10	3
transmitter current	TCVR	I <sup>2</sup> C	10	3
receiver current	TCVR	I <sup>2</sup> C	10	3
boot count	Flash Storage	I <sup>2</sup> C	12	3
boot time				
year	RTC	I <sup>2</sup> C	12	3
month	RTC	I <sup>2</sup> C	4	1
date	RTC	I <sup>2</sup> C	8	2
hour	RTC	I <sup>2</sup> C	8	2
minute	RTC	I <sup>2</sup> C	8	2
seconds	RTC	I <sup>2</sup> C	8	2
msp430 temperature	SFC430	A/D	12	3
		<b>Total</b>	<b>312</b>	<b>84</b>

## 5.2 Detumble Operating Mode

The detumble operating mode is designed to stabilize the satellite about its three axes. Detumble operation is a timed operation and the time period is a function of the variable detumble loop-time as shown in the flowchart in Fig. 5-4. The operation is a

Table 5-2. Safe-hold Mode Uplink Command

Description	Bits	Hex	Value	Description
	Char-	ac-	ters	
Operating mode ID	8	2	00	Safe-hold mode = 00
Beacon interval	8	2	XX (00 to FF)	00 corresponds to 30 s; XX corresponds to increments of 10 seconds; The frequency can be varied from 10 seconds to 2550 seconds (42 minutes)
Launch flag	8	1	X (1 or 0)	Default flag is 0; Antennas can be attempted to be redeployed using the flag; flag == 1 indicates deployment should be repeated
<b>Total</b>	<b>32</b>	<b>7</b>	<b>00XXX</b>	

sub routine of the main program and is initiated by a ground command which includes the parameters detumble loop time and a timeout period. Since the main goal of the operating mode is to stabilize the angular rates of the satellite the function queries the IMU rates and compares them against predefined threshold values.

The detumble mode is a relatively power intensive operation compared to the safe-hold mode. To ensure the batteries have enough energy for executing the operation the function queries the battery board through the I2C communication link to EPS. Based on the predetermined threshold values for angular rates of the satellite and the available power the detumbling task is performed. The design makes provision for recording the operation success as a status flag in the flash storage. To detumble the satellite, magnetic coils embedded in the solar panels [85] are energized by the flight computer (SFC430). A provision is made to terminate the detumble operation from a ground station through the receiver. The detumble operation can also terminate autonomously if the angular rates are estimated to be below a threshold. To assist the ground command in making decisions to terminate the operation the satellite transmits its health data at specified intervals. Additionally the satellite is programmed to record

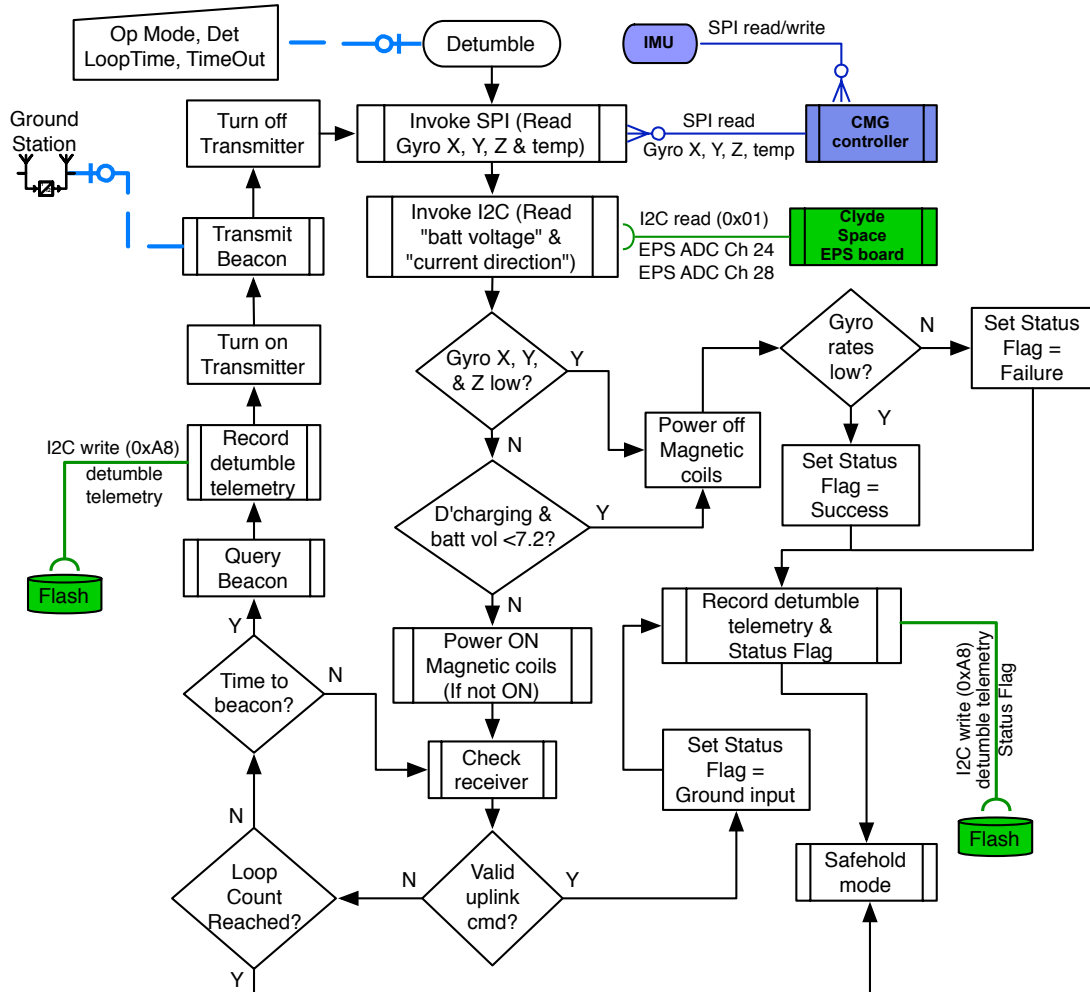


Figure 5-4. Detumble Operating Mode

detumble telemetry into the flash storage at specified intervals. The recorded data is transmitted during the Comms operation. The process details of record telemetry and energizing the magnetic coils tasks are shown in Fig. 5-5.

### 5.2.1 Detumble mode downlink telemetry

The downlink telemetry for the detumble operating mode validates the capability of the magnetic coils, embedded in the solar panels, to detumble the CubeSat and execute the secondary mission objectives. The satellite autonomously terminates the detumble operation in the case of a successful stabilization or insufficient power. To perform a ground analysis of the detumble operation and its termination the satellite

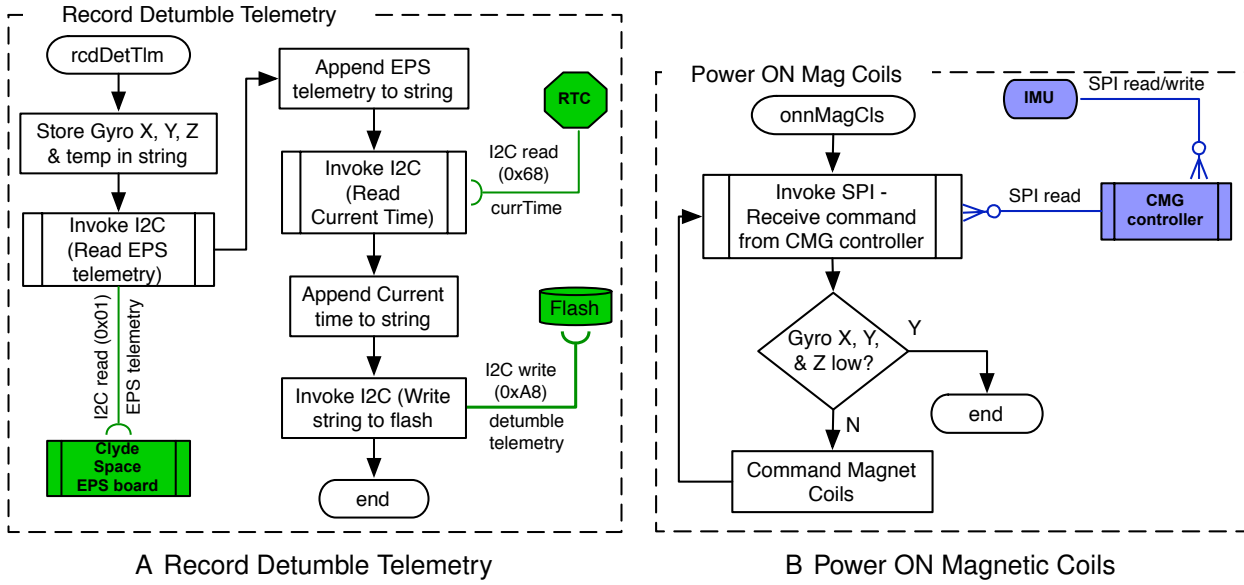


Figure 5-5. Detumble Operating Mode Functions

angular rates are recorded from the IMU as part of the downlink telemetry. The power generation capacity of solar cells has been researched by several CubeSat missions and traditional satellites. Solar cell voltages, currents and temperatures are included as part of the detumble telemetry to analyze the power generation capacity of the CubeSat in a spinning state. Battery characteristics are included in the telemetry to record the satellite's health as a function of its spin rate and determine the power consumption of the operating mode. The telemetry data and its details for detumble operating mode are shown in Table 5-3.

### 5.2.2 Detumble mode uplink command

The detumble operation is initiated through an uplink command, the details of which are shown in Table 5-4. The mode is identified by the operating mode id, which is “01”. Since the operation transmits real time satellite health data, the beacon interval makes provision for specifying this interval from ground. The cell voltage is a direct measure of the battery capacity [86] as shown in Fig. 5-6 [86] and is used as a termination criteria of the operation. The battery voltage threshold value can be varied and is included as part of the uplink command. Once the CubeSat has been on orbit for a few days and the

Table 5-3. Detumble Mode Downlink Telemetry

Quantity	Hardware	Interface	Bits	Hex Characters
time stamp				
year	RTC	I <sup>2</sup> C	12	3
month	RTC	I <sup>2</sup> C	4	1
date	RTC	I <sup>2</sup> C	8	2
hour	RTC	I <sup>2</sup> C	8	2
minute	RTC	I <sup>2</sup> C	8	2
seconds	RTC	I <sup>2</sup> C	8	2
IMU X	IMU	SPI	14	4
IMU Y	IMU	SPI	14	4
IMU Z	IMU	SPI	14	4
IMU temperature	IMU	SPI	12	3
solar cell voltage 1	EPS	I2C	10	3
solar cell voltage 2	EPS	I2C	10	3
solar cell voltage 3	EPS	I2C	10	3
solar cell voltage 4	EPS	I2C	10	3
solar cell voltage 5	EPS	I2C	10	3
solar cell current 1	EPS	I2C	10	3
solar cell current 2	EPS	I2C	10	3
solar cell current 3	EPS	I2C	10	3
solar cell current 4	EPS	I2C	10	3
solar cell current 5	EPS	I2C	10	3
side temperature 1	EPS	I2C	10	3
side temperature 2	EPS	I2C	10	3
side temperature 3	EPS	I2C	10	3
side temperature 4	EPS	I2C	10	3
side temperature 5	EPS	I2C	10	3
battery voltage	EPS	I <sup>2</sup> C	10	3
battery current	EPS	I <sup>2</sup> C	10	3
battery current direction	EPS	I <sup>2</sup> C	10	3
battery temperature	EPS	I <sup>2</sup> C	10	3
<b>Total</b>		<b>292</b>		<b>84</b>

corresponding telemetry data downloaded the time taken to detumble for a particular angular velocity of the spacecraft can be determined. At this stage the spacecraft can be commanded to detumble for a specific period of time and the loop count parameter is included in the command for this purpose. To address the initial gyro bias and enable the mean to be zero the uplink command includes an offset value and a bounding factor

for the three gyros. The offsets can be varied between  $-0.99$  deg/s to  $+0.99$  deg/s and the bounds can be varied from 0 deg/s to 2 deg/s.

Table 5-4. Detumble Mode Uplink Command

Description	Bits	Hex Chars	Value	Description
Operating mode ID	8	2	01	Detumble Mode = 01
Beacon interval	8	2	XX (00 to FF)	00 corresponds to 30 s; XX corresponds to increments of 10 seconds; The frequency can be varied from 10 seconds to 2550 seconds (42 minutes)
Battery voltage	8	2	XX (00 to FF)	Signed two's complement integer; 0 corresponds to 7.0v; each increment is 0.01 v
Loop count	8	2	XX (00 to FF)	Minimum = 100 loops; increments correspond to multiples of 100; 00 corresponds to infinite loops (until the angular rates are reached or interrupted by ground command)
Angular rate threshold				
X offset	16	4	XXXX (0000 to FFFF)	Default desired angular rate = 0 deg/s; XX corresponds to increments of 0.01 deg/s;
Y offset	16	4	XXXX (0000 to FFFF)	Angular rates can be varied between -0.99 deg/s to +0.99 deg/s; 00 corresponds to the default value of 0 deg/s
Z offset	16	4	XXXX (0000 to FFFF)	
X bound	8	2	XX (00 to FF)	
Y bound	8	2	XX (00 to FF)	Bounds range from 0 to 2 deg/s
Z bound	8	2	XX (00 to FF)	
<b>Total</b>	<b>104</b>	<b>26</b>	<b>01XXXXXXXXXXXXXXXXXXXXXX</b>	

### 5.3 Comms Operating Mode

Mission validating data is stored on board the flash storage during the execution of detumble, ADS and CMG operations. The comms operating mode is designed as a sub routine of the main program to downlink the data to ground control. The operation, described in the form of a flowchart, is shown in Fig. 5-7. The detumble mode telemetry

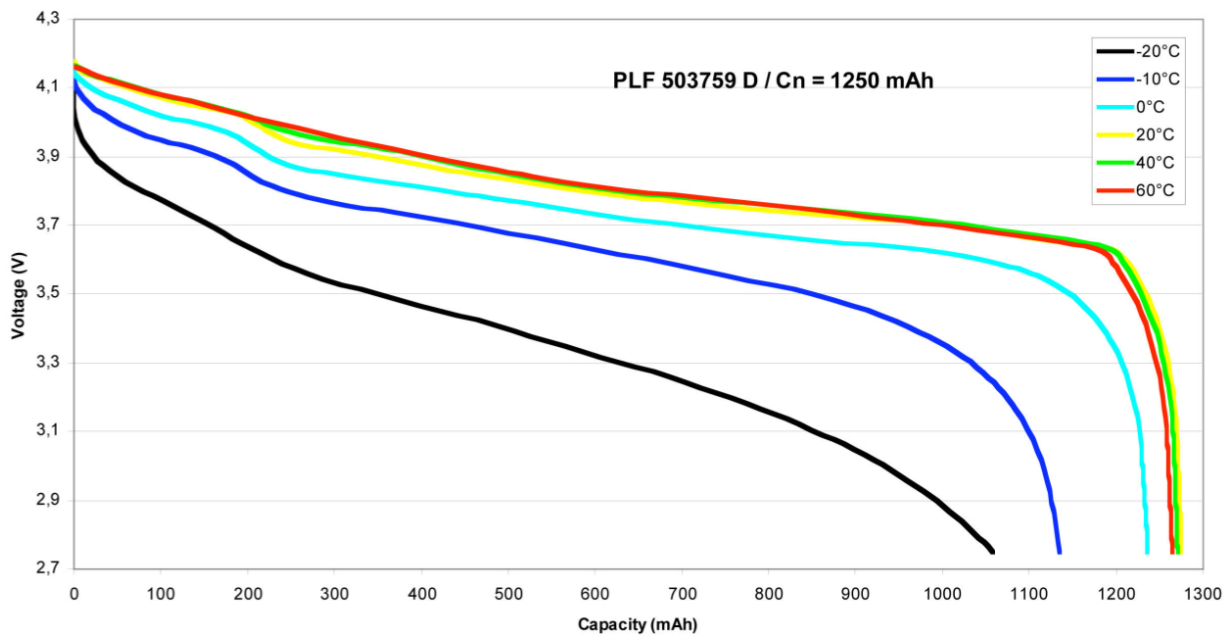


Figure 5-6. Battery Capacity Expressed as Voltage

data is recorded on the flight computer flash storage and the ADS mode and CMG Ops mode telemetry is recorded on the auxiliary computer (CMG controller) flash storage. Based on the data type being requested, the comms operation implements one of the two telemetry access functionalities shown in Fig. 5-8. Similar to the detumble operation the comms mode is a relatively power intensive operation and a power check is performed to ensure the satellite is capable of operating in this mode. Based on the available power resources the satellite proceeds to access mission validating data for a particular operating mode and prepares to downlink it to a ground station. A provision is made in the sub routine to terminate the operation autonomously and through ground control. The satellite is also programmed to transmit real time health data for decision making at specified intervals during the operation. Unlike the other 4 operating modes the comms operation is not associated with any downlink telemetry.

### 5.3.1 Comms mode uplink command

The comms operation is invoked from within the safe-hold mode with an uplink command, the details of which are shown in Table 5-5. Comms operation is assigned

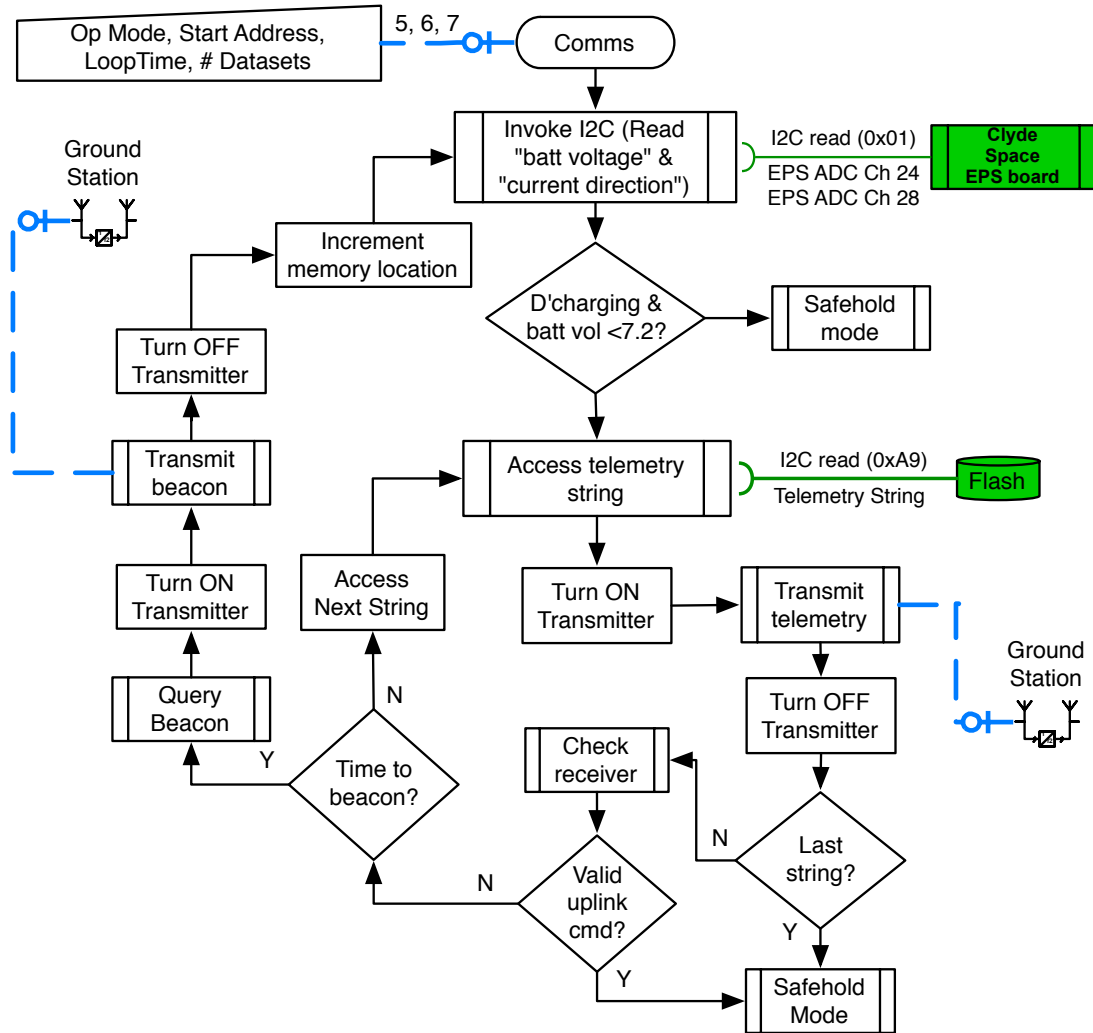


Figure 5-7. Comms Operating Mode

the operating mode id “03”. Apart from transmitting the stored telemetry data, the operation also transmits real time health data at intervals specified through the beacon interval parameter. Since comms mode transmits at intervals smaller than the safe-hold mode, the operation is relatively more power intensive. A threshold value for the battery voltage is passed as a parameter of the uplink command and the operation terminates if the threshold is reached. The uplink command specifies the operating mode for which the data is to be downlinked through the data type parameter. The flash storage is divided into pages of size 4096 bytes each and can be identified through an address. Each operating mode stores telemetry data in pages and the page address is passed as

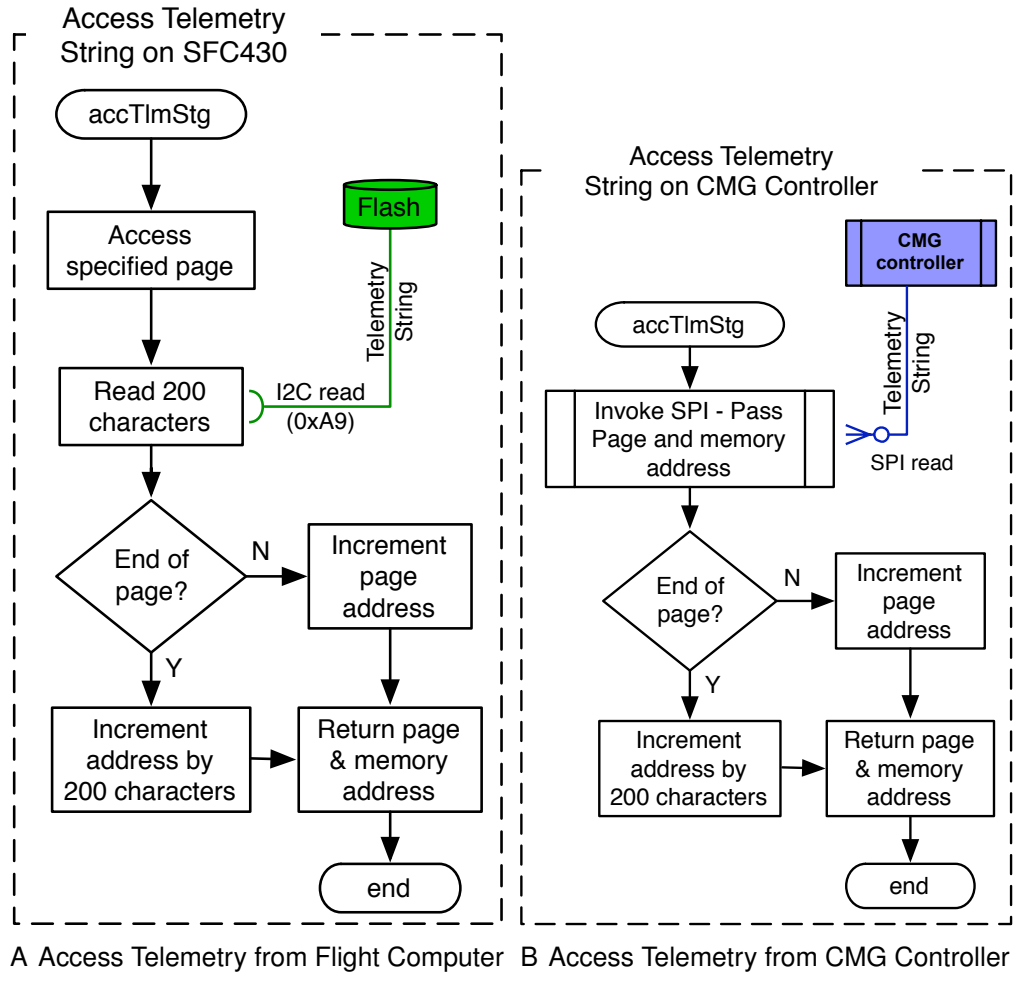


Figure 5-8. Comms Operating Mode Functions

a parameter to identify the data specific to a maneuver. To facilitate the downlinking of multiple pages the uplink command includes the number of pages as well. Just like the beacon interval the comms interval can be varied through the comms interval parameter. Although a CubeSat on orbit is capable of transmitting mission validating telemetry data, all of the data transmitted may not be captured by a ground station on Earth and there may be a need for retransmissions. To accommodate retransmissions, a parameter is included as part of the comms mode uplink command.

#### 5.4 ADS Operating Mode

The ADS operating mode and the CMG Ops operating mode are designed to address a distributed computing architecture. The attitude sensors, Sun sensors and

Table 5-5. Comms Mode Uplink Command

Description	Bits	Hex Chars	Value	Description
Operating mode ID	8	2	02	Comms Mode = 01
Beacon interval	8	2	XX (00 to FF)	00 corresponds to 30 s; XX corresponds to increments of 10 seconds; The frequency can be varied from 10 seconds to 2550 seconds (42 minutes)
Battery voltage	8	2	XX (00 to FF)	Signed two's complement integer; 0 corresponds to 7.0v; each increment is 0.01 v
Data type	8	2	XX	Detumble - 01; ADS - 03; CMG Ops - 04
Page number	12	3	XXX	Starting page number in memory
Number of pages	12	3	XXX	Number of pages to transmit
Comms interval	8	2	XX (00 to 99)	Transmission interval; starts at 0 and increments in 100 ms
Transmission repetitions	4	1	X (0 to F)	Number of repeats of broadcast (0 to 15 repetitions)
<b>Total</b>	<b>68</b>	<b>17</b>	<b>02XXXXXXXXXXXXXX</b>	

magnetometer, are interfaced to the flight computer and the IMU is interfaced to the CMG controller. Attitude determination and estimation algorithms are also hosted on the CMG controller. An SPI link enables communication between the flight computer and the CMG controller. ADS operating mode addresses tasks on flight computer to validate the subsystem and diagnose the attitude and inertial sensors when needed. A flowchart of the operating mode is shown in Fig. 5-9. A significant design feature of the ADS operating mode is to accommodate interaction between flight computer and CMG controller. The operation starts by querying for power and based on the state of batteries the flight computer commands the CMG controller to initiate the process of ADS validation. Attitude determination is accomplished using QUEST [87] and Murrell's version [88] of the extended Kalman filter (EKF) [89, 90] is used for attitude estimation. ADS validation process starts with the execution of the EKF algorithm. EKF is hosted on

the CMG controller and requests body vector measurements from the flight computer through the SPI link and the reference vectors from the mathematical models which are implemented on the CMG controller. QUEST is programmed as a sub routine and is invoked from within the EKF with two set of vector measurements as function parameters. ADS operating mode communicates the body vector measurements to the CMG controller on a request basis. To assist ground control in decision making the operating mode transmits real-time health data at specified intervals. Similar to the detumble mode and the comms mode the ADS mode can also be terminated autonomously or through ground control.

#### **5.4.1 ADS mode downlink telemetry**

The downlink telemetry for the ADS operating mode validates and diagnosis on orbit the attitude sensors, attitude determination and estimation algorithms. The details of the downlink telemetry for the ADS operation are shown in Table 5-6. For validating the sensors, the operating mode stores sun sensor, magnetometer and IMU data on board the CMG controller flash storage. Additionally the downlink telemetry also stores the attitude quaternion computed by QUEST. The ADS telemetry data is bit packaged during storage and downlinked via the comms operation.

#### **5.4.2 ADS mode uplink command**

Similar to the detumble and comms operation, the ADS operation is invoked from within the safe-hold mode through an uplink command. The details of the uplink command are shown in Table 5-7. The operating mode id assigned to the operation is “04”. Beacon interval and battery voltage serve the same purpose as they do for the detumble and the comms operation. The attitude determination and CMG operations require precise time data and this data is communicated from ground through the time parameter. The CubeSat is capable of propagating its orbit but needs to be initialized with position and velocity parameter. The orbital position and orbital velocity parameters within the uplink command are for initializing the satellite’s position and velocity.

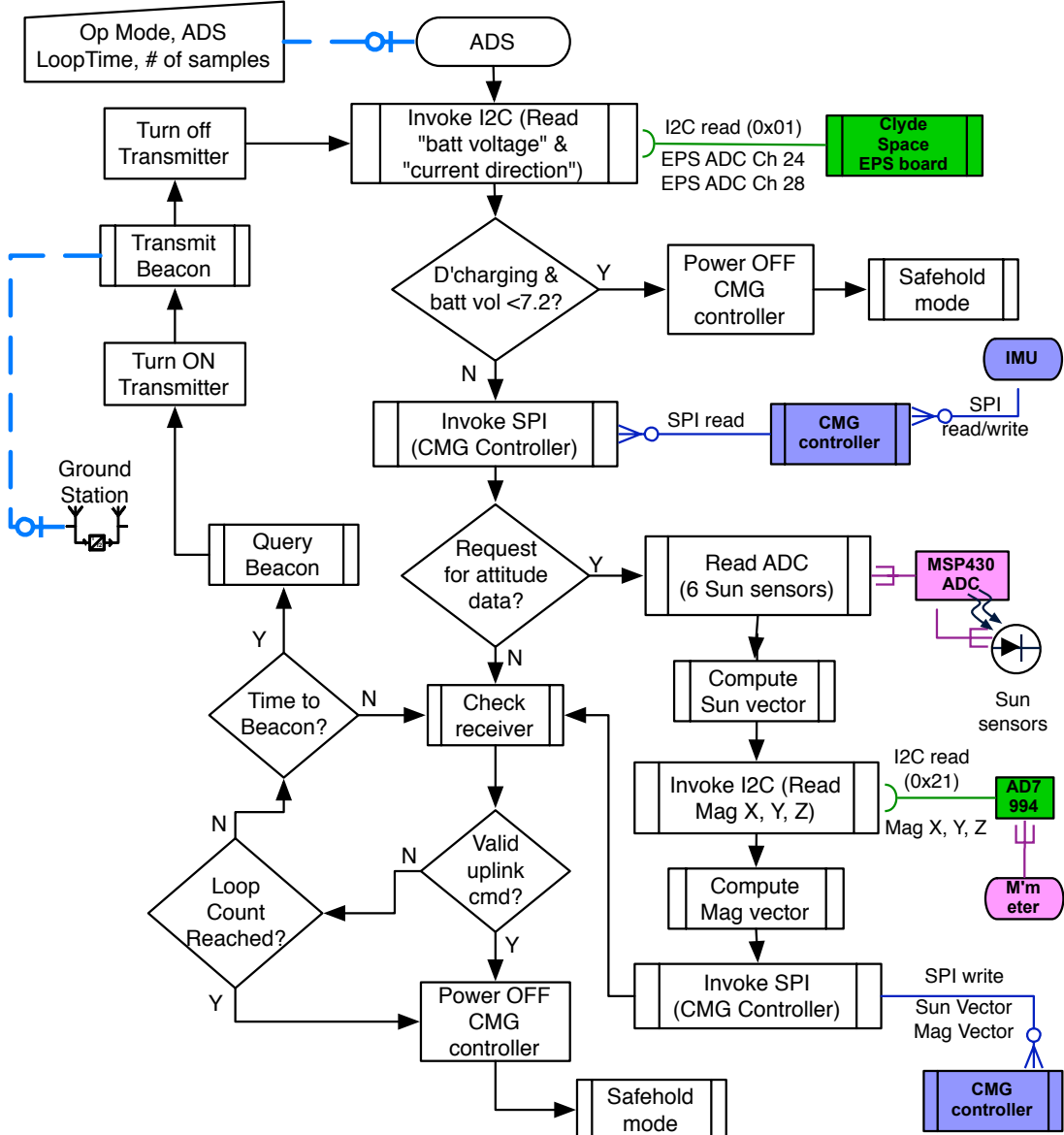


Figure 5-9. ADS Operating Mode

Effectively the uplink command updates the two line elements (TLEs) by updating the RTC, satellite position and satellite velocity. The ADS operation is specifically a timed operation and the number of samples parameter determines the time period of the operation. QUEST estimates the initial satellite attitude and EKF's convergence to the true attitude is determined by the accuracy of this initial estimate. The uplink command includes a parameter for QUEST weights to improve on the initial attitude estimate.

Table 5-6. ADS Mode Downlink Telemetry

<b>Quantity</b>	<b>Hardware</b>	<b>Interface</b>	<b>Bits</b>	<b>Hex Characters</b>
time stamp				
year	RTC	I <sup>2</sup> C	12	3
month	RTC	I <sup>2</sup> C	4	1
date	RTC	I <sup>2</sup> C	8	2
hour	RTC	I <sup>2</sup> C	8	2
minute	RTC	I <sup>2</sup> C	8	2
seconds	RTC	I <sup>2</sup> C	8	2
IMU X	IMU	SPI	14	4
IMU Y	IMU	SPI	14	4
IMU Z	IMU	SPI	14	4
IMU temperature	IMU	SPI	12	3
magnetometer x	SFC430	I2C	12	3
magnetometer y	SFC430	I2C	12	3
magnetometer z	SFC430	I2C	12	3
sun sensor 1	SFC430	ADC	12	3
sun sensor 2	SFC430	ADC	12	3
sun sensor 3	SFC430	ADC	12	3
sun sensor 4	SFC430	ADC	12	3
sun sensor 5	SFC430	ADC	12	3
sun sensor 6	SFC430	ADC	12	3
quaternion q1	TI-DSP	SPI	64	16
quaternion q2	TI-DSP	SPI	64	16
quaternion q3	TI-DSP	SPI	64	16
quaternion q4	TI-DSP	SPI	64	16
<b>Total</b>	<b>466</b>		<b>118</b>	

## 5.5 CMG Ops Operating Mode

As with the ADS operating mode, the CMG Ops lays emphasis on establishing an efficient communication link between the flight computer and the CMG controller. A flowchart describing the CMG operating mode is shown in Fig. 5-10. CMG Ops operating mode is similar in functionality to the ADS operating mode and is invoked as a sub routine from within the safe-hold mode. To conserve electrical energy and enable the CMG controller to be autonomous, the transmitter is completely turned off during this operation. The receiver, however, is powered on and the operation can be commanded from ground, based on an estimated position of the satellite. Along with QUEST and EKF the CMG control and singularity avoidance algorithms are in execution

Table 5-7. ADS Mode Uplink Command

Description	Bits	Hex Chars	Value	Description
Operating mode ID	8	2	01	Detumble Mode = 01
Beacon interval	8	2	XX (00 to FF)	00 corresponds to 30 s; XX corresponds to increments of 10 seconds; The frequency can be varied from 10 seconds to 2550 seconds (42 minutes)
Battery voltage	8	2	XX (00 to FF)	Signed two's complement integer; 0 corresponds to 7.0v; each increment is 0.01 v
Uplink time	48	12	XXX X XX XX XX XX	year month hour day minute second
Orbital position	192	48	XXXXXXXX XXXXXXXX XXXXXXXX XXXXXXXX XXXXXXXX XXXXXXXX	XXXXXXXX orbital position in 0.5 meter resolution, ranging from 0 to 8388.608 km
Orbital velocity	192	48	XXXXXXXX XXXXXXXX XXXXXXXX XXXXXXXX XXXXXXXX	XXXXXXXX orbital velocity in 0.25 meter/s resolution, ranging from 0 to 16.384 km/s
Number of samples	24	5	XXXXX	number of samples ranging from 0 to 1,048,575
QUEST weights	8	2	XX (0 to 15)	(0 to 1) each increment represents 0.05
<b>Total</b>	<b>488</b>	<b>121</b>		

during this operating mode and the sub routine on the flight computer is responsible for communicating attitude, power data, and ground commands to the CMG controller.

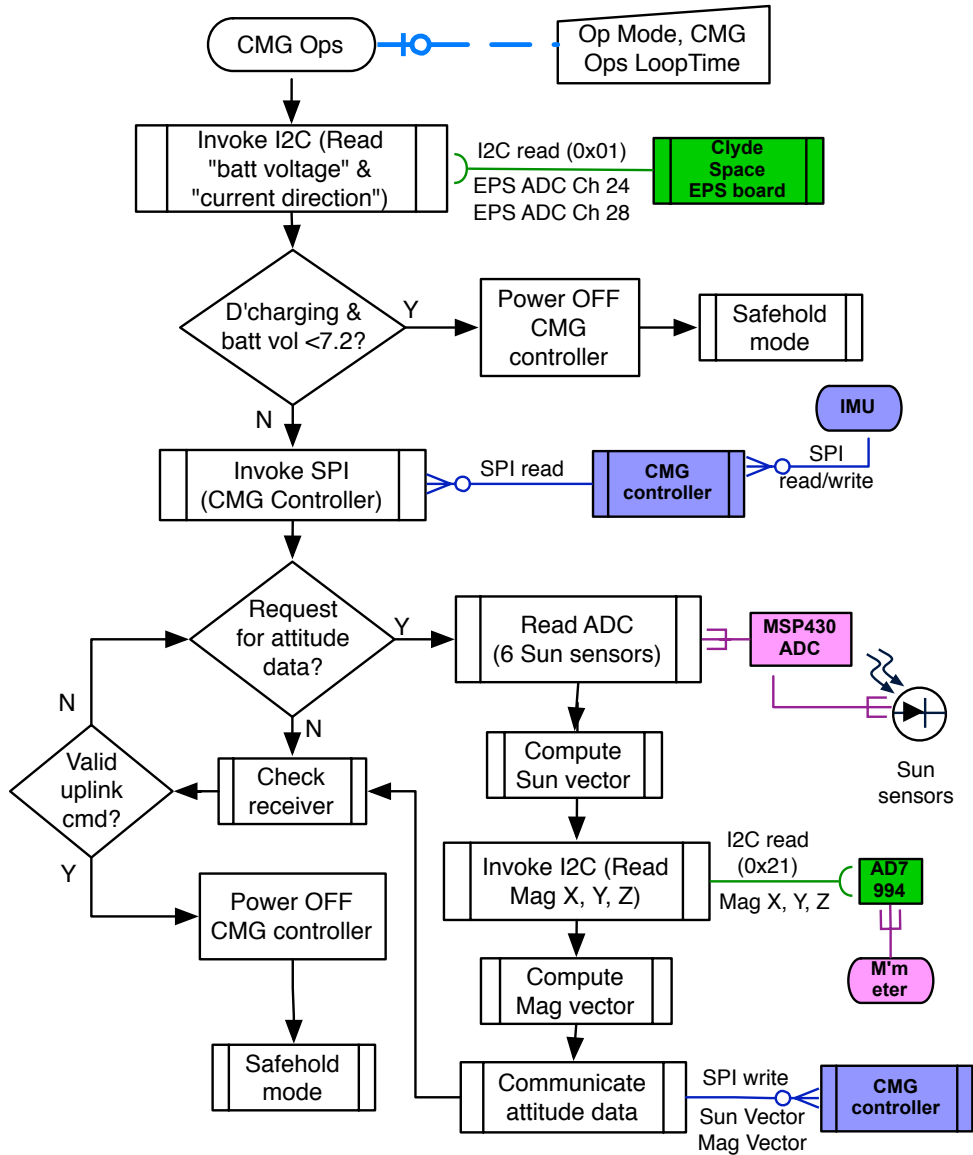


Figure 5-10. CMG Ops Operating Mode

### 5.5.1 CMG Ops mode downlink telemetry

Similar to the downlink telemetry associated with other operating modes, the downlink telemetry for CMG Ops attempts to validate the attitude control subsystem and in the process provides data for mission validation. The downlink telemetry is identified in the Table 5-8. Similar to any attitude control operations CMG maneuvers are specifically validated with the on board ADS and the data associated with the attitude sensors and attitude mathematics is included as part of the CMG Ops telemetry. The

downlink telemetry also includes CMG actuator and sensor data. To facilitate ground based validation of the CMG operations, each telemetry string is time stamped during the maneuver and downlinked.

### **5.5.2 CMG Ops mode uplink command**

The flight computer is responsible for initiating CMG maneuvers and communicate data contained within the uplink command to the CMG controller. The uplink command for CMG operations is similar to the uplink command for ADS operation. Apart from identifying the operating mode id and uplinking the beacon interval, the uplink command updates the TLEs of the satellite. Additionally the uplink command identifies the maneuver type and the maneuver time to be executed by SwampSat.

The mission mapping process translates the mission definition into implementable tasks. As described in Chapter 3, these tasks are used as building blocks to design operating modes as per the mission CONOPS. For a pico- and nano-class CubeSat, it can be argued that the mission CONOPS gets elaborated as flight software. By translating mission definition into components, interface and tasks, the top-down design approach facilitates a bottom-up coding scheme. The interfaces are accommodated as protocols and components as drivers or controllers within tasks implemented as routines or functions. The operating modes, designed around these routines, collectively form the flight software. The computation cost associated with tasks can be used to estimate the computational overhead of each operating mode and the complete flight software. Similarly the telemetry overhead associated with each component can be used to estimate the telemetry overhead of each operating mode and the complete flight software.

Table 5-8. CMG Ops Mode Downlink Telemetry

<b>Quantity</b>		<b>Hardware</b>	<b>Interface</b>	<b>Bits</b>	<b>Hex Characters</b>
time stamp					
	year	RTC	I <sup>2</sup> C	12	3
	month	RTC	I <sup>2</sup> C	4	1
	date	RTC	I <sup>2</sup> C	8	2
	hour	RTC	I <sup>2</sup> C	8	2
	minute	RTC	I <sup>2</sup> C	8	2
	seconds	RTC	I <sup>2</sup> C	8	2
IMU X	IMU	SPI		14	4
IMU Y	IMU	SPI		14	4
IMU Z	IMU	SPI		14	4
IMU temperature	IMU	SPI		12	3
MMDB temperature 1	TI-DSP	SPI		12	3
MMDB temperature 2	TI-DSP	SPI		12	3
SMDB temperature 1	TI-DSP	SPI		12	3
SMDB temperature 2	TI-DSP	SPI		12	3
flywheel speed 1	TI-DSP	SPI		12	3
flywheel speed 2	TI-DSP	SPI		12	3
flywheel speed 3	TI-DSP	SPI		12	3
flywheel speed 4	TI-DSP	SPI		12	3
gimbal rate 1	TI-DSP	SPI		12	3
gimbal rate 2	TI-DSP	SPI		12	3
gimbal rate 3	TI-DSP	SPI		12	3
gimbal rate 4	TI-DSP	SPI		12	3
gimbal angle 1	TI-DSP	SPI		12	3
gimbal angle 2	TI-DSP	SPI		12	3
gimbal angle 3	TI-DSP	SPI		12	3
gimbal angle 4	TI-DSP	SPI		12	3
magnetometer x	SFC430	I <sup>2</sup> C		12	3
magnetometer y	SFC430	I <sup>2</sup> C		12	3
magnetometer z	SFC430	I <sup>2</sup> C		12	3
sun sensor 1	SFC430	ADC		12	3
sun sensor 2	SFC430	ADC		12	3
sun sensor 3	SFC430	ADC		12	3
sun sensor 4	SFC430	ADC		12	3
sun sensor 5	SFC430	ADC		12	3
sun sensor 6	SFC430	ADC		12	3
quaternion q1	TI-DSP	SPI		64	16
quaternion q2	TI-DSP	SPI		64	16
quaternion q3	TI-DSP	SPI		64	16
quaternion q4	TI-DSP	SPI		64	16
<b>Total</b>	<b>658</b>		<b>166</b>		

Table 5-9. CMG Ops Mode Uplink Command

Description	Bits	Hex Chars	Value	Description
Operating mode ID	8	2	01	Detumble Mode = 01
Beacon interval	8	2	XX (00 to FF)	00 corresponds to 30 s; XX corresponds to increments of 10 seconds; The frequency can be varied from 10 seconds to 2550 seconds (42 minutes)
Battery voltage	8	2	XX (00 to FF)	Signed two's complement integer; 0 corresponds to 7.0v; each increment is 0.01 v
Uplink time	48	12	XXX X XX XX XX XX	year month hour day minute second
Orbital position	192	48	XXXXXXXXXXXX XXXXXXXXXXXX XXXXXXXXXXXX XXXXXXXXXXXX XXXXXXXXXXXX XXXXXXXXXXXX	orbital position in 0.5 meter resolution, ranging from 0 to 8388.608 km
Orbital velocity	192	48	XXXXXXXXXXXX XXXXXXXXXXXX XXXXXXXXXXXX XXXXXXXXXXXX XXXXXXXXXXXX	orbital velocity in 0.25 meter/s resolution, ranging from 0 to 16.384 km/s
QUEST weights	8	2	XX (0 to 15)	(0 to 1) each increment represents 0.05
Maneuver type	4	1	X (0 or 1)	0 = R2; 1 = sun pointing
Maneuver time	48	12	XXX X XX XX XX	year month hour day minute
			XX	second
<b>Total</b>			<b>516 129</b>	

## CHAPTER 6

### DESIGN OF ATTITUDE DETERMINATION AND ESTIMATION SYSTEM

For pico- and nano-class CubeSats, distributed computing can be adopted to overcome the limitations of power. In such a scenario, the elements of a subsystem can get distributed and its critical to address the distributed operation of such a subsystem. The attitude determination and estimation system of SwampSat is discussed in this context. The on board computing consists of a low power flight computer and a high speed auxiliary processor. The attitude determination and estimation system is distributed across these two computing units. This chapter discuss the distributed design of the attitude determination and estimation system. The attitude sensors for pico- and nano-class CubeSats are often selected to be COTS based components. Murrell's version of the extended Kalman filter [89, 90] is adapted for: (i) distributed platform and (ii) using different sensor configurations. A level of redundancy is introduced into the spacecraft through the different sensor configurations and specific implementation of the estimation algorithm. Before delving into the detail design, the deterministic and stochastic methods relevant for pico- and nano-class CubeSats are surveyed. Attitude kinematics of a spacecraft are described to lead into the system and filter design.

#### 6.1 Deterministic Attitude Determination

In recent times, QUaternion ESTimator (QUEST) [87] has been extensively used as a deterministic attitude determination algorithm, but before QUEST, TRIaxial Attitude Determination (TRIAD) [91, 92] and its variants were used for attitude determination. The TRIAD algorithm is still in use due to its relatively low computational effort compared to QUEST [93]. Euler's theorem, which states that the most general motion of a rigid body with one fixed point is a rotation about some axis, was the basis for the development of the TRIAD algorithm. Euler's theorem shows that the attitude matrix, which is represented by a 3x3 orthogonal and proper matrix, is an element

of the three parameter group SO(3). The three parameters can constitute a rotation angle and two parameters specifying the unit vector along the rotation axis. The TRIAD algorithm computes the spacecraft attitude from a orthonormal triad of vectors in a reference frame and its corresponding representation in the spacecraft body frame. The algorithm forms the orthonormal triad from two vectors. If  ${}^B\underline{V}_1$  and  ${}^B\underline{V}_{12}$  are two vectors coordinatized in the spacecraft body frame and  $'\underline{V}_1$  and  $'\underline{V}_{12}$  are their representations in the Earth centered inertial (ECI) [94] frame then the orthonormal triads in the body frame,  $\{{}^B\underline{V}_1, {}^B\underline{V}_2, {}^B\underline{V}_3\}$  and the ECI frame,  $'\underline{V}_1, '\underline{V}_2, '\underline{V}_3$  are computed as

$$\begin{aligned} {}^B\underline{V}_2 &= \frac{{}^B\underline{V}_1 \times {}^B\underline{V}_{12}}{|{}^B\underline{V}_1 \times {}^B\underline{V}_{12}|} \\ {}'\underline{V}_2 &= \frac{'\underline{V}_1 \times {}'\underline{V}_{12}}{|'V_1 \times {}'\underline{V}_{12}|} \\ {}^B\underline{V}_3 &= \frac{{}^B\underline{V}_1 \times {}^B\underline{V}_2}{|{}^B\underline{V}_1 \times {}^B\underline{V}_2|} \\ {}'\underline{V}_3 &= \frac{'\underline{V}_1 \times {}'\underline{V}_2}{|'V_1 \times {}'\underline{V}_2|} \end{aligned}$$

It is important to note that if  ${}^B\underline{V}_1$  and  ${}^B\underline{V}_{12}$  or  $'\underline{V}_1$  and  $'\underline{V}_{12}$  are parallel or antiparallel the orthonormal triad cannot be formed. Once the orthonormal triad is formed the transformation matrix or the attitude matrix can be estimated using the expression in Eq. (6–1). The estimate in Eq. (6–1) is one way of computing the attitude matrix from the orthonormal triad. Alternate expressions for estimating the attitude matrix from a orthonormal triad are discussed in Reference [93].

$$\underline{\underline{C}}_{IB} = \begin{bmatrix} {}'\underline{V}_{1x} & {}'\underline{V}_{2x} & {}'\underline{V}_{3x} \\ {}'\underline{V}_{1y} & {}'\underline{V}_{2y} & {}'\underline{V}_{3y} \\ {}'\underline{V}_{1z} & {}'\underline{V}_{2z} & {}'\underline{V}_{3z} \end{bmatrix} \begin{bmatrix} {}^B\underline{V}_{1x} & {}^B\underline{V}_{2x} & {}^B\underline{V}_{3x} \\ {}^B\underline{V}_{1y} & {}^B\underline{V}_{2y} & {}^B\underline{V}_{3y} \\ {}^B\underline{V}_{1z} & {}^B\underline{V}_{2z} & {}^B\underline{V}_{3z} \end{bmatrix}^{-1} \quad (6-1)$$

The TRIAD algorithm solves the attitude problem specifically for two vector observations and the condition  ${}^B\underline{V}_1 \cdot {}^B\underline{V}_2 = {}'\underline{V}_1 \cdot {}'\underline{V}_2$  should be valid to obtain identical estimates [93]. But when  ${}^B\underline{V}_1 \cdot {}^B\underline{V}_2 \neq {}'\underline{V}_1 \cdot {}'\underline{V}_2$  Bar-Itzhack and Harman propose

the use of the “Optimized TRIAD” algorithm [95]. It is important to note here that the estimate obtained using the optimized TRIAD algorithm is not optimal or completely orthogonal. To orthogonalize the attitude matrix, the algorithm proposes to extract a quaternion from an attitude matrix, normalize the resulting quaternion and compute back the attitude matrix. The attitude matrix obtained from a normalized quaternion is known to be orthogonal [96, 97].

For small satellite applications, CubeSats in particular, quaternion representation are desired for storing and transmitting attitude information. Quaternions can store a satellite’s full attitude information in 4 elements compared to the 9 elements of an direction cosine matrix (DCM) matrix. The method of extracting a quaternion from a DCM is undesirable in cases where the attitude is represented as a quaternion. An approach which directly leads to attitude estimate represented as a quaternion is preferred. Several approaches to estimating spacecraft attitude as a quaternion have been proposed [87, 98, 99]. One of the simplest methods to estimate attitude as a quaternion was proposed by Reynolds [98, 99]. In terms of computational effort the algorithm consumed 50 floating point operations (FLOPS) as compared to 190 for QUEST[93]. Reynold’s method of estimating the attitude using the direct quaternion method eludes to two asymmetrical and one symmetrical quaternion estimates.

$$\bar{q}_1 = c_1^{-\frac{1}{2}}[(^B\underline{V}_1 - ' \underline{V}_1) \times (^B\underline{V}_2 - ' \underline{V}_2), (^B\underline{V}_1 + ' \underline{V}_1) \cdot (^B\underline{V}_2 - ' \underline{V}_2)] \quad (6-2)$$

$$\bar{q}_2 = c_2^{-\frac{1}{2}}[(^B\underline{V}_1 - ' \underline{V}_1) \times (^B\underline{V}_2 - ' \underline{V}_2), (^B\underline{V}_2 + ' \underline{V}_2) \cdot (' \underline{V}_1 - ^B\underline{V}_1)] \quad (6-3)$$

Here  $\bar{q}_1$  and  $\bar{q}_2$  are asymmetrical quaternion estimates and Eq. (6-3) and Eq. (6-3) their respective expressions. If  ${}^B\underline{V}_1 \cdot {}^B\underline{V}_2 = ' \underline{V}_1 \cdot ' \underline{V}_2$  then the symmetrical quatenion estimate is given by

$$\bar{q}_1 = c_1^{-\frac{1}{2}}[(^B\underline{V}_1 - ' \underline{V}_1) \times (^B\underline{V}_2 - ' \underline{V}_2), (^B\underline{V}_2 \cdot ' \underline{V}_1 - {}^B\underline{V}_1 \cdot ' \underline{V}_2)]$$

Solutions which minimize the cost function of Wahba's problem [100] have been considered as optimal estimators and are capable of determining attitude using more than 2 vectors. Wahba proposed the problem of minimizing the loss function, shown in Eq. (6–4), to find the orthogonal DCM  $\underline{\underline{C}}_{IB}$ . The loss function rewritten in the form shown in Eq. (6–5) led to the observation that maximizing  $\text{trace}(\underline{\underline{C}}_{IB}\underline{\underline{B}})^T$  minimized the loss function in Eq. (6–4). The solutions to Wahba's problem including the ones which computed attitude quaternion were based on this observation.

$$L(A) = \frac{1}{2} \sum_i A_i |{}^B\underline{V}_i - \underline{\underline{C}}_{IB}^T \underline{V}_i|^2 \quad (6-4)$$

where,

${}^B\underline{V}_i$  = set of n unit vectors measured in the satellite body frame

$'\underline{V}_i$  = set of n unit vectors measured in the inertial reference frame

$A_i$  = non-negative weights

$$L(A) = \sum_i A_i - \text{trace}(\underline{\underline{C}}_{IB}\underline{\underline{B}}^T) \quad (6-5)$$

where,

$$\underline{\underline{B}} = \sum_i A_i {}^B\underline{V}_i \underline{V}_i^T$$

QUEST was introduced as a deterministic attitude determination algorithm with some statistical filtering. As stated by Shuster, the algorithm gave a maximum likelihood solution to Wahba's problem [101]. QUEST has been acknowledged as one of the most implemented solutions for spacecraft attitude determination and since its discovery several variants have been proposed including filter QUEST [102], recursive QUEST (REQUEST) [103] and extended QUEST [104]. These QUEST variants have proposed an EKF like solution to the attitude determination problem. Due to their relatively suboptimal solutions compared to an EKF, the QUEST variants involving filtering have

not been implemented in practice [105]. The extended Kalman filter, by far, has provided better performances compared to these alternatives [105].

The TRIAD algorithm and the direct quaternion method provide 3 options for estimating the attitude of a spacecraft given two vector observations. Similar to the TRIAD algorithm the direct quaternion method is ill determined and can encounter singularities when both the vector and scalar components take the indeterminate value of  $\frac{0}{0}$ . The direct quaternion does not provide optimal estimates but considering the computational effort and simplicity the method can be considered for CubeSat applications when coupled with an estimation algorithm like the extended Kalman filter. F Landis Markley in his published work [93] has compared the computational effort of some of the most commonly used attitude determination algorithms for two vector observations. The scenarios considered are for a spacecraft with coarse Sun sensors and a magnetometer [93]. The published work is relevant for CubeSat applications with the current state of the sensors available. Additionally the computational effort computed as FLOPS provides data points for selecting an algorithm for a particular CubeSat application. The computational effort of the various determination algorithms are summarized in Table 6-1 [93]. Its apparent from the table that symmetric methods are relatively more expensive than the asymmetric ones. The table compares four methods which can yield both the attitude matrix (A output) and quaternion (q output). However, only the Optimized TRIAD method can be used to directly achieve a quaternion and hence its computational effort for q output is lesser than that for the A output. It can be seen from the table that the methods which compute quaternion in particular without any A output are better suited for pico- and nano-class CubeSats. A direct quaternion approach with singularity avoidance approach may be better suited as an initial attitude estimator for CubeSats due to the computational benefit.

Table 6-1. Computational Effort of Estimation Algorithm in FLOPS

Algorithm	A output	q output
Asymmetric TRIAD	143	172
Symmetric TRIAD	166	195
Optimal Two-Measurement Estimator	265	294
Optimized TRIAD	335	273
Asymmetric Direct Quaternion	N/A	46
Asymmetric Direct Quaternion with Singularity Avoidance	N/A	108
Symmetric Direct Quaternion	N/A	50
Symmetric Direct Quaternion with Singularity Avoidance	N/A	112
QUEST	N/A	190

## 6.2 Stochastic Attitude Estimation

Attitude determination and propagation systems are developed using star trackers, sun sensors, magnetometers and inertial sensors. The systems and sensors developed to facilitate attitude determination have noise and bias issues. In the absence of precise attitude sensors reliable attitude determination is achieved by sophisticated data processing [106]. Attitude determination with sophisticated data processing is often referred to as attitude estimation. Attitude estimation is a two phase process: (i) Attitude determination from body measurements and known reference observations (ii) Filtering noisy measurement data [105]. The Kalman filter [89, 90] and its extensions have proved to be effective and used extensively for spacecraft attitude estimation [107].

In Reference 106, Farrell employed Kalman filter to determine the attitude of spinning satellite with moment of inertia of  $150 \text{ Kg}\cdot\text{m}^2$ ,  $100 \text{ Kg}\cdot\text{m}^2$  and  $100 \text{ Kg}\cdot\text{m}^2$  about the roll, pitch and yaw axes, respectively. As with the current state of the CubeSats, the simulated spacecraft hosted multiple Sun sensors with accuracies of 0.01 rad and a magnetometer with rms accuracies of  $10^{-6}$  weber/m<sup>2</sup> as attitude sensors. The attitude sensors sampled the vector measurements at 1 Hz and the spacecraft had an initial angular rate of 1 rad/s about the symmetric axis. Although not very significant, it is interesting to note that the spin rates assumed for these small satellites were much higher than those measured for CubeSats launched out of the P-POD [3].

The uncertainties assumed for simulation were on the order of 0.1 rad for angular displacement and 0.05 rad/s for angular rates. The published results showed the attitude accuracies achieved for spacecraft with a single line of reference was much poorer than those with two line of references. Additionally the optimum angular separation between the two line of references was determined to be optimum at  $90^0$ . The results also advocated for large angle measurements to address the errors arising due to nonlinearities. During the time the state of spacecraft were similar to the current state of CubeSats. Crude attitude sensors were used on the spacecraft then and it is particularly the case for CubeSats now.

Statistical data processing for attenuating noise can be divided into 3 categories: (i) filtering - real time data processing (ii) observer - perfect observation and (iii) smoothing - batch data processing. Spacecraft attitude estimation is two-point filtering - real time data processing: (i) estimating the attitude from body measurements and known reference observations (ii) filtering the noisy measurements [105]. Kalman filter based attitude estimation has been most commonly implemented in 3 forms:

1. Minimal representation extended Kalman filter [108]
2. Multiplicative extended Kalman filter (MEKF) [88, 109, 110]
3. Additive extended Kalman filter (AEKF) [111–113]

Minimal representation EKFs involving Rodrigues parameters and modified Rodrigues parameters are known to be of particular interest to agile spacecraft. For a space proven version of SwampSat the minimal representation EKF might be well suited. The AEKF uses a nonsingular representation of the attitude and most commonly the quaternion. The AEKF employs a quaternion estimate  $\hat{q}$  and an error component  $\Delta q$ . It relaxes the unit norm constraint on the attitude quaternion but in the process increases the computational complexity. To account for the loss in quaternion normalization AEKF increases the size of the covariance matrix and in turn the computational effort associated with updating the matrix. For CubeSat applications this form of EKF is undesirable. An AEKF has a constrained form and an unconstrained

form. The constrained form is mathematically equivalent to the MEKF. Multiplicative extended Kalman filter has fared well among the different variants of EKF [105]. In this form of EKF the attitude is computed as the product of an estimated attitude and a 3 component deviation. The 3-component error vector,  $\phi$ , can be represented using Rodrigues parameter, modified Rodrigues parameter. The error vector  $\phi$  represents small attitude errors and is very unlikely to encounter singularities. The multiplicative EKF has the form

$$\bar{q} = \delta\hat{q}(\phi) \otimes \hat{q}$$

where,

$$\begin{aligned}\hat{q} &= \text{unit estimated quaternion} \\ \delta\hat{q}(\phi) &= \text{unit quaternion parameterized by a three component error vector}\end{aligned}$$

Spacecraft attitude be represented using direction cosines, Euler angles or quaternions [110]. Early attitude estimation algorithms based on EKF used Euler angles but it suffered from a gimbal lock problem [106]. Quaternion parameterizations are of particular interest as they are free of singularities and the kinematic equations can be treated linearly. On the downside the quaternion representation poses a problem due to the dependence of its components and the constraint of unit norm. Attitude parameterizations such as Euler angles, the Rodrigues parameters are avoided in filter designs due to singularities. Almost all attitude representations are either known to have a redundant component or singularities. Presented in the remainder of this section is an algorithm for estimating the attitude of a pico-class CubeSat with limited computational resources. The attitude is represented using quaternion and the estimation algorithm is designed by coupling QUEST with Murrell's version of the EKF [88].

### 6.3 Spacecraft Attitude Kinematics

The attitude of a spacecraft is its orientation in space with respect to a known reference frame. Often the known reference frame is selected to be an inertial reference frame like the ECI frame. The ECI (J2000) frame has its origin at the Earth's center of mass, the positive Z-axis points in the North Pole direction while coinciding with Earth's rotational axis, the positive X-axis is in the Earth's equatorial plane and points in the direction of vernal equinox and the Y-axis completes the right handed orthogonal Cartesian frame [94]. The J2000 refers to January 1, 2000 12:00 UTC as the time of epoch for this ECI frame. Referring to Fig. 6-1, if  $(X_B, Y_B, Z_B)$  were to represent the coordinate frame attached to the spacecraft and  $(X_I, Y_I, Z_I)$  the ECI frame, the transformation matrix or the DCM  $\underline{\underline{C}}_{BI}$  would map representations in the ECI frame to the spacecraft body frame. The mapping could also be equally represented by an attitude quaternion  $\bar{q}$ , defined in terms of an angle  $\theta$  and a unit vector  $\hat{e}$ . It is important to note that  $\bar{q}$  and  $-\bar{q}$  represent the same attitude and  $\bar{q}$  is of unit length [114]. If the spacecraft were to be rotated by an angle  $\theta$  about a unit vector  $\hat{e}$  it would align itself with the ECI frame. If the quaternion  $\bar{q}$  is

$$\bar{q} = \begin{bmatrix} q \\ \frac{q}{q_4} \end{bmatrix}$$

where

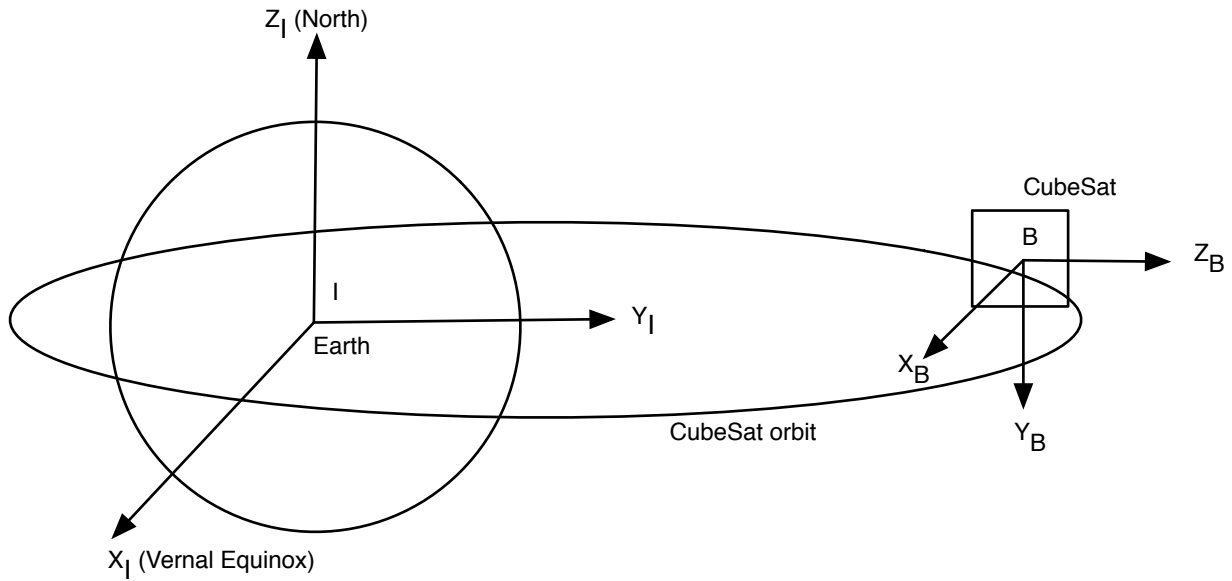
$$\begin{aligned} \bar{q} &= [q_1 q_2 q_3] = \hat{e} \sin \theta / 2 \\ q_4 &= \cos \theta / 2 \end{aligned}$$

and the corresponding DCM  $\underline{\underline{C}}_{BI}$  is given by

$$\underline{\underline{C}}_{BI} = \Xi^T(q)\Psi(q) \quad (6-6)$$

where,

$$\begin{aligned}\Xi(\underline{q}) &= \begin{bmatrix} q_4 I_{3 \times 3} + [\underline{q}]^\times \\ -\underline{q}^T \end{bmatrix} \\ \Psi(\underline{q}) &= \begin{bmatrix} q_4 I_{3 \times 3} - [\underline{q}]^\times \\ -\underline{q}^T \end{bmatrix}\end{aligned}$$



$(X_I, Y_I, Z_I)$  - Inertial frame

$(X_B, Y_B, Z_B)$  - CubeSat body frame

Figure 6-1. Spacecraft Body and Inertial Reference Frames

If the angular velocity of the spacecraft with respect to the ECI frame  $\underline{\omega} = [\omega_1 \ \omega_2 \ \omega_3]^T$ , then the spacecraft attitude kinematics are governed by

$$\begin{aligned}\frac{d}{dt}(\underline{\underline{C}}_{BI}) &= -[\underline{\omega}]^\times \underline{\underline{C}}_{BI} \\ \frac{d}{dt}(\bar{q}) &= \frac{1}{2} \underline{\Omega}(\underline{\omega}) \bar{q}\end{aligned}\tag{6-7}$$

where,

$$[\underline{\omega}]^{\times} = \begin{pmatrix} 0 & -\omega_3 & \omega_2 \\ \omega_3 & 0 & -\omega_1 \\ -\omega_2 & \omega_1 & 0 \end{pmatrix}$$

$$\underline{\Omega}(\omega) = \begin{pmatrix} -[\underline{\omega}]^{\times} & \underline{\omega} \\ -\underline{\omega}^T & 0 \end{pmatrix}$$

It is clear from the development of attitude kinematics that an initial estimate of the spacecraft attitude and its angular velocities are key for maintaining spacecraft attitude knowledge. The attitude kinematics developed here are the starting point for an attitude estimation algorithm.

#### 6.4 Distributed Attitude Determination and Estimation System

Pico- and nano-class CubeSat have a limited form factor and hence limited power generation capability. However, missions with high computing needs, which have power requirements greater than the average power generation capability, distributed computing can be adopted. In such a scenario, a subsystem, one or more on board operations may be required to be distributed. The distributed design of attitude determination and estimation is addressed in this context. The schematic shown in Fig. 6-2 identifies the main hardware and software components of the distributed attitude determination and estimation system.

The attitude determination system is designed taking into consideration the computational and power resources available on the CubeSat. The 1U CubeSat form factor limits the use of a conventional star tracker and CCD (charge-coupled device) based star trackers are in a development phase, hence the CubeSat is designed to accommodate coarse attitude sensors. Primarily, modified light-to-voltage converters (LTV) as sun sensors and a low power magnetometer are interfaced to the flight computer. A MEMS based IMU, is interfaced to the auxiliary computer (CMG controller).

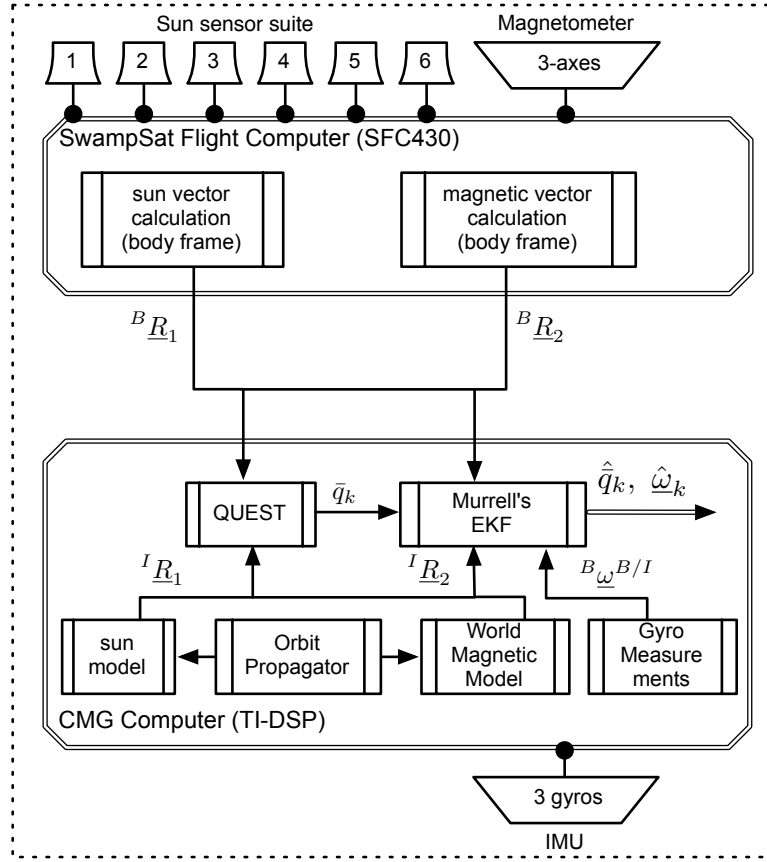


Figure 6-2. SwampSat ADS as a Distributed System

Initial attitude of the spacecraft is computed as a quaternion using attitude sensors and propagated using IMU.

#### 6.4.1 Attitude Sensors

Although LTVs as coarse Sun sensors and MEMS based magnetometers are limited in their ability to precisely determine the reference vectors in the satellite body frame, they are conveniently available in sizes suitable for picosatellite applications and their impact on the satellite power budget is significantly low. If the error sources of these sensors can be mathematically modeled and incorporated, they can be effectively used for attitude computations. A sensor model based on the design and analyses of an LTV based sun sensor [73] is considered for evaluating the attitude estimation design. A magnetometer, the HMC2003 from Honeywell [115], is selected as the other

attitude sensor due to its availability in a form factor suitable for picosatellites and its effectiveness in a low Earth orbit. The maximum magnetic field strength experienced on the Earth's surface is limited to 0.6 gauss, as calculated by the International Geophysical Data Center and the HMC2003 is capable of measuring up to  $\pm 2$  gauss at a resolution of 40  $\mu$ gauss. The mathematical model considered for these attitude sensors is discussed below.

#### 6.4.1.1 Attitude sensor model

Let  ${}^B\underline{R}_i$  represent the  $i^{th}$  measurement of a vector in frame  $\mathcal{F}_B$  and  $'\underline{R}_i$  its representation in a reference frame  $\mathcal{F}_I$ . The discrete time measurement of the vector and its representation in both frames can be modeled to follow [116]

$${}^B\underline{R}_i = \underline{C}_{BI} {}' \underline{R}_i + \underline{\vartheta}_i$$

Here the sensor error vector  $\underline{\vartheta}_i$  is Gaussian with the following properties.

$$E\{\underline{\vartheta}_i\} = 0$$

$$E\{\underline{\vartheta}_i \underline{\vartheta}_i^T\} = \sigma_i^2 I$$

**Sun sensor.** The Sun sensors on each face of a CubeSat are modeled individually. The voltage measured from the Sun sensor on the  $i^{th}$  face is modeled using a cosine profile as,

$$\tilde{V}_i = \begin{cases} {}^B\hat{\underline{R}}_i \cdot {}^B\hat{\underline{n}}_i + \eta_s (1 - {}^B\hat{\underline{R}}_i \cdot {}^B\hat{\underline{n}}_i) & \text{if } {}^B\hat{\underline{R}}_i \cdot {}^B\hat{\underline{n}}_i \geq 0 \\ 0 & \text{otherwise} \end{cases}$$

where  $\eta_s$  is a zero-mean normally distributed random number with standard deviation  $\sigma_s = 0.1$  V. It was observed that the voltage generated matched the cosine profile more closely when the angle of incidence was closer to zero [73]. Accordingly, the Sun vector

in the body frame is expressed as,

$${}^B\underline{R}_i = \frac{1}{(\sum_{i=1}^6 \tilde{V}_i^2)^{0.5}} \sum_{i=1}^6 \tilde{V}_i {}^B\underline{\hat{n}}_i$$

**Magnetometer.** The magnetic field vector is modeled according to the following expression,

$${}^B\underline{R}_i = \underline{C}_{BI} {}^I\underline{R}_i + \eta_m + \beta_m$$

where  $\eta_m$  is a white random vector with each component having a standard deviation of  $\sigma_m = 0.005 \|{}^B\underline{R}_i\|$ . The vector  $\beta_m$  is a bias vector incorporating the influence of spacecraft environment.

#### 6.4.2 Inertial Measurement Unit (IMU)

The ADIS16405 [117], a MEMS based IMU from Analog Devices, is identified for measuring the body rates of the Cubesat. The IMU is equipped with gyros operating in rate mode and can be sampled at frequencies of up to 350 Hz. The ADIS16405 is selected based on a trade study done of the available MEMS based inertial sensors [39]. The low power constraint, port available to interface with the onboard computer, operating temperature range and the size/mass were some of the characteristics evaluated for the selection process. The ADIS16405 sensor has an operating temperature range of  $-40^0$  C to  $+85^0$  C, interfaces with the on board computer through the serial peripheral interface (SPI) port and consumes 33 mA @ 5 V when operating in a normal mode. The unit weighs 16 g and is approximately  $23 \times 23 \times 23$  mm in dimension. For evaluating the attitude estimation design, a mathematical model of the gyros, discussed below, is considered.

The IMU was subjected to analysis and testing to verify the sensor integrity and determine the initial bias characteristics. To verify the integrity of the gyros the IMU was subjected to testing on a rotary table with precision encoders. A setup of the precision rotary table and the plots verifying the integrity of the gyros are shown in Fig. 6-3. To determine the initial bias characteristics the IMU was placed on a stationary platform

and the gyro readings were sampled for a period of 60 minutes. The mean of the sampled gyro measurements about each axes was adopted as the initial gyro bias.

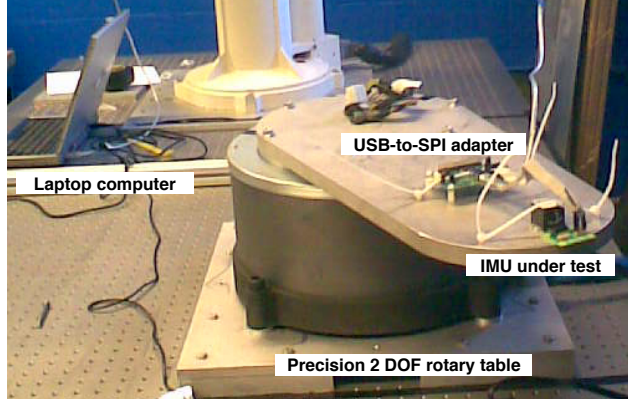
#### 6.4.2.1 Gyro model

As discussed in the gyro model developed by Farrenkopf [118] and applied by Hoffman and McElroy [119], sensor measurements are affected by drift rate bias and drift rate noise. The gyro model relating the gyro output vector  $\tilde{\omega}$ , the satellite angular velocity  $\omega$ , drift rate bias  $\beta$  and drift rate noise  $\eta_v$  is expressed as

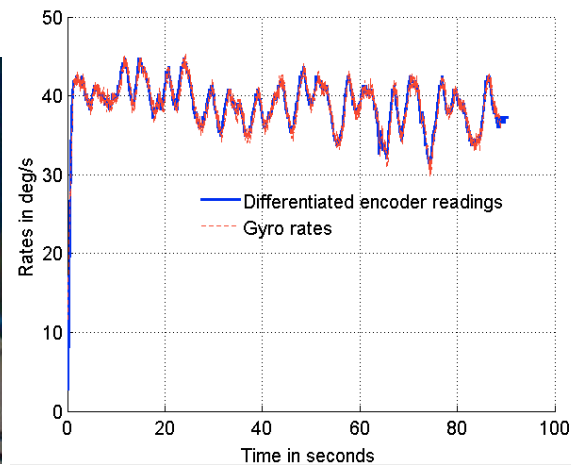
$$\tilde{\omega} = \omega + \beta + \eta_v$$

$$\dot{\beta} = \eta_u$$

Here  $\eta_v$  and  $\eta_u$  are uncorrelated zero-mean Gaussian white-noise processes with standard deviations of  $\sigma_v = 0.007^0/\text{s}^2$ ,  $\sigma_u = 2^0/\text{hr}$ , respectively, and having the same properties as the attitude sensor error vector  $\vartheta_i$ . The values of standard deviation are obtained from the sensor data sheet [117].



A Precision 2 DOF Rotary Table



B IMU Rates vs Differentiated Encoder Readings

Figure 6-3. IMU Calibration Experiment

### 6.4.3 Attitude Estimation

The attitude estimation algorithm is shown as a flow diagram in Fig. 6-4. The filter is designed as a 6-state EKF to be implemented in two phases - (i) attitude determination (ii) attitude propagation. The states, which include three attitude errors and three gyro drift rate biases, are propagated as a 6x6 error covariance matrix. The three components of attitude error incorporate the inaccuracies in the attitude sensors and the gyro drift rate bias makes up for the inaccuracies in the MEMS gyros. The attitude estimation algorithm shown in Fig. 6-4 is evaluated for three different attitude sensor configurations: (i) Attitude estimation using Sun sensors and magnetometer (ii) Attitude estimation using the magnetic field vector and its time derivative and (iii) Attitude estimation using the magnetic field vector. All three configurations employ gyros for measuring satellite angular rates. The use of Murrell's version of the EKF has been beneficial in accommodating all three configurations of attitude sensors efficiently. The estimation algorithm is described for all three sensor configurations.

#### 6.4.3.1 Attitude estimation using Sun sensors and magnetometer

During the attitude determination phase, the error covariance matrix,  $P_k^-$ , is initialized with values determined from experiments, models and component data sheets of the attitude sensors and gyros. The initial bias of the gyros,  $\hat{\beta}_k^-$ , is assigned with values determined from experiments. The sun and magnetic field vector are acquired in the body and inertial frames to initialize the CubeSat attitude quaternion,  $\hat{q}_k^-$ , from QUEST. The corresponding attitude matrix,  $C_{BI}$  and the vector part of the quaternion is computed from Eq. (6-6) and stored as separate variables for use in the algorithm.

Since two measurements are used to compute the attitude quaternion the algorithm performs two iterations of Eq. (6-8) through Eq. (6-12) to calculate the sensitivity matrix  $H_k$  (Eq. (6-8)), Kalman gain  $K_k$  (Eq. (6-9)), error covariance  $P_k^+$  (Eq. (6-10)), residual  $\epsilon_k$  (Eq. (6-11)) and error state  $\Delta\hat{x}_k^+$  (Eq. (6-12)). The parameters computed in Eq. (6-8) through Eq. (6-12) are used to update the quaternion  $\hat{q}_k^+$ , gyro bias  $\hat{\beta}_k^+$  and

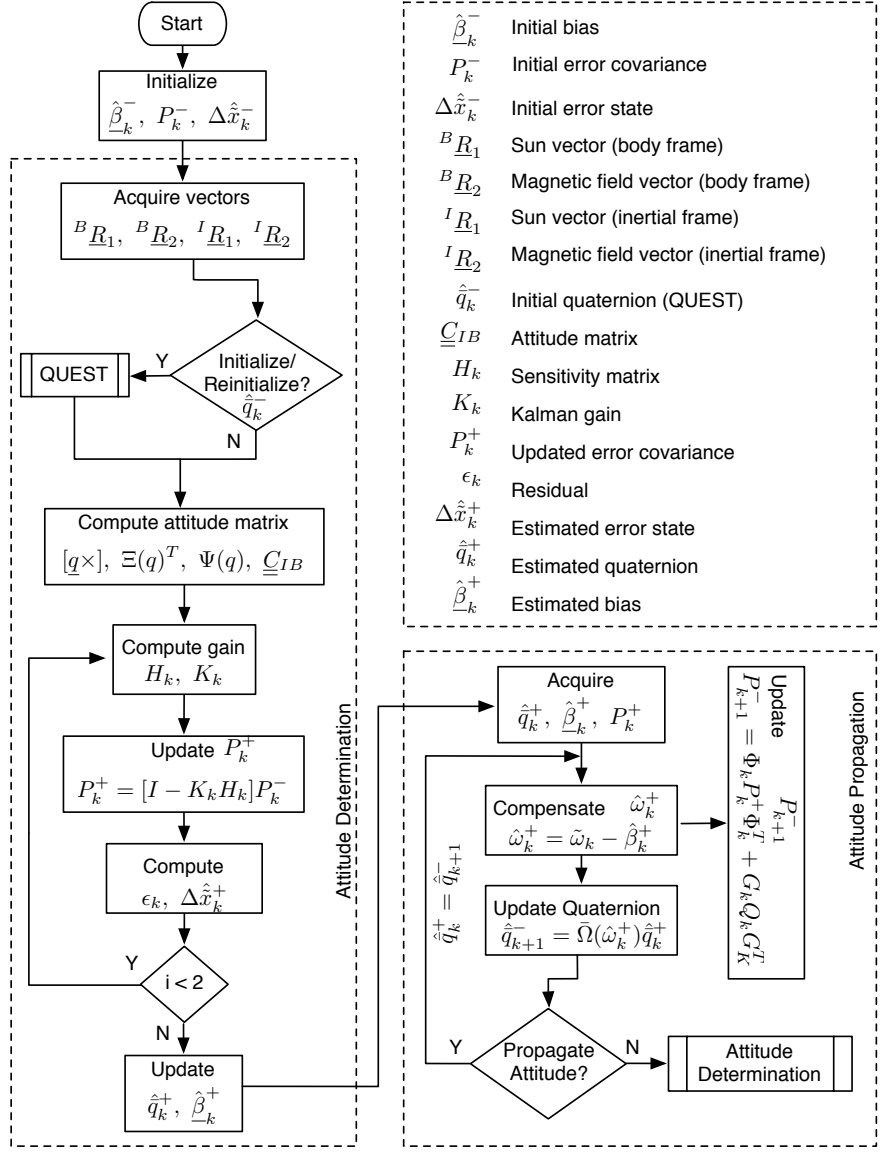


Figure 6-4. Attitude Estimation Algorithm for SwampSat

error covariance matrix  $\hat{P}_k^+$ .

$$H_k = \begin{bmatrix} [\underline{\underline{C}}_{BI} {}^I R_i]^* & 0_{3 \times 3} \end{bmatrix} \quad (6-8)$$

$$K_k = P_k^- H_k^T [H_k P_k^- H_k^T + \sigma_i^2 I]^{-1} \quad (6-9)$$

$$P_k^+ = [I - K_k H_k] P_k^- \quad (6-10)$$

$$\epsilon_k = ({}^B \tilde{R}_i - \underline{\underline{C}}_{BI} {}^I R_i) \quad (6-11)$$

$$\Delta\hat{x}_k^+ = \Delta\hat{x}_k^- + K_k [\epsilon_k - H_k \Delta\hat{x}_k^-] \quad (6-12)$$

$$\Delta\hat{x}_k^+ = [\delta\hat{\alpha}_k^{+T} \Delta\hat{\beta}_k^{+T}]^T \quad (6-13)$$

$$\hat{q}_k^+ = \hat{q}_k^- + \frac{1}{2}\Xi(\hat{q}_k^-)\delta\hat{\alpha}_k^+ \quad (6-14)$$

$$\hat{\beta}_k^+ = \hat{\beta}_k^- + \Delta\hat{\beta}_k^+ \quad (6-15)$$

The quaternion, gyro bias and the error covariance matrix computed during the attitude determination phase are passed as arguments to the attitude propagation phase. The satellite angular rates are acquired from the gyro measurements and the gyro bias is compensated in Eq. (6–16). The estimated satellite angular rates are used within this phase to propagate the satellite attitude using Eq. (6–17).

$$\underline{\hat{\omega}}_k^+ = \tilde{\omega}_k - \hat{\beta}_k^+ \quad (6-16)$$

$$\hat{q}_{k+1}^- = \bar{\Omega}(\underline{\hat{\omega}}_k^+)\hat{q}_k^- \quad (6-17)$$

where,

$$\begin{aligned} \bar{\Omega}(\underline{\hat{\omega}}_k^+) &= \begin{bmatrix} \cos(\frac{1}{2}||\underline{\hat{\omega}}_k^+||\Delta t)I_{3\times 3} - [\hat{\psi}_k^+]^\times & \hat{\psi}_k^+ \\ -\hat{\psi}_k^{+T} & \cos(\frac{1}{2}||\underline{\hat{\omega}}_k^+||\Delta t) \end{bmatrix} \\ \hat{\psi}_k^+ &= \frac{\sin(\frac{1}{2}||\underline{\hat{\omega}}_k^+||\Delta t)\underline{\hat{\omega}}_k^+}{||\underline{\hat{\omega}}_k^+||} \end{aligned}$$

Additionally the error covariance matrix is also propagated using Eq. (6–8) through Eq. (6–12) during this phase to update the states of the satellite.

$$P_{k+1}^- = \Phi_k P_k^+ \Phi_k^T + G_k Q_k G_k^T$$

where,

$$\begin{aligned}
G_k &= \begin{bmatrix} -I_{3 \times 3} & 0_{3 \times 3} \\ 0_{3 \times 3} & I_{3 \times 3} \end{bmatrix} \\
Q_k &= \begin{bmatrix} (\sigma_v^2 \Delta t + \frac{1}{3} \sigma_u^2 \Delta t^3) I_{3 \times 3} & -(\frac{1}{2} \sigma_u^2 \Delta t^2) I_{3 \times 3} \\ -(\frac{1}{2} \sigma_u^2 \Delta t^2) I_{3 \times 3} & (\sigma_u^2 \Delta t) I_{3 \times 3} \end{bmatrix} \\
\Phi &= \begin{bmatrix} \Phi_{11} & \Phi_{12} \\ \Phi_{21} & \Phi_{22} \end{bmatrix} \\
\Phi_{11} &= I_{3 \times 3} - [\hat{\omega}]^{\times} \frac{\sin(||\hat{\omega}||\Delta t)}{||\hat{\omega}||} + [\hat{\omega}]^{\times 2} \frac{\{1 - \cos(||\hat{\omega}||\Delta t)\}}{||\hat{\omega}||^2} \\
\Phi_{12} &= [\hat{\omega}]^{\times} \frac{\{1 - \cos(||\hat{\omega}||\Delta t)\}}{||\hat{\omega}||_2} - I_{3 \times 3} \Delta t - [\hat{\omega}]^{\times} \frac{\{||\hat{\omega}||\Delta t - \sin(||\hat{\omega}||\Delta t)\}}{||\hat{\omega}||^3} \\
\Phi_{21} &= 0_{3 \times 3} \\
\Phi_{22} &= I_{3 \times 3}
\end{aligned}$$

Here,  $\sigma_v^2$  and  $\sigma_u^2$  are the variances associated with the random drift  $\eta_v$  and drift rate ramp  $\eta_u$  components of the on board gyros. The components are discussed as part of the gyro model. The sampling interval is captured by the parameter  $\Delta t$ . The filter is implemented in two phases to account for the distributed implementation of the attitude determination and estimation system. During the attitude determination phase, measurements are obtained from the attitude sensors which are interfaced to the flight computer. During the attitude propagation phase, measurements are obtained from the on board gyros which are interfaced to the CMG controller. The propagation phase when operated independently from the determination phase can propagate the initialized attitude until a new set of set of attitude measurements are available.

#### 6.4.3.2 Attitude estimation using magnetic field vector and its time derivative

To mitigate any limitations in the on board Sun sensors, attitude estimation using the magnetic field vector and its first time derivative is explored. The estimation scheme is designed to accommodate this particular sensor configuration. Referring back to

the attitude kinematics of Fig. 6-1, let  $\underline{\underline{C}}_{BI}$  represent the transformation from inertial reference frame to spacecraft body frame i.e.,

$${}^B() = \underline{\underline{C}}_{BI} {}^I()$$

$\underline{\omega}$  is the angular velocity of the satellite body frame with respect to the inertial frame i.e.,

$$\dot{\underline{\underline{C}}}_{BI} = [\underline{\omega}]^\times \underline{\underline{C}}_{BI}$$

Let  $\underline{B}$  is the magnetic field vector measured in both frames, then

$${}^I\underline{B} = \underline{\underline{C}}_{BI}^{T_B} \underline{B}$$

Now, let  $\underline{B}$  be measured @ times  $t_1$  and  $t_2$

Then,

$$\begin{aligned} {}^I\underline{B}(t_2) &= \underline{\underline{C}}_{BI}^T(t_2) {}^B\underline{B}(t_2) \\ {}^I\underline{B}(t_1) &= \underline{\underline{C}}_{BI}^T(t_1) {}^B\underline{B}(t_1) \end{aligned}$$

Furthermore,

$$\begin{aligned} \underline{\underline{C}}_{BI}(t_2) &= \underline{\Delta C}_{BI}(t_2 - t_1) \underline{\underline{C}}_{BI}(t_1) \\ \underline{\underline{C}}_{BI}(t_2) &= (1 - [\underline{\Delta\theta}(t_1)]^\times) \underline{\underline{C}}_{BI}(t_1) \end{aligned}$$

Conversely, it can be stated (i.e., reversing time propagation)

$$\begin{aligned} \underline{\underline{C}}_{BI}(t_1) &= \underline{\Delta C}_{BI}(t_1 - t_2) \underline{\underline{C}}_{BI}(t_2) \\ \underline{\underline{C}}_{BI}(t_1) &= (1 - [\underline{\Delta\theta}(t_2)]^\times) \underline{\underline{C}}_{BI}(t_2) \end{aligned}$$

where,

$$\underline{\Delta\theta}(t_2) = -\underline{\Delta\theta}(t_1)$$

$\Rightarrow$

$$\underline{\underline{C}}_{BI}(t_1) = (1 + [\Delta\theta(t_1)]^\times) \underline{\underline{C}}_{BI}(t_2)$$

Thus,

$$\begin{aligned} {}^I\underline{B}(t_2) &= \underline{\underline{C}}_{BI}^T(t_2) {}^B\underline{B}(t_2) \\ {}^I\underline{B}(t_1) &= \underline{\underline{C}}_{BI}^T(t_2)(1 - [\Delta\theta(t_1)]^\times) {}^B\underline{B}(t_1) \\ {}^I\underline{B}(t_2) - {}^I\underline{B}(t_1) &= \underline{\underline{C}}_{BI}^T(t_2)[{}^B\underline{B}(t_2) - {}^B\underline{B}(t_1) + [\Delta\theta(t_1)]^\times {}^B\underline{B}(t_1)] \end{aligned}$$

Dividing by  $\Delta t = t_2 - t_1$ ,

$$\begin{aligned} \frac{{}^I\underline{B}(t_2) - {}^I\underline{B}(t_1)}{\Delta t} &= \underline{\underline{C}}_{BI}^T(t_2) \left[ \frac{{}^B\underline{B}(t_2) - {}^B\underline{B}(t_1)}{\Delta t} + \frac{\Delta\theta(t_1)}{\Delta t} {}^B\underline{B}(t_1) \right] \\ \therefore \frac{{}^I\underline{B}(t_2) - {}^I\underline{B}(t_1)}{\Delta t} &= \underline{\underline{C}}_{BI}^T(t_2) \left[ \frac{{}^B\underline{B}(t_2) - {}^B\underline{B}(t_1)}{\Delta t} + [\omega]^\times(t_1) {}^B\underline{B}(t_1) \right] \end{aligned}$$

Summarizing the development, it can be concluded that the magnetic field vector  $\underline{B}$  and its first time derivative  $\dot{\underline{B}}$  have the following relationship, which can be exploited to acquire two vectors for attitude determination [120, 121].

$$\begin{aligned} \underline{\underline{C}}_{BI} {}^I\underline{B} &= {}^B\underline{B} \\ \underline{\underline{C}}_{BI} {}^I\dot{\underline{B}} &= {}^B\dot{\underline{B}} + [\omega]^\times {}^B\underline{B} \end{aligned}$$

Within the attitude estimation algorithm, the magnetic field and its first time derivative are acquired in the inertial and body frame and passed as arguments to QUEST for initializing the CubeSat attitude quaternion. The satellite angular velocity with respect to the inertial frame coordinatized in the body axes is acquired from the on board gyros for computing the complete time derivative of the magnetic field vector. The rest of the estimation algorithm is executed as described in the flowchart shown in Fig. 6-4.

#### 6.4.3.3 Attitude estimation using magnetic field vector

Although the deterministic approach described for the above configuration is in theory better suited for attitude determination and propagation the nonlinearities associated with the magnetic field vector can significantly influence the time derivative vector and subsequently the attitude estimate. To address the limitations of this approach attitude estimation using magnetic field as the only attitude vector is explored. The use of Murrell's version of the EKF has proved to be advantageous and an efficient approach for accommodating this sensor configuration. QUEST being an optimal estimator requires at least two vectors to compute an attitude estimate. In its place, Shuster's method of constructing a suboptimal attitude quaternion from a single vector in two frames is adopted for initializing the CubeSat attitude [122]. The expression for constructing the suboptimal attitude quaternion is

$$\bar{q} = \sqrt{\frac{1 + {}^B\underline{B} \cdot {}^B\underline{B}}{2}} \begin{bmatrix} \frac{{}^B\underline{B} \times {}^B\underline{B}}{1 + {}^B\underline{B} \cdot {}^B\underline{B}} \\ 1 \end{bmatrix}$$

The initialized attitude quaternion is iteratively processed through Eq. (6–8) to Eq. (6–18) for estimating the satellite attitude and gyro bias. Unlike the above two configurations, Eq. (6–8) through Eq. (6–12) are updated only once. The remainder of the estimation algorithm is executed as in the above two configurations. The simulations carried out to evaluate the performance of each of these sensor configurations and their results are described in the following section.

## 6.5 Simulation and Results

To evaluate the effectiveness of the attitude estimation algorithms described above, simulations are performed with data generated from satellite tool kit (STK) [123]. The picosatellite orbit is simulated in a low Earth orbit with parameters shown in Table 6-2. The picosatellite is assumed to be launched from a P-POD and have angular rates of up to  $\pm 3$  deg/s about each axes. A satellite in a low Earth orbit of a STK scenario

initialized with these rates is considered. The data generated using STK consists of the quantities shown in Table 6-3. The true quaternion in the data set is used for comparing the estimated quaternion from the attitude estimation algorithm. The attitude data set for each scenario is generated for 100 minutes with a 25 Hz sampling frequency. To emulate sensor measurements on orbit, the data is corrupted with bias and noise values determined from component data sheets, experiments, and models.

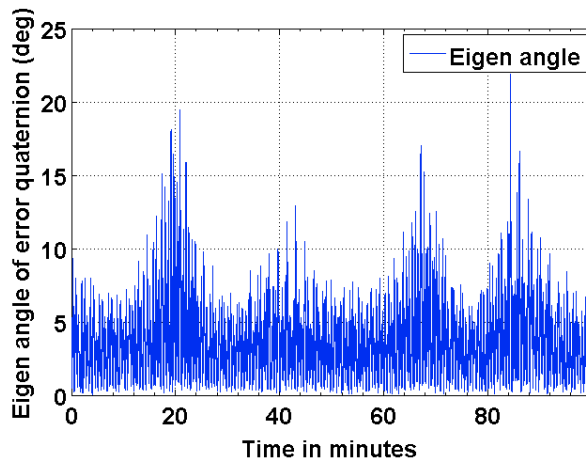
To identify the need for attitude estimation, simulations are carried out to compare attitude determination results of a deterministic approach with the true quaternions obtained from STK. The effect of varying sampling rate of the attitude sensor measurements to emulate the distributed implementation, is captured in four subplots. It can be seen from the plots shown in Fig. 6-5 that the attitude error has an approximate upper bound of  $21^{\circ}$  when sampled at 12 Hz and  $24^{\circ}$  when sampled at 1 Hz. The attitude error justifies the need for attitude estimation of the CubeSat. To evaluate the effectiveness of the algorithm shown in Fig. 6-4, attitude estimation simulations are performed using the corrupted sensor measurements. All three sensor configurations are evaluated through simulations and comparison of their performance is presented.

Table 6-2. LEO Parameters for STK Scenario

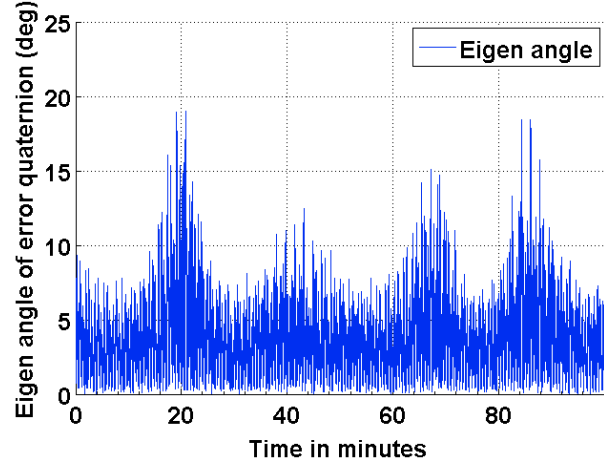
Semimajor axis (a)	6703.14 Km
Eccentricity (e)	0
Inclination (i)	$51.6$ deg
Argument of perigee ( $\omega$ )	0 deg
Longitude of ascending node ( $\Omega$ )	0 deg
True anomaly ( $\vartheta$ )	0 deg

Table 6-3. Attitude Data Generated for Simulation

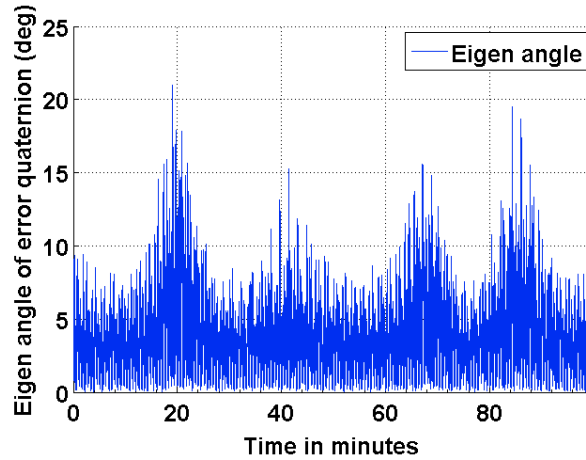
Quantity	Description
${}^B\dot{R}_1$	3x1 magnetic field vector coordinatized in body frame
${}^B\dot{R}_2$	3x1 Sun vector coordinatized in body frame
${}^E\dot{R}_1$	3x1 magnetic field vector coordinatized in ECI frame
${}^E\dot{R}_2$	3x1 Sun vector coordinatized in ECI frame
${}^B\omega$	3x1 angular velocity vector coordinatized in body frame
$\bar{q}$	4x1 quaternion representing true attitude



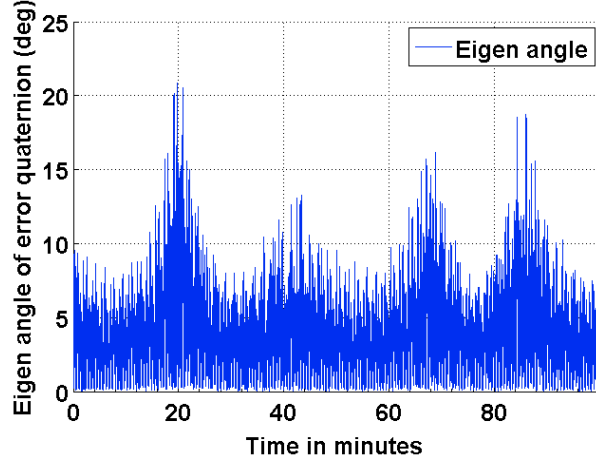
A Attitude Sensors Sampled @ 1 Hz



B Attitude Sensors Sampled @ 3 Hz



C Attitude Sensors Sampled @ 6 Hz



D Attitude Sensors Sampled @ 12 Hz

Figure 6-5. ADS Error - Eigen Angle of Error Quaternion

The algorithm is adapted with the goal of filtering attitude error due to noisy vector measurements and estimate gyro biases for all three axes. According to the sensor models discussed previously, the Sun vector measurements are corrupted with Gaussian white random noise with zero mean and a standard deviation  $\sigma_s = 0.1$  V. The magnetic field measurements are also corrupted with similar random noise components with zero mean and a standard deviation of  $\sigma_m = 0.005\|{}^B R_i\|$ . The gyro measurements are modeled as described previously with standard deviations of  $\sigma_v = 0.007^0/\text{s}^2$ ,  $\sigma_u = 2^0/\text{hr}$ . As simulation parameters the standard deviation

of attitude error covariance is set to  $3.4^0$  obtained from sensor data sheet and the standard deviation of gyro drift covariance is set to  $[0.0311 \ 0.0303 \ 0.0272]^0/s$  which is experimentally determined. The initial bias for each axis, determined experimentally, is set to  $[-0.0724 \ -0.1927 \ 0.0205]^0/s$ .

### 6.5.1 Estimation Results Using Sun Sensors and Magnetometer

The results of the attitude estimation simulations performed using Sun sensors and magnetometer are shown in Fig. 6-6, Fig. 6-7 and Fig. 6-8. The error in attitude accuracy is captured as eigen angle and eigen axis of the error quaternion, the error being computed between the estimated quaternion and the true quaternion as described in Reference 124. The error in angular rates is determined by taking the finite difference between the components of the estimated angular rates and true angular rates. With the available on board attitude sensors, the estimation algorithm improves upon the attitude determination results shown in Fig. 6-5. The simulation parameters used for this scenario are summarized in Table 6-6. It can be seen from Fig. 6-6 and Fig. 6-7 that the accuracy of the attitude estimate and estimate angular rates increase with increase in the sampling frequency of the attitude sensors. The distributed implementation of the attitude determination and estimation system enables the gyros to be sampled at a higher rate than the attitude sensors. The subplots shown in Fig. 6-6 investigate the effect of varying sampling frequency of the attitude sensors, while maintaining the sampling frequency of the gyros at 25 Hz. It can be observed that approximately  $1^0$  pointing accuracy can be achieved if the attitude sensors can be sampled at 12 Hz with the gyros being sampled at 25 Hz. The simulations are carried out for 100 minutes to qualify and evaluate the estimation algorithm. The estimation algorithm requires a finite time to converge to a steady error, which can be accommodated in the system. The plots shown in Fig. 6-7 and Fig. 6-8 capture the error in estimated angular rates about each axes of the satellite and the error in each of the estimated quaternion components.

The error in each of these components can be observed to decrease with increase in the sampling frequency of the attitude sensors.

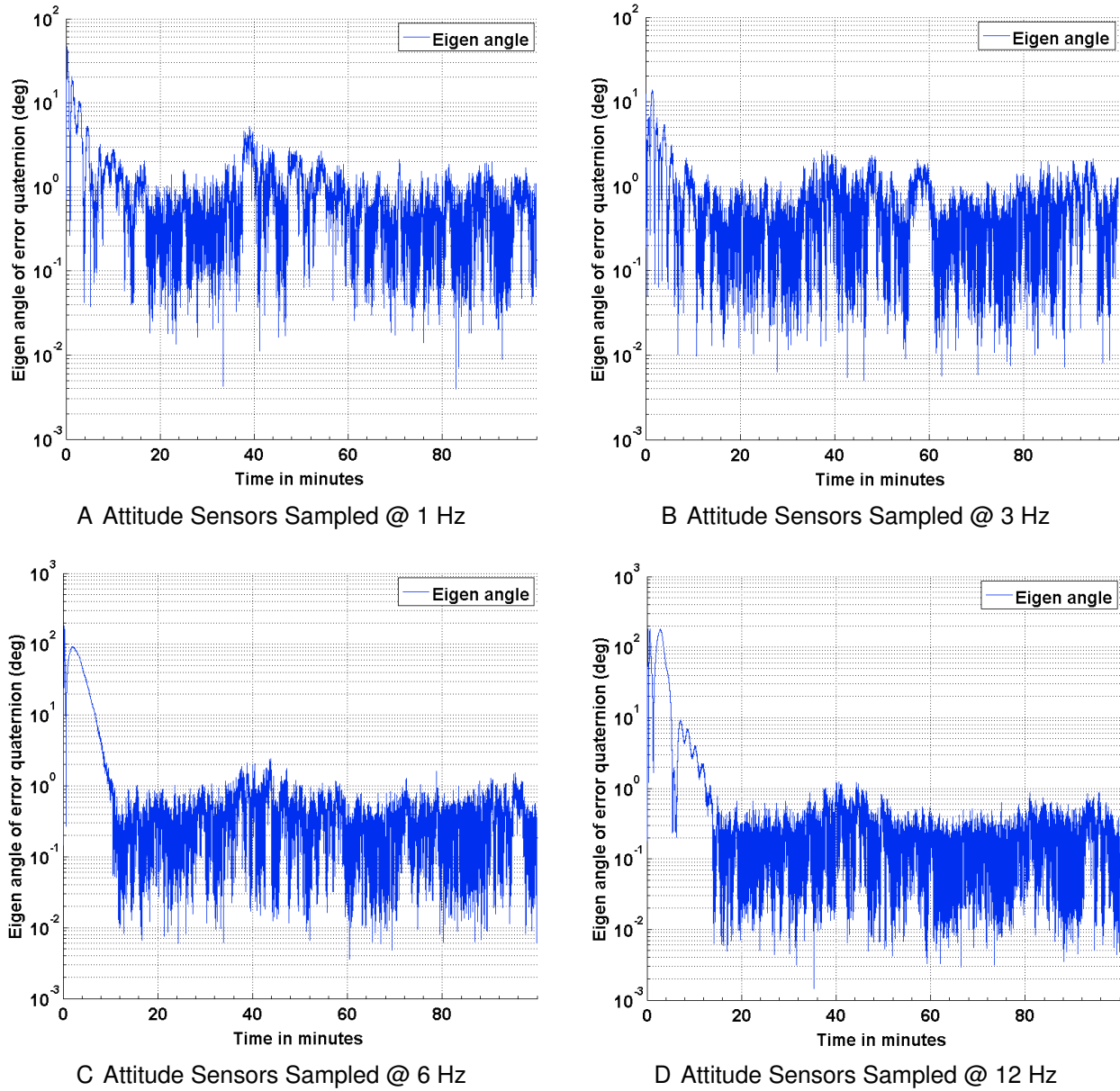


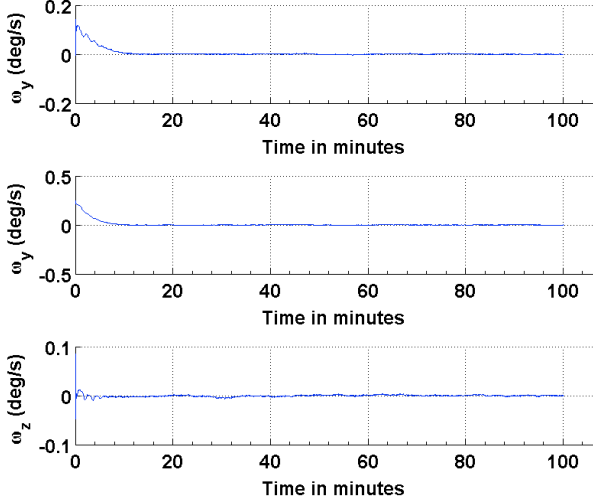
Figure 6-6. Estimation Error - Eigen Angle of Error Quaternion

### 6.5.2 Estimation Results Using Magnetic Field Vector

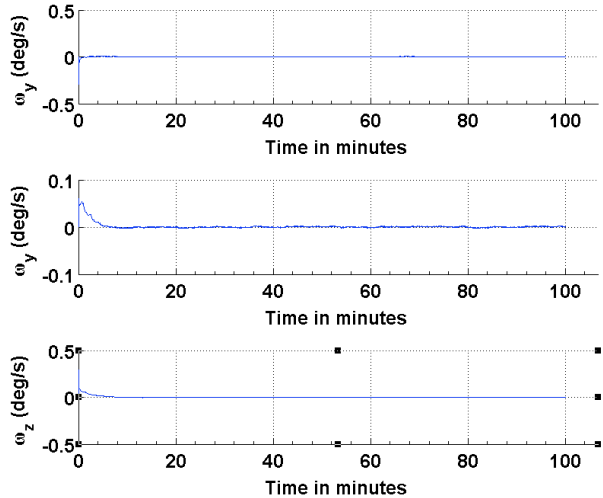
To address any possible limitations in the Sun sensor and enable attitude estimation during eclipse time, simulations are carried out to investigate the performance of the EKF using magnetic field vector from the magnetometer and gyros. The results of the

Table 6-4. Simulation Parameters for Estimation Using Sun Sensors and Magnetometer

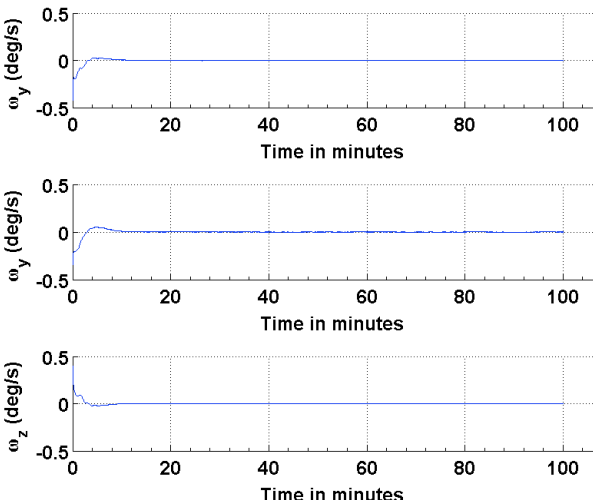
Parameter/Variable	Value
$P_k^-$	$[0.03142^2, 0.03142^2, 0.03142^2, 0.0311^2, 0.0303^2, 0.0272^2]$
$\hat{\beta}_k^-$	$[-0.0724, -0.1927, 0.0205]^T$
$[\sigma_1 \sigma_2]$	$[100, 5]$
$[\sigma_U \sigma_V]$	$[0.001 \times \pi/180, 1 \times \pi/180/3600]$



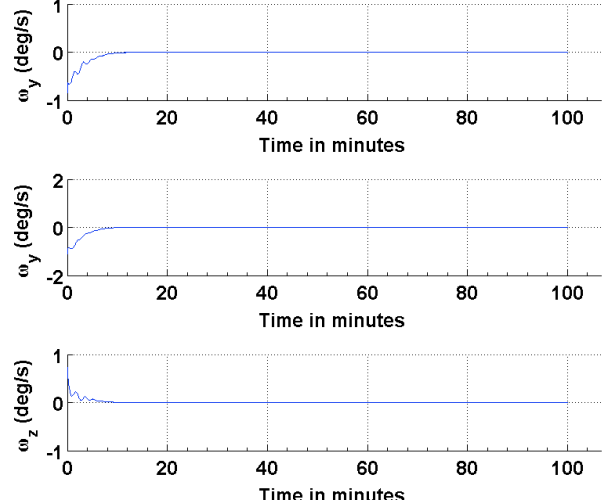
A Attitude Sensors Sampled @ 1 Hz



B Attitude Sensors Sampled @ 3 Hz



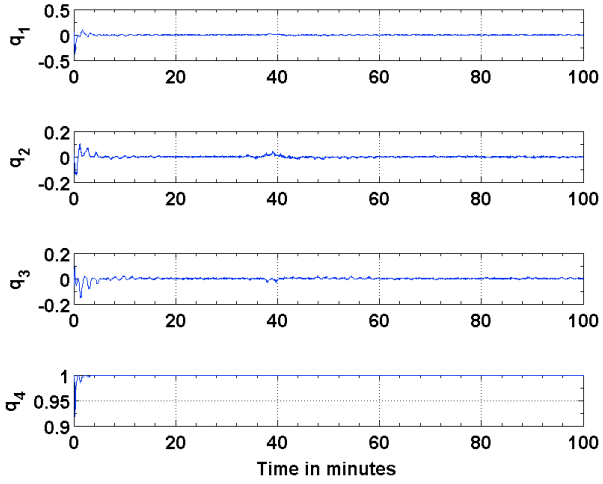
C Attitude Sensors Sampled @ 6 Hz



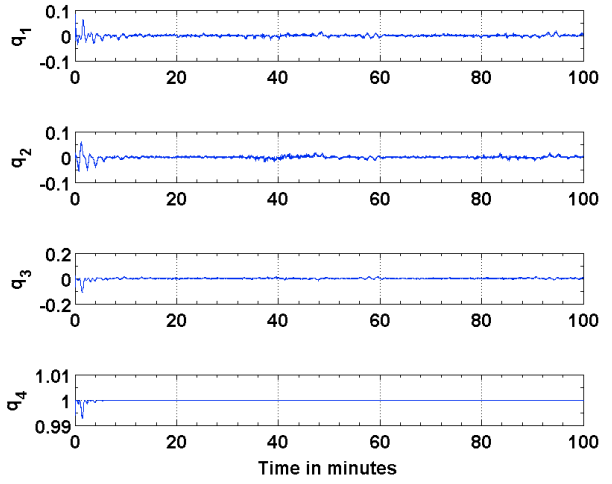
D Attitude Sensors Sampled @ 12 Hz

Figure 6-7. Error in Estimated and True Angular Rates

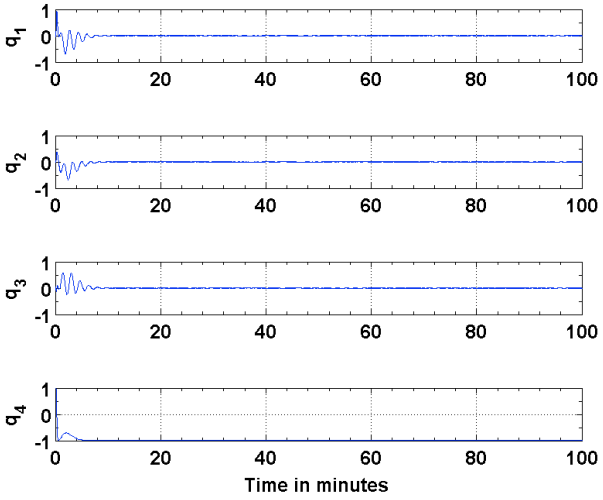
simulations are shown in Fig. 6-9, Fig. 6-10 and Fig. 6-11. The performance is evaluated in terms of attitude accuracy, error in estimated satellite angular rates and error in estimated quaternion components. It can be seen by comparing the plots in Fig. 6-9



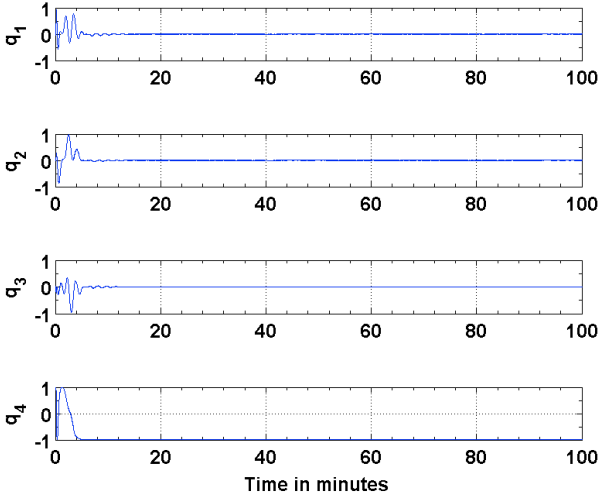
A Attitude Sensors Sampled @ 1 Hz



B Attitude Sensors Sampled @ 3 Hz



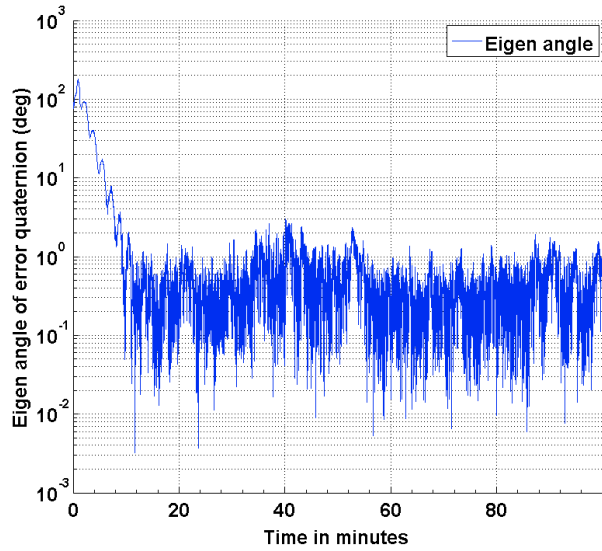
C Attitude Sensors Sampled @ 6 Hz



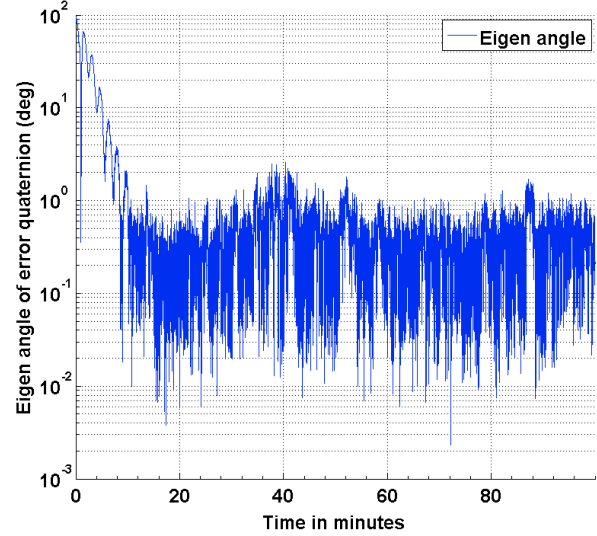
D Attitude Sensors Sampled @ 12 Hz

Figure 6-8. Error in Attitude Quaternion

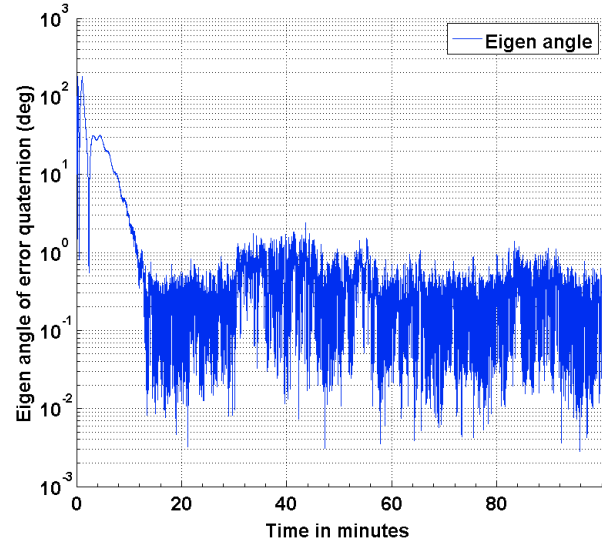
and Fig. 6-6 that the EKF in this sensor configuration takes longer time to converge to a steady state. The attitude estimate though, has better accuracies compared to those in the previous configuration, particularly with decrease in the sampling rate of the attitude sensors. Since a quaternion and its negative represent the same attitude [114] the convergence of the scalar component of the quaternion  $q_4 = \cos \theta/2$  to a value of 1 or  $-1$  imply the same result.



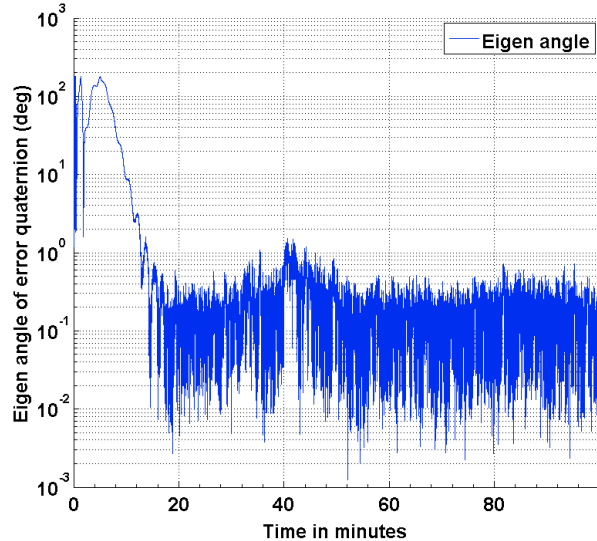
A Attitude Sensors Sampled @ 1 Hz



B Attitude Sensors Sampled @ 3 Hz



C Attitude Sensors Sampled @ 6 Hz

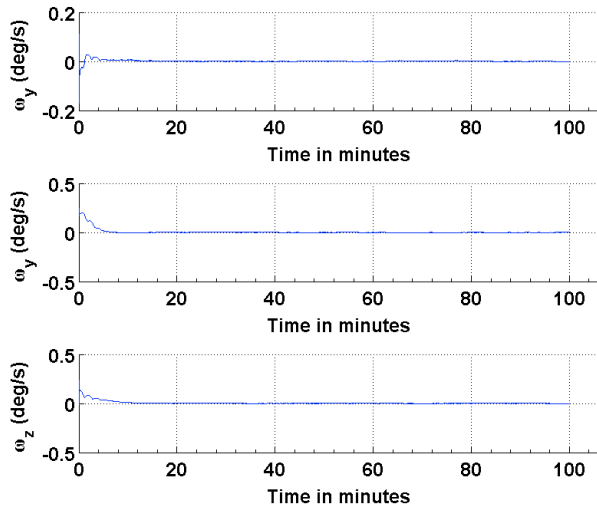


D Attitude Sensors Sampled @ 12 Hz

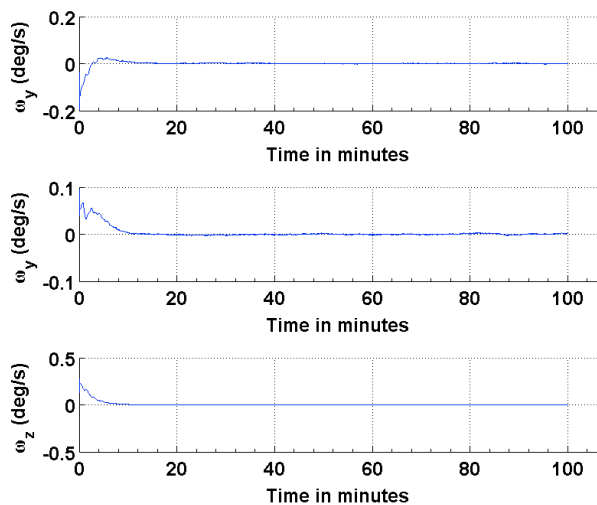
Figure 6-9. Estimation Error - Eigen Angle of Error Quaternion

Table 6-5. Simulation Parameters for Estimation Using Magnetic Field Vector

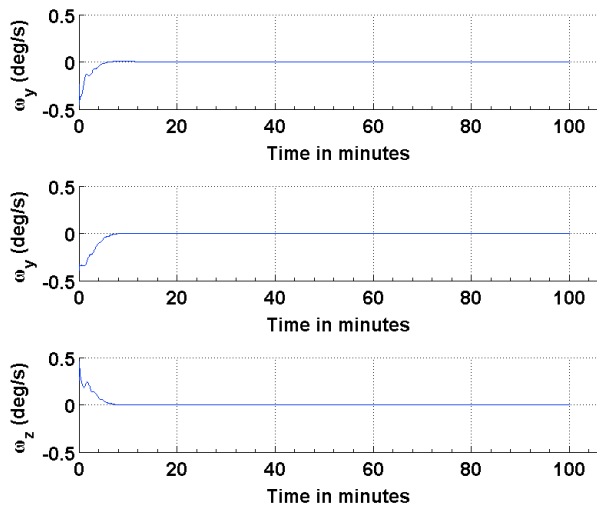
Parameter/Variable	Value
$P_k^-$	$[0.03142^2, 0.03142^2, 0.03142^2, 0.0311^2, 0.0303^2, 0.0272^2]$
$\hat{\beta}_k^-$	$[-0.0724, -0.1927, 0.0205]^T$
$\sigma$	175
$[\sigma_U \sigma_V]$	$[0.001 \times \pi/180, 1 \times \pi/180/3600]$



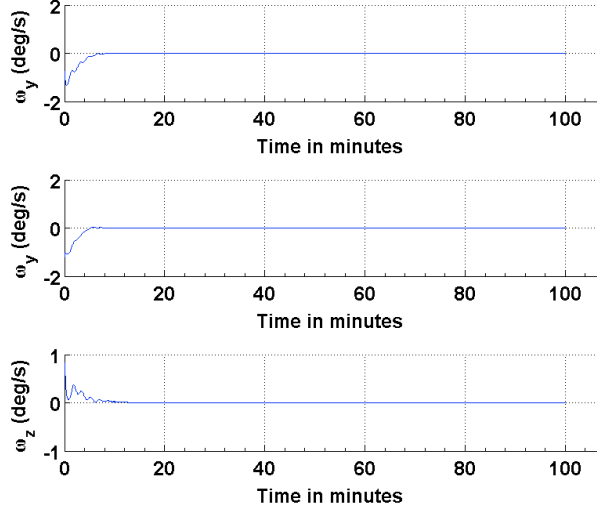
A Attitude Sensors Sampled @ 1 Hz



B Attitude Sensors Sampled @ 3 Hz



C Attitude Sensors Sampled @ 6 Hz

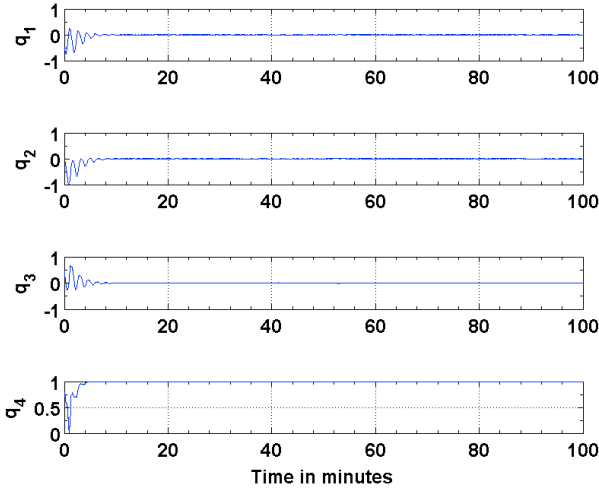


D Attitude Sensors Sampled @ 12 Hz

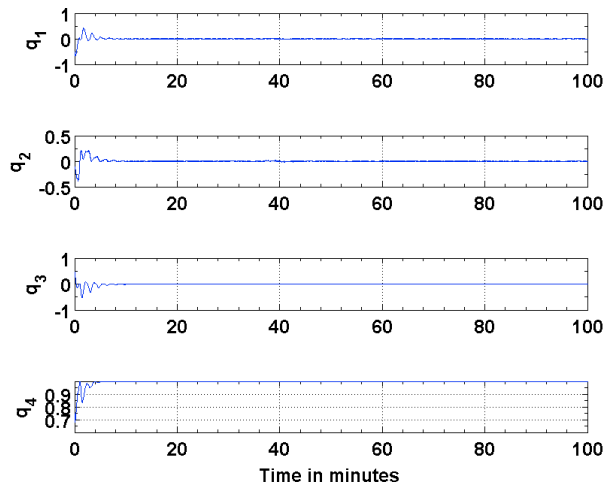
Figure 6-10. Error in Estimated and True Angular Rates

### 6.5.3 Estimation Results Using Magnetic Field Vector and its Time Derivative

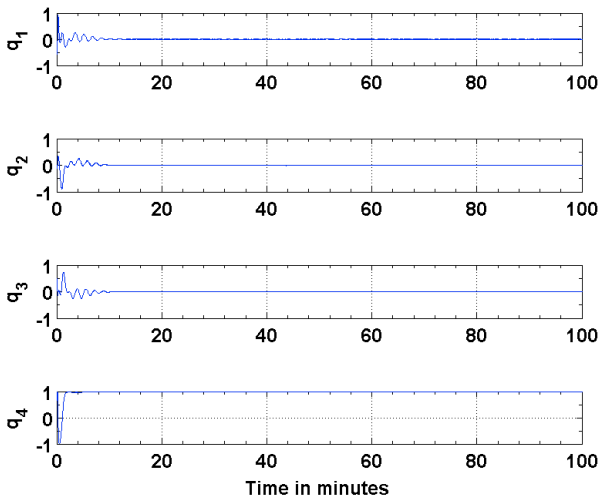
Attitude estimation using the magnetic field vector and its first time derivative was first proposed by Natanson et al. in 1991 [121]. It was observed that the Earth's magnetic field was constantly changing and could be used as a vector for computing the attitude of satellites particularly those in low earth orbits. To evaluate the performance of this configuration, simulations are performed and the results are compared to the above two configurations. The results of the attitude estimation are shown in Fig. 6-12,



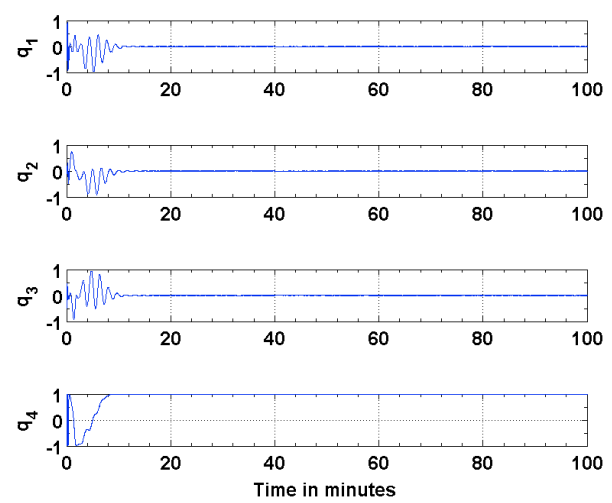
A Attitude Sensors Sampled @ 1 Hz



B Attitude Sensors Sampled @ 3 Hz



C Attitude Sensors Sampled @ 6 Hz



D Attitude Sensors Sampled @ 12 Hz

Figure 6-11. Error in Attitude Quaternion

Fig. 6-13 and Fig. 6-14. It can be seen from the plots that the EKF outperforms for the previous two configurations than this one. Poor performance of the EKF for this particular configuration can be attributed to the influence of nonlinearity of the magnetic field vector on its time derivation. Additionally the attitude determination part of the algorithm uses spacecraft angular velocity acquired from the on board gyros to compute its derivative vector. Although filtered gyro measurements are used to compute the derivative vector, the residual noise and bias influence vector calculation and the a priori

attitude estimate. The attitude accuracy achieved using the magnetic field vector and its time derivate approach is on the same order as that achieved using the other two methods.

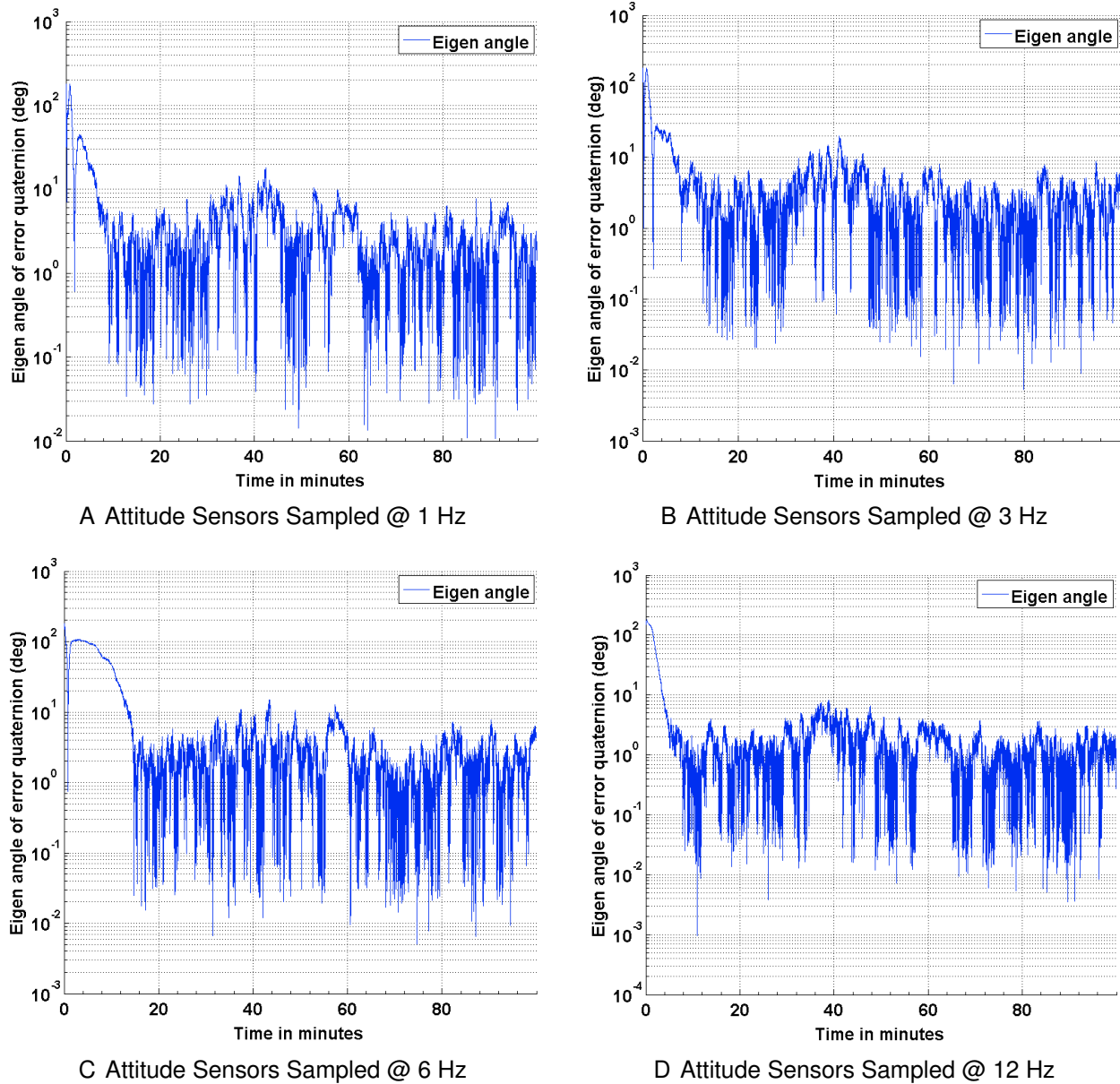
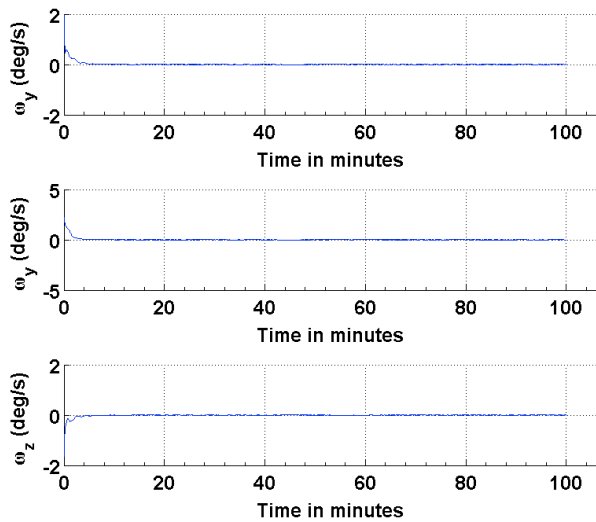


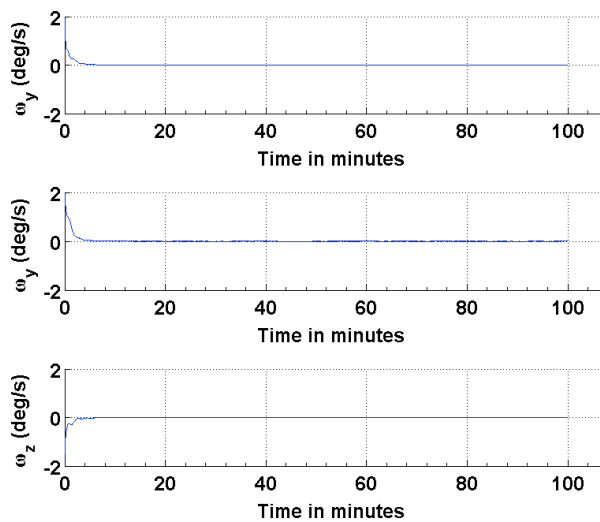
Figure 6-12. Estimation Error - Eigen Angle of Error Quaternion

Table 6-6. Simulation Parameters for Estimation Using Magnetic Field Vector and its Derivative

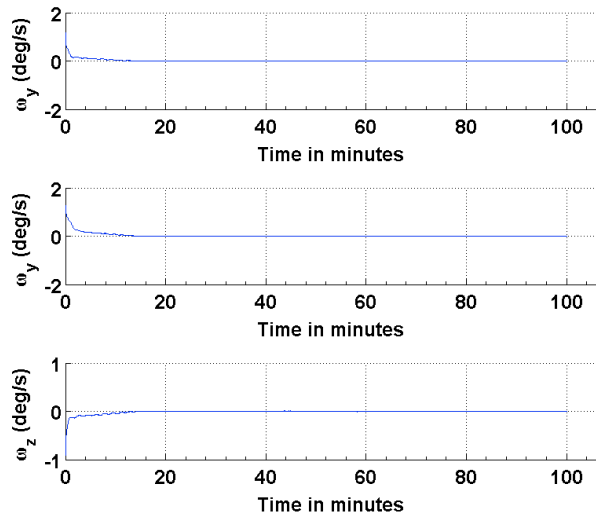
Parameter/Variable	Value
$P_k^-$	$[0.003491^2, 0.003491^2, 0.003491^2, 0.0311^2, 0.0303^2, 0.0272^2]$
$\hat{\beta}_k^-$	$[-0.85, -1.1205, 0.7205]^T$
$[\sigma_1, \sigma_2]$	$[200, 2000]$
$[\sigma_U \sigma_V]$	$[0.001 \times \pi/180, 1 \times \pi/180/3600]$



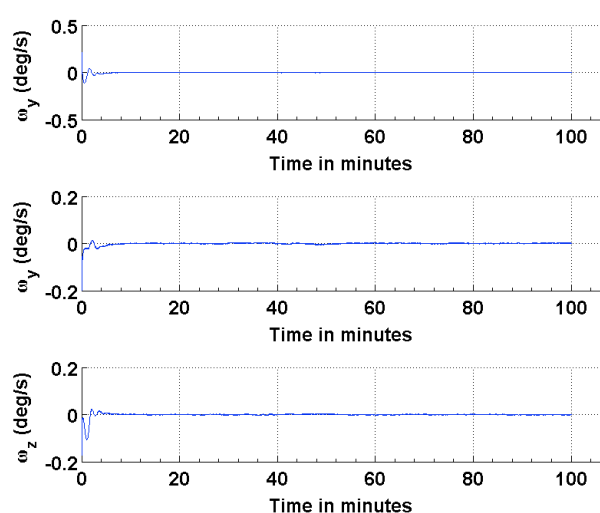
A Attitude @ 1 Hz



B Attitude Sensors Sampled @ 3 Hz

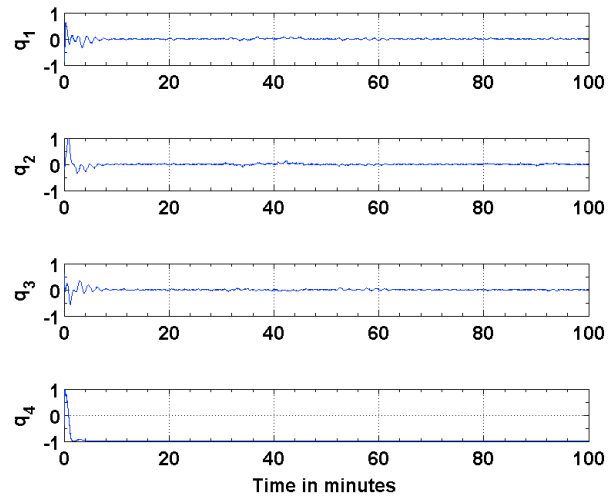


C Attitude Sensors Sampled @ 6 Hz

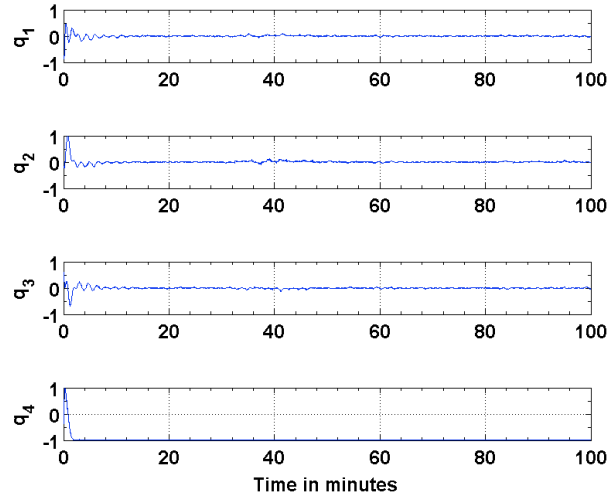


D Attitude Sensors Sampled @ 12 Hz

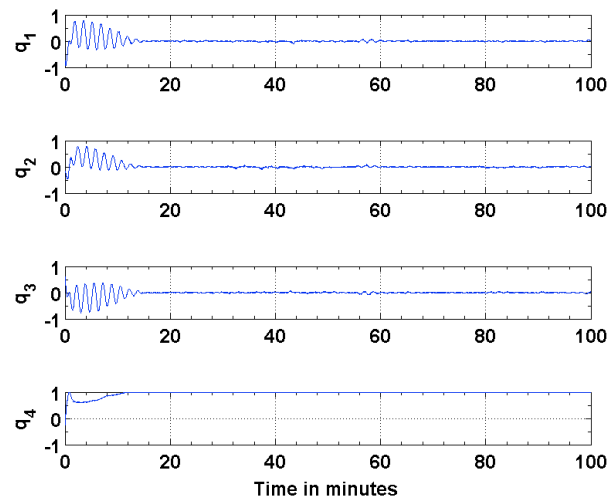
Figure 6-13. Error in Estimated and True Angular Rates



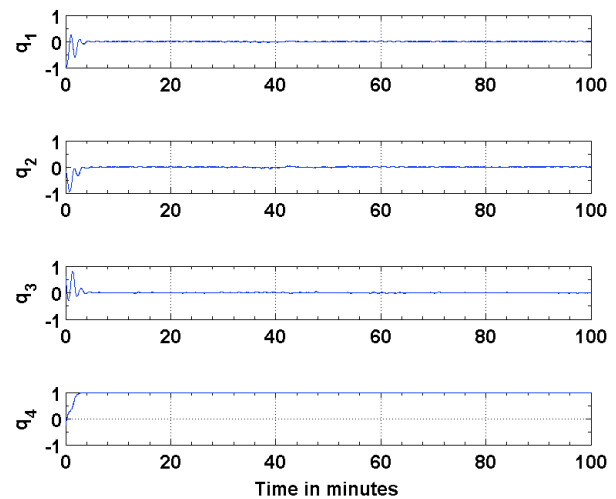
A Attitude Sensors Sampled @ 1 Hz



B Attitude Sensors Sampled @ 3 Hz



C Attitude Sensors Sampled @ 6 Hz



D Attitude Sensors Sampled @ 12 Hz

Figure 6-14. Error in Attitude Quaternion

An algorithm adapted for estimating the attitude of a picosatellite with a distributed computing platform is discussed. The distributed platform addresses the computational limitation and an approach for utilizing the on board power resources effectively. The adaptation presents a design for implementing an attitude determination and estimation system for pico- and nano-class CubeSats. Murrell's EKF is selected over conventional EKF to improve on the computational efficiency [88, 124] and accommodate various sensor configurations. QUEST and the suboptimal estimator are used as initial attitude estimates for faster convergence with the true attitude. The simulation results shown in Fig. 6-5, Fig. 6-6, Fig. 6-9 and Fig. 6-12 justify the need and effectiveness of attitude estimation for a picosatellite hosting the type of sensors discussed above. The EKF performance for the three sensor configurations is presented in Table 6-7.

Table 6-7. EKF Performance Comparison for Three Sensor Configurations

	<b>Magnetometer and Sun Sensors</b>	<b>One Magnetic Field Vector</b>	<b>Two Magnetic Field Vectors</b>
Attitude accuracy (@ 12 Hz)	< 1.5°	< 1.5°	< 8°
Attitude accuracy (@ 1 Hz)	< 5°	< 3°	20°
Converging Time (minutes)	5	10	8
Computational iterations (Eq. (6-8) - Eq. (6-12))	Two	One	Two
Eclipse time estimation	Not possible	Possible	Possible
Sensor power consumption (mW)	360	285	300

For a pico-class CubeSat hosting the type of attitude sensor discussed above, magnetometer based attitude estimation is better suited than the other two approaches. Except for the convergence time, the approach is shown to have a relatively better performance in terms of computational resources, power consumption and overall attitude accuracy. As the sampling frequency of the attitude sensors is reduced the degradation in attitude accuracy is lesser for magnetometer based attitude estimation than the other two approaches. The operating modes accommodate a provision for the time required for convergence of the attitude estimate. Magnetometer based

attitude estimation can be performed during eclipse time which can be utilized for EKF convergence.

A pico- or a nano-class CubeSat hosted with both these type of sensors can be operationally designed to utilize a particular sensor configuration based on a ground command. A level of redundancy can be built into a CubeSat by exploiting the use of different sensor configurations. To account for a possible failure or uncertainties associated with a sensor type, the attitude estimation algorithm, implemented in Murrell's form, can be operationally commanded to use the best suited sensor configuration.

## CHAPTER 7

### CONCLUSION AND FUTURE WORK

#### 7.1 Conclusion

Small satellites, particularly the pico- and nano-class CubeSats, are being recognized for their utility and as potential candidates for addressing the challenges of an operationally responsive space. While the ORS office seeks a new business model for meeting U.S. space capabilities, NASA's Franklin and Edison program intend to mature technologies relevant for small satellites and support missions to prove these technologies. To address the challenges of the ORS office and NASA's Franklin and Edison programs it is critical to standardize satellite systems and reduce the uniqueness of each satellite design. The pico- and nano-class CubeSats could be capable of addressing these challenges but contrary to the design and development of traditional satellites, CubeSat designs have mostly been ad hoc. As recognized by ORS, the approach adopted by traditional satellites cannot be directly applied for the design and development of these CubeSats. To address this issue, a pico- and nano-class CubeSat systems engineering approach, partially based on the guidelines of NASA's Systems Engineering Handbook, is described and presented in the context of SwampSat mission.

CubeSat designs have accommodated the use of COTS based subsystems, components and sensors available for autonomous air, ground and under water systems. Lesson learned from the evaluation of subsystems integration, components, sensors and model based diagnosis on a terrestrial ground robot have facilitated understanding of their operation in the context of CubeSats. The design and development of the terrestrial ground robot has most importantly identified the need for a system engineering basis for designing pico- and nano-class CubeSats. A system engineering approach is developed as a design methodology for pico- and nano-class CubeSats. SwampSat is used as a candidate mission for describing and verifying the approach. The requirements flowdown is used to translate mission definition to satellite building

blocks. To facilitate the estimation of mission overhead in terms of power, telemetry and computation a cost is associated with these building blocks. Mission mapping through N2 diagrams and mission CONOPS is described using the SwampSat mission as a test case. The approach is elaborated by describing the detail design of SwampSat subsystems.

The electrical power system is designed and developed around COTS based components. The process of integrating COTS based components in the design and development of CubeSats is described. The significance of one or more custom designed components for accommodating COTS based development is described through the design and development of multifunctional solar panels. The importance of formulating an overall power budget for determining the power requirements of a CubeSat mission and duty cycling of components and subsystems through the formulation of operating mode power budget is described. The systems approach also identifies unit level testing as a part of the COTS based design and development. The CubeSat form factor limits the surface area available for mounting solar cells and as a consequence the power generation capability. To address the limitation of power generation associated with particularly the pico-class CubeSats, the on board computing may be designed as a distributed system. The well designed mission CONOPS is important for addressing distributed operation design and the limited power generation capability. The design of command and data handling software to address the distributed computing architecture and the limited power generation capability is described. The CDH software is designed as operating modes from the building blocks derived through the mission mapping process. A downlink telemetry and an uplink command are formulated within the limitations of the AX.25 protocol for mission validation and tuning on board the satellite operations. The process of estimating the mission cost in terms of power, telemetry and computation through the cost elements associated with the building blocks is briefly described. The distribute

computing platform within a CubeSat system can impact the design of a subsystem and distribute its components. The distributed design of an attitude determination and estimation system is described in this context. An attitude estimation algorithm is adapted to address the needs of a distributed system and accommodate three sensor configurations. The attitude estimation algorithm is evaluated for these sensor configurations and their performances compared. The utility of the algorithm to accommodate redundancies in the form of sensor configuration and address failure of a sensor type is briefly described.

## 7.2 Future Work

An approach for the design and development of pico- and nano-class CubeSats is presented and verified through SwampSat. As part of future work there is scope for optimizing the design approach and validate and validate SwampSat on orbit. The following areas are identified as part of the future work:

- EPS design and development
  - Design and develop an EPS board which can be customized to support 1U, 2U and 3U CubeSat missions
  - Characterize solar cell mounting techniques including soldering and epoxy mounting
  - Design battery boards for 1U, 2U and 3U CubeSat missions
- Command, data and telemetry handling design and development
  - Validate on orbit the command, data and telemetry handling design
  - Evaluate current design against an event based alternative
  - Evaluate on orbit the uplink and downlink budgets
- Attitude estimation design and development
  - Characterize the magnetic field due to CMGs, its effect on the flight magnetometer and the performance of the attitude estimation algorithm
  - Incorporate a model to address the ill effects of the magnetic field due to CMGs

Apart from the items listed above the work also leads into performing a failure mode impact analysis of a CubeSat system. Research in these areas is the focus of ongoing post graduate study.

APPENDIX: TESTS TO QUALIFY ELECTRICAL POWER SYSTEM

# SWAMP*SAT*

## SWAMPSAT TEST REPORT

Space Systems Group,

Advanced Space Technologies Research and Engineering Center

University of Florida  
Gainesville

---

**Test name:** Electrical Power System Characterization and Functionality

**Description of item under test:** SwampSat Electrical Power System Board

**Subsystem:** Electrical Power System

**Document # –** 08/A1/TD/04/04

**Document revision –** 1

Document Control			
	Name	Date	Signature
Prepared	<i>Sharan Asundi</i>	12/31/08	<i>Sharan Asundi</i>
Reviewed	<i>Shawn Allgeier</i>	01/21/09	<i>Shawn Allgeier</i>
Approved	<i>Norman Fitz-Coy</i>		

**Test Serial # -** 1

**Test date –** 12/30/2008

**Location –** SwampSat Avionics Room, NEB185A

<b>Test:</b> EPS characterization	<b>Test serial no:</b> 1	<b>Part /Assembly #</b>
<b>Date:</b> 12/30/08	<b>Doc. #:</b> <u>08/A1/TD/04/04</u>	<b>Part/Assy type:</b> Prototype/Flight

Document classification	
Uncontrolled	
Internal only	X
Classified	

This document has 6 main pages and 0 pages in attachment.



<b>Test:</b> EPS characterization	<b>Test serial no:</b> 1	<b>Part /Assembly #</b>
<b>Date:</b> 12/30/08	<b>Doc. #:</b> <u>08/A1/TD/04/04</u>	<b>Part/Assy type:</b> Prototype/Flight

### **Objective:**

Characterize and test SwampSat Electrical Power System Functionality. Specifically test the ability of the EPS to regulate power on the 5V, 3.3V and battery buses with and without an external power source charging the battery pack.

### **Material Required:**

1. EPS mounted with battery board
2. Multi-meter, Alligator clips
3. Gloves, anti-static mat & anti-static strap
4. CubeSat kit development board with a USB cable

### **Special Instructions**

1. The EPS board and the battery mounted on top of it should be handled with care using gloves. The EPS board should be placed on ESD mat and straps should be used while handling the electronics.
2. Special care should be taken to activate the pull pin and the separation switch only when the EPS is being tested. When storing the pins should be deactivated and battery should be charged to a voltage between 6.4V to 7.5V.
3. The EPS should NEVER be left with the pull pin and the separation switch activated (Refer to the “TEST SET-UP” section on page 15 of the Clyde Space 1U CubeSat Power System User Manual for information on activating the pull pin and separation switch). This can drain off the batteries and make them unusable.

### **Procedure**

1. Put on the gloves and strap yourself so that the static charges on the body are grounded. Place the CubeSat kit dev board, EPS board and the other electronics on the ESD mat. Setup shown in Figure 1.
2. If the battery board is already interfaced with the EPS board unmount the battery board and measure the voltage across the screw holes on the edge opposite the battery connector as shown in figure 2.
3. Mechanically mount the batteries over the studs provided on the EPS board and electrically interface the EPS board through the connector.
4. Activate the pull pin (short H2.33-34 to H2.41-44) and the separation switch (short H2.35-36 to H2.41-44) by following the instructions in the Clyde Space user manual for the 1U EPS (Refer to the “TEST SET-UP” section on page 15 of the Clyde Space 1U CubeSat Power System User Manual for information on activating the pull pin and separation switch).
5. Using a voltmeter/multimeter, measure the voltage across the studs (shown in figure 3) closest to the cubesat kit header/connector (bus).



<b>Test:</b> EPS characterization	<b>Test serial no:</b> 1	<b>Part /Assembly #</b>
<b>Date:</b> 12/30/08	<b>Doc. #:</b> <u>08/A1/TD/04/04</u>	<b>Part/Assy type:</b> Prototype/Flight

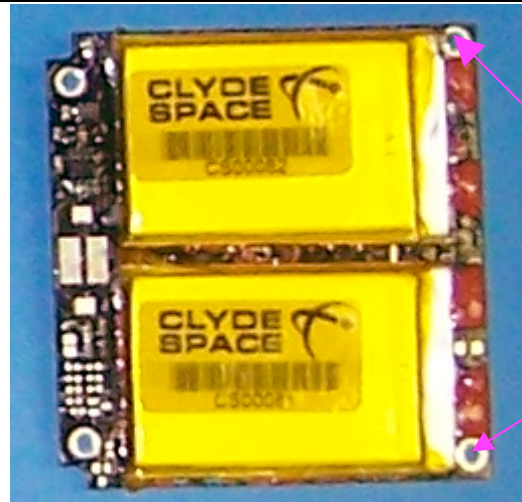


**Figure 1 - Battery board**

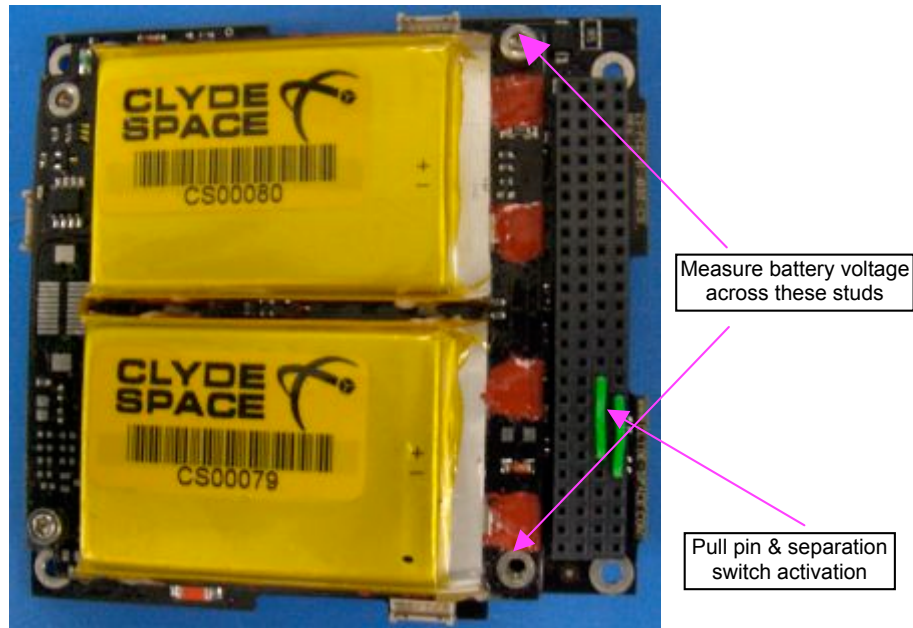


**Figure 2 - EPS with separation switch and pull pin activated**

6. Using a voltmeter/multimeter, measure the voltage across pins H2.26 (5V) & H2.30 (GND) and the voltage across H2.28 (3.3V) & H2.30 (GND).
7. Note the multimeter readings in the results section of this document.
8. Deactivate the separation switch and pull pin by following the instructions in the Clyde Space user manual.
9. Connect the battery mounted EPS board on the CubeSat kit dev board through the CubeSat kit connector (**DO NOT POWER** the dev board before the pull pin and separation switch are activated. This can damage the battery charge regulators).
10. Activate the separation switch and pull pin by following the instructions in the Clyde Space user manual for the 1U EPS (pg. 11 & 15).



<b>Test:</b> EPS characterization	<b>Test serial no:</b> 1	<b>Part /Assembly #</b>
<b>Date:</b> 12/30/08	<b>Doc. #:</b> 08/A1/TD/04/04	<b>Part/Assy type:</b> Prototype/Flight

11. Repeat the steps 4 & 5 and note down the multimeter readings in the results section of this document.
12. Power the CubeSat kit development board through USB.
13. Repeat steps 4 & 5 and note down the multimeter readings in the results section of this document

### Test Setup

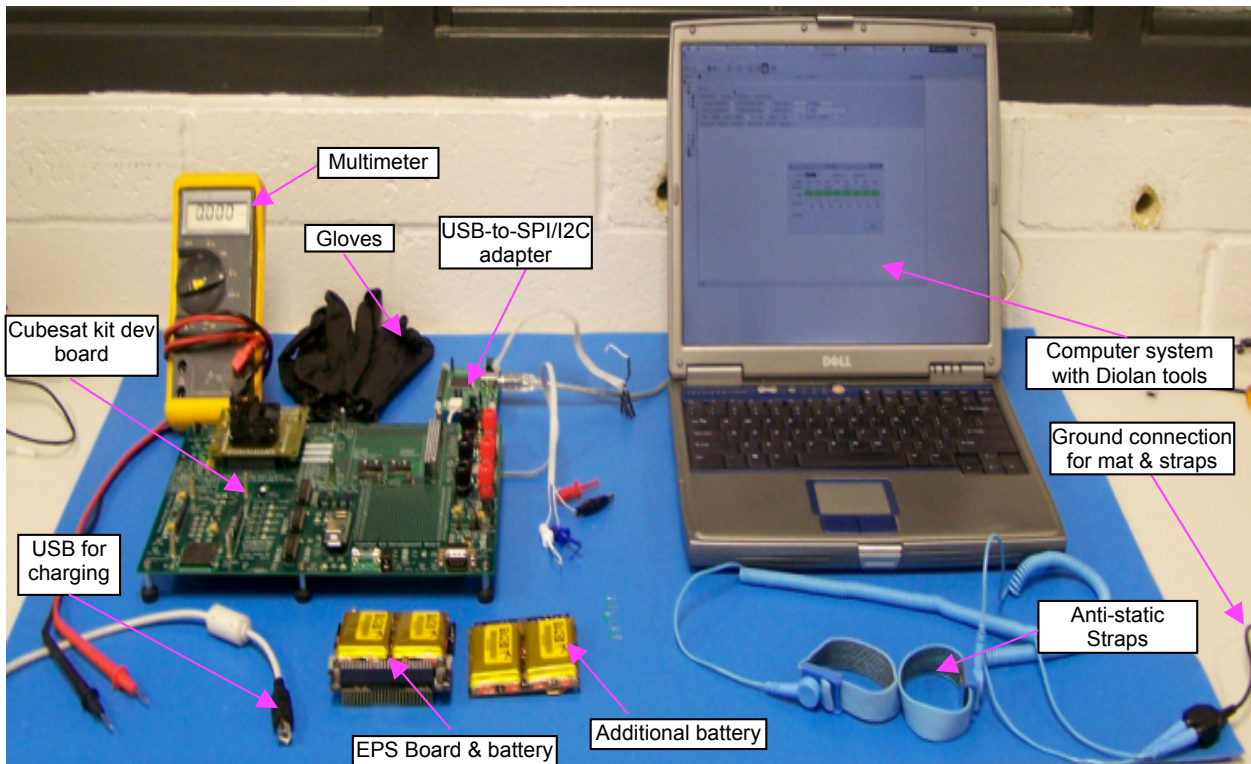


**Figure 3 - Setup for Testing EPS Functionality**

### Test Results

Voltage measure across the screw holes after step 2 = 0.68V

Voltage measured after step 5

- across the studs = 0.68V
- across pins H2.26 & H2.30 = 0.0V
- across pins H2.28 & H2.30 = 0.0V

Voltage measured across the studs after step 10 = 0.68V

- across the studs = 0.68V
- across pins H2.26 & H2.30 = 0.0V
- across pins H2.28 & H2.30 = 0.0V

Voltage measured after step 12



<b>Test:</b> EPS characterization	<b>Test serial no:</b> 1	<b>Part /Assembly #</b>
<b>Date:</b> 12/30/08	<b>Doc. #:</b> <u>08/A1/TD/04/04</u>	<b>Part/Assy type:</b> Prototype/Flight

- across the studs = 8.24V
- across pins H2.26 & H2.30 = 4.9V

across pins H2.28 & H2.30 = 3.3V

#### Test Personnel:

1. Sharan Asundi
- 

#### Conclusion

Specifically two battery packs have been tested at 3 stages.

- i. As standalone daughter boards without mounting them on the EPS board
- ii. Interfacing with the EPS board through the connector and activating the separation switch and pull pin
- iii. Interfacing the EPS with the CubeSat kit dev board and activating the separation switch and pull pin

The expected voltage across the battery bus when the separation switch and the pull pin are activated or the screw holes in any of the 3 stages is between 6.1V and 8.26V depending on the state of the charge. The actual voltage measured across the battery bus or the screw holes (studs) of the EPS is around 0.68V. The actual voltage measured across the 5V and 3.3V bus is 0V. Only when the CubeSat kit is USB powered the actual battery, 5V or the 3.3V bus matches the expected voltage.

The experiment leads to the conclusion that the batteries have been discharged below the critical limit of 6.1V and cannot be used to store electric charge anymore.



# SWAMP SAT

## SWAMPSAT TEST REPORT

Space Systems Group,

Advanced Space Technologies Research and Engineering Center

University of Florida  
Gainesville

**Test name:** Communicating with EPS Through I<sup>2</sup>C

**Description of item under test:** Electrical Power System Board and Battery

**Subsystem:** Electrical Power System

**Document # –** 08/A1/TD/04/02

**Document revision –** Rev.1

Document Control			
	Name	Date	Signature
Prepared	<i>Sharan Asundi</i>	12/17/08	<i>Sharan Asundi</i>
Reviewed	<i>Shawn Allgeier</i>	01/21/09	<i>Shawn Allgeier</i>
Approved	<i>Norman Fitz-Coy</i>		

**Test Serial # -** 1

**Test date –** 12/16/2008  
**Location –** SSG Avionics Room, NEB185A

Document classification	
Uncontrolled	
Internal only	X

<b>Test:</b> Communicating with EPS through I <sup>2</sup> C	<b>Test serial no:</b> 1	<b>Part /Assembly #</b>
<b>Date:</b> 12/16/08	<b>Doc. #:</b> <u>08/A1/TD/04/02</u>	<b>Part/Assy type:</b> Prototype/Flight

Classified	
------------	--

This document has 6 main pages and 0 pages in attachment.



<b>Test:</b> Communicating with EPS through I <sup>2</sup> C	<b>Test serial no:</b> 1	<b>Part /Assembly #</b>
<b>Date:</b> 12/16/08	<b>Doc. #:</b> <u>08/A1/TD/04/02</u>	<b>Part/Assy type:</b> Prototype/Flight

### Objective:

To read health related data, battery voltage, current & temperature, on the EPS board through I<sup>2</sup>C using the U2C-12 USB-I<sup>2</sup>C/SPI/GPIO Interface Adapter Board (USB-I<sup>2</sup>C/SPI adapter) from Diolan (<http://www.diolan.com/i2c/u2c12.html>).

### Material Required:

1. EPS board mounted with the battery
2. USB-to-I<sup>2</sup>C/SPI adapter with a I<sup>2</sup>C cable and a USB cable for interfacing a computer system
3. Multi-meter, Alligator clips
4. A computer with diolan tools installed
5. CubeSat kit development board with a USB cable

### Special Instructions

1. The EPS board and the battery mounted atop the EPS should be handled with extreme care using gloves. The EPS board should be placed on ESD mat and straps should be used while handling the electronics.
2. Special care should be taken to activate the pull pin and the separation switch only when the EPS is being tested. When storing the pins should be deactivated and battery should be charged to a voltage between 6.4V to 7.5V.
3. The EPS should NEVER be left with the pull pin and the separation switch activated (Refer to the “TEST SET-UP” section on page 15 of the Clyde Space 1U CubeSat Power System User Manual for information on activating the pull pin and separation switch). This can drain off the batteries and make them unusable.

### Procedure

1. Put on the gloves and strap yourself so that the static charges on the body are grounded. Place the CubeSat kit dev, EPS board and the other electronics on the ESD mat. Setup shown in Figure 3.
2. Connect the battery mounted EPS board on the dev board through the CubeSat kit connector (**DO NOT POWER** the dev board before the pull pin and separation switch are activated. This can damage the battery charge regulators)
3. Activate the pull pin (short H2.33-34 to H2.41-44) and the separation switch (short H2.35-36 to H2.41-44) by following the instructions in the Clyde Space user manual for the 1U EPS (Refer to the “TEST SET-UP” section on page 15 of the Clyde Space 1U CubeSat Power System User Manual for information on activating the pull pin and separation switch).
4. Power the CubeSat kit development board through USB.
5. Connect the I<sup>2</sup>C\_ON pin, shown in Figure 1, on the CubeSat kit connector/header, H1.24 to one of the GPIO pins, shown in figure 3, on the USB-I<sup>2</sup>C/SPI adapter.
6. Similarly connect the I<sup>2</sup>C bus (H1.41 & H1.42), shown in Figure 1, on the EPS to the I<sup>2</sup>C bus, shown in Figure 2, on the USB-to-I<sup>2</sup>C/SPI adapter.



<b>Test:</b> Communicating with EPS through I <sup>2</sup> C	<b>Test serial no:</b> 1	<b>Part /Assembly #</b>
<b>Date:</b> 12/16/08	<b>Doc. #:</b> 08/A1/TD/04/02	<b>Part/Assy type:</b> Prototype/Flight

7. Following the message formats specified in the EPS user manual (figure 5.1, pg 20) and using the libraries provided by diolan write programs to communicate with the EPS. (Refer the Programmers Reference Manual for USB-I2C/SPI/GPIO Interface Adapter available at [http://www.diolan.com/i2c/doc/u2c\\_12\\_manual.0.1.5.pdf](http://www.diolan.com/i2c/doc/u2c_12_manual.0.1.5.pdf) for information on libraries).



Figure 1 - EPS Connector Positions on the CubeSat Bus

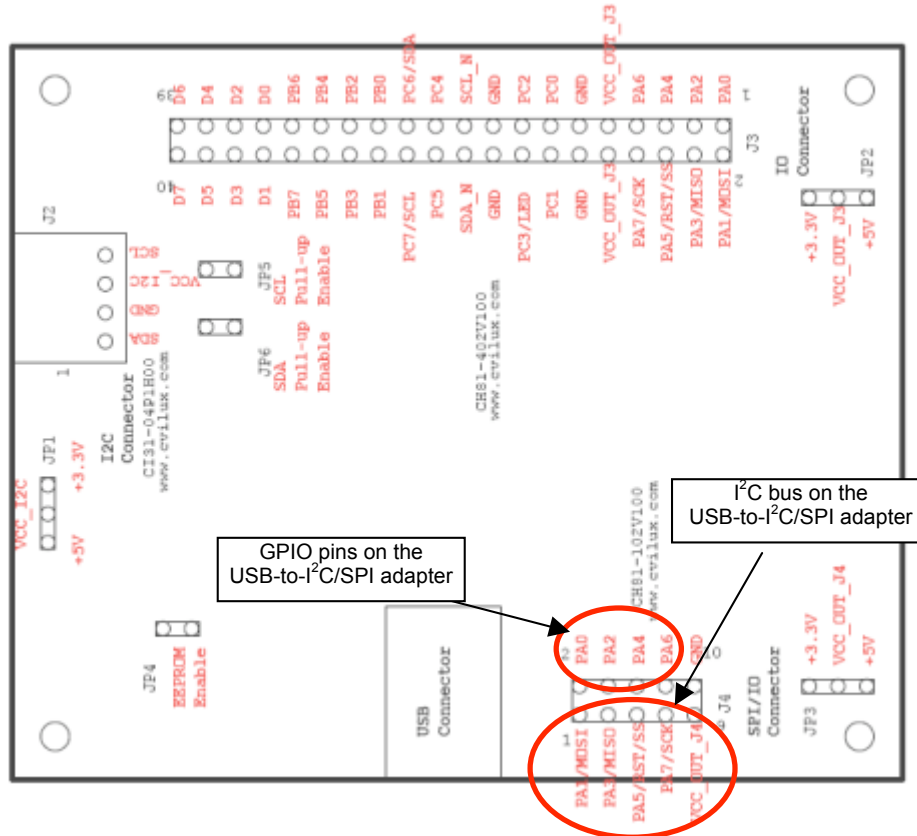


Figure 2 - USB-to-I2C/SPI Adapter Schematics

8. Read the various analog to digital channels and follow the calibration formulas given in the EPS user manual to verify the readings. Use a procedure similar to the one described below.
9. To read an ADC channel, send the following commands via I2C:
- Initiate a start condition with "U2C\_Start (myEPS);", where myEPS is a handle to the device.
  - Initiate a write of the slave address with "U2C\_PutByteWithAck(myEPS,0x02);"
    - 0x01 is the 7-bit slave address of the EPS board
    - The least-significant bit is for read & write (R/~W)



<b>Test:</b> Communicating with EPS through I <sup>2</sup> C	<b>Test serial no:</b> 1	<b>Part /Assembly #</b>
<b>Date:</b> 12/16/08	<b>Doc. #:</b> <u>08/A1/TD/04/02</u>	<b>Part/Assy type:</b> Prototype/Flight

- In this case, this is a write instruction so bit 0 is 0.
- III. Initiate a write of the command address with "U2C\_PutByteWithAck(myEPS,command);"
    - 0x00 is the command for the ADC
  - IV. Initiate a write of the command data with "U2C\_PutByteWithAck(myEPS,channel);"
    - 0x17 (23 in decimal) is the 23rd channel corresponding to the battery temperature
  - V. Pause for 1-2 ms with "Sleep(2);"
  - VI. Initiate a RESTART condition with "U2C\_RepeatedStart(myEPS);"
  - VII. Initiate a read and the slave address with "U2C\_PutByteWithAck(myEPS, 0x03);"
    - 0x01 is the 7-bit slave address of the EPS board
    - The least-significant bit is for read & write (R/~W)
      - In this case, this is a read instruction so bit 0 is 1.
  - VIII. Initiate a read from the EPS board for the 1st byte of data with "U2C\_GetByteWithAck(myEPS,rbyte1,TRUE);"
    - rbyte1 is a pointer to the reply byte from the EPS board
    - TRUE is to send an acknowledgement (ACK) bit after receiving a byte from the EPS board
    - bits 7 - 2 are always 0 since the EPS' ADC is 10-bits
  - IX. Initiate a read from the EPS board for the 2nd byte of data with "U2C\_GetByteWithAck(myEPS,rbyte0,FALSE);"
    - FALSE is to not send an acknowledgement bit after receiving a byte from the EPS board
      - this is required for the EPS board's I2C protocol
  - 10. Initiate a stop condition with "U2C\_Stop(myEPS);" to end the I2C communication



<b>Test:</b> Communicating with EPS through I <sup>2</sup> C	<b>Test serial no:</b> 1	<b>Part /Assembly #</b>
<b>Date:</b> 12/16/08	<b>Doc. #:</b> 08/A1/TD/04/02	<b>Part/Assy type:</b> Prototype/Flight

### Test Setup

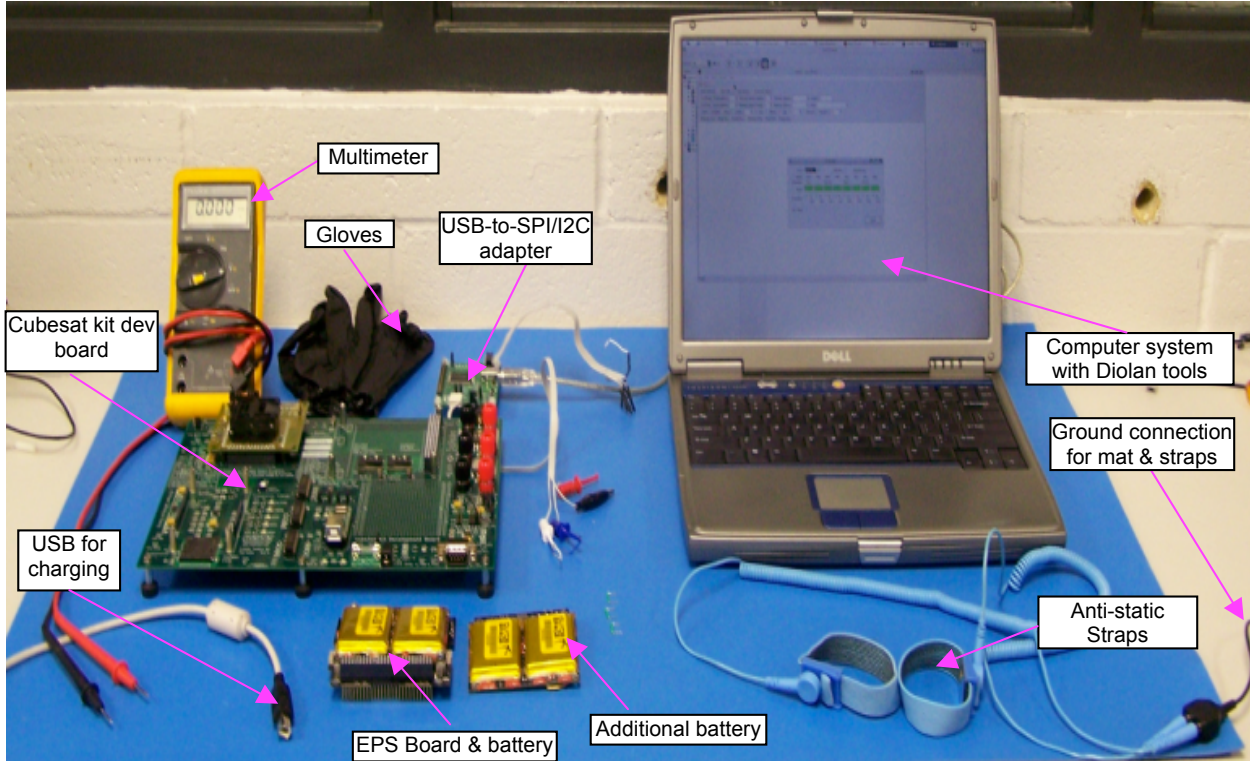


**Figure 3 - Setup for Establishing a I<sup>2</sup>C Communication with SwampSat EPS**

### Test Results

For the Firmware -

- command == 0x04
- rbyte1 = 1
- rbyte0 = 2
- We concluded that the Firmware version is 1.2

For the battery #1 temperature -

- command == 0x00
- channel == 0x17 (23)
- rbyte1 = 2
- rbyte0 = 37
- ADC = 549
- $T=(-0.163 \times \text{ADC})+110.7 = 21.213$  degrees Celsius
- We concluded that the temperature was ~ 70.18 degrees Fahrenheit, which corresponded well to the room temperature



<b>Test:</b> Communicating with EPS through I <sup>2</sup> C	<b>Test serial no:</b> 1	<b>Part /Assembly #</b>
<b>Date:</b> 12/16/08	<b>Doc. #:</b> <u>08/A1/TD/04/02</u>	<b>Part/Assy type:</b> Prototype/Flight

For the battery #2 temperature -

- command == 0x00
- channel == 0x12 (18)
- rbyte1 = 2
- rbyte0 = 36
- ADC = 548
- $T=(-0.163*ADC)+110.7 = 21.376$  degrees Celsius
- We concluded that the temperature was ~ 70.48 degrees Fahrenheit, which corresponded well to the room temperature

For the Battery #1 Voltage -

- command == 0x00
- channel == 0x18 (24)
- rbyte1 = 3
- rbyte0 = 184
- ADC = 907
- $9.75 - 9.52 = 0.23$  V
- Perhaps there is a relay which detaches the battery voltage from the board when USB power is applied
- further research must be done

For the Cell #1 Voltage -

- command == 0x00
- channel == 0x19 (25)
- rbyte1 = 3
- rbyte0 = 139
- ADC = 907
- $9.75 - 9.07 = 0.68$  V
- Perhaps there is a relay which detaches the battery voltage from the board when USB power is applied
- further research must be done

Test Personnel:

1. Sharan Asundi
2. Sal Torre

## Conclusion

The battery voltage value read on the I<sup>2</sup>C bus is not conforming to the expected value. The ADC value read on the I<sup>2</sup>C bus when converted to a voltage value using the formula given in the EPS user manual do not match the expected voltage value. The battery #1 expected voltage is between 6.1V and 8.26V depending on the state of the charge and the voltage value read on the I<sup>2</sup>C bus is around 0.23V.

The experiment leads to the conclusion that the batteries have been discharged below the critical limit of 6.1V and cannot be used to store electric charge anymore.



# SWAMPSAT

## SWAMPSAT TEST REPORT

Space Systems Group

Advanced Space Technologies Research and Engineering Center

University of Florida  
Gainesville

**Test name:** Characterizing SwampSat Transceiver Power Consumption for 9600 and 1200 baud rates

**Description of item under test:** SwampSat Transceiver

**Subsystem:** Telemetry, Tracking and Command  
**Document # –** 10/A1/TD/05/01

**Document revision – Rev #1**

Document Control			
	Name	Date	Signature
Prepared	Sharan Asundi	03/23/2010	<i>Sharan Asundi</i>
Reviewed	Tzu Yu (Jimmy) Lin	03/29/2010	<i>Tzu Yu Lin</i>
Reviewed	Dante Buckley	04/01/2010	<i>Dante Buckley</i>
Reviewed	Vivek Nagabhushan	04/02/2010	<i>Vivek Nagabhushan</i>
Reviewed	Shawn Allgeier	04/04/2010	<i>Shawn Allgeier</i>
Approved	Norman Fitz-Coy	MM/DD/YYYY	

**Test Serial # - 1**

**Test date – 03/24/2010**

**Location – SSG Avionics Lab, NEB 185A, University of Florida**

<b>Test:</b> Characterizing power consumption of transceiver	<b>Test serial no:</b> 01	<b>Part /Assembly #</b>
<b>Date:</b> 03/24/10	<b>Doc. #:</b> 10/A1/TD/05/01	<b>Part/Assy type:</b> Flight

Document classification	
Uncontrolled	
Internal only	X
Classified	

This document has 6 main pages and 0 pages in attachment.



<b>Test:</b> Characterizing power consumption of transceiver	<b>Test serial no:</b> 01	<b>Part /Assembly #</b>
<b>Date:</b> 03/24/10	<b>Doc. #:</b> 10/A1/TD/05/01	<b>Part/Assy type:</b> Flight

### Objective:

The intent of the test is to characterize the power consumed by SwampSat transceiver when transmitting at 9600 and 1200 baud. Specifically the test identifies the voltage drop in the SwampSat battery pack when the transceiver is transmitting at these baud rates. Parameters like telemetry string length, test time and the delay between transmissions are ensured to be the same when transmitting at these baud rates.

### Material Required:

1. SwampSat transceiver and an antenna system for transmission
2. SwampSat EPS with battery boards mounted on top
3. Pumpkin Inc's FM430 or a CubeSat kit development board
4. JTAG for accessing the microcontroller
5. Computer system with a parallel port
6. Hand radio and TNC setup for verifying transmission
7. IAR Embedded workbench for MSP430 and HyperTerminal utility
8. MSP430 embedded code for transmitting telemetry string via SwampSat transceiver
9. Multimeter, gloves, grounded ESD mat, stop watch

### Special Instructions:

1. The SwampSat transceiver, CubeSat kit board and the EPS are required to be handled with gloves and anti-static protection.
2. For powering the system using EPS the separation switch and remove before flight pin are closed. Refer to the EPS manual (Clyde Space Power System User Manual C1-USM-5003-CS-EPS) for making the connection and maintaining caution.

### Procedure:

1. Charge the SwampSat battery pack to ~8V
2. Stack the FM430, EPS and SwampSat transceiver through the CubeSat bus ensuring the system is powered by the EPS – Refer to the EPS manual (C1-USM-5003-CS-EPS) for using the battery board as the power source.
3. Generate a telemetry string of length 160 hexadecimal characters (0-9 & A-F) to emulate SwampSat beacon.
4. Set the baud rate of the SwampSat transceiver to be 9600 baud.
5. Prepare (compile and build) the embedded code to transmit the telemetry string with a delay of 10 seconds between every transmission
6. Download the code to msp430 through the JTAG and record the current time and battery voltage.
7. Execute the transmission for a set period (~ 4 hours) and measure the battery voltage and time elapsed.
8. Repeat steps 1 through 7 by changing the baud rate setting in step 4 to be 1200 and record the battery voltage and elapsed time.



<b>Test:</b> Characterizing power consumption of transceiver	<b>Test serial no:</b> 01	<b>Part /Assembly #</b>
<b>Date:</b> 03/24/10	<b>Doc. #:</b> 10/A1/TD/05/01	<b>Part/Assy type:</b> Flight

## **Test Setup:**

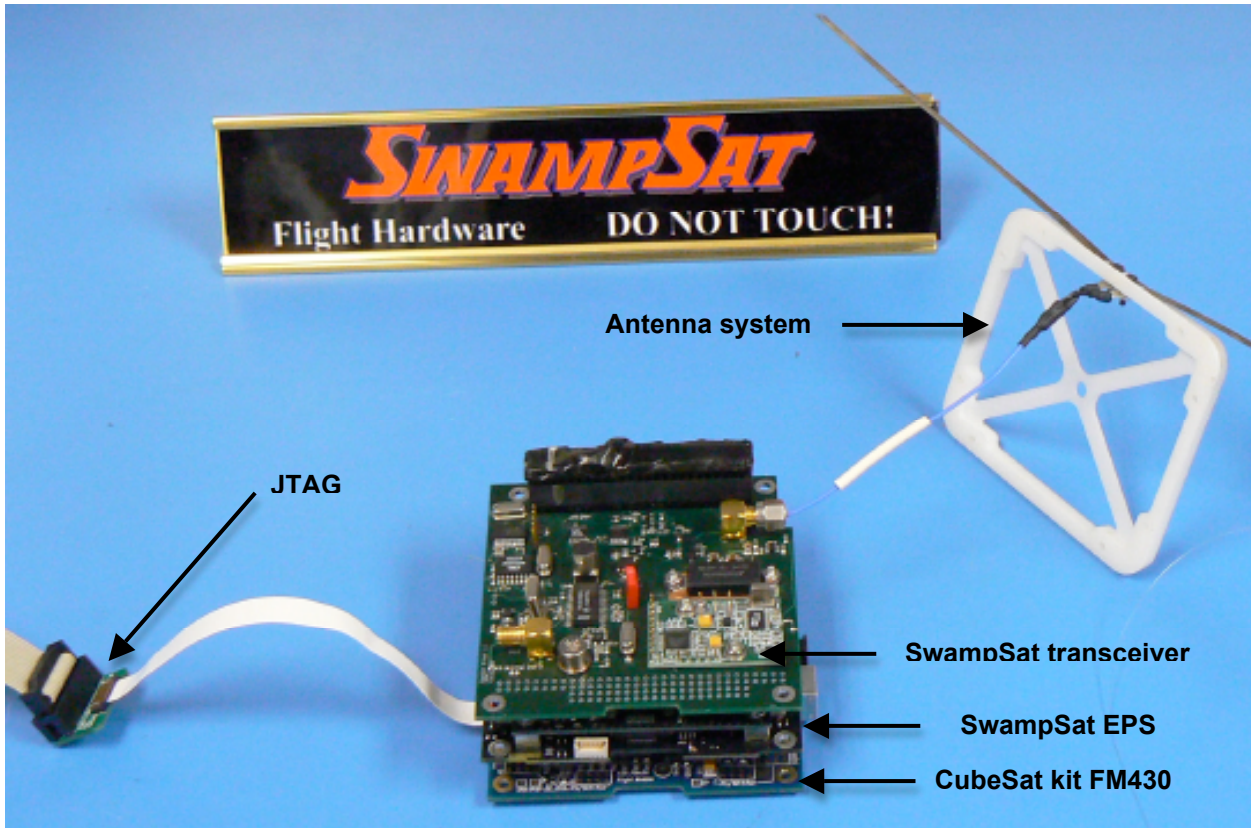


**Figure 1 - Setup for Characterizing Power Consumption of SwampSat Transmissions**

## Test Data:

(i) Data recorded for 9600 baud transmissions

Initial battery voltage – 7.97V

**Test Duration – 4 hours**

Transmission interval - ~10.5 seconds

Final battery voltage – 7.54V

## Transmit data



<b>Test:</b> Characterizing power consumption of transceiver	<b>Test serial no:</b> 01	<b>Part /Assembly #</b>
<b>Date:</b> 03/24/10	<b>Doc. #:</b> 10/A1/TD/05/01	<b>Part/Assy type:</b> Flight

Observations - The transceiver was transmitting for the entire duration. The hand radio used to verify the transmissions confirmed this observation

(ii) Data recorded for 1200 baud transmissions

Initial battery voltage – 7.96V

**Test Duration – 4 hours**

Transmission interval - ~11.5 seconds

Final battery voltage – 7.12V

## Transmit data

**Observations** – The transmissions stopped at least 30 minutes before the end of test duration. During these 30 minutes, the FM430 continued to run the program of transmitting the data but the battery source seemed incapable of supplying the required power for the transmitter. The multimeter indicated an intermittent voltage drop across the EPS battery terminals to

## **Conclusion:**

1. The voltage drop for 1200 baud was higher than that for 9600 baud. The power consumed by the transceiver during its operation can be estimated from the discharge profile shown in Figure 2.
  2. From the discharge profile the power consumed when operating at 1200 baud rate is 3 times more than that consumed when operating at 9600 baud.
  3. At the end of test duration the stack of FM430, SwampSat EPS and the transceiver was observed to be healthier when transmitting at 9600 baud compared to 1200 baud. This conclusion was drawn from the observations made at the end of test duration.
  4. For the duration, the total transmit data for 9600 baud was higher than 1200 baud.
  5. It was concluded that 9600 baud would be the favored baud rate for SwampSat transmissions and the equipment and infrastructure required for the ground station to receive and interpret the transmissions would be researched.



<b>Test:</b> Characterizing power consumption of transceiver	<b>Test serial no:</b> 01	<b>Part /Assembly #</b>
<b>Date:</b> 03/24/10	<b>Doc. #:</b> 10/A1/TD/05/01	<b>Part/Assy type:</b> Flight

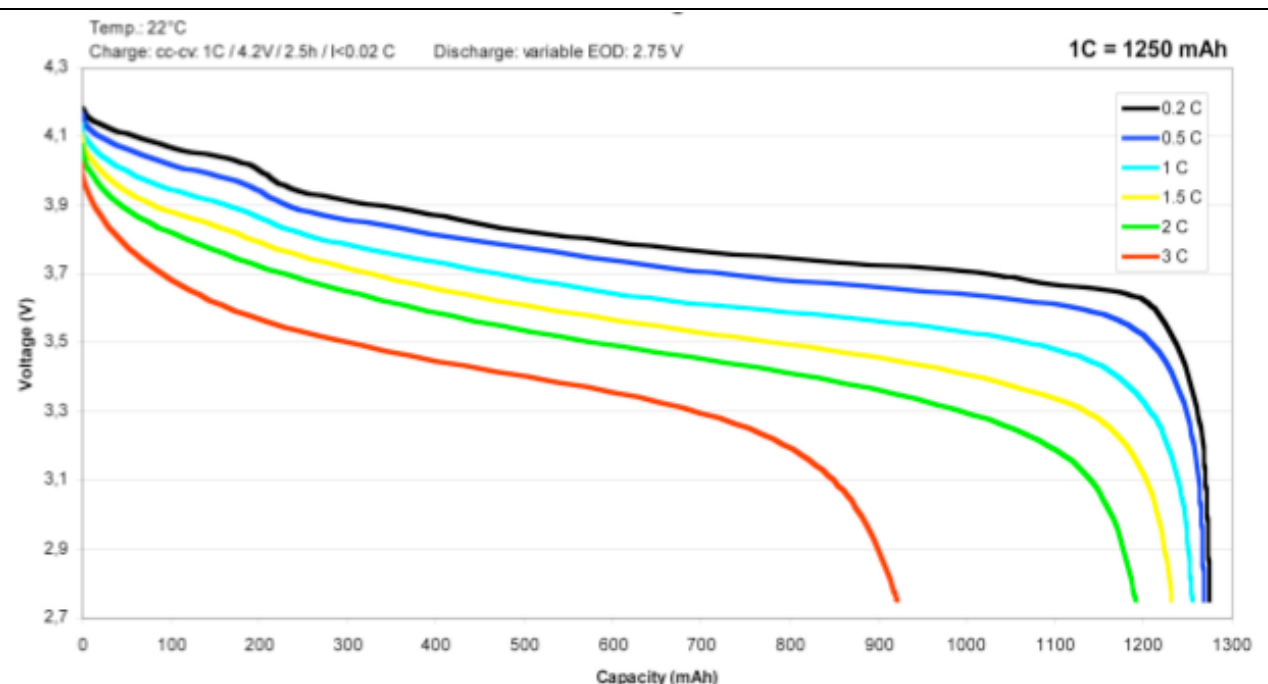


Figure 2 - Discharge Profile for Each Cell in the Battery



# SWAMPSAT

## SWAMPSAT TEST REPORT

Space Systems Group

Advanced Space Technologies Research and Engineering Center

University of Florida  
Gainesville

**Test name:** Outgassing of EPS components

**Description of item under test:** SwampSat EPS board, battery, and cable

**Subsystem:** EPS

**Document # –** 10/A1/TD/04/05

**Document revision – #** 1

Document Control			
	Name	Date	Signature
Prepared	Shawn Allgeier	02/19/2010	Shawn Allgeier
Reviewed	Sharan Asundi	02/28/2010	Sharan Asundi
Approved	Vivek Nagabhushan	03/23/2010	Vivek Nagabhushan

**Test Serial #** -001

**Test date –** 02/18/2010  
**Location –** University of Florida NEB 185

Document classification	
Uncontrolled	
Internal only	X
Classified	

This document has 3 main pages and 0 pages in attachment.

<b>Test:</b> EPS board out gassing	<b>Test serial no:</b> 001	<b>Part /Assembly #</b>
<b>Date:</b> 02/18/10	<b>Doc. #:</b> 10/A1/TD/04/05	<b>Part/Assy type:</b> Flight

### **Objective:**

The purpose of this test was to quantify out gassing levels in the SwampSat EPS board, battery board, and solar cell harness supplied by Clyde Space.

---

### **Material Required:**

1. Clyde Space EPS board with battery board mounted
  2. Wire harness used to connect solar cells to EPS board
  3. Electronic balance (resolution of 0.005g)
  4. Vacuum chamber
- 

### **Special Instructions**

1. The thermal vacuum (Tvac) chamber (DVI 3600 model) should be operated in accordance with its documentation, laboratory safety procedures, and proper handling of test pieces.
  2. Electronic components with active circuitry should be handled with ESD considerations.
  3. The EPS board should not be placed in contact with conductive surfaces, which could short the battery terminals or PC104 bus pins. Use a sheet of kapton or mylar to avoid contact with the platen.
  4. High vacuum condition may damage test pieces. When testing multiple components, care should be given to ensure that a failure of one item will not damage another in the vacuum chamber, e.g., exploding batteries could contaminate other items.
  5. No thermal cycles are conducted for this experiment.
- 

### **Procedure**

1. Record the mass of each item to be tested for out gassing. Test pieces should be handled with gloves to prevent the accumulation of skin oils. Identical components should be labeled so that they can be distinguished from one another.
  2. Place the test items in the vacuum chamber with sufficient space between them so that they are not in contact with one another.
  3. Conduct a vacuum cycle, which includes a sufficient level of evacuation and maintains a low pressure environment for a duration sufficient to allow out gassing of the test pieces.
  4. At the conclusion of the vacuum cycle, handle the components in the same way as before and promptly record the mass of the test items after removing them from the vacuum chamber. Observe for any physical changes (color, shape or size) in the components.
  5. Subject the EPS board to charging and discharging cycles to verify the functionality after the test.
- 

### **Test Setup**

The EPS board and solar cell harness were placed inside the Tvac on the platen as shown in Figure 1. The EPS board was placed on a mylar ESD bag to electrically isolate the battery pins and PC104 bus pins. The chamber was pumped down to the micro-torr level and maintained



<b>Test:</b> EPS board out gassing	<b>Test serial no:</b> 001	<b>Part /Assembly #</b>
<b>Date:</b> 02/18/10	<b>Doc. #:</b> 10/A1/TD/04/05	<b>Part/Assy type:</b> Flight

for in this state for 19 hours. The measured masses of each test piece before and after the test are listed in Table 1. The vacuum cycle parameters are listed in Table 2. The initial temperature of the samples was 19.9 °C (ambient room temperature).



**Figure 1: EPS board and Solar Cell Harness on Platen**

## Test Data

**Table 1: Mass Data**

Item	Initial mass (g)	Final mass (g)	Percent change
EPS & battery board	151.055	150.985	-0.046
EPS solar cell harness	3.525	3.530	0.142

**Table 2: Vacuum Parameters**

Vacuum start time	2/18/2010 23:00 UTC
Vacuum end time	2/19/2010 18:00 UTC
Vacuum duration	19 hours
Maximum vacuum	$7.82 \times 10^{-7}$ Torr

## Conclusion

A change of 0.07g, or 0.046% was observed in the EPS board and battery pack together. In addition the battery pack experienced physical deformation indicating outgassing. Subsequent to the outgassing tests the battery pack experienced close to 100% increase in volume (puffing), as shown in Figure 2 and compared in Figure 3, after undergoing two charging and discharging cycles. The battery pack was charged to a voltage of 7.8V and discharged to about 6.7V. The EPS board along with the battery pack was connected to the CubeSat Kit's FM430 flight board and the USB port was used for charging the battery. Similar charging and discharging cycles before subjecting the EPS board and its battery pack to vacuum testing did not indicate such



<b>Test:</b> EPS board out gassing	<b>Test serial no:</b> 001	<b>Part /Assembly #</b>
<b>Date:</b> 02/18/10	<b>Doc. #:</b> 10/A1/TD/04/05	<b>Part/Assy type:</b> Flight

deformation and high increase in volume. It was decided to contact the manufacturer (Clyde Space) for the physical deformation of the battery pack.

A mass gain was recorded for the solar cell wire harness. This is due to the low resolution of the balance, which is +/- 0.005 g. The balance does not have the resolution necessary to measure the out gassing levels of these components.

The out gassing level of the wire harness was not determined from this test. Further testing is required, using a higher precision balance, or a larger sample of wire. The rate of out gassing should also be included for consideration in specifying the length of the vacuum cycle.

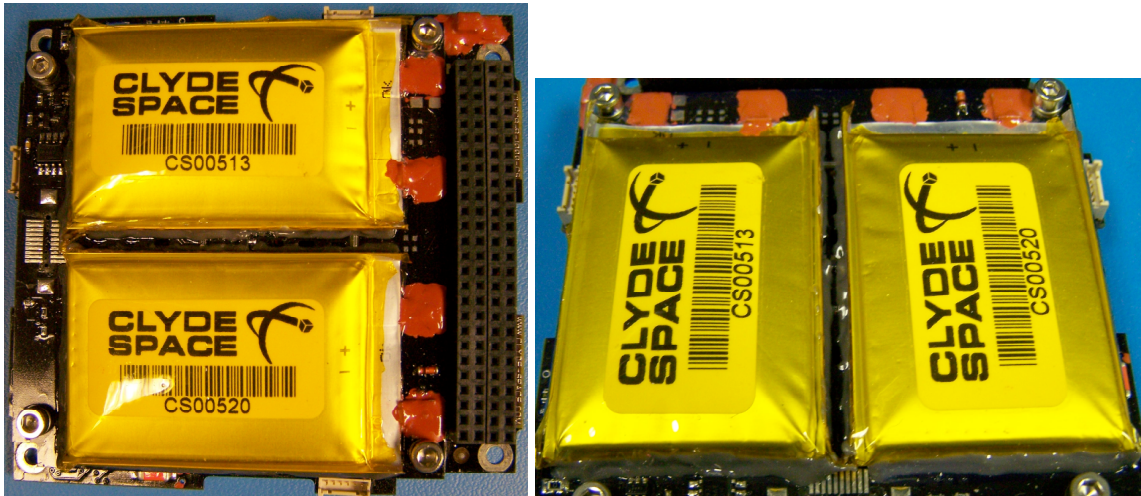


Figure 2: Views of EPS battery pack indicating deformation



Figure 3: Deformed battery compared to a regular battery





## SWAMPSAT TEST REPORT

Space Systems Group,

Advanced Space Technologies Research and Engineering Center

University of Florida  
Gainesville

---

**Test name:**Random vibration test of single PCB solar panel

**Description of item under test:**PCB solar panel assembly

**Subsystem:**EPS/Structures

**Document #** –10/A1/TD/04/09

**Document revision** –Rev.0

Document Control			
	Name	Date	Signature
Prepared	<i>SharanAsundi Shawn Johnson Kunal patankar</i>	03/11/2010	

**Test Serial #** - 1

**Test date** – 08/18/2009  
**Location** – TIMCO, Gainesville, FL

Document classification	
Uncontrolled	
Internal only	X
Classified	

This document has 12 main pages and 0 pages in attachment.

<b>Test:</b> Solar panel Random Vibration	<b>Test serial no:</b> 1	<b>Part /Assembly #</b>
<b>Date:</b> --/--/2010	<b>Doc. #:</b> 10/A1/TD/04/09	<b>Part/Assy type:</b> Prototype

### **Objective:**

---

The objective of this test is to check the functionality and structural integrity of the solar panel PCB assembly after subjecting it to random vibration levels conforming to the PSD table in the LSP PPOD ICD for ElaNa mission.

---

### **Material Required:**

1. Solar panel PCB assembly with all components integrated
  2. Multimeter
  3. Vibration table
  4. Mounting fixture (figure 3)
  5. PCB Panel Fixture
  6. PCB Panel (L-Bracket) Fixture
  7. Tri-axial accelerometers
  8. DAQ system
- 

### **Reference Documents**

1. Solar panel PCB layout and drawing
  2. Solar panel assembly functionality test document (10A1TD04xx)
- 

### **Special Instructions**

1. Do not touch the solar cells by hand or anything that might grease them
  2. The solar panel must be handled carefully so as not to damage the solar cells mounted on them
  3. Take precautions for ESD protection
- 

### **Procedure**

1. Determine qualification parameters for success of the test.
2. Perform functionality check of the panel assembly as per document 10A1TD04xx
3. List the recorded qualification parameters below
  - a. Visual inspection of assembly
  - b. Solar cell voltage
  - c. Magnet coil conductivity
  - d. Temperature sensor bonding
4. Mount the panel on the panel mounting fixture
5. The mounting fixture is then secured to the vibration table using bolts according to the axis being tested. The bolts are tightened using a torque wrench and the torque values are noted down.
6. Control accelerometer is mounted on the mounting fixture and connected to the vibration control system



<b>Test:</b> Solar panel Random Vibration	<b>Test serial no:</b> 1	<b>Part /Assembly #</b>
<b>Date:</b> --/--/2010	<b>Doc. #:</b> 10/A1/TD/04/09	<b>Part/Assy type:</b> Prototype

7. Accelerometers to monitor the frequency response of the panel are mounted at convenient locations on the panel using mounting wax. Take picture of the assembly showing the mounting locations
8. X- axis test
  - a. Steps 4-7 are repeated (axis specific)
  - b. Take picture of setup
  - c. Mount accelerometer in convenient location and take picture
  - d. The assembly is subjected to a sine sweep according to the values in Table 1
  - e. An amplitude-frequency plot is obtained from the PC connected to the DAQ and labeled "Plot X1"
  - f. Major resonant frequencies are marked on the plot
  - g. The assembly is then subjected to a random vibration according to Table 2 and Figure 3 for 2 minutes
  - h. A plot of the PSD is obtained from the PC connected to the DAQ and labeled "Plot X2"
  - i. The assembly again subjected to a sine sweep according to values in Table 1
  - j. An amplitude-frequency plot is obtained from the PC connected to the DAQ and labeled "Plot X3"
  - k. The functionality test is conducted again (step 2) and the parameter values are recorded in the results below
  - l. The assembly is removed from the vibration table

### X –AXIS Test Result

- a. Visual inspection of assembly : No visible damage
- b. Solar cell voltage: 1.5 V
- c. Magnet coil conductivity: OK
- d. Temperature sensor bonding : OK
9. Y- axis test
  - a. Steps 4-7 are repeated (axis specific)
  - b. Take picture of setup
  - c. Mount accelerometer in convenient location and take picture
  - d. The assembly is subjected to a sine sweep according to the values in Table 1
  - e. An amplitude-frequency plot is obtained from the PC connected to the DAQ and labeled "Plot Y1"
  - f. Major resonant frequencies are marked on the plot
  - g. The assembly is then subjected to a random vibration according to Table 2 and Figure 3 for 2 minutes
  - h. A plot of the PSD is obtained from the PC connected to the DAQ and labeled "Plot Y2"
  - i. The assembly again subjected to a sine sweep according to values in Table 1
  - j. An amplitude-frequency plot is obtained from the PC connected to the DAQ and labeled "Plot Y3"
  - k. The functionality test is conducted again (step 2) and the parameter values are recorded in the results below
  - l. The assembly is removed from the vibration table



<b>Test:</b> Solar panel Random Vibration	<b>Test serial no:</b> 1	<b>Part /Assembly #</b>
<b>Date:</b> --/--/2010	<b>Doc. #:</b> 10/A1/TD/04/09	<b>Part/Assy type:</b> Prototype

### Y –AXIS Test Result

- a. Visual inspection of assembly : No visible damage
- b. Solar cell voltage: 1.48 V
- c. Magnet coil conductivity: OK
- d. Temperature sensor bonding : OK

#### 10. Z- axis test

- a. Steps 7-9 are repeated (axis specific)
- b. Take picture of setup
- c. Mount accelerometer in convenient location and take picture
- d. The assembly is subjected to a sine sweep according to the values in Table 1
- e. An amplitude-frequency plot is obtained from the PC connected to the DAQ and labeled “Plot Z1”
- f. Major resonant frequencies are marked on the plot
- g. The assembly is then subjected to a random vibration according to Table 2 and Figure 3 for 2 minutes
- h. A plot of the PSD is obtained from the PC connected to the DAQ and labeled “Plot Z2”
- i. The assembly again subjected to a sine sweep according to values in Table 1
- j. An amplitude-frequency plot is obtained from the PC connected to the DAQ and labeled “Plot Z3”
- k. The functionality test is conducted again (step 2) and the parameter values are recorded in the results below
- l. The assembly is removed from the vibration table

### Z –AXIS Test Result

- a. Visual inspection of assembly : No visible damage
- b. Solar cell voltage: 1.43 V
- c. Magnet coil conductivity: OK
- d. Temperature sensor bonding : OK



<b>Test:</b> Solar panel Random Vibration	<b>Test serial no:</b> 1	<b>Part /Assembly #</b>
<b>Date:</b> --/--/2010	<b>Doc. #:</b> 10/A1/TD/04/09	<b>Part/Assy type:</b> Prototype

### Tables and Figures



**Figure 1: Vibration Shaker**

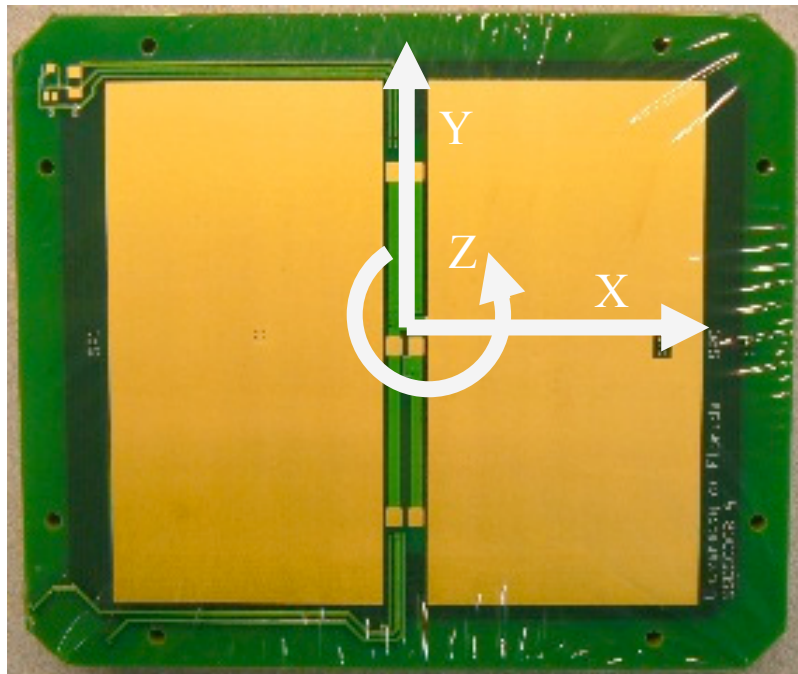


**Figure 2: PCB panel showing reference co-ordinate system**



<b>Test:</b> Solar panel Random Vibration	<b>Test serial no:</b> 1	<b>Part /Assembly #</b>
<b>Date:</b> --/--/2010	<b>Doc. #:</b> 10/A1/TD/04/09	<b>Part/Assy type:</b> Prototype

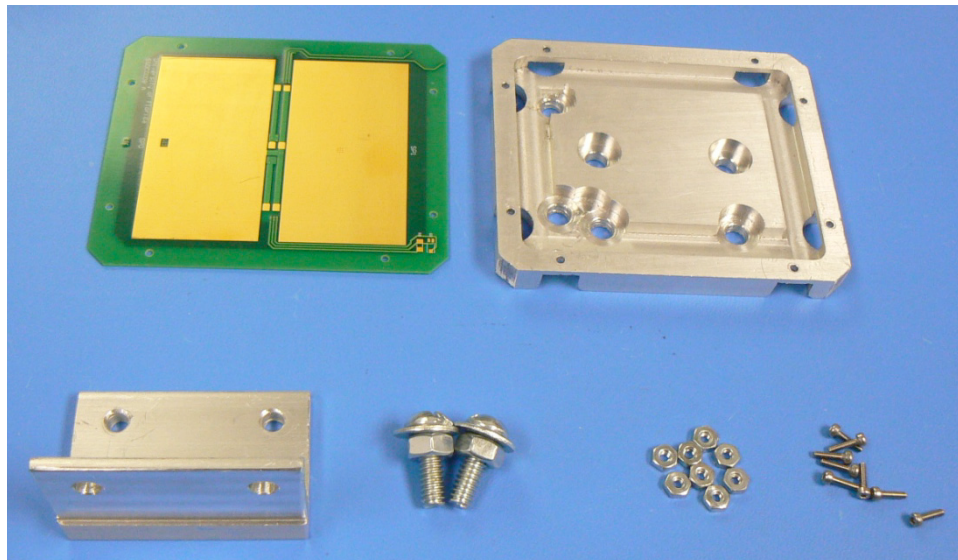


**Figure 3: Fixture**

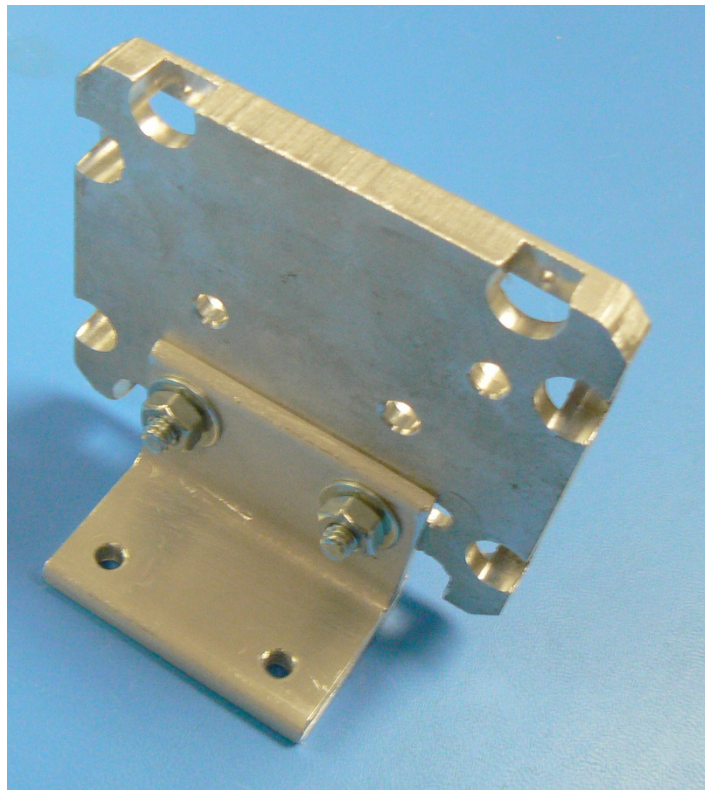


**Figure 4: Fixture assembly for X axis testing**



<b>Test:</b> Solar panel Random Vibration	<b>Test serial no:</b> 1	<b>Part /Assembly #</b>
<b>Date:</b> --/--/2010	<b>Doc. #:</b> 10/A1/TD/04/09	<b>Part/Assy type:</b> Prototype

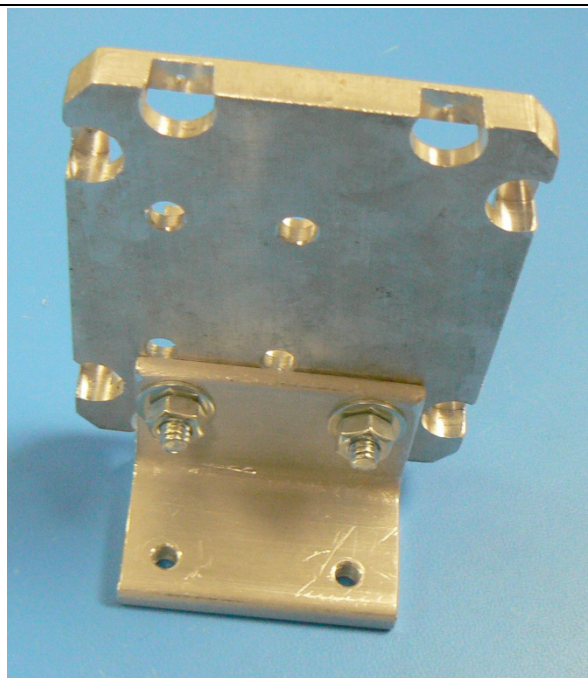


**Figure 5: Fixture assembly for Y axis testing**

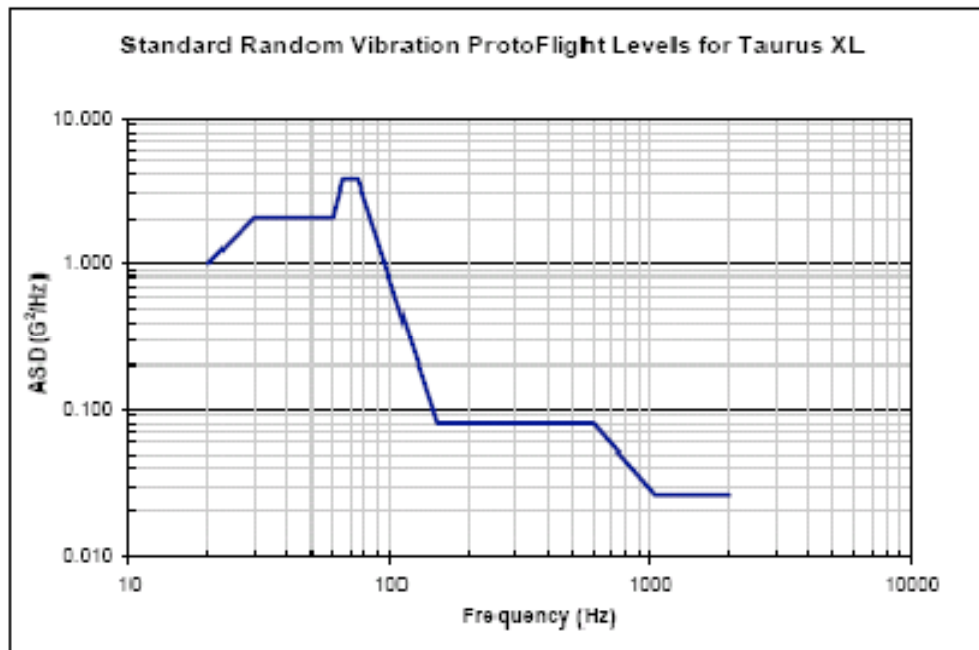


**Figure 6.Random vibration levels (Ref.Figure 10, LSP-PPOD ICD Rev 0.1 dated 2/23/10)**



<b>Test:</b> Solar panel Random Vibration	<b>Test serial no:</b> 1	<b>Part /Assembly #</b>
<b>Date:</b> --/--/2010	<b>Doc. #:</b> 10/A1/TD/04/09	<b>Part/Assy type:</b> Prototype

**Table 1: Sine vibration levels**

<b>Frequency Range (Hz)</b>	<b>Sine Level (g)</b>	<b>Sweep Rate</b>
20-2000	0.5	3 Octaves/min
2000-20	0.5	3 Octaves/min

**Table 2: Random vibration levels**

<b>Frequency (Hz)</b>	<b>ASD (G<sup>2</sup>/Hz)</b>
20	0.9880
30	2.0800
60	2.0800
65	3.7200
75	3.7200
150	0.0800
600	0.0800
1050	0.0262
2000	0.0262
<b>Overall Grms</b>	<b>16.4</b>
<b>Duration</b>	<b>120 sec/axis</b>

## Test Data

Test Personnel:

1. Vivek Nagabhushan
2. Kunal Patankar
3. Dante Buckley
4. Sharan Asundi

Location: TIMCO, Gainesville, FL

Date: 03/26/2010

Time: 6.30 PM EST

Temperature:

Humidity



<b>Test:</b> Solar panel Random Vibration	<b>Test serial no:</b> 1	<b>Part /Assembly #</b>
<b>Date:</b> --/--/2010	<b>Doc. #:</b> 10/A1/TD/04/09	<b>Part/Assy type:</b> Prototype

### Pictures

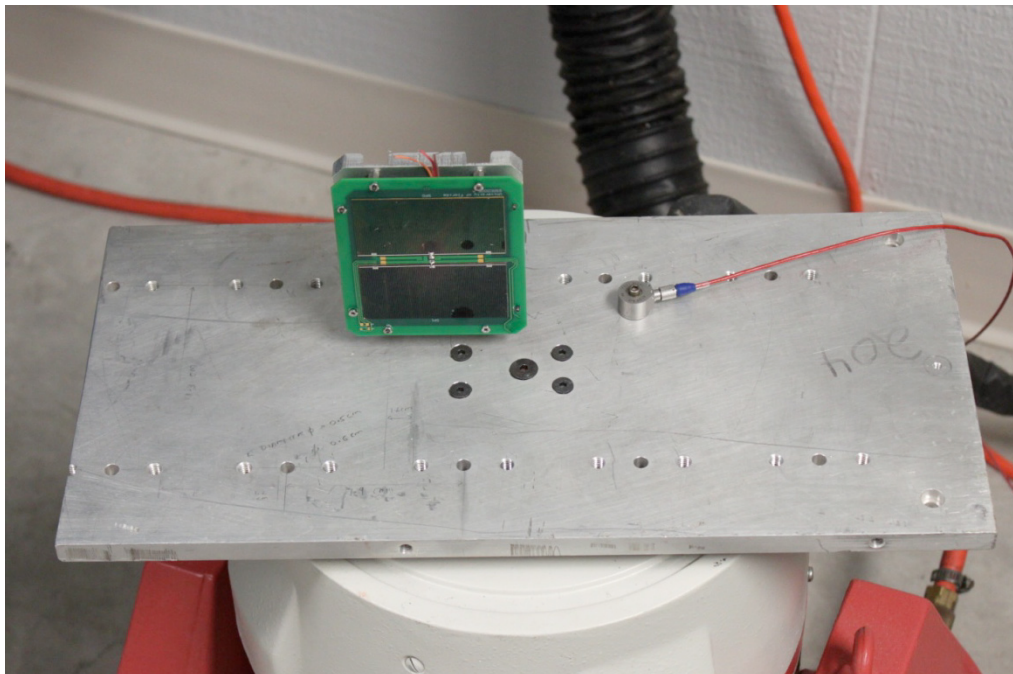


**Figure 7: X axis testing**



**Figure 8: Y axis testing**



<b>Test:</b> Solar panel Random Vibration	<b>Test serial no:</b> 1	<b>Part /Assembly #</b>
<b>Date:</b> --/--/2010	<b>Doc. #:</b> 10/A1/TD/04/09	<b>Part/Assy type:</b> Prototype

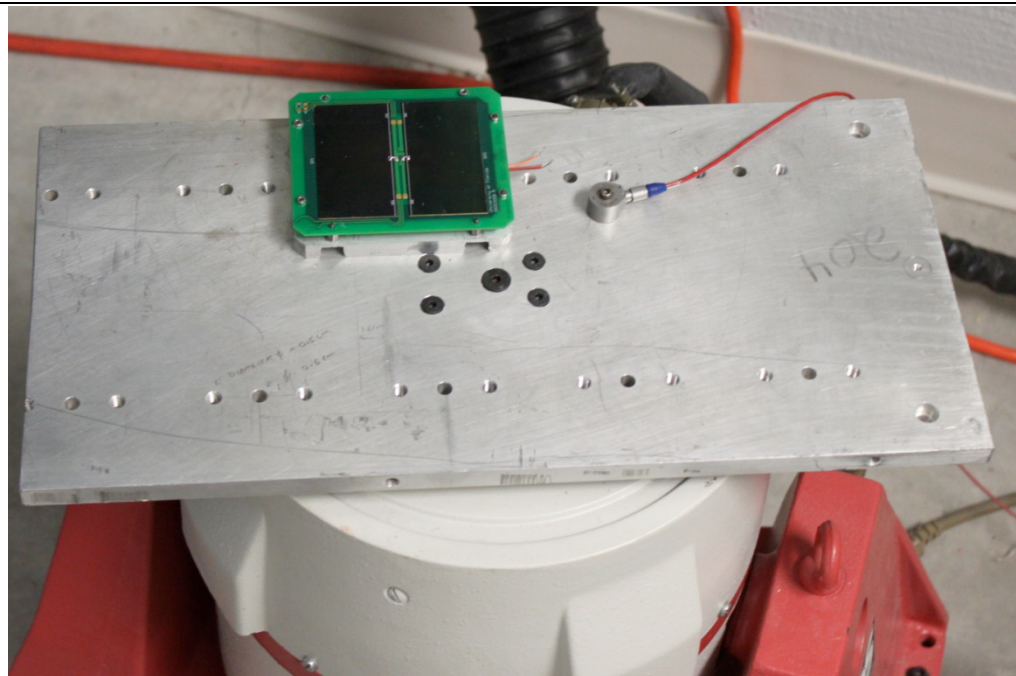


**Figure 9: Z axis testing**

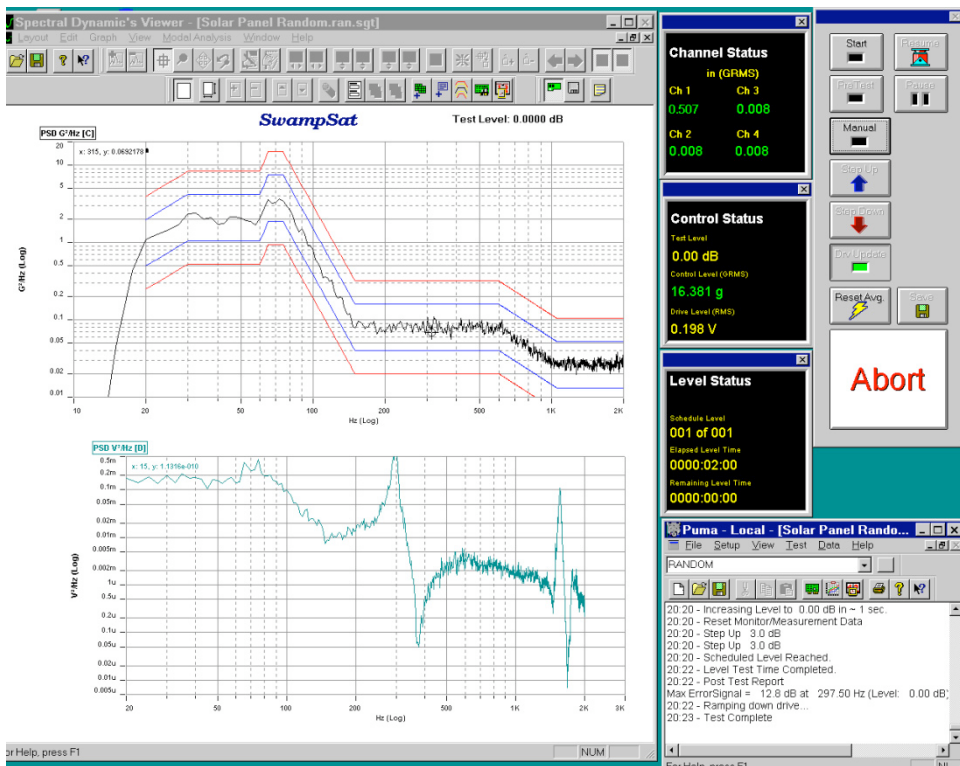


**Figure 10: Random vibration levels for X axis testing**



<b>Test:</b> Solar panel Random Vibration	<b>Test serial no:</b> 1	<b>Part /Assembly #</b>
<b>Date:</b> --/--/2010	<b>Doc. #:</b> 10/A1/TD/04/09	<b>Part/Assy type:</b> Prototype

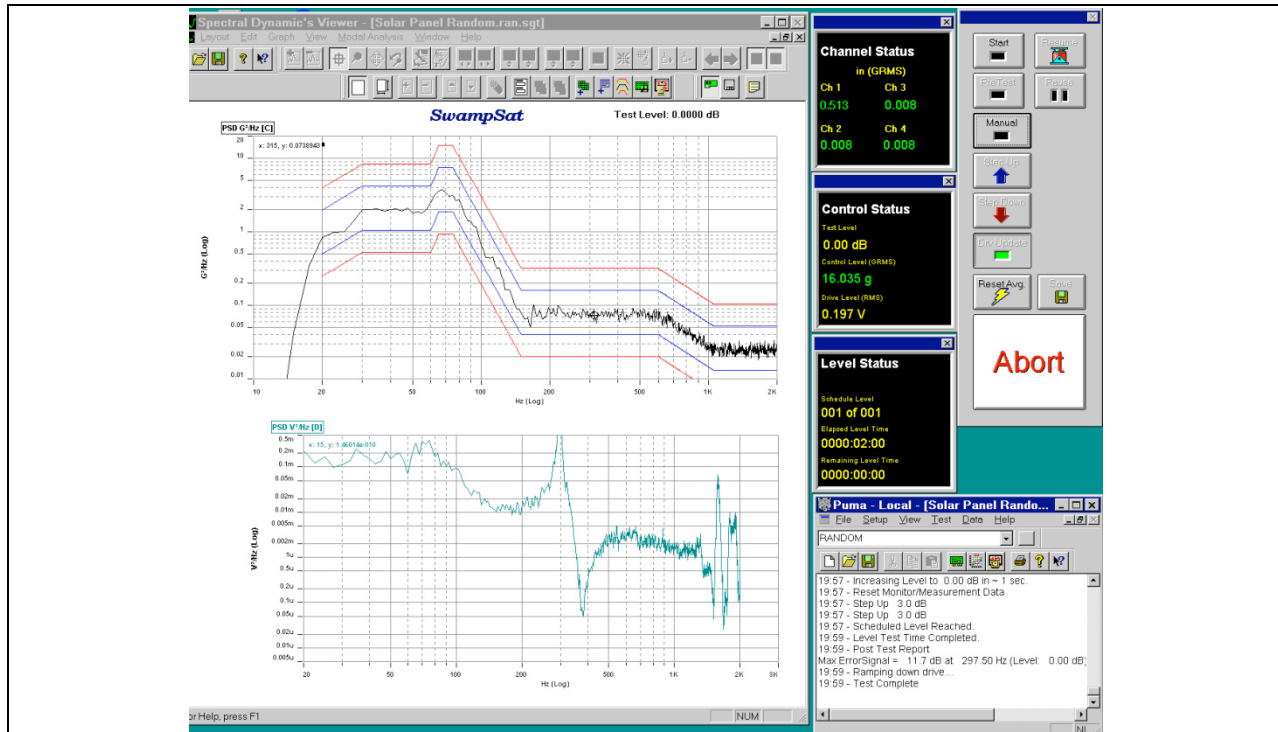


Figure 11: Random vibration levels for Y axis testing

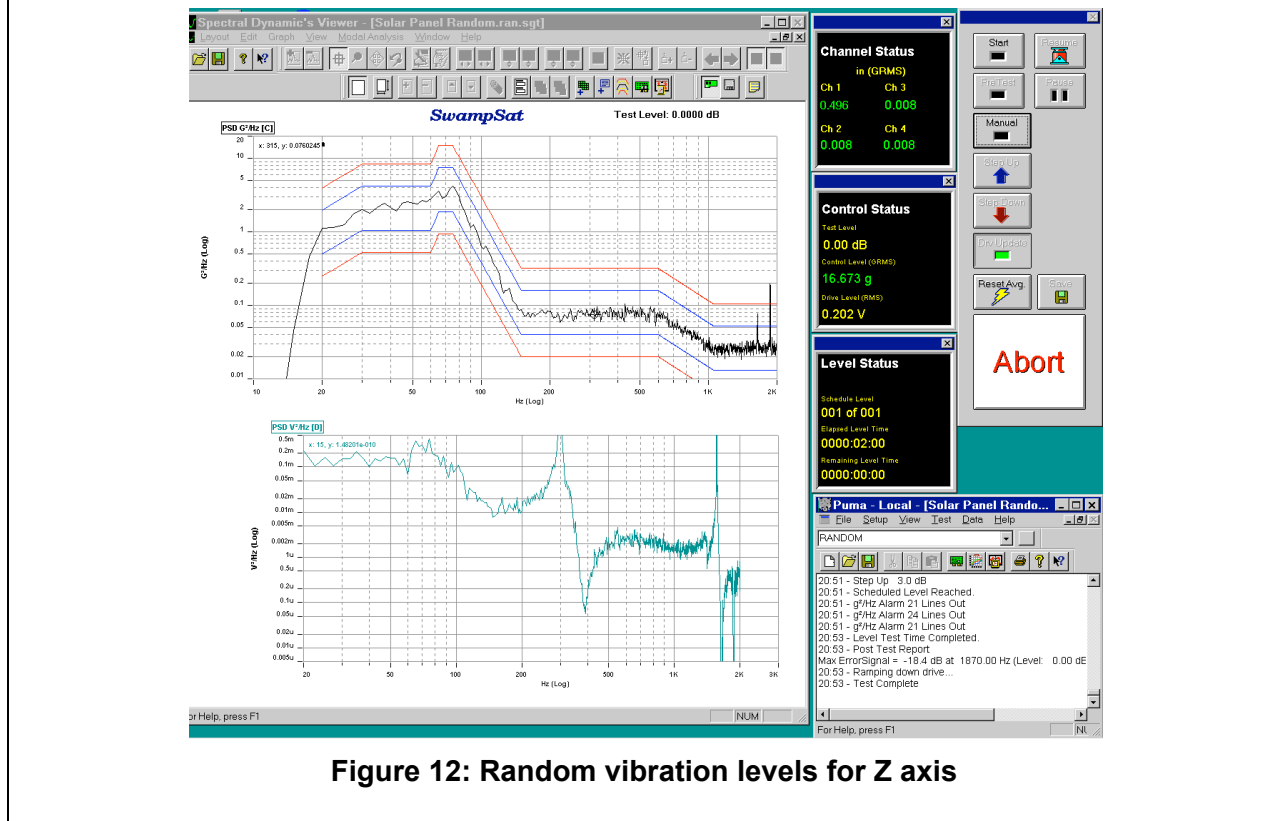


Figure 12: Random vibration levels for Z axis



<b>Test:</b> Solar panel Random Vibration	<b>Test serial no:</b> 1	<b>Part /Assembly #</b>
<b>Date:</b> --/--/2010	<b>Doc. #:</b> 10/A1/TD/04/09	<b>Part/Assy type:</b> Prototype

## Conclusion

The success of the test is based upon following criteria:

1. Identical functionality and performance of the assembly before and after the test
2. Identical response to sine vibration before and after the random vibe test
3. Integrity of the assembly before and after the test

Additional accelerometer was not available, thus response to sine vibrations could not be found out. However assembly was functional and there were no visual signs of any damage.



# SWAMP SAT

## SWAMPSAT TEST REPORT

Space Systems Group

Advanced Space Technologies Research and Engineering Center

University of Florida  
Gainesville

**Test name:** Characterization of magnetic coils in a PCB panel

**Description of item under test:** PCB panel with electrical traces embedded as magnetic coils

**Subsystem:** Electrical Power System

**Document # –** 10/A1/TD/04/06

**Document revision – Rev #1**

Document Control			
	Name	Date	Signature
Prepared	Sharan Asundi	02/28/2010	<i>Sharan Asundi</i>
Reviewed	Dante Buckley	03/01/2010	<i>Dante Buckley</i>
Reviewed	Tzu Yu (Jimmy) Lin	03/01/2010	<i>Jimmy Lin</i>
Reviewed	Norman Fitz-Coy	03/01/2010	<i>Norman Fitz-Coy</i>
Reviewed	Shawn Allgeier	03/02/2010	<i>Shawn Allgeier</i>
Approved	Norman Fitz-Coy		

**Test Serial # - 1**

**Test date –** 02/26/2010  
**Location –** NEB 185A – SSG Avionics Room

<b>Test:</b> Characterization of PCB panels	<b>Test serial no:</b> 1	<b>Part /Assembly #</b>
<b>Date:</b> 02/26/10	<b>Doc. #:</b> 10/A1/TD/04/06	<b>Part/Assy type:</b> Prototype

Document classification	
Uncontrolled	
Internal only	X
Classified	

This document has 9 main pages and 0 pages in attachment.



<b>Test:</b> Characterization of PCB panels	<b>Test serial no:</b> 1	<b>Part /Assembly #</b>
<b>Date:</b> 02/26/10	<b>Doc. #:</b> 10/A1/TD/04/06	<b>Part/Assy type:</b> Prototype

### Objective:

The objective of the experiment is to characterize the magnetic field of magnetic coils embedded as electrical traces in a printed circuit board (PCB) solar panel. Specifically the aim is to identify the power consumed by the coils in producing a magnetic field for detumbling SwampSat within the available power resources.

### Material Required:

1. PCB panel with connections soldered to access the magnetic coils
2. Power supply capable of supplying +5V for magnetic coils
3. Composite panel with embedded magnetic coils OR the magnetic coils (Figure 2)
4. A magnetometer - Bartington Mag-03
5. Power supply with +/-12V output for powering the magnetometer
6. Magnetometer interface box
7. Magnetometer interface cable
8. Oscilloscope or data acquisition unit (DAQ)
9. Alligator connectors, oscilloscope cables, multimeter, gloves, grounded ESD mat

### Special Instructions

1. The power supply units are required to be handled with caution
2. When supplying power the ground wire should be connected first
3. The components under test are required to be handled with gloves
4. Take precautions to handle the equipment in a clean environment
5. The setup can be considered to consist of two parts – (i) magnetometer setup & (ii) component under test setup
6. Refer to document “09A1TD9902 Magnetometer” for (i)

### Procedure

1. Put on the gloves and strap to ground the static charges on body
2. Arrange the equipment in a setup as shown in Figure 1
3. Refer to document “09A1TD9902 Magnetometer” for instructions on powering and using the magnetometer
4. Switch ON the power supply unit for the magnetic coils
5. Place the component under test, the PCB panel, on the ESD mat such that the Y-axis of the magnetometer is perpendicular to the surface of the PCB panel as shown in
6. Place the magnetometer over the PCB panel as shown in Figure 2 such that the Y-axis passes through the center of the magnetic coils
7. The alligator connectors are chosen to interface with the power supply on one end and clip on wires soldered to the PCB panel on other end
8. Power ON the magnetometer and the oscilloscope
9. Adjust the scale on the oscilloscope to read the magnetometer output
10. Power ON the magnetic coils such that the current is variable on the power supply
11. Supply a current of 100mA and record the corresponding magnetometer output voltage and the supply voltage
12. Increase the supply current in increments of 10mA and record the corresponding magnetometer output voltage and the supply voltage



<b>Test:</b> Characterization of PCB panels	<b>Test serial no:</b> 1	<b>Part /Assembly #</b>
<b>Date:</b> 02/26/10	<b>Doc. #:</b> 10/A1/TD/04/06	<b>Part/Assy type:</b> Prototype

13. Repeat step 12 until the supply current has reached 200mA
14. Calculate the power dissipated by the magnetic coils and plot it against the magnetic field output from the coils
15. Repeat steps 5 through 14 by replacing the PCB panel with magnetic coils used in the composite panel

### Test Setup

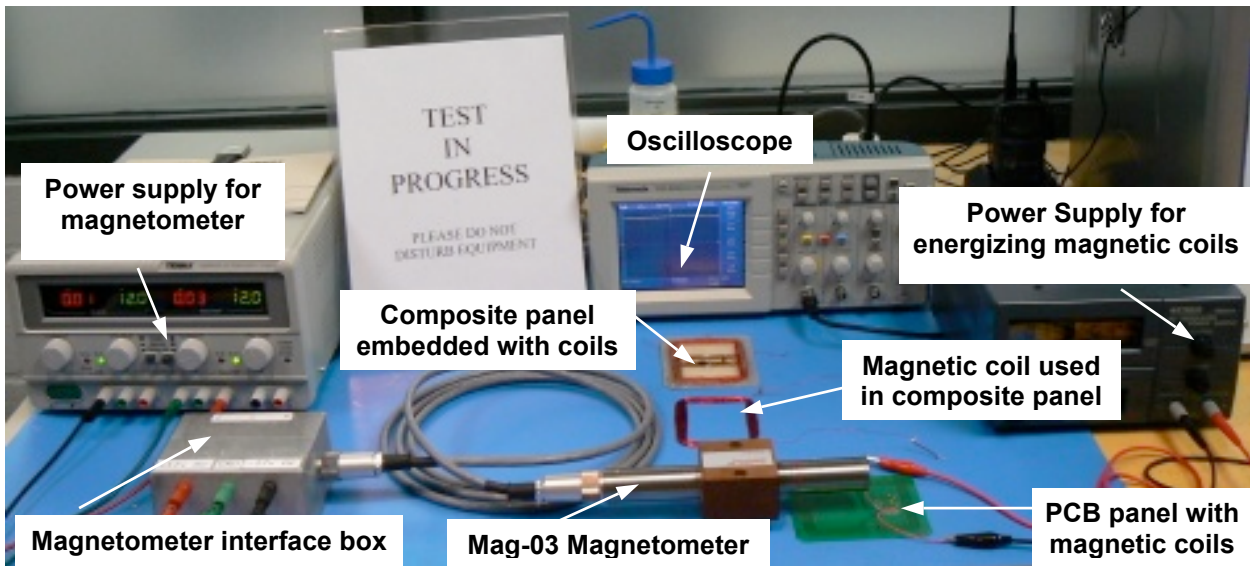


**Figure 1 - Setup for Characterizing the Magnetic Coils in the PCB Panel**

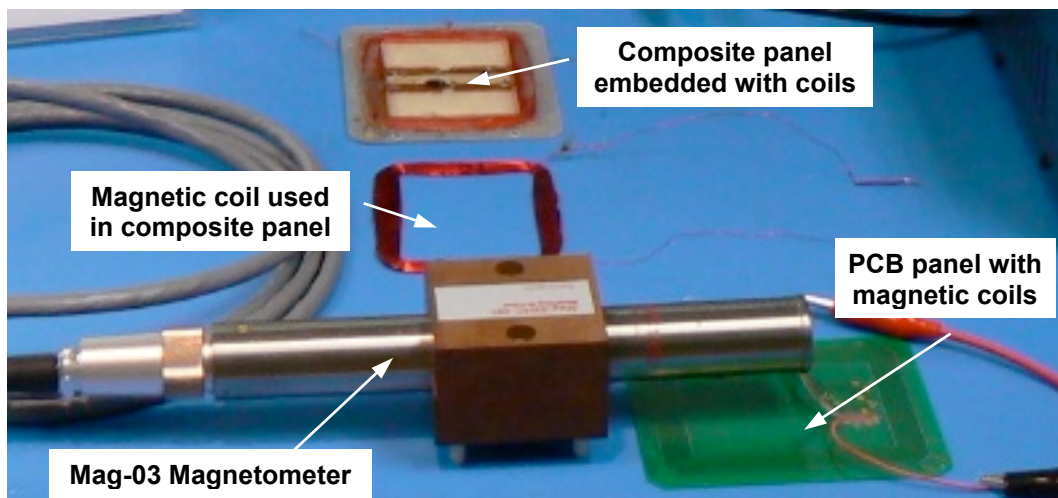


**Figure 2 - Components Under Test and the Main Testing Equipment**



<b>Test:</b> Characterization of PCB panels	<b>Test serial no:</b> 1	<b>Part /Assembly #</b>
<b>Date:</b> 02/26/10	<b>Doc. #:</b> 10/A1/TD/04/06	<b>Part/Assy type:</b> Prototype

### Test Data

The test data for analyzing the performance of PCB panels against the magnetic coils used in the composite panel is recorded as the following parameters:

1. Current consumed by the magetic traces/coils
2. Supply voltage for the current drawn
3. Magnetic field output by the magnetic traces/coils

Table 1 and



<b>Test:</b> Characterization of PCB panels	<b>Test serial no:</b> 1	<b>Part /Assembly #</b>
<b>Date:</b> 02/26/10	<b>Doc. #:</b> 10/A1/TD/04/06	<b>Part/Assy type:</b> Prototype

Table 2 show the data recorded for magnetic traces in the PCB panel and the magnetic coils used in the composite panel. The magnetic field is sensed as a voltage by the Mag-03 magnetometer where 0.1V corresponds to 1 uT. The power consumed is computed from the current and voltage values. The resistances of the magnetic traces in the PCB panel and the magnetic coils used in the composite panel are 14.7Ω and 7.2Ω respectively. To compare the performance of the magnetic coils used in the PCB panels and the composite panels plots are shown below. Figure 3 shows a plot of magnetic field output as a function of power consumed by the two types of coils. Figure 4 shows a plot of current drawn as a function of power consumed and Figure 5 shows a plot of magnetic field vs current drawn.

**Table 1 - Test Data for PCB Panels**

Current (mA)	Voltage (V)	Power (mW)	Magnetic field (uT)		
			X	Y	Z
96.39	1.43	137.49	4.20	61.50	27.65
107.84	1.60	172.11	5.90	70.50	31.25
115.20	1.71	196.42	6.30	74.50	33.55
127.70	1.89	241.36	9.20	83.50	37.15
139.19	2.06	286.73	9.80	87.50	40.35
147.64	2.19	322.58	10.00	95.50	42.55
156.76	2.32	363.68	10.70	103.50	45.35
167.23	2.48	413.89	11.20	108.50	48.05
177.36	2.63	465.58	11.90	115.50	50.95
187.30	2.77	519.19	12.60	121.50	53.85
196.89	2.91	573.74	13.20	126.50	56.25



<b>Test:</b> Characterization of PCB panels	<b>Test serial no:</b> 1	<b>Part /Assembly #</b>
<b>Date:</b> 02/26/10	<b>Doc. #:</b> 10/A1/TD/04/06	<b>Part/Assy type:</b> Prototype

**Table 2 - Test Data for Magnetic Coils used in Composite Panels**

Current (mA)	Voltage (V)	Power (mW)	Magnetic field (uT)		
			X	Y	Z
100.56	0.72	72.80	7.50	75.70	33.15
108.61	0.78	84.93	8.20	80.20	35.75
118.33	0.85	100.82	10.12	86.50	38.95
128.89	0.93	119.61	11.15	93.60	42.35
137.50	0.99	136.13	12.95	99.30	45.25
147.22	1.06	156.06	13.77	105.90	48.45
156.39	1.13	176.09	14.77	112.10	51.55
166.39	1.20	199.33	15.69	119.00	54.45
177.50	1.28	226.85	16.37	126.10	58.05
185.28	1.33	247.16	17.18	131.20	60.35
193.61	1.39	269.89	20.10	136.70	62.95

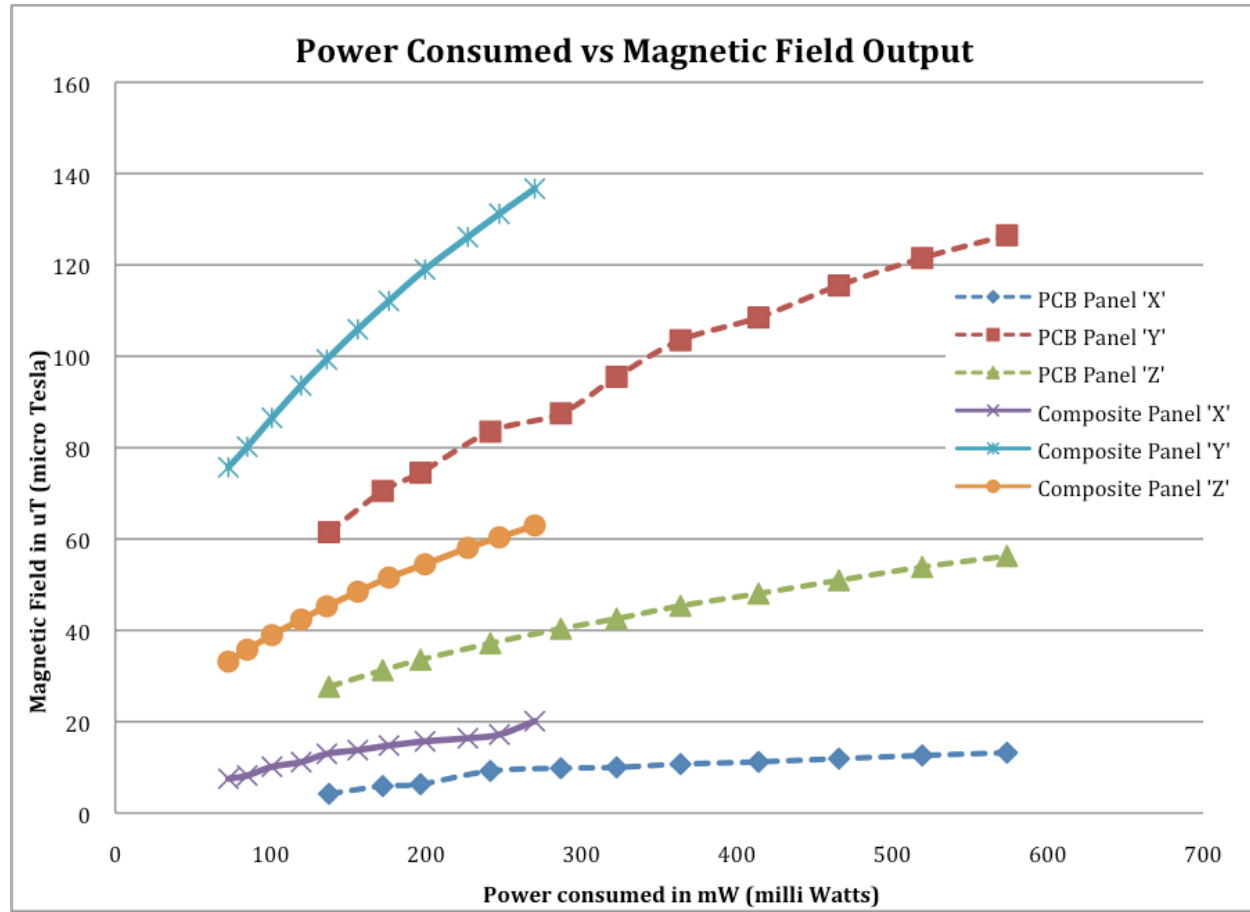


**Figure 3 - Plot of Magnetic Field as a Function of Power Consumed**



<b>Test:</b> Characterization of PCB panels	<b>Test serial no:</b> 1	<b>Part /Assembly #</b>
<b>Date:</b> 02/26/10	<b>Doc. #:</b> 10/A1/TD/04/06	<b>Part/Assy type:</b> Prototype

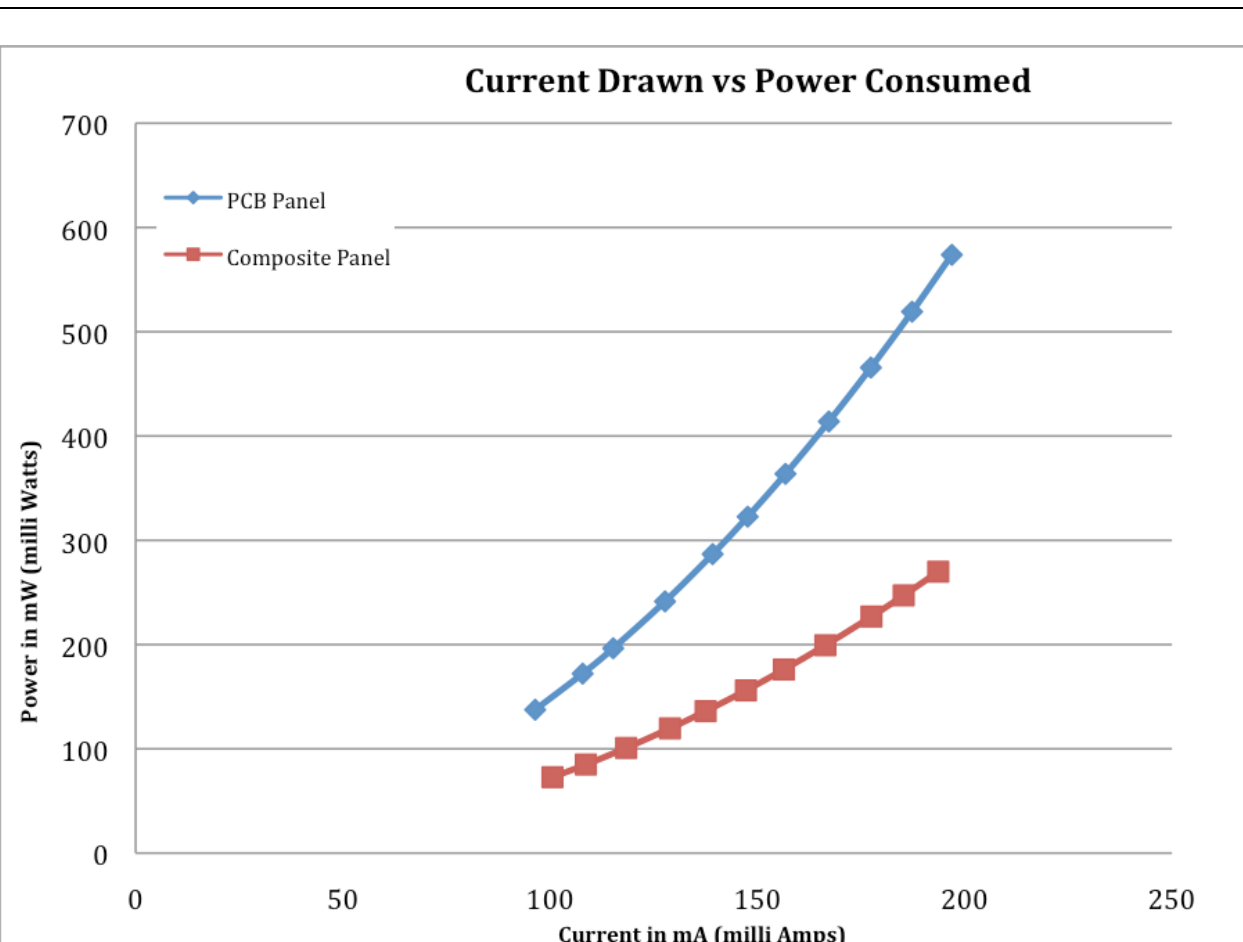


**Figure 4 - Plot of Supply Current vs Power Consumed**



<b>Test:</b> Characterization of PCB panels	<b>Test serial no:</b> 1	<b>Part /Assembly #</b>
<b>Date:</b> 02/26/10	<b>Doc. #:</b> 10/A1/TD/04/06	<b>Part/Assy type:</b> Prototype

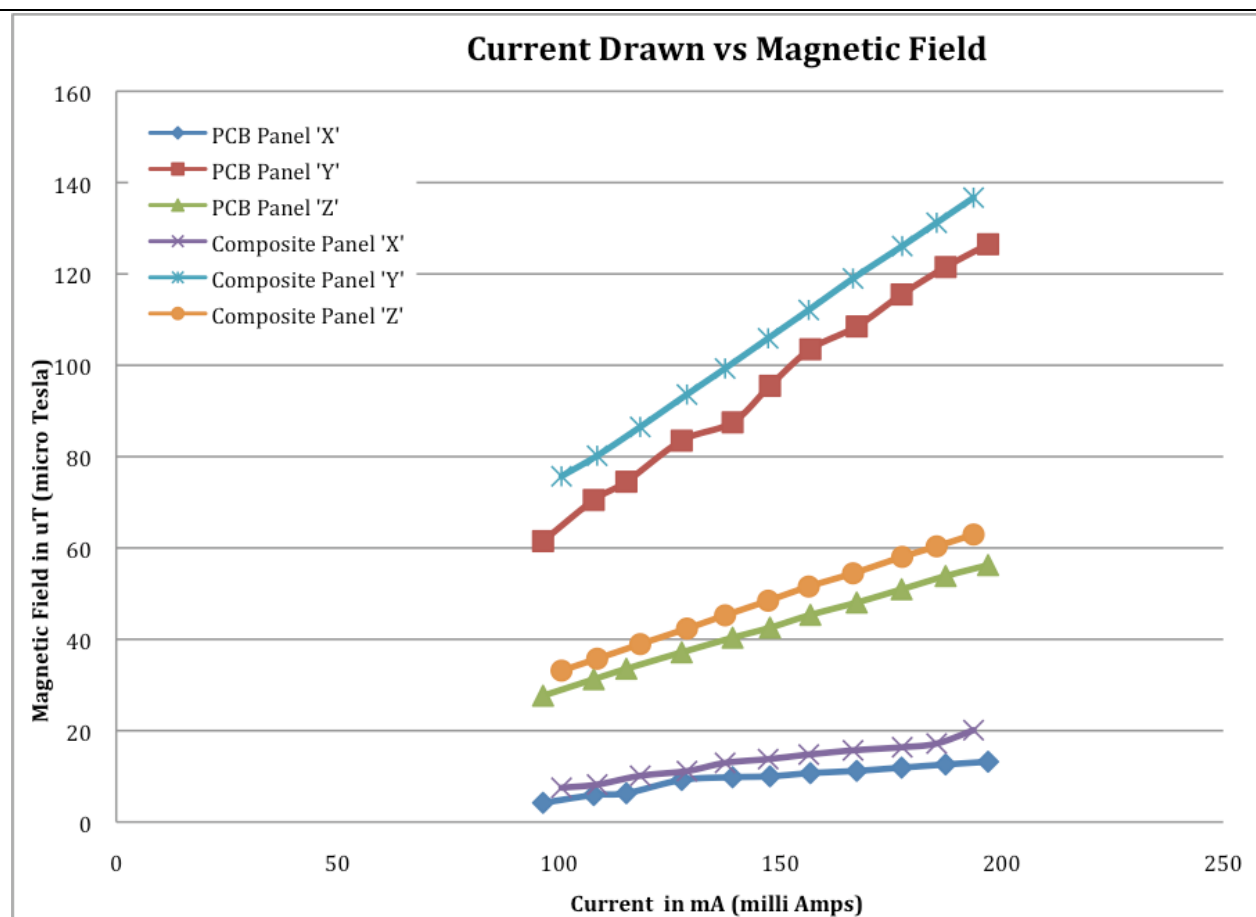


**Figure 5 - Plot of Magnetic Field as a Function of Supply Current**

## Conclusion

- The power consumed by the PCB panels to generate a magnetic field to detumble SwampSat can be accommodated in the power budget
- Performance of the magnetic coils is measured in terms of magnetic field output per unit of power consumed – uT/W (Tesla per Watt)
- As shown in Figure 3, a comparison of the magnetic coils embedded as electrical traces in the PCB panel against those used in the composite panel shows the latter have a better performance

## Tips for the experiment

- The power supply unit used for magnetic coils can read a voltage value up to a single decimal place and the multimeter is capable of reading it up to 3 decimal places
- For recording more precise voltage readings use the setup shown in Figure 6
- Adhesive tape can be considered for securing the PCB panels and magnetic coils as shown in Figure 7



<b>Test:</b> Characterization of PCB panels	<b>Test serial no:</b> 1	<b>Part /Assembly #</b>
<b>Date:</b> 02/26/10	<b>Doc. #:</b> 10/A1/TD/04/06	<b>Part/Assy type:</b> Prototype

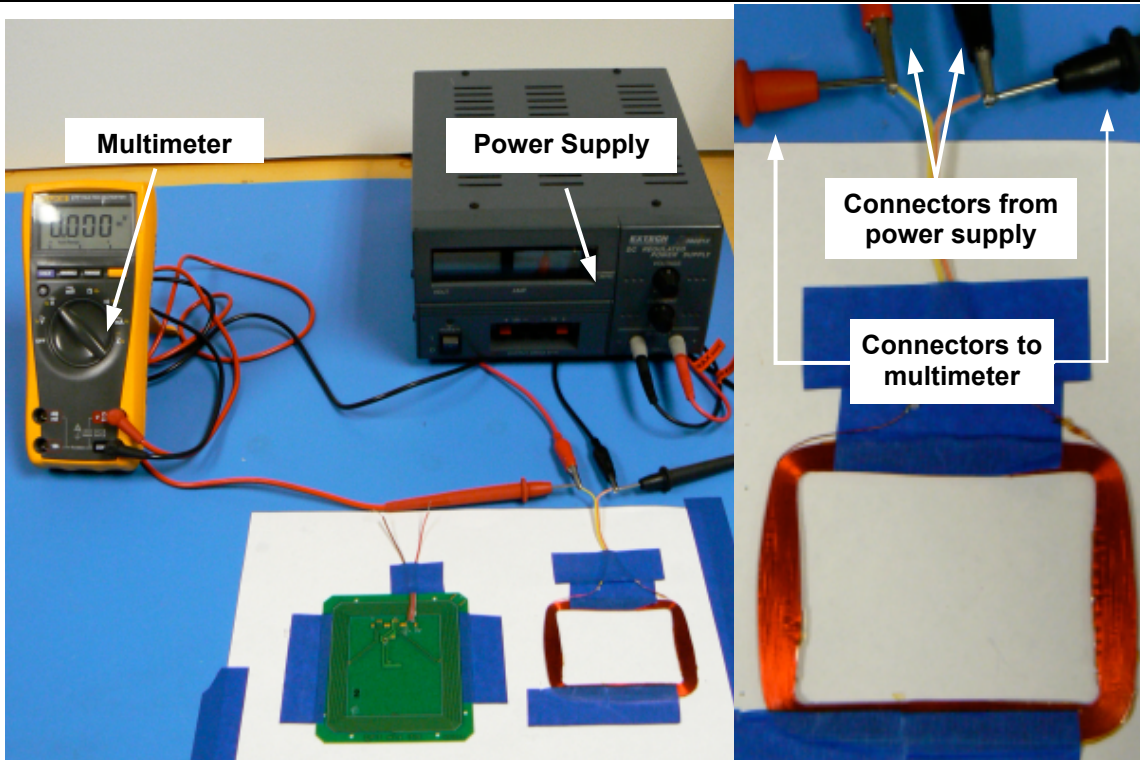


**Figure 6 - Setup for Getting a More Precise Voltage Reading of the Power Supply**

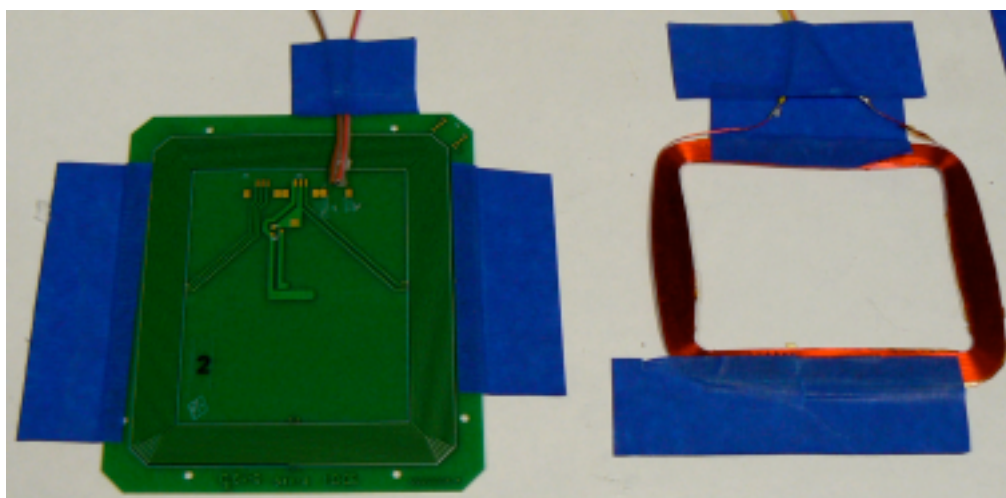


**Figure 7 - Setup for Securing PCB Panels and Magnetic Coils**



## REFERENCES

- [1] Woellert, K., Ehrenfreund, P., Ricco, A., and Hertzfeld, H., "Cubesats: Cost-Effective Science and Technology Platforms for Emerging and Developing Nations," *Advances in Space Research*, 2010.
- [2] Heidt, H., Puig-Suari, J., Moore, A., Nakasuka, S., and Twiggs, R., "CubeSat: A new generation of picosatellite for education and industry low-cost space experimentation," *Proceedings of the Utah State University Small Satellite Conference, Logan, UT*, Citeseer, 2001, pp. 1–2.
- [3] Schaffner, J. and Puig-Suari, J., "The Electronic System Design, Analysis, Integration, and Construction of the Cal Poly State University CP1 CubeSat," *16th AIAA/USU on Small Satellites Conference, Logan, UT*, Citeseer, 2002, pp. 1–2.
- [4] Larsen, B., Klumper, D., Wood, M., Hunyadi, G., Jepsen, S., and Omland, M., "Microcontroller design for the Montana Earth orbiting pico-explorer (MEROPE) CubeSat-class satellite," *Aerospace Conference Proceedings, 2002. IEEE*, Vol. 1, IEEE, 2005, p. 1.
- [5] Waydo, S., Henry, D., and Campbell, M., "CubeSat design for LEO-based Earth science missions," *Aerospace Conference Proceedings, 2002. IEEE*, Vol. 1, IEEE, 2005, p. 1.
- [6] Long, M., Lorenz, A., Rodgers, G., Tapiro, E., Tran, G., Jackson, K., Twiggs, R., and Bleier, T., "A cubesat derived design for a unique academic research mission in earthquake signature detection," *Proc. AIAA Small Satellite Conference*, 2002.
- [7] Kitts, C., Hines, J., Agasid, E., Ricco, A., Yost, B., Ronzano, K., and Puig-Suar, J., "The GeneSat-1 Microsatellite Mission: A Challenge in Small Satellite Design," *Proc 20th Annual AIAA/USU Conf on Small Satellites, Logan UT*, 2006.
- [8] Nakaya, K., Konoue, K., Sawada, H., Ui, K., Okada, H., Miyashita, N., Iai, M., and Matunaga, S., "Tokyo Tech CubeSat: CUTE-I- Design and development of flight model and future plan," *21st AIAA International Communications Satellite Systems Conference(ICSSC) and Exhibit*, 2003.
- [9] Toorian, A., Blundell, E., Suari, J., and Twiggs, R., "CubeSats as responsive satellites," *Aerospace Engineering*, Vol. 805, pp. 756–6479.
- [10] Tsuda, Y., Sako, N., Eishima, T., Ito, T., Arikawa, Y., Miyamura, N., Kanairo, K., Ukawa, S., Ogasawara, S., and Ishikawa, S., "University of Tokyo's CubeSat" XI" as a student-built educational pico-satellite- Final design and operation plan," *Proceedings of the twenty-third international symposium on space technology and science(Selected papers), vol. II*, 2002, pp. 1372–1377.

- [11] Baker, K. and Jansson, D., "Space satellites from the world's garage-the story of AMSAT," *Aerospace and Electronics Conference, 1994. NAECON 1994., Proceedings of the IEEE 1994 National*, IEEE, 2002, pp. 1174–1181.
- [12] Alminde, L., "Educational benefits from the AAU-cubesat student satellite project," *54th International Astronautical Congress; Bremen; Germany*, International Astronautical Federation, 8-10 rue Mario-Nikis, Paris Cedex, 15, France,, 2003.
- [13] Hales, J. and Pedersen, M., "Two-axis MOEMS sun sensor for pico satellites," *Power*, Vol. 1, pp. 2W.
- [14] Wells, G., Stras, L., and Jeans, T., "Canadas Smallest Satellite- The Canadian Advanced Nanospace eXperiment(CanX-1)," *Breakthrough Technologies- The Foundation of the Future*, 2002.
- [15] Flagg, S., Bleier, T., Dunson, C., Doering, J., DeMartini, L., Clarke, P., Franklin, L., Seelback, J., Flagg, J., Klenk, M., et al., "Using Nanosats as a proof of concept for space science missions: QuakeSat as an operational example," *Proc. of 18th Annual AIAA/USU Conference on Small Satellites*.
- [16] Lee, S. and Puig-Suari, J., *Coordination of Multiple CubeSats on the Dnepr Launch Vehicle: A Thesis*, California Polytechnic State University, 2006.
- [17] "The Dnepr Launcher," [http://www.russianspaceweb.com/dnepr\\_007\\_belka.html](http://www.russianspaceweb.com/dnepr_007_belka.html), 2006.
- [18] Lappas, V., Steyn, W., and Underwood, C., "Attitude control for small satellites using control moment gyros," *Acta Astronautica*, Vol. 51, No. 1-9, 2002, pp. 101–111.
- [19] Munkata, R., "CubeSat Design Specification Rev. 12," August, 2009.
- [20] Toorian, A., Diaz, K., and Lee, S., "The cubesat approach to space access," *Aerospace Conference, 2008 IEEE*, IEEE, 2008, pp. 1–14.
- [21] Puig-Suari, J., Turner, C., and Ahlgren, W., "Development of the standard CubeSat deployer and a CubeSat class PicoSatellite," *Aerospace Conference, 2001, IEEE Proceedings.*, Vol. 1, 2001.
- [22] Nugent, R., Munakata, R., Chin, A., Coelho, R., and Puig-Suari, J., "The cubesat: The picosatellite standard for research and education," *Aerospace Engineering*, Vol. 805, 2008, pp. 756–5087.
- [23] Lan, W., "Poly Picosatellite Orbital Deployer Mk III ICD," [http://cubesat.calpoly.edu/images/LaunchProviders/mk\\_iii\\_icd5.pdf](http://cubesat.calpoly.edu/images/LaunchProviders/mk_iii_icd5.pdf), 2007.
- [24] Levinson, M., *The box: how the shipping container made the world smaller and the world economy bigger*, Princeton Univ Pr, 2006.

- [25] “Yet Another Housekeeping Unit (YAHU),” No RISC, No Fun! (<http://www.amsat-dl.org/yahue.html>), April 1998.
- [26] Schneider, J., “PC104 Embedded Consortium,” PC104 Embedded Consortium (<http://www.pc104.org>).
- [27] “PC104 Consortium,” PC104 Consortium CPU-Z530 (<http://www.pc104.org/product.php?id=111>).
- [28] Bleier, T., Clarke, P., Cutler, J., DeMartini, L., Dunson, C., Flagg, S., Lorenz, A., and Tapiro, E., “Quakesat lessons learned: Notes from the development of a triple cubesat,” *Online:[http://www.quakefinder.com/services/quakesatssite/documents/Lessons\_Learned\_Final.pdf]*, 2004.
- [29] Ubbels, W., Bonnema, A., van Breukelen, E., Doorn, J., van den Eikhoff, R., Van der Linden, E., Aalbers, G., Rotteveel, J., Hamann, R., and Verhoeven, C., “Delfi-C3: a student nanosatellite as a test-bed for thin film solar cells and wireless onboard communication,” *Proceedings of 2nd International Conference on Recent Advances in Space Technologies, 2005. RAST 2005*, 2005, pp. 167–172.
- [30] Silver, M., D. B. W. P. W. S. A. V., “Development of a deployable gravity-gradient boom CubeSat,” *6th Cubesat Developers Workshop, Logan, UT*, 2009.
- [31] Kraus, V., Holik, M., Bartovsky, J., Georgiev, V., Jakubek, J., and Schneider, D., “Space Weather Monitor Based on the Timepix Single Particle Pixel Detector,” *18th Telecommunications Forum TELFOR 2010, Belgrade, Serbia*, 2010.
- [32] Vertat, I., Hrouda, J., and Hofman, J., “Spectrolab triangular solar cell evaluation for usage in PilsenCUBE picosatellite,” *Applied Electronics (AE), 2010 International Conference on*, IEEE, pp. 1–4.
- [33] Clark, C. and Mazarias, A., “Power System Challenges for Small Satellite Missions,” *Proceedings of the 4S Symposium Small Satellites, Systems and Services, ESA SP-625*, 2006.
- [34] “Satellite Detail - CubeSat-OSCAR 55,” 2009.
- [35] Fujiwara, K., Omagari, K., Iljic, T., Masumoto, S., Konda, Y., Yamanaka, T., Tanaka, Y., Maeno, M., Ueno, T., Ashida, H., et al., “Tokyo Tech Nano-Satellite Cute-1.7+ APD Flight Operation Results and The Succeeding Satellite,” *The 17th IFAC Symposium on Automatic Control in Aerospace*, pp. 25–29.
- [36] Rankin, D., Kekez, D., Zee, R., Pranajaya, F., Foisy, D., and Beattie, A., “The CanX-2 nanosatellite: expanding the science abilities of nanosatellites,” *Acta Astronautica*, Vol. 57, No. 2-8, 2005, pp. 167–174.
- [37] Barousse, M. and Oliver, T., “The applications of a software defined radio in space,” *5th Annual Cubesat Developers Workshop. San Louis Obispo, CA*, 2009.

- [38] Herfort, M., Berlin, M., Geile, H., and Yoon, Z., “BeeSat Attitude Determination and Control System,” *Small Satellites for Earth Observation*, pp. 255–264.
- [39] Leve, F., Allgeier, S., Nagabhushan, V., Asundi, S., Buckley, D., Waldrum, A., and Hiramatsu, T., “ASTREC-I Detailed Design Report, FUNSAT IV Design Competition,” 2007–2008.
- [40] Svartveit, K., “Attitude determination of the NCUBE satellite,” *Norwegian University of Science and Technology. Department of Engineering Cybernetics*, 2003.
- [41] Leve, F., *Novel steering and control algorithms for single-gimbal control moment gyroscopes*, Ph.D. thesis, University of Florida, 2010.
- [42] “eoPortal - Sharing Earth Observing Resources Embedded Consortium,” [http://directory.eoportal.org/get\\_announce.php?an\\_id=8501](http://directory.eoportal.org/get_announce.php?an_id=8501), 2010.
- [43] Kitts, C., Ronzano, K., Rasay, R., Mas, I., Williams, P., Mahacek, P., Minelli, G., Hines, J., Agasid, E., Friedericks, C., et al., “Flight Results from the GeneSat-1 Biological Microsatellite Mission,” *21 st Annual AIAA/USU Conference on Small Satellites*.
- [44] Kitts, C., Ronzano, K., Rasay, R., Mas, I., Acain, J., Neumann, M., Bica, L., Mahacek, P., Minelli, G., Beck, E., et al., “Initial Flight Results from the PharmaSat Biological Microsatellite Mission,” *Proc. 23nd Annual AIAA/USU Conf on Small Satellites, Logan UT*, 2009.
- [45] Diaz-Aguado, M., Ghassemieh, S., Van Outryve, C., Beasley, C., and Schooley, A., “Small Class-D spacecraft thermal design, test and analysis-PharmaSat biological experiment,” *Aerospace conference, 2009 IEEE*, IEEE, 2009, pp. 1–9.
- [46] Minelli, G. Ricco, A. S. D. B. C. H. J. e. a., “O/OREOS: A Multi-Payload Technology Demonstration,” *Proceedings of the 24th Annual AIAA/USU Conference on Small Satellites, Logan UT*, 2010.
- [47] Klenzing, J., Rowland, D., Hill, J., and Weatherwax, A., “FIREFLY: A cubesat mission to study terrestrial gamma-ray flashes,” *AGU Fall Meeting Abstracts*, Vol. 1, 2009, p. 1577.
- [48] Bahcivan, H., Cutler, J., Buonocore, J., and Bennett, M., “Radio Aurora Explorer: Mission overview and the science objectives,” *AGU Fall Meeting Abstracts*, Vol. 1, 2009, p. 05.
- [49] “QB50 PROJECT,” QB50, an international network of 50 CubeSats for multi-point, in-situ measurements in the lower thermosphere and re-entry (<http://www.vki.ac.be/QB50/project2.php>), March 2010.
- [50] Bourne, W., “NRO CubeSat Experiments (Qb X),” 2009.

- [51] "About the ESA SSETI Program," 2010.
- [52] Aguado, F., V. J. P-S. J. C. S., "HUMSAT Project: International initiative for a United Nations satellite constellation," 2010.
- [53] "STUDsat project site," <http://www.teamstudsat.com/about.html>, 2010.
- [54] NAKASUKA, S., SAKO, N., TSUDA, Y., EISHIMA, T., FUNASE, R., NAKAMURA, Y., NAGAI, M., OISHI, C., and ISHIKAWA, S., "Flight and Operation Results of University of Tokyo's Nano-Satellite CubeSat XI," *Uchu Kagaku Gijutsu Rengo Koenkai Koenshu (CD-ROM)*, Vol. 47, 2003, pp. 1450–1455.
- [55] Zhang, H., Yang, C., and Qiu, Z., "The GPS receiver for micro/nanosatellites," *Nanotech 2002, Houston, TX*, 2002.
- [56] Ryba, J., "NASA - ELaNa: Educational Launch of Nanosatellites," [http://www.nasa.gov/offices/education/centers/kennedy/technology/elana\\_feature.html](http://www.nasa.gov/offices/education/centers/kennedy/technology/elana_feature.html).
- [57] Slane, F., D. R. and Cook, D., "Use of Model-Driven Architectures to Increase Responsiveness and Reduce Cost," *Reinventing Space Conference, Los Angeles, CA*, March 2-5, 2011.
- [58] Sega, R. and Cartwright, J., "Plan for Operationally Responsive Space, Tech. rep., Department of Defense Executive Agent for Space and US Strategic Command," 2007.
- [59] "Plan for Operationally Responsive Space Report to Congressional Defense Committees," <http://www.acq.osd.mil/nss/oors/Plan for Operationally Responsive Space Report to Congressional Defense Committees April 17 2007.pdf>, 2007.
- [60] Allgeier, S., N. V. F-C. N. and Edmonson, W., "The Role of Universities in Developing a Responsive Space Industry," *8th Responsive Space Conference, Los Angeles, CA*, March 8-11, 2010.
- [61] Klamper, A., "NRO Embraces Cubesats for Testing Advanced Technologies," 2009.
- [62] Sellers, J. and Lawrence, T., "Building a Cadre of Space Professionals: Hands-On Space Experience at the USAF Academy," *1st Responsive Space Conference, Redondo Beach, CA*, April 1-3, 2003.
- [63] Smith, C., "Leveraging COTS Hardware for Rapid Design and Development of Small Satellites at the USAF Academy," *2nd Responsive Space Conference, Los Angeles, CA*, April 19-22, 2004.
- [64] Swartwout, M., "Bandit: A Platform for Responsive Educational and Research Activities," *Proceedings of the 4th Responsive Space Conference, Los Angeles, CA*, Vol. 26, 2006.

- [65] Kuwahara, T., A. F. A. and Roser, H., "Effective Project Management of Small Satellite Projects from the System Engineers Point of View, An Example of the Small Satellite Flying Laptop Project," *Transactions of Space Technology Japan*, Vol. 7, 2009.
- [66] Kitts, C. and Tillier, C., "A world wide web interface for automated spacecraft operation," *INTERNATIONAL TELEMETERING CONFERENCE-PROCEEDINGS-*, Vol. 32, Citeseer, 1996, pp. 931–938.
- [67] Khullar, R., Eftekharzadeh, S., and Brownlow, L., "Picosatellite missions and applications," *Space Technology*, Vol. 25, No. 1, 2005, pp. 27–35.
- [68] "Office of the Chief Technologist: Small Spacecraft Program," [http://www.nasa.gov/pdf/474015main\\_SmallSat\\_Conference\\_8\\_9\\_10.pdf](http://www.nasa.gov/pdf/474015main_SmallSat_Conference_8_9_10.pdf), 2010.
- [69] Aeronautics, N. and Administration, S., *NASA Systems Engineering Handbook*, National Aeronautics and Space Administration, 2007.
- [70] Gage, D., CONTROL, N. C., RDT, O. S. C., and CA, E. D. S. D., "UGV history 101: A brief history of Unmanned Ground Vehicle (UGV) development efforts," 1995.
- [71] Albus, J., "A theory of intelligent systems," *Control and Dynamic Systems*, Vol. 45, 1991, pp. 197–248.
- [72] Williams, B. and Nayak, P., "A model-based approach to reactive self-configuring systems," *Proceedings of the National Conference on Artificial Intelligence*, 1996, pp. 971–978.
- [73] Allgeier, S., Mahin, M., and Fitz-Coy, N., "Design and Analysis of a Coarse Sun Sensor for Pico-Satellites," *Proceedings of the AIAA Infotech@ Aerospace Conference*, 2009.
- [74] Bajwa, A. and Sweet, A., "The Livingstone model of a main propulsion system," *Proceedings of the IEEE Aerospace Conference*, Citeseer, 2003.
- [75] van Soest, D. C., *Modeling for model-based diagnosis*, Master's thesis, Universiteit Twente, 1993.
- [76] Doyne, T., W. P. R.-R. H. M. J. M. and Weldy, K., "A TacSat and ORS Update Including TacSat-4," *4th Responsive Space Conference, Los Angeles, CA*, April 24-27, 2006.
- [77] Payton, G. E., "Air Force Space Acquisition," *High Frontier*, Vol. 6, No. 1, 2009, pp. 3,4.
- [78] Peck, M., Miller, L., Cavender, A., Gonzalez, M., and Hintz, T., "An airbearing-based testbed for momentum control systems and spacecraft line of sight," *Advances in the Astronautical Sciences*, Vol. 114, 2003, pp. 427–446.

- [79] Nagabhushan, V., "SwampSat Mission Requirements and Traceability, Tech. Rep. 09A1SD0001," 2009.
- [80] Clark, C. and Fletcher, W., "CubeSat Power System User Manual, Document No.: C1-USM-5003-CS-EPS Issue: L," 23rd July 2008.
- [81] Leve, F., *Development of the Spacecraft Orientation Buoyancy Experimental Kiosk*, Master's thesis, University of Florida, 2008.
- [82] International, A., "Designation E 595 07 Standard Test Method for Total Mass Loss and Collected Volatile Condensable Materials from Outgassing in a Vacuum Environment," *Annual Book of ASTM Standards*, 2007.
- [83] Nugent, R., "CubeSat to P-POD Interface Control Document Rev 0.1," February, 2010.
- [84] Galysh, V., "KATYSAT Radio Board, Rev 2.4," January 2008.
- [85] Asundi, S., Mahin, M., Nagabhushan, V., Lin, T., and Fitz-Coy, N., "Composite and PCB Based Implementations of a Solar Panel Design for SwampSat," *SmallSat Conference*, 2010.
- [86] "VARTA PoLiFlexPLF 503759 D," .
- [87] Shuster, M. and Oh, S., "Three-axis attitude determination from vector observations," *Journal of Guidance and Control*, Vol. 4, No. 1, 1981, pp. 70–77.
- [88] Murrell, J., "Precision attitude determination for multimission spacecraft," *Guidance and Control Conference, Palo Alto, Calif., August 7-9, 1978, Technical Papers.(A78-50159 22-01) New York, American Institute of Aeronautics and Astronautics, Inc., 1978, p. 70-87.*, 1978.
- [89] Kalman, R., "A new approach to linear filtering and prediction problems," *Journal of Basic Engineering*, Vol. 82, No. 1, 1960, pp. 35–45.
- [90] Kalman, R. and Bucy, R., "New results in linear filtering and prediction theory," *Random Processes*, 1973.
- [91] Black, H., "A passive system for determining the attitude of a satellite," *AIAA Journal*, Vol. 2, No. 7, 1964, pp. 1350–1351.
- [92] Lerner, G., "Three-axis attitude determination," *Spacecraft Attitude Determination and Control*, 1978, pp. 420–428.
- [93] Markley, L., "Attitude Determination Using Two Vector Measurements," *NASA CONFERENCE PUBLICATION*, NASA, 1999, pp. 39–52.
- [94] Wertz, J., *Spacecraft attitude determination and control*, Kluwer Academic Pub, 1978.

- [95] Bar-Itzhack, I. and Harman, R., "Optimized TRIAD algorithm for attitude determination," *Journal of Guidance, Control, and Dynamics*, No. 1, 1997, pp. 208–211.
- [96] Shuster, M., "Survey of attitude representations," *Journal of the Astronautical Sciences*, Vol. 41, 1993, pp. 439–517.
- [97] Markley, F., "Parameterization of the Attitude," *Spacecraft Attitude Determination and Control*, pp. 414–416.
- [98] Reynolds, R., "Quaternion parameterization and global attitude estimation," *TRW Space and Electronics Group, Flight Mechanics Symposium 1997 p 347- 355(SEE N 97-19546 01-13)*, 1997.
- [99] Reynolds, R., "Quaternion parametrization and a simple algorithm for global attitude estimation," *Journal of Guidance, Control, and Dynamics*, Vol. 21, No. 4, 1998, pp. 669–671.
- [100] Wahba, G., "A least squares estimate of spacecraft attitude," *SIAM Review*, Vol. 7, No. 3, 1965, pp. 409.
- [101] Shuster, M., "The QUEST for better attitudes," *Journal of the Astronautical Sciences*, Vol. 54, No. 3/4, 2006, pp. 657.
- [102] SHUSTER, M., "A simple Kalman filter and smoother for spacecraft attitude," *Journal of the Astronautical Sciences*, Vol. 37, 1989, pp. 89–106.
- [103] Bar-Itzhack, Y., "REQUEST: A Recursive QUEST Algorithm for Sequential Attitude Determination," *Journal of Guidance, Control and Dynamics*, Vol. 19, No. 5, 1996, pp. 1034–1038.
- [104] Psiaki, M., "Attitude-determination filtering via extended quaternion estimation," *Journal of Guidance, Control, and Dynamics*, Vol. 23, No. 2, 2000, pp. 206–214.
- [105] Crassidis, J., Markley, F., and Cheng, Y., "Survey of nonlinear attitude estimation methods," *Journal of Guidance Control and Dynamics*, Vol. 30, No. 1, 2007, pp. 12.
- [106] Farrell, J., "Attitude determination by Kalman filtering," *Automatica*, Vol. 6, No. 3, 1970, pp. 419–430.
- [107] Schmidt, S., "The Kalman Filter: Its Recognition and Development for Aerospace Applications," *Journal of Guidance Control and Dynamics*, 1981.
- [108] Psiaki, M., "Backward-smoothing extended Kalman filter," *Journal of Guidance Control and Dynamics*, Vol. 28, No. 5, 2005, pp. 885.

- [109] Lefferts, E., Markley, F., and Shuster, M., "Kalman filtering for spacecraft attitude estimation," *Journal of Guidance, Control, and Dynamics*, Vol. 5, No. 5, 1982, pp. 417–429.
- [110] Markley, F. et al., "Attitude error representations for Kalman filtering," *Journal of Guidance Control and Dynamics*, Vol. 26, No. 2, 2003, pp. 311–317.
- [111] Bar-Itzhack, I. and Oshman, Y., "Attitude determination from vector observations: quaternion estimation," *IEEE Transactions on Aerospace and Electronic Systems*, 1985, pp. 128–136.
- [112] Bar-Itzhack, I., Deutschmann, J., and Markley, F., "Quaternion normalization in additive EKF for spacecraft attitude determination," *Flight Mechanics/Estimation Theory Symposium, 1991 p 403-421(SEE N 92-14070 05-13)*, 1991.
- [113] Deutschmann, J., Bar-Itzhack, I., and Galal, K., "Quaternion normalization in spacecraft attitude determination," *AIAA/AAS Astrodynamics Conference*, 1992, pp. 27–37.
- [114] Markley, F., "Attitude Estimation or Quaternion Estimation?" *Journal of Astronautical Sciences*, Vol. 52, No. 1, 2004, pp. 221–238.
- [115] "Honeywell Magnetometer HMC2003,"  
<http://www.ssec.honeywell.com/magnetic/datasheets/hmc2003.pdf>.
- [116] Crassidis, J. and Markley, F., "Unscented filtering for spacecraft attitude estimation," *Journal of Guidance Control and Dynamics*, Vol. 26, No. 4, 2003, pp. 536–542.
- [117] "Analog Devices Tri-Axis Inertial Sensor with Magnetometer ADIS16405,"  
[http://www.analog.com/static/imported-files/data\\_sheets/ADIS16405.pdf](http://www.analog.com/static/imported-files/data_sheets/ADIS16405.pdf).
- [118] Farrenkopf, R., "Analytic Steady-State Accuracy Solutions for Two Common Spacecraft Attitude Estimators," *Journal of Guidance and Control*, Vol. 1, No. 4, 1978, pp. 282–284.
- [119] Hoffman, D. and McElroy, T., "HEAO attitude reference design," *American Astronautical Society, Annual Rocky Mountain Guidance and Control Conference, Keystone, Colo., Mar. 10-13, 1978, 21 p.*, 1978.
- [120] Natanson, G., Challa, M., Deutschmann, J., and Baker, D., "Magnetometer-only attitude and rate determination for a gyro-less spacecraft," *Space Mission Operations and Ground Data Systems*, Vol. 1, 1994, pp. 791–798.
- [121] Natanson, G., McLaughlin, S., and Nicklas, R., "A method of determining attitude from magnetometer data only," *Flight Mechanics/Estimation Theory Symposium*, Vol. 1, 1990, pp. 359–378.

- [122] Shuster, M., "SCAD—A Fast Algorithm for Star Camera Attitude Determination," *Journal of the Astronautical Sciences*, Vol. 52, No. 3, 2004, pp. 391–404.
- [123] "Analytical Graphics, Inc. (AGI) - Satellite Tool Kit (STK)," <http://www.stk.com/>.
- [124] Crassidis, J. and Junkins, J., *Optimal estimation of dynamic systems*, Chapman & Hall, 2004.

## BIOGRAPHICAL SKETCH

Sharanabasaweshwara Ashok Asundi was born in Belgaum, a small town in southern India. He completed his bachelor's degree in mechanical engineering from Bangalore University in Spring 2001 and worked as a systems engineer for 3 years with Tata Infotech Ltd now a part of Tata Consultancy Services.

Mr. Asundi joined the graduate program of Mechanical and Aerospace Engineering at University of Florida in 2004 with assistantship support from Dr. Norman Fitz-Coy and the department. His research interests include design of autonomous ground and space systems, spacecraft attitude determination and estimation, vehicle health monitoring and design of small satellite mission operations.